



Lawrence Berkeley Laboratory

UNIVERSITY OF CALIFORNIA

Materials & Molecular Research Division

RECEIVED
LAWRENCE
BERKELEY LABORATORY
DEC 16 1981
LIBRARY AND
DOCUMENTS SECTION

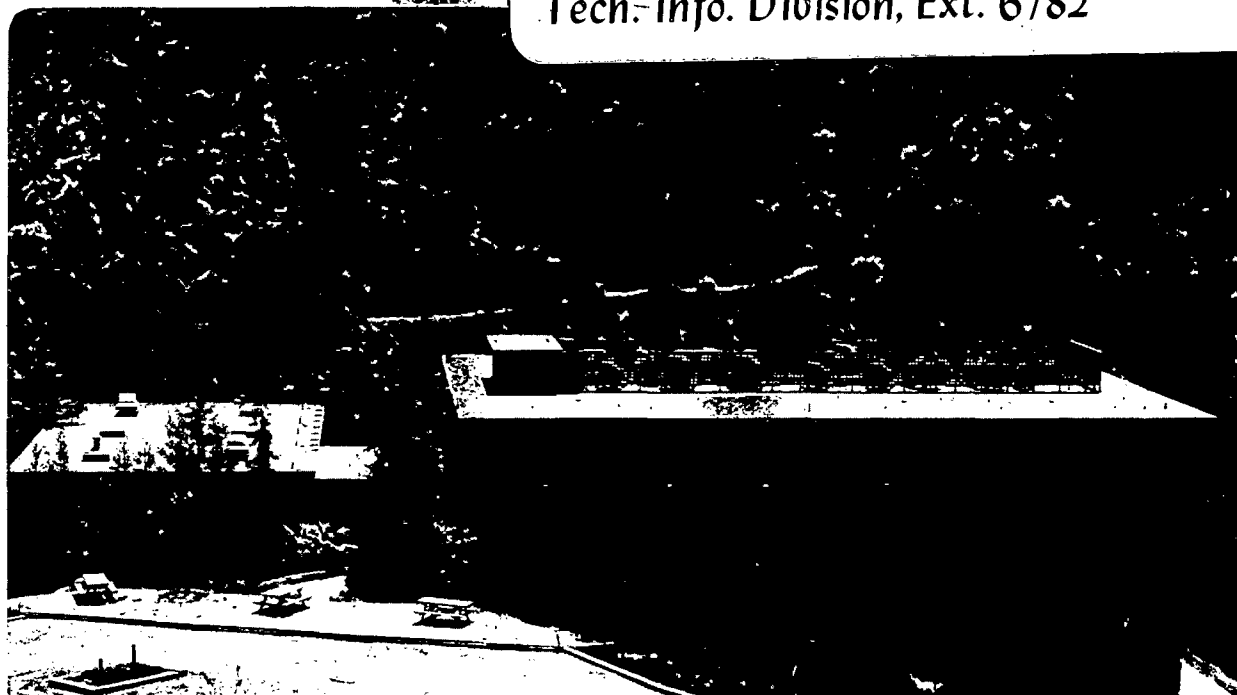
PHOTOCATALYTIC HYDROGEN PRODUCTION FROM WATER AND
INTERMETALLIC COMPOUND FORMATION ON SINGLE-CRYSTAL
SURFACES OF TITANIUM OXIDES

Frederick Tadeusz Wagner
(Ph.D. thesis)

September 1981

TWO-WEEK LOAN COPY

*This is a Library Circulating Copy
which may be borrowed for two weeks.
For a personal retention copy, call
Tech. Info. Division, Ext. 6782*



LBL-13634
c.2

DISCLAIMER

This document was prepared as an account of work sponsored by the United States Government. While this document is believed to contain correct information, neither the United States Government nor any agency thereof, nor the Regents of the University of California, nor any of their employees, makes any warranty, express or implied, or assumes any legal responsibility for the accuracy, completeness, or usefulness of any information, apparatus, product, or process disclosed, or represents that its use would not infringe privately owned rights. Reference herein to any specific commercial product, process, or service by its trade name, trademark, manufacturer, or otherwise, does not necessarily constitute or imply its endorsement, recommendation, or favoring by the United States Government or any agency thereof, or the Regents of the University of California. The views and opinions of authors expressed herein do not necessarily state or reflect those of the United States Government or any agency thereof or the Regents of the University of California.

PHOTOCATALYTIC HYDROGEN PRODUCTION FROM WATER AND
INTERMETALLIC COMPOUND FORMATION ON SINGLE-CRYSTAL
SURFACES OF TITANIUM OXIDES

Copyright © 1981

by

Frederick Tadeusz Wagner

Ph.D. Thesis

September 1981

Materials and Molecular Research Division
Lawrence Berkeley Laboratory
University of California
and
Department of Chemistry
University of California
Berkeley, CA 94720

The United States Department of Energy has the right to use this thesis for any purpose whatsoever including the right to reproduce all of any part thereof.

This work was supported by the Division of Chemical Sciences, Office of Basic Energy Sciences of the U.S. Department of Energy under Contract Number W-7405-ENG-48.

PHOTOCATALYTIC HYDROGEN PRODUCTION FROM WATER AND
INTERMETALLIC COMPOUND FORMATION ON SINGLE-CRYSTAL
SURFACES OF TITANIUM OXIDES

Frederick Tadeusz Wagner

Materials and Molecular Research Division
Lawrence Berkeley Laboratory
University of California

and
Department of Chemistry
University of California
Berkeley, CA 94720

September, 1981

ABSTRACT

The photocatalytic and photoelectrochemical properties of SrTiO_3 surfaces were studied in several different gas and liquid-phase environments. Platinized SrTiO_3 crystals catalyzed the dissociation of water to hydrogen and oxygen when illuminated with bandgap radiation in aqueous alkaline electrolytes or in water vapor when covered by films of basic deliquescent compounds. The rate of photodissociation increased rapidly at alkali hydroxide concentrations above 5M. No photoactivity was seen in neutral or acidic solutions, nor in water vapor at 300°K in the absence of basic films.

Platinum-free SrTiO_3 was also active for hydrogen photogeneration. All chemistry occurred on the illuminated surface of the semiconductor. Photoactivity on metal-free surfaces also increased at higher hydroxide concentrations. The mechanisms by which both surface and electrolyte hydroxide species can promote photocatalysis at the gas-solid interface were explored. The differences between the catalysis of water

photodissociation at the liquid-solid and gas-solid interfaces are discussed.

The structure and composition of ultra-thin films of Pd and Au on TiO_2 (110) and (750), $\alpha\text{-Al}_2\text{O}_3$ (0001), and highly oriented pyrolytic graphite were studied by low energy electron diffraction (LEED) and Auger electron spectroscopy (AES). Partially ordered films were grown on TiO_2 , with the epitaxial relationships for Pd being altered by the presence of steps on the (750) surface. AES and LEED gave evidence for the formation of an intermetallic compound upon annealing Pd films on TiO_2 . No ordering was seen in the films on $\alpha\text{-Al}_2\text{O}_3$ or graphite, where AES gave no indication of chemical interaction between substrate and deposit. Auger peak shape changes for Pd films correlated with metal particle size. Auger electron attenuation data were used for the determination of film morphology.

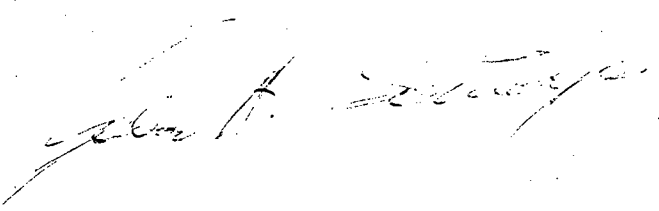


TABLE OF CONTENTS

Table of contents.....	i
Acknowledgements.....	vii
Chapter I: Introduction.....	1
Chapter II: Theory of Semiconductor Photoelectrochemistry and Heterogeneous Photocatalysis.....	6
II-1 Introduction.....	6
II-2 Photosynthetic Electrochemical Cells.....	7
II-2-1 Depletion Layer Formation.....	9
II-2-2 Origin of the Surface Barrier Potential.....	12
II-2-3 The Flatband Potential.....	13
II-2-4 The Energetics of Water Photodissociation.....	17
II-2-5 Energy Levels in Aqueous Solutions.....	19
II-2-6 Charge Transfer at the Semiconductor-Electrolyte Interface.....	22
II-2-7 Surface State Mediation of Charge Transfer.....	24
II-3 Kinetics of Photoelectrochemical Cells.....	27
II-3-2 Light Absorption and Bulk Recombination.....	29
II-3-3 Surface Recombination.....	32
II-3-4 Back and Side Reactions.....	34
II-3-5 Summary of Photoelectrochemical Theory.....	36
II-4 Theory of Heterogeneous Photocatalysis.....	38
II-4-1 Introduction.....	38

II-4-2 Photocatalysts as Micro-PEC Cells.....	39
II-4-3 Photocatalysis as a Localized Process.....	40
II-4-4 Comparison of the Gas-Solid and Liquid-Solid Interfaces.....	43
II-5 The Solar Resource and Quantum Conversion.....	51
References.....	56
Chapter III: Selective Review of the Photochemical and Photocatalytic Experimental Literature.....	60
III-1 Photosynthetic Cells.....	60
III-1-1 PEC Cells for Water Photoelectrolysis.....	60
III-1-2 PEC Cells for CO ² Reduction.....	66
III-2 Liquid Junction Solar Cells.....	68
III-3 Photocatalytic Systems: Catalytic Criteria.....	70
III-4 Photocatalysis at the Liquid-Solid Interface.....	72
Single-phase photocatalysts in liquid electrolytes.....	74
III-5 Photocatalysis at the Gas-Solid Interface.....	75
III-6 Surface States in Photoelectrochemistry and Photocatalysis.....	79
References.....	85
Chapter IV: Experimental Apparatus and Techniques.....	91
IV-1 Reaction Vessels for the Study of Heterogeneous Photochemistry.....	91

IV-1-1 Unified Surface Analysis - Photoreaction Chamber.....	91
IV-1-2 Photocatalytic Experiments in Bulk Liquid Electrolytes.....	94
IV-1-3 Photoelectrochemical Measurements.....	94
IV-2 Gaseous Product Detection.....	95
IV-3 Light Source.....	100
IV-4 Sample Preparation.....	101
IV-5 Gases and Reagents.....	105
IV-6 Other Surface Analysis Equipment Used in Photochemical Studies.....	106
IV-7 Apparatus for Deposition and Characterization of Thin Metal Films.....	106
References.....	111
Chapter V: Photocatalysis on SrTiO ₃ - Experimental Results.....	113
V-1 The Structure and Chemical Composition of the SrTiO ₃ (111) Surface.....	113
V-1-1 The (111) Termination of the SrTiO ₃ Bulk Structure.....	113
V-1-2 The Unit Mesh of the SrTiO ₃ (111) Surface.....	115
V-1-3 Compositional changes with Surface Pre-Treatment.....	115
V-2 Photocatalytic Activity of Clean SrTiO ₃ and SrTiO ₃ /Pt with Water Vapor and Other Gases.....	120

V-2-1 Water Vapor and CO ₂	120
V-2-2 SrTiO ₃ in Mixed Vapors of Water and Volatile Bases....	121
V-2-3 H ₂ Production from Reduced SrTiO ₃ at Elevated Temperatures in Room Temperature Water Vapor.....	128
V-2-4 Back Reactions.....	131
V-3 Photoactivity of NaOH-coated SrTiO ₃	133
V-3-1 Photoactivity of NaOH-coated Platinized SrTiO ₃	133
V-3-2 Hydrogen photogeneration on NaOH-coated, Metal-free SrTiO ₃	144
V-4 Photoactivity of SrTiO ₃ in Bulk Aqueous Electrolyte.....	148
V-4-1 Platinized SrTiO ₃ in Aqueous Electrolytes.....	148
V-4-2 Photoactivity of Pt-free SrTiO ₃ in Aqueous Electrolytes.....	157
Hydroxide Dependence.....	161
Pertitanates and soluble titanium.....	161
Other Concentrated Electrolytes.....	163
Electrolyte Purity.....	164
Photochemistry on Other Oxides.....	167
Post-reaction Surface Analysis.....	168
References.....	182
 Chapter VI: LEED-Auger Studies of Ultra-thin Pd and Au Films on Graphite, α-Al ₂ O ₃ , and TiO ₂ . Film Structure and Thermal Intermetallic Compound Formation.....	
VI-1 Introduction.....	187

VI-2 Deposition of Pd and Au on Graphite: Particle Size Effects...	195
VI-3 Au and Pd on α -Al ₂ O ₃	208
VI-4 Pd and Au on TiO ₂	219
VI-4-1 The Structure of Clean Rutile Surfaces.....	220
VI-4-2 Auger Spectroscopy of Clean TiO ₂	228
VI-4-3 Auger Spectroscopy and LEED of Pd and Au on TiO ₂	230
1) LEED patterns indicative of weak substrate-overlayer interactions.....	233
2) Auger evidence for intermetallic compound formation.....	239
3) LEED patterns indicative of stronger Pd-TiO ₂ interactions.....	239
4) Film morphology by Auger.....	249
VI-5 Comparison of Results for Pd and Au on Graphite, α -Al ₂ O ₃ , and TiO ₂	257
References.....	261
Chapter VII: General Discussion.....	264
VII-1 Hydrogen Production on Metal-free Oxides.....	264
VII-2 Hydroxide Concentration Effects on SrTiO ₃ Photoactivity....	275
VII-3 Gas-Phase Considerations.....	288
VII-4 Photochemical and Catalytic Significance of Intermetallic Compound Formation.....	292

VII-5 Suggestions for Future Research.....	294
VII-5-1 Choice of Future Photocatalysts for Water Photolysis	294
Semiconductor-Electron Affinity.....	295
Photocorrosion.....	301
VII-5-2 Other Photocatalytic Reactions.....	305
VII-6 Summary of Proposed Future Photochemical Work.....	306
References.....	308
Appendix: Film Morphology by Auger Electron Spectroscopy.....	312

ACKNOWLEDGEMENTS

I wish to sincerely thank my research advisor, Professor Gabor A. Somorjai, for his unwavering support, his encouragement, and his scientific guidance throughout my graduate career. His group has proven a most stimulating environment in which to learn the ways and means of science. Special thanks are owed to many individuals in the group for their scientific insights, technical aid, and friendship. Steve Overbury dutifully launched me on my first Auger spectrometer. Larry Firment and Dave Castner taught me the many virtues of tantalum foil and otherwise introduced me to the tricks of the trade. Steve Abensohn and Larry Du Bois brightened the long nights down on D-level; Jon Sokol, Sylvia Ceyer, Bill Gillespie, and Ad Sachtler kept the darkened halls alive on the hill. Mark Davis was a constant source of accurate information, good humor, and inspiration by his maintenance of linguistic diversity through four years. The (molecularly) beaming faces of Bill Guthrie and Te-hua Lin were always welcome sights. I would like to thank John Hemminger for introducing me to the field of photocatalysis. Salvador Ferrer, Roger Carr, and Marjorie Langell provided many thoughtful discussions on oxides and semiconductor photochemistry. Jean-Paul Biberian was helpful with LEED patterns and thin film growth. The undergraduate assistance of Tony Ricco in performing the light intensity dependence measurements is gratefully acknowledged.

I would like to thank Dr. Philip Ross, Jr. for many illuminating discussions and the use of apparatus in the latter parts of this work. I was most fortunate to T.A. under Professor Tony Cheatham, whose pedagogy was a true inspiration. Conversations with Drs. A.J. Nozik and Frank Mares, and Professors W.K. Hall, G. Munuera, and M.S. Wrighton

were of great help in this research.

The entire technical and support staff of MMRD deserves thanks for making progress possible. Phil Eggers and Jim Severns miraculously restored burnt, frazzled, or just plain tuckered out electronics to useful activity. Emery Kozak, Bob McAllister, and Weyland Wong performed wonders with tool and mind. Lee Johnson's cheerful presence shortened the long grinds in the metallographic lab. Johns Jacobson and Holthuis kept the furnace fires burning for sample preparation. Glenn Baum provided help in many ways, even though he still hasn't taught his nose to sniff out helium without a mass spectrometer. The facile pen and infinite patience of Gloria Pelatowski are responsible for the many fine drawings in this thesis - the squirmy ones are my own.

My parents and brothers get my great thanks for their support and for putting up with this strange beast of a scientist in their midst. Last but foremost I would like to express my gratitude to Barbara Shohl, whose quiet wisdom, playful sense of humor, and constant encouragement have made the later part of this work, and a fuller life, possible. I hope that the completion of this tome will give her fingers time to fly from the word processor where they've been dancing overlong to another, more melodious, keyboard where they belong.

I would also like to thank the people of the State of California and the United States of America for their continued faith in the value of education and research. Specifically, this work was supported under Contract Number W-7405-ENG-48 with the Division of Chemical Sciences, Office of Basic Energy Science, U.S. Department of Energy.

I. Introduction

Metal oxides form essential parts of heterogeneous catalytic systems. In some cases, such as petroleum reforming on alumina-supported platinum, the oxide serves as a relatively inert means of dispersing an expensive active metal catalyst. In other systems the oxide provides unique active sites which work synergistically with metal sites to catalyze the desired overall reaction. Metal oxides themselves are important catalysts in a number of commercial processes, such as SO_2 oxidation.

While most oxides commonly employed in catalytic systems (e.g. SiO_2 , Al_2O_3 , Cr_2O_3) are insulators which undergo no chemical excitation by sunlight, a number of oxides (e.g. TiO_2 , Fe_2O_3 , SrTiO_3 , ZnO) are medium bandgap semiconductors which can be excited by part of the solar spectrum. This solar absorptivity raises the possibility of photoassisted heterogeneous catalysis, in which the influence of light may lead to unique catalytic pathways. Photon energy can also be used to drive endergonic "thermodynamically uphill" reactions on semiconductor surfaces, allowing solar energy to be stored as a chemical fuel. Technical perfection of such a process would effectively allow sunlight and a common low energy compound to be burnt together as a fuel. Of all such reactions, the photoassisted decomposition of water has received the most research attention due to the negligible costs of water as a reactant and the value of hydrogen as a chemical feedstock and an environmentally benign fuel. The most effective direct solar water-dissociating device to date is a photoelectrochemical cell using a SrTiO_3 photoanode and a platinum cathode which achieves a 1% solar-energy-to-hydrogen conversion efficiency. Although a large number of

photoelectrochemical systems have been investigated and the thermodynamic parameters governing their operation have been identified, the catalytic effects at the interfaces and the details of the reaction mechanisms are as yet inadequately understood. Photocatalytic devices other than photoelectrochemical cells have also remained little explored. This thesis embodies part of a study designed to fill some of these gaps in knowledge.

The advent in the 1960s of ultra-high vacuum surface analytical techniques has made possible the understanding of heterogeneous catalysis at the atomic level. Improvements in technology have allowed clean, well-ordered and well-characterized catalytic surfaces to be prepared, gas phase reactions on the surface to be followed at pressures up to several atmospheres, and the surface to be again analyzed after the gases have been pumped away. These techniques have permitted, for example, the effects of surface structure, chemical pretreatment, and carbon overlayer formation on hydrocarbon catalysis by platinum to be discerned. Comparison of these studies with industrial catalysis is facilitated by the ability to study single-crystal catalysis over a wide enough pressure range (10^{-7} torr - 1 atm) that extrapolation of results becomes possible.

The study of water photodissociation at the atomic scale requires an even better understanding of how the interface changes as the density of the fluid phase increases. Before the inception of these studies, sustained photodissociation of water on semiconductors had been reported only in aqueous solution, while surface analytical techniques in general require very low ($< 10^{-7}$ torr) gas pressures. Of necessity, the results

reported in this thesis span a wide range of reaction conditions. Topics considered include: (1) the structure and chemical composition of clean SrTiO_3 and TiO_2 surfaces prepared in ultra-high vacuum, (2) the limits to photoreactivity of these materials in water vapor at up to 20 torr pressure, (3) the dependence of the photoreactivity of these materials in aqueous electrolytes on the electrolyte composition, (4) the surface composition of semiconductors exposed to and illuminated in aqueous electrolytes, and (5) the effects of transition metal films on semiconductor photoreactivity in aqueous solution and the thermal reactions of these films with semiconductors in vacuo. Throughout the discussions an attempt will be made to clarify the similarities and discrepancies among the properties of the vacuum-semiconductor, gas-semiconductor, and liquid electrolyte-semiconductor interfaces.

Chapter II provides an overview of the theory of photoelectrochemical cells and heterogeneous photocatalysis. Separation of photogenerated charge carriers, charge transfer across the interface, and recombination effects are considered for PEC cells. The energetics of water dissociation are related to the semiconductor band structure, and required properties of photoelectrodes for water dissociation are delineated. Several models for the operation of heterogeneous photocatalytic systems are compared, and important differences between the gas-semiconductor and liquid-semiconductor interfaces are outlined.

A brief review of important experimental developments in photocatalysis and photoelectrochemistry are given in Chapter III. No attempt at exhaustive coverage is made, but the major classes of materials being investigated as possible photocatalysts are reviewed with particular

emphasis on water photodissociation and the reduction of carbon dioxide.

Chapter IV describes the experimental equipment and methods used in the present investigations. Both the equipment used for detailed surface studies and that used for the more exploratory work are covered.

Chapter V contains the results of the surface photochemical investigations. The structure and composition of clean SrTiO_3 surfaces are described. Details of attempts to measure photocatalytic activity at the gas- SrTiO_3 interface are given, and the possibilities of a catalytic back-reaction are probed. The photoactivity of SrTiO_3 and $\text{SrTiO}_3\text{-Pt}$ in films of various ionic compounds, and the effects of the concentration of aqueous hydroxide solutions on photoactivity are shown. The locus of hydrogen evolution on metal-free SrTiO_3 is determined. Several other oxide semiconductors are shown to be photocatalytically inert under identical conditions. The effects on surface composition of contact with and illumination in several aqueous electrolytes is described.

Chapter VI summarizes some more classical surface science studies of the deposition of ultra-thin Pd and Au films on graphite, alumina, and titania. The Pd Auger peak shape is shown to vary with the size of metal particles. Several LEED patterns occur for Pd on TiO_2 , and the presence of steps on the surface alters the epitaxial relationships. LEED and Auger evidence for the formation of a Pd-Ti intermetallic compound are discussed, and suggestions for further work along these lines are made.

In Chapters V and VI relatively minor points of controversy are discussed as they arise in the results. The more major experimental find-

ings, such as the photocatalytic generation of hydrogen on metal-free SrTiO_3 and the hydroxide concentration dependence of the photoactivity are discussed in greater detail in Chapter VII. The implications of the results for photochemistry at the gas-solid interface are also dealt with. General guidelines for the choice of materials for use as photoelectrodes and photocatalysts are given, and a number of materials and reactions for further photochemical study are suggested.

Appendix I explains some of the Auger modeling techniques used in the determinations of film morphology discussed in Chapter VI.

This thesis reports a rather odd mix of some detailed surface characterization work and a mass of exploratory research using photocatalysts with less well-defined surfaces. Surface photochemistry is a young field whose coarse characteristics have yet to be completely defined - one must be prepared to excavate the veins of knowledge with a steam shovel as well as with a dental pick. It is hoped that the work described herein may serve to define some of the similarities and differences between photocatalytic systems using gaseous reactants and photoelectrochemical cells operating in liquid electrolytes. By understanding both systems and their interrelations we can obtain a more fundamental understanding of surface photochemistry than could be obtained from either system alone.

Chapter II: Theory of Semiconductor Photoelectrochemistry and Heterogeneous Photocatalysis

II-1. Introduction

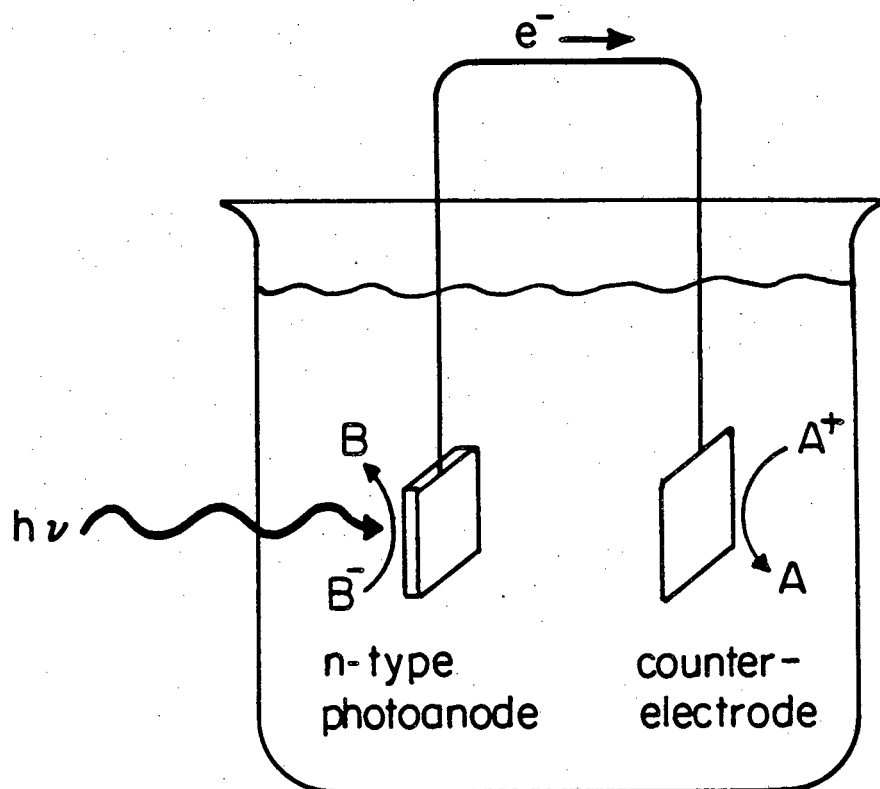
A photoexcited semiconductor can theoretically drive any endergonic chemical reaction whose ΔG is less than the bandgap of the semiconductor. A number of configurations of the semiconductor, reactants, and auxiliary catalysts have been explored in hopes of bringing about such chemistry. Most research effort to date has been devoted to photoelectrochemical (PEC) cells utilizing discrete electrodes immersed in liquid electrolytes. PEC cells can be divided into three classes. Photosynthetic cells, those of most interest here, drive net chemical reactions with positive free energy changes. In liquid junction solar cells no net chemical reaction occurs, but electric power is generated. Photocatalytic cells accelerate thermodynamically downhill reactions. The theory of all three types of cells has been rather extensively reviewed.

While PEC cells have been more thoroughly investigated, simpler devices for heterogeneous photocatalysis also show promise. In these systems no discrete electrodes exist; rather, the semiconductor and cocatalysts are simply placed in contact with the reactants, which may be in the solid, liquid, and/or gas phase(s). Both the theoretical and experimental aspects of heterogeneous photocatalysis are less advanced than in the case of PEC cells. This chapter provides a comparative review of the theory of photosynthetic PEC cells and of heterogeneous photocatalysis, concentrating on the photodissociation of water. The similarities and differences between the semiconductor-liquid and

semiconductor-gas interfaces are considered, and the roles of surface species are stressed throughout.

II-2. Photosynthetic Electrochemical Cells

A schematic diagram of a photosynthetic PEC cell is given in Figure II-1. The cell consists of a semiconductor electrode (n-type anode, as here, or p-type cathode) and a passive counterelectrode immersed in a liquid electrolyte containing a reducible substrate A^+ and an oxidizable substrate B^- . An external circuit connects the two electrodes. Upon illumination of the (n-type) semiconductor with supra-bandgap radiation ($h\nu \geq E_g$), electrons flow to the counterelectrode, driving the half-reaction $A^+ + e^- \rightarrow A$. Holes flow to the semiconductor surface, driving an oxidation reaction: $h^+ + B^- \rightarrow B$. The net reaction is $A^+ + B^- \rightarrow A + B$. The electrical circuit is completed by ion transport between the electrodes. The key steps in the operation of the cell are (1) photogeneration and separation of charge carriers (electrons and holes), (2) charge transfer across the solid-electrolyte interface, and (3) catalyzed reactions leading to the final products. These steps compete with bulk and surface recombination processes. Charge carrier separation is effected by the electric field within the majority carrier depletion layer, which forms on the semiconductor side of the interface; charge transfer rates depend upon the available energy states on both sides of the interface.



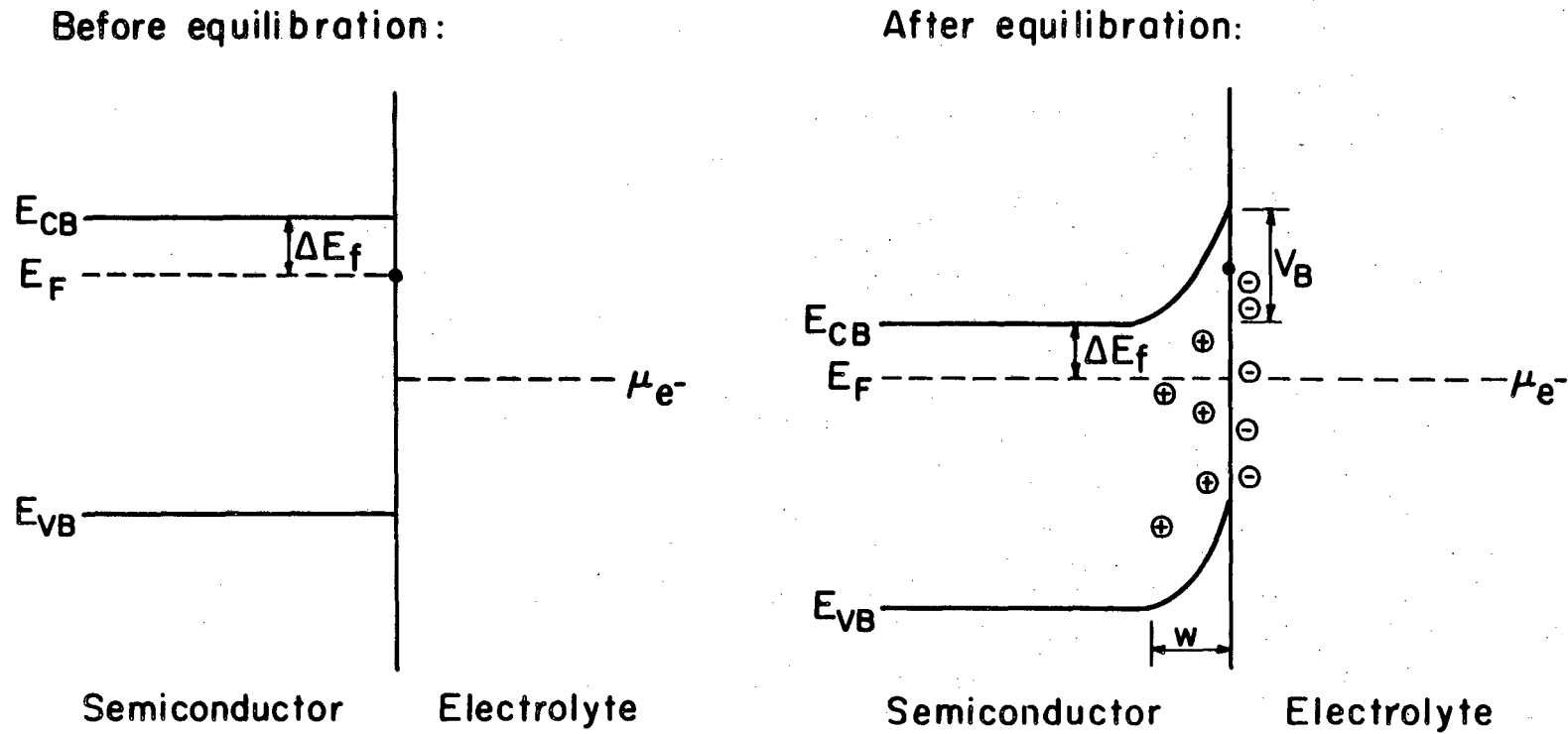
XBL 818-6326

Fig. II-1. A photosynthetic photoelectrochemical cell.

II-2-1. Depletion Layer Formation

The first-order theory of depletion layer formation in PEC cells draws concepts from solid-state physics and the Schottky treatment of the semiconductor-metal interface. Figure II-2 outlines barrier formation at the semiconductor-electrolyte interface. Before equilibration, the Fermi level of the (n-type) semiconductor lies above (i.e. closer to the vacuum level than) the chemical potential of electrons in the electrolyte. Upon equilibration in the dark, electrons flow from semiconductor to electrolyte until the chemical potential of electrons is equal throughout the system, and a double-layer barrier is formed at the interface. This double-layer is highly asymmetric, due to the different maximum charge densities which can be sustained in the two phases. In the electrolyte both positive and negative carriers (ions) are mobile, and surface charge densities greater than 10^{14} cm^{-2} can easily develop. Essentially all of the charge transferred to the electrolyte resides right at the interface. In the n-type semiconductor, however, only electrons are mobile in the dark; and the maximum positive charge density which can be developed is set by the concentration of immobile ionized donor states, which has a maximum of 10^{19} cm^{-3} ($\sim 10^{12} \text{ cm}^{-2}$) in highly doped oxide semiconductors. The semiconductor will be completely depleted of mobile electrons for many layers beneath the surface, leaving a region of constant positive charge density N_D . The potential in this region can be treated by Poisson's equation in one dimension, x , the distance in from the semiconductor surface:

Fig. II-2 DEPLETION LAYER FORMATION



$$w = \left(\frac{2 \epsilon \epsilon_0 V_B}{q N_D} \right)^{1/2}$$

XBL 802-4703

$$\frac{d^2V}{dx^2} = \frac{-qN_D}{\epsilon\epsilon_0} \quad (\text{II-1})$$

where q is the electronic charge and ϵ the semiconductor dielectric constant. Integrating and applying the boundary conditions $V(0) = V_s$, $V'(w) = 0$, $V(w) = 0$, one finds

$$V(x) = \frac{N_D}{2\epsilon\epsilon_0} x^2 - \frac{N_D w}{\epsilon\epsilon_0} x + V_s \quad (\text{II-2})$$

where $w = \left(\frac{2\epsilon\epsilon_0 V_s}{qN_D} \right)^{1/2}$ is the width of the depletion layer, typically 200 - 10,000 Å. In this simple treatment V_s is the initial difference between the chemical potential of electrons in the two phases.

Similar treatment of the electrolyte side of the interface requires an additional Boltzmann concentration term due to the mobility of the charge carriers, and the required definition of a dielectric constant in the near-surface region poses great problems. The full Guoy-Chapmann approach (which assumes a constant dielectric constant), shows that charge layer thicknesses less than 10 Å would be expected for reasonable electrolyte concentrations. The electrolyte side of the interface is then best treated as a single Helmholtz layer of ions and solvent molecules rather than as a diffuse layer. Low-mass particles such as electrons can easily tunnel through the potential barrier associated with this thin layer.

Absorption of a photon with energy greater than the bandgap of the semiconductor promotes an electron from the valence band into the con-

duction band, leaving a hole in the former. The electron and hole will recombine unless spatially separated by the electric field in the depletion layer. Efficient conversion of photon energy thus requires that photons be absorbed within the depletion layer. 95% of photons will be absorbed within $3/\alpha$ of the surface, where α is the absorption coefficient for the particular wavelength of the photon. Since w , the depletion layer width, depends upon V_s , the surface barrier height, knowledge of the latter is necessary to predict the properties of PEC cells.

II-2-2. Origin of the Surface Barrier Potential

The surface barrier is set, to first approximation, by the initial difference in chemical potentials of electrons in the electrolyte and semiconductor. The "chemical potential of electrons in the electrolyte", sometimes called the "Fermi level of the electrolyte",¹ is a slippery concept. If there is only one active redox couple in the electrolyte, and if a good catalyst for the interconversion of the reduced and oxidized species is present, then the electron chemical potential is simply the concentration-dependent redox potential of the couple. An example of such an ideal electrolyte is an aqueous potassium ferro-ferricyanide solution in the presence of a platinum catalyst. Electrochemical energies can be related to the general vacuum level by a thermodynamic cycle which places the level of the normal hydrogen electrode 4.5 eV below vacuum.² In photosynthetic cells there are two active redox couples in solution and, at least after operation of the cell, not all reactants and products in the two couples will be in equilibrium. For example, after operation of a water electrolysis cell the cathode will be charged with hydrogen at ~ 1 atm and the anode with oxygen at ~ 1 atm. The

pressure of hydrogen and oxygen in equilibrium with water is $\sim 10^{-14}$ atmospheres. Contrary to common usage in the photoelectrochemical literature, no single chemical potential of electrons can exist in such a system. One must then understand which part of the electrolyte system, if any, equilibrates electronically with the semiconductor, and the strict analogy with Schottky barrier formation breaks down.

Hydrogen evolution on platinum is very close to a reversible process, as overpotentials of less than 0.05 V are common at the 1 mA cm^{-2} current densities typical of PEC cells. Once the Pt is saturated with hydrogen, the Fermi level of the platinum is fixed at the level of the hydrogen redox couple in the electrolyte. If direct contact is provided between the platinum and semiconductor, the dark Fermi levels of both electrodes will be fixed at the hydrogen redox potential. Oxygen evolution from aqueous electrolytes on oxide semiconductors is a highly non-reversible process, requiring overpotentials of several tenths of volts at mA cm^{-2} current densities. This irreversibility decouples the semiconductor surface oxygen pressure from the Fermi level of the electrodes as long as the platinum remains saturated with hydrogen.

II-2-3. The Flatband Potential

The relative position of the semiconductor band edges and the hydrogen couple can be determined by measuring the differential capacity of the semiconductor electrode as a function of applied potential. The Mott-Schottky equation ^{3,4} predicts a linear relation between the inverse square surface capacitance and an applied potential V_a :

$$C^{-2} = \left(\frac{1}{2} q N_D kT \ll \epsilon_0 A^2 \right)^{-1} \left(V_a - V_{fb} - \frac{kT}{e} \right)$$

(II-3)

Here $V_a - V_{fb} = V_s$. V_{fb} , the flatband potential, is the potential of the Fermi level of the semiconductor when the surface barrier potential is completely compensated by the external potential. In the commonly used heavily doped oxides the energy difference between the Fermi level and conduction band, ΔE_F , is small under flatband conditions, and the flatband potential is a good approximation of the position of the conduction band edge. When the n-type semiconductor rests at a potential anodic (positive) of V_{fb} , a depletion layer is present. If the flatband potential of an n-type semiconductor lies cathodic (negative, or above) the hydrogen redox couple, hydrogen photogeneration with no applied potential is possible. Essentially all of an applied potential appears across the semiconductor depletion layer rather than the electrolyte Helmholtz layer due to the difference in the charge densities which the phases can support. This effect has been confirmed experimentally.

Figure II-3 (after Nozik)⁵ summarizes flatband potential data for a number of semiconductors. It can be seen that while some oxides (SrTiO_3 , KTaO_3) and other semiconductors are thermodynamically capable of hydrogen evolution from water with no external applied potential, others (SnO_2 , WO_3) are not. Butler and Ginley⁶ have shown that the flatband potential of a compound semiconductor correlates well with the geometric mean of the Mulliken electronegativities of the constituent atoms. One can thus predict the changes in flatband potential which would accompany a change in surface composition - addition of an element with a low electronegativity to the semiconductor will in general shift

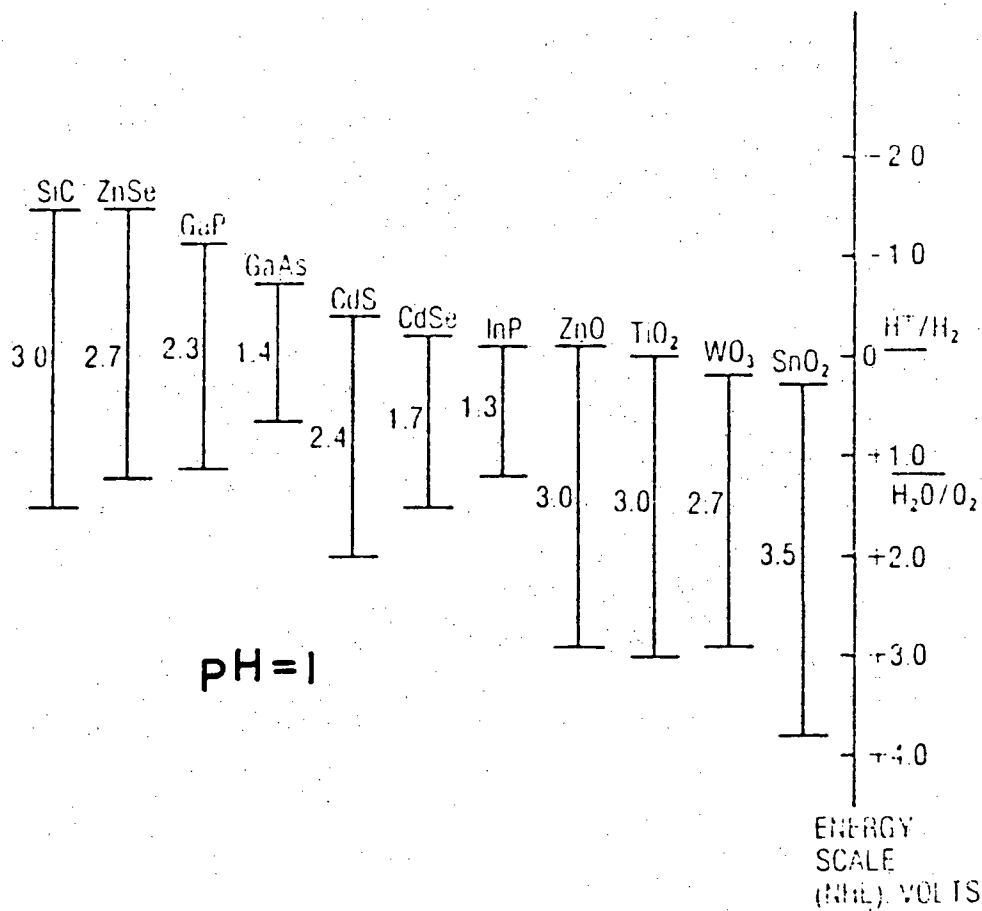


Fig. II-3. Band edges of a number of semiconductors with respect to the hydrogen and oxygen redox couples. (After Nozik).

the flatband potential in a cathodic direction.

The flatband potential is derived from an electrochemical measurement at the semiconductor-electrolyte interface. It includes properties of both the semiconductor and the electrolyte Helmholtz layer: ⁷

$$V_{fb}(\text{vsRHE}) = (X_{sc} + \Delta E_F + V_H) - 4.5 = (\phi_{sc} + V_H) - 4.5 \quad (\text{II-4})$$

where X_{sc} and ϕ_{sc} are the electron affinity and work function, respectively, of the semiconductor and V_H is the potential drop across the Helmholtz layer. ϕ_{sc} can be measured by a number of capacitance and photoemission techniques, though it is difficult to separate out effects due to band-bending in the latter.

The potential drop across the Helmholtz layer arises not only from the initial Fermi level difference between the semiconductor and electrolyte, but also from specific chemical interactions at the interface. On oxides the major species adsorbed from aqueous electrolytes are hydronium and hydroxide ions. For each oxide there is an electrolyte pH at which equal numbers of hydroxide and hydronium ions are adsorbed and $V_H = 0$; this pH is referred to as the point of zero zeta potential (PZZP). If surface adsorption follows simple reversible acid-base chemistry, the dependence of V_H on pH will follow a simple form derived from the Nernst equation:

$$V_H = 0.059(\text{PZZP} - \text{pH}) \quad (\text{II-5})$$

The flatband potential then shows a parallel behavior. For a number of

oxide semiconductors, including SrTiO_3 and TiO_2 , measurements of surface capacitance as functions of applied potential and electrolyte pH have born out both the Mott-Schottky relation (Eq. II-3) and the pH dependence of the flatband potential (Eqns II-4, II-5) up to pH's of ~ 13 .⁸ It should be noted that the redox potentials of the hydrogen and oxygen couples also become more negative by 59 mV for every unit increase in pH. The relative energies of the band edges and redox couples in water-dissociating cells are thus expected to be unaltered by a change in electrolyte pH.

II-2-4. The Energetics of Water Photodissociation

The basic dark energetics of a PEC cell for water photolysis are shown in Figure II-4 (after Nozik)⁷. The diagram is drawn assuming that the flatband potential of the semiconductor lies above (cathodic to) the hydrogen redox couple (RHE) so that photogeneration of hydrogen is possible without an applied potential. If V_{fb} lies below RHE an anodic potential must be applied to the n-type semiconductor to maintain band-bending while lifting photogenerated electrons to more cathodic potentials so that hydrogen can be evolved. Application of an external potential does not shift positions of the band edges, rather, the band energies in the bulk are lowered. All band edges and both redox couples shift 59 mV to more cathodic potentials (upwards) for each unit increase in electrolyte pH, assuming that the surface stoichiometry is altered only through adsorption of hydroxide and hydronium ions. Other changes in surface stoichiometry could alter the electron affinity of the surface and shift the band edges with respect to the redox couples. The vacuum levels shown in Figure II-4 are local ones corresponding to the

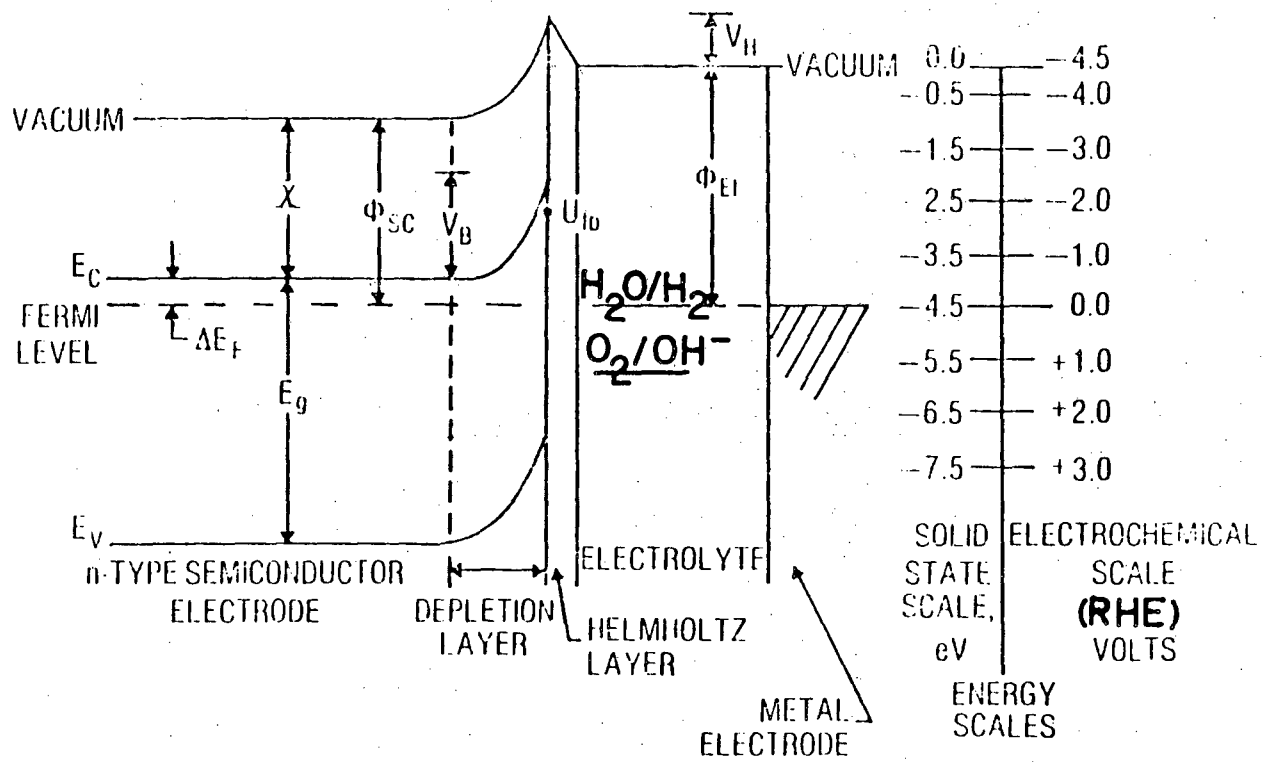


Fig. II-4. Energetics of water dissociation with a semiconductor photoanode.

(After Nozik).

removal of an electron, not to infinite separation, but rather to a distance just beyond the range of chemical interactions.⁹ The energy levels in Figure II-4 are derived from electrochemical measurements; correlation of these measurements with the in vacuo electronic structure of the clean surfaces is as of yet imperfect.

The hydrogen and oxygen redox potentials represent the thermodynamic potentials required for reversible electron transfer to the oxidant or from the reductant in the couple. Since hydrogen evolution on platinum is essentially reversible, the energy at which electrons are transferred across the interface is very close to this thermodynamic potential. Oxygen evolution on semiconductors, however, is highly irreversible, and the mechanism of charge transfer across the interface should be considered.

II-2-5. Energy Levels in Aqueous Solution

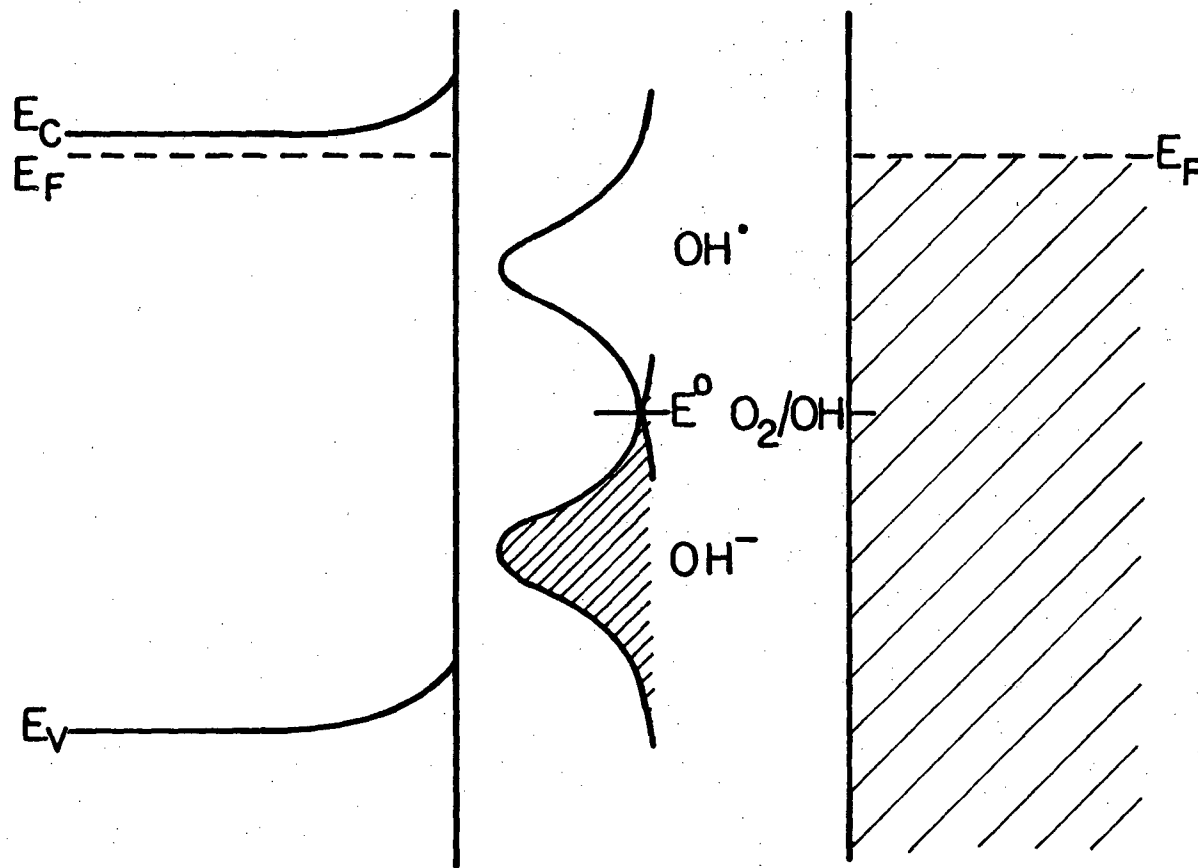
The structure of liquids, unlike that of solids, is in a constant state of flux. This is especially true in water, where the high level of directional hydrogen bonding leads to the temporary formation of partially ordered molecular aggregates. An aqueous ion therefore finds itself in a rapidly shifting local environment. Fluctuations in solvent polarization energy on the order of several tenths of an electron volt, which is many times kT , are thought to be common.¹⁰

Following the theory of Marcus,¹¹ the single-electron aqueous redox couple can be represented as two Gaussian distributions of states, one filled distribution for the reduced species and one empty distribution for the oxidized species (Figure II-5). The centers of the two

distributions are offset by the solvent reorganization energy (Franck-Condon shift) corresponding to the different charge states of the ion which is on the order of 0.5 - 1.5 V.¹² The width parameter of each distribution is determined by the strength of the solvent polarization fluctuations. Simple models treat these fluctuations as arising from harmonic interactions in the outer solvation sphere,¹³ but Bockris¹⁴ challenges this pure outer-sphere view. Regardless of their origin, the solvent polarization energy fluctuations provide filled and unfilled states over much wider energy ranges than would be found in similar gas-phase species. At a reversible electrode, electron transfer between reduced and oxidized states proceeds most rapidly at that potential where the product of the filled and unfilled density of states is a maximum. The Fermi level of a reversible electrode is then pinned at this potential, which is the (concentration-dependent) thermodynamic redox potential E of the couple. At non-reversible semiconductor photoelectrodes, however, charge carriers are provided at the band edges, not at the Fermi level. The oxidized and reduced forms of the electroactive species are not in equilibrium at the surface. Electron transfer is then not governed by alignment of the Fermi level with the redox potential, but rather by the density of filled electrolyte states at the energy of the semiconductor valence band edge or the density of unfilled states at the conduction band edge.

In the foregoing discussion only single electron-transfer reactions involving no bond-breaking were considered. In the redox couples involved in water electrolysis two electrons per H_2 molecule and four electrons per O_2 molecule are transferred, and bond scission and formation occur. Under these conditions the simple view of a redox couple as

Fig. II-5. Simplified view of filled and unfilled electrolyte states involved in O_2 evolution, in which the reaction is treated as a single-electron, outer-sphere charge transfer.



XBL 818-6327

sets of filled and unfilled distributions in the electrolyte is not in general adequate. The reactions probably proceed through surface-bound single-electron intermediates which experience polarization energy fluctuations intermediate between the small effects seen in the bulk solid and the large effects in liquid electrolyte. Even in these cases, the Marcus view of the electrolyte provides insight into the distribution of the initial acceptor states in the electrolyte. In the case of the highly irreversible oxygen evolution, the single hole-transfer product may be chemically similar to the activated complex. The critical energy for hole transfer from the semiconductor to the oxygen couple may thus be nearer to the maximum of the filled state distribution than to the thermodynamic redox potential.

II-2-6. Charge Transfer at the Semiconductor-Electrolyte Interface

Photogenerated holes at the valence band edge of an n-type semiconductor face a potential barrier to their transfer to electrolyte species. If the hole acceptor state is in the bulk electrolyte, the hole must travel over or through the Helmholtz layer. At a typical value of $V_H \sim 260$ mV, the probability of thermal excitation over the barrier at room temperature is 10^{-5} . The tunneling probability of a free electron through a 260 mV square barrier 10 \AA thick is $\sim 10^{-2}$. Tunneling thus can provide a more facile mechanism for charge transfer across the interface but requires a high density of states at a given energy on both sides of the interface. Inelastic tunneling processes have been demonstrated, but they are generally thought to have a much lower probability than elastic events.

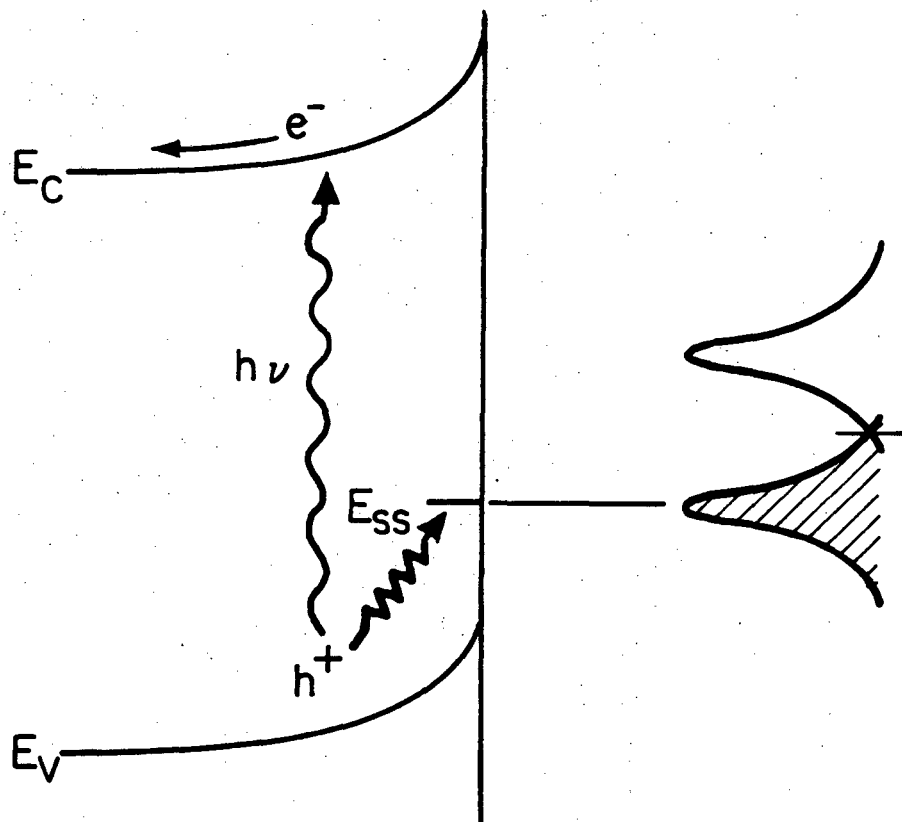
Charge transfer may occur from the semiconductor to a species within the Helmholtz layer. In this case the full height of the Helmholtz layer barrier need not be surmounted. However, the attraction between a charge leaving the surface and the image charge formed in a highly-doped semiconductor provides another potential barrier which must be overcome, now by a particle of much higher mass and concomitantly lower tunneling probability. Charge transfer at the surface of an electrode should thus quite generally be considered an electron or hole tunneling process between states of equal energy. The energy levels involved in the oxidation of water on n-type oxide semiconductors are outlined in Figure II-5. Holes photogenerated within the semiconductor depletion layer are driven by the electric field to the surface. They arrive at the surface with the redox potential of the valence band edge (if the holes have been fully thermalized, i.e., have relaxed to the lowest-energy allowed state in the band through interactions with phonons) or with a slightly more anodic potential (if they are non-thermalized "hot" holes). Since solvent polarization fluctuations provide a fair density of filled states for aqueous OH^- at the energy of the surface holes, tunneling can occur, leading to the reaction $\text{OH}^-_{(\text{aq})} + h^+ \rightarrow \cdot\text{OH}_{(\text{aq})}$. $\cdot\text{OH}_{(\text{aq})}$ is a highly unstable species, and back-transfer of the hole to the semiconductor might be expected to be facile. However, Williams and Nozik¹⁶ have shown that the time required for reorganization of the solvation spheres τ_R is likely to be much shorter than the tunneling time τ_t . Reorganization of the solvent spheres alters the energy distribution of the hole-acceptor, so that the (now-unfilled) state which accepted the hole is no longer aligned in energy with the valence band edge, and back-tunneling of the hole cannot occur. The peculiar energetics of

aqueous species and the dearth of states within the semiconductor bandgap thus render charge transfer across the semiconductor-electrolyte interface a largely irreversible process. Charge transfer to a species adsorbed at the gas-solid interface is expected to be more reversible.

The density of states diagram in Figure II-5 is highly simplified. Even after solvent reorganization, the $\text{OH}_{(\text{aq})}^{\bullet}$ is a highly reactive species and will adsorb onto the surface and/or react further to yield hydrogen peroxide or oxygen. The relevant states of the species formed upon oxidation of OH^- thus cannot be drawn with much certainty. The density of states of the oxidized species at the energy of initial hole transfer E_T is not of great importance as long as rapid solvent reorganization prevents back-tunneling. Electron injection from platinum to the hydrogen couple, on the other hand, occurs at the thermodynamic redox potential $E_{\text{H}_2\text{O}/\text{H}_2}$ since the exchange current in this essentially reversible reaction is sufficiently great to pin the Pt Fermi level at $E_{\text{H}_2\text{O}/\text{H}_2}$. In a number of previous theoretical treatments of PEC cells the redox couple has been treated as a single energy level. While such an approach can be useful in the description of charge transfer at a reversible electrode, it is not applicable to complex irreversible processes such as oxygen evolution on oxide semiconductors, where E^0 is merely a thermodynamic limit, not a charge acceptor level.

II-2-7 Surface-state Mediation of Charge Transfer

Efficient tunneling across the semiconductor-electrolyte interface requires a high density of states at a given energy on both sides of the interface. If the maximum of the electrolyte acceptor density of states



XBL818-6328

Fig. II-6. Role of surface state in accelerating transfer of photogenerated holes to the electrolyte.

lies at an energy within the semiconductor bandgap, surface states within the bandgap may mediate the transfer of charge. Figure II-6 illustrates this process. A hole created within the valence band may relax through interactions with phonons to a surface state from which quantum mechanical charge transfer to the electrolyte may prove facile. Such surface states, however, may also facilitate electron-hole recombination at the surface, as both electrons and holes can thermally relax to the energy of the surface state. The relative rates of these two processes depend both upon the extent of band-bending in the semiconductor and on the chemical nature of the surface state. Evidence for surface-state mediation of charge transfer has been observed in a number of redox systems,¹⁷⁻¹⁹ and intentional derivitization of Si and GaAs surfaces has allowed the performance of chemistry which is impossible on the clean surfaces.²⁰ In water-splitting reactions, however, much of the emphasis on surface state mediation of hole transfer has been derived from the belief that hole transfer could occur only at the redox potential of the oxygen couple, which lies well within the bandgap of most oxide semiconductors. While adsorbed intermediates undoubtedly are essential to oxygen evolution, a hole-donating surface state within the semiconductor at the energy level of the oxygen E is not necessary as long as a high density of filled states in the electrolyte lies at the valence band edge.

II-3. Kinetics of Photoelectrochemical Cells

In the preceding sections it has been shown that the height and width of the depletion layer barrier for a semiconductor held in the dark can be estimated from knowledge of the flatband potential and the

carrier concentrations in the semiconductor. Illumination with bandgap radiation, however, drastically alters the concentrations of free electrons and holes in the semiconductor bands and modifies the depletion layer characteristics. A number of attempts at a self-consistent mathematical treatment have been made.^{21,22} Even with simplifying assumptions (e.g. no surface recombination) these treatments become too ponderous for general solution and comparison with experimental data (see, for example, Reiss, p. 947). Here the major competing processes in PEC cells are delineated and their relative importance discussed in light of data in the literature.

The quantum efficiency ϕ of a photochemical device is defined as the ratio of the number of photons which turn over the desired chemical process to the total number of incident photons. The incident flux is described by a spectral distribution $I(h\nu)$ (for the solar spectral distribution, see Section II-5). The flux of photons which lead to the desired chemical reaction, $I_{\text{Eff}}(h\nu)$, is the incident flux minus a number of losses:

$$I_{\text{Eff}}(h\nu) = I(h\nu) - A(h\nu) - R_B(h\nu) - R_S(h\nu) - B(h\nu) \quad (\text{II-6})$$

where $A(h\nu)$ represents photons not absorbed by the semiconductor, $R_B(h\nu)$ accounts for bulk recombination losses, $R_S(h\nu)$ for surface recombination, and $B(h\nu)$ encompasses chemical reactions due to branching side reactions or back reactions. The terms in Eq. II-6 are not independent; rather they are interrelated in a complex manner innocently indicated above by a common dependence on $h\nu$.

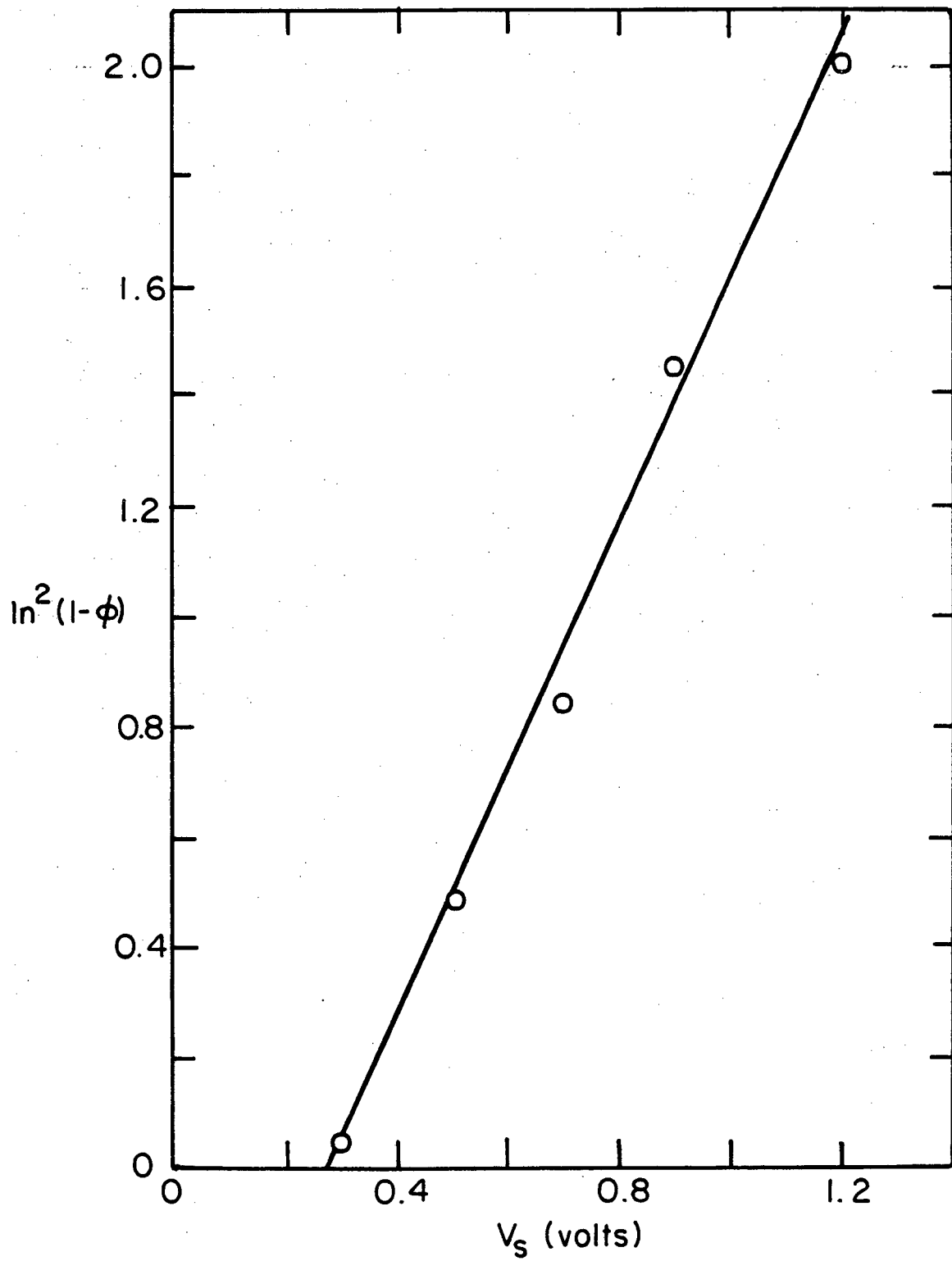
II-3-2. Light Absorption and Bulk Recombination

Absorption of light within a material is described by Lambert's law:

$$\frac{I_{\text{abs}}(h\nu, x)}{I_{\text{inc}}} = 1 - e^{-\alpha(h\nu) x} \quad (\text{II-7})$$

where x is the depth into the material and α is the absorption coefficient, which varies for semiconductors and photon energies above E_g from $10^3 - 10^6 \text{ cm}^{-1}$. 95% of incident light is absorbed within $\frac{3}{\alpha}$ of the surface, so essentially all bandgap light should be absorbed by any semiconductor layer greater than 30μ thick. However, only photons absorbed within the depletion layer lead efficiently to the desired chemistry.

The rate of electron-hole recombination in the bulk of a semiconductor is usually expressed as the lifetime of the minority carrier. Neither this nor the carrier mobilities have been definitively measured for oxide semiconductors. Absorption of a photon outside of the semiconductor depletion layer could form slightly bound excitons which recombine rapidly. Within the depletion layer the electric field separates photo-generated holes and electrons, preventing the formation of excitons and retarding recombination. Nozik has probed the relative efficacy of photons absorbed within and without the depletion layer by measuring the quantum yield in a TiO_2/Pt water photoelectrolysis cell as a function of surface band-bending, but has not published an analysis of the data¹⁶. If one assumes that all photons absorbed outside the depletion layer



XBL 818-6329

Fig. II-7. Plot of Nozik's data, testing model described in text.

thing, the true flatband potential lies cathodic to the value commonly reported. The quantum efficiency falls off too rapidly with decreasing band-bending to agree with a model in which efficiency losses are due entirely to the recombination of electron-hole pairs created outside the depletion zone. It thus appears that other losses, including surface recombination, may be of great importance in PEC cells using oxide semiconductors.

II-3-3. Surface Recombination

Wilson et. al. ²⁶ have shown that different surface pre-treatments of TiO_2 photoanodes can modify the quantum efficiencies of PEC cells, particularly under conditions where there is small band-bending. Mechanically polished surfaces give lower quantum yields than chemically etched surfaces. Polishing apparently produces states at the surface or in the near-surface regions which facilitate recombination. Heller et. al. ²⁷ have delineated the properties of a surface state which would make it a facile recombination center. On an n-type semiconductor such a state should lie within several hundred millivolts below the conduction band edge and below the electron acceptor level maximum in the electrolyte. In the absence of tunneling through the depletion layer barrier, surface recombination should decrease with increased band bending due to lower concentration of majority carriers at the surface. The minimum thermodynamic concentration of majority carriers at the surface can be roughly approximated by assuming that electrons are photogenerated at the conduction edge and then are thermally excited over the remaining depletion layer barrier between the point of excitation and the surface. The probability of an incident photon leading to a

majority carrier at the surface is then roughly

$$P = e^{-\alpha x} e^{-\left[\frac{V_s - V(x)}{kT}\right]} dx \quad (\text{II-10})$$

where $V(x)$ is given by Eq. (II-2). The integration cannot be done in closed form, but approximate graphical solutions for several values of V_s in a SrTiO_3 crystal with a doping level of 10^{19} cm^{-3} are given in Table II-1. Absorption coefficients α of $6 \times 10^3 \text{ cm}^{-1}$ at 3.4 eV ²⁸ and $3 \times 10^5 \text{ cm}^{-1}$ at 3.9 eV ²⁹ are assumed.

Table II-1. Probability of Photoelectrons Classically Surmounting the Remaining Depletion Layer Barrier

h ν	V_s		
	0.1V	0.5V	1.0V
3.9eV	7.6×10^{-2}	3.1×10^{-2}	1.7×10^{-2}
3.4eV	1.8×10^{-3}	-	4.4×10^{-2}

If one assumes that the surface recombination rate is proportional to the flux of photoelectrons thermally excited over the depletion barrier, it can be seen that excitation wavelength and therefore depth of adsorption should have a larger effect on surface recombination than band-bending.

Surface recombination can also occur when the majority carrier photogenerated in the depletion layer tunnels through the barrier to a surface state or solution species which can also trap a minority carrier

which has been driven to the surface. Heller et. al.³⁰ have documented a case in which this appears to occur. The magnitude of the recombination loss of this sort will be roughly proportional to the fraction of bandgap photons absorbed within that region of the depletion layer where the conduction band (for an n-type semiconductor) lies above the energy of the surface state. It will fall off as a negative exponential of the width of the depletion layer potential barrier at the energy of the surface state. This shunting process should therefore be most prevalent on highly doped semiconductors with narrow depletion layers. The relative sensitivity of this shunting recombination to changes in photon wavelength as compared to its sensitivity to changes in applied potential depends upon the energy difference between the surface state and the conduction band edge. Only if this energy difference is rather large will an applied potential (anodic for n-type) significantly augment recombination via this route.

II-3-4 Back and Side Reactions

Williams and Nozik have argued that charge transfer between a semiconductor¹⁶ and a species in a liquid electrolyte is likely to be highly irreversible because solvent relaxation characteristic times are faster than those for tunneling through the Helmholtz layer. Before back-tunneling can occur, the solution species will have relaxed so that the newly filled state is no longer at the same energy as the band edge or surface state from which tunneling originally occurred. Rather, the newly-filled state will be at an energy at which there is a very low density of states in the semiconductor. If Nozik's postulate of irreversibility is correct, back-reactions will occur in PEC cells only

through diffusion of anodic products to the cathode and vice versa, or by catalytic recombination of the oxidized and reduced products. In PEC cells back-reactions can be avoided by separate collection of gaseous anodic and cathodic products or through use of a semipermeable membrane to separate liquid-phase anodic and cathodic products. As will be seen (Section V-2-5), back reactions impose much more severe constraints on photocatalytic systems.

Several types of side reactions can decrease the quantum yield of photosynthetic cells. Most pernicious is photocorrosion, the typical behavior for most nonoxide semiconductors in most aqueous solutions. If the kinetics of oxidation (for n-type) of the semiconductor itself are faster than those for the oxidation of water or of some other desired substrate in solution, the quantum efficiency for the desired reaction may approach zero. Some correlations have been made between the rate of oxidation of various solution species and their standard redox energies²⁰ - in general, the more cathodic the standard redox potential, the faster the oxidation on an n-type semiconductor. This correlation of kinetics with thermodynamics seems to have little theoretical justification unless all semiconductor photochemistry proceeds by photocorrosion followed by redeposition of semiconductor material if a more easily oxidizable substrate is present. Surface morphological studies do not support such a mechanism, and the relative kinetics of photocorrosion and electrolyte oxidation must in fact be determined empirically.

Other side-reactions involving impurities and dopants can alter quantum yields of desired products. For example, if carbon is present on n-type semiconductor surfaces, CO_2 , rather than O_2 , may be evolved

upon illumination in aqueous solution. Such effects make interpretation of transient electrochemical currents without product and surface analysis quite risky. Similar transient effects may be seen as the near-surface region of an n-type oxide semiconductor reaches a steady-state oxygen vacancy concentration. To obtain meaningful steady-state results, a given condition should be maintained long enough to pass many times the charge equivalent to an adsorbed impurity monolayer ($\sim 10^{-4}$ coulomb cm^{-2}) and to reach steady-state in the near-surface region ($\sim 10^{-2}$ coulomb cm^{-2}).

II-3-5 Summary of Photoelectrochemical Theory

The following criteria must be met by materials used for photoelectrodes in photosynthetic cells (use of a single photoelectrode is assumed):

- (1) E_g must exceed the free energy change for the reaction being driven.
- (2) E_g should match the spectrum of the available light source. Using solar light, the percentage of incoming solar radiation which produces useful excitation of the semiconductor (electron and hole formation) is maximized at a bandgap of 1.24 eV.
- (3) To allow operation at zero applied potential, the conduction band edge must lie at or closer to the vacuum level than the electron acceptor level of the electrolyte. The valence band edge must lie farther from the vacuum level than the hole acceptor state in the electrolyte. For water dissociation on n-type semiconductors, this means that the flatband potential must be more negative on the elec-

trochemical scale than the reference hydrogen electrode (RHE) in the same electrolyte.

- (4) To obtain rapid charge-transfer kinetics at the semiconductor-electrolyte interface there must be good overlap between the band edges (or surface states) and the distributions of densities of acceptor states in the electrolyte.
- (5) To minimize bulk recombination, sufficient ($> \sim 0.1$ V) band-bending must be maintained and the semiconductor bulk should be free of local states which can serve as efficient recombination centers. Minimizing surface recombination may require quenching surface states and/or fine-tuning the applied potential vs. the incident wavelength.

While simple photoelectrochemical theory provides insight into proper design of PEC systems, several weaknesses remain: (1) The quantum mechanical treatment of charge transfer at the semiconductor-electrolyte interface applies only to electrolytes containing a simple one-electron, outer-sphere redox pair. Only in such cases is the "Fermi level of the electrolyte" reasonably well defined. And even in these cases, the effects of the surface on the energy levels of the species in solution cannot be adequately predicted by theory. (2) Although charge transfer steps are crucial, they may not be rate-limiting. The complex chemistry involved in water photolysis and other photosynthetic reactions involves crucial catalytic steps which are not dealt with in standard PEC theory. (3) The relative rates of surface and bulk recombination and of the desired reactions cannot be predicted. In general, simple PEC theory defines thermodynamic limits to the types of reactions which can occur.

on a given semiconductor, but kinetics must be determined experimentally. Even the thermodynamic predictions can be upset on less strongly doped semiconductors by Fermi level pinning³¹ or, at high applied potentials, by band edge unpinning³² (see Section III-6).

II-4 Theory of Heterogeneous Photocatalysis

II-4-1. Introduction

Heterogeneous photocatalysis is defined here as a process whereby the final fate of a reactant in one phase is affected by illumination of another phase. It is distinguished from photoelectrochemistry by a lack of physical separation of anode and cathode, though distinct anodically and cathodically active phases may be present in a photocatalyst particle. Photocatalysis is taken to include both exergonic and endergonic reactions; the distinction made between photocatalytic (exergonic) and photosynthetic (endergonic) PEC cells is not made here. Photocatalytic systems can operate at liquid-solid or gas-solid interfaces. Since photoelectrochemistry, the most thoroughly studied branch of semiconductor photochemistry, operates only at the solid-liquid interface, liquid-solid photocatalysis constitutes an intermediate stage between PEC and gas-solid photocatalysis. It is necessary to understand both to what extent analogies can be drawn between these three surface photochemical systems and where the important differences lie.

II-4-2 Photocatalysts as Micro-PEC Cells

Bard³³ and several others³⁴ have viewed the action of photocatalysts as being strictly analogous to the operation of PEC cells. Metallized semiconductor particles are seen as short-circuited microelectrochemical cells, and in a number of cases identical chemistry has been observed for the two systems operating in liquid electrolytes. On a metallized n-type semiconductor the metal particles are considered microcathodes while the free semiconductor surface forms the photoanode. Photogenerated electrons flow through the semiconductor to the metal particles; negative ions diffuse through the electrolyte from the cathode particles to the anodic regions, thereby completing the electrical circuit. The metal particles and open areas are considered sufficiently large that lateral interactions do not disrupt the depletion layer formation in the metal-free regions. Since photogenerated electrons must travel considerable distances through the semiconductor, photoactivity by such a mechanism should decrease with lower conductivity (lighter doping) of the semiconductor. Inherent in the micro-PEC cell view of photocatalysis is the assumption that one half-cell reaction is carried out entirely on the photoanode regions ($2\text{OH}^- \rightarrow \frac{1}{2} \text{O}_2 + \text{H}_2\text{O} + 2\text{e}^-$ for water dissociation in basic electrolyte) and the other half-cell ($2\text{H}_2\text{O} + 2\text{e}^- \rightarrow \text{H}_2 + 2\text{OH}^-$) proceeds on the metal-particle cathodes. Such a process requires diffusion of OH^- (or H^+) between the microelectrodes. Slow diffusion of ionic species would be expected to pose a problem for photocatalysis at the gas-solid interface since production of gas-phase ions requires energies greater than those available in the photons used, and all ionic diffusion must take place on the surface.

II-4-3 Photocatalysis as a Localized Process

Mechanisms of photocatalysis which do not require ionic diffusion between microelectrodes have also been proposed. Chung et. al.³⁵ have suggested that water dissociation on TiO_2 and SrTiO_3 proceed through photogeneration of a delocalized hole and an electron trapped in a local Ti^{3+} state. Adsorption of water on Ti^{3+} yields a bound hydrogen atom and an adsorbed hydroxyl ion. Hydrogen atoms diffuse over the surface until they recombine and leave the surface as H_2 . Adsorbed hydroxide ions react with holes to yield oxygen, possibly through a peroxide intermediate. Platinum increases photoactivity by serving as a hydrogen atom recombination catalyst rather than as a hydrogen evolution catalyst as in PEC cells. Going one step farther than Chung et. al., Van Damme and Hall³⁶ have tentatively proposed a mechanism for water splitting (see Figure VII-4) in which photoexcitation leads to local trapping of both electrons and holes. These mechanisms differ from the PEC cell analogy in two important ways: (1) Production of zero-valent hydrogen and oxygen both occur on the semiconductor. The species diffusing between semiconductor and metal sites is a neutral atom rather than an ion. (2) The primary reductant for water is an electron in a local state rather than an electron in the delocalized conduction band.

Point (1) may be important for gas-solid photoreactions. Production of gas-phase atomic hydrogen also requires energies greater than those supplied by available photons. However, a neutral atom would be expected to feel the corrugations in the electrostatic potential of the oxide semiconductor surface less strongly than an ionic species, and surface diffusion to Pt particles or intrinsic hydrogen recombination

sites should be more rapid than hydroxide ion diffusion. Thus a local mechanism in which at least the first electron transfer for both of the half-cell reactions occurs on the same surface could yield higher quantum efficiencies at the gas-solid interface than the PEC analog. A local process could also yield unique disproportionation chemistry requiring interspersed oxidizing and reducing sites.

In PEC cells electron-hole recombination is avoided through the spatial separation of the carriers by the electric field in the depletion layer. In a local process where both oxidative and reductive chemistry occur on the same surface, carrier separation must be chemical rather than spatial, and carrier recombination rates are likely to be higher. Back-reaction of the final products is also likely to be more important. The local process faces problems with the lifetime of the photoexcited state somewhat similar to those encountered in homogeneous photochemical systems. Recent advances in the use of aqueous photoreceptors for water-splitting³⁷ have relied on addition of micelle and/or solid phases to allow more efficient physical separation of oxidized and reduced species, in effect mimicking the spatial separation of carriers obtained in PEC cells. Purely local processes also face fundamental limitations to the amount of light which can be effectively absorbed similar to those encountered in attempts to sensitize semiconductors to visible light by adsorbing a monolayer of a dye - no monolayer can absorb more than 1% of incident light (see Section VII-1). To achieve quantum efficiencies greater than 1% there must be some efficient mechanism whereby light absorbed deep within the semiconductor can lead to excitation of the surface - a requirement which has not always been noted in past proposals of local mechanisms. On the other hand,

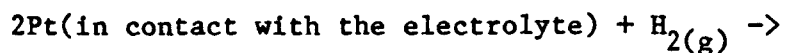
discussions drawing analogies between photocatalysts and PEC cells have often ignored the catalytic aspects of the chemistry leading to the final products (H_2 and O_2 for water splitting). The relative rates of these catalytic chemical steps and of carrier recombination become more critical under the conditions of zero applied potential which obtain on photocatalysts than in PEC cells operated with high applied potentials.

Photochemistry on metal-free semiconductors does not fit easily into the PEC cell analog, since there is no clearly defined phase to serve as a cathode. A number of mechanisms, based on both delocalized and localized approaches, whereby photogenerated electrons could reach the surface of an n-type semiconductor are discussed in Section VII-1 in light of data obtained in this work. The classification of photochemical devices as following a local or delocalized mechanism is of course somewhat artificial. Carriers formed in delocalized bands may be trapped in local states before reacting with species in the gas or electrolyte phase. Even Bard's group, the quoted source of the treatment of photocatalysis in analogy to PEC cells, has invoked local surface electron traps³³ to explain some chemistry on metal-free surfaces. The local vs. delocalized (or photocatalysis vs. PEC) dichotomy, though somewhat artificial, has been stressed here in an attempt to identify those areas of thought where, in the past, photoelectrochemists on one side, and surface and catalysis scientists on the other, have at times talked past each other without communicating completely.

II-4-4 Comparison of the Gas-Solid and Liquid-Solid Interfaces

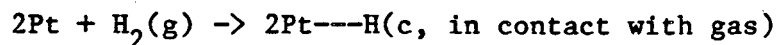
While the established body of data on surface photochemistry has been gathered from PEC cells operating in liquid electrolytes, a large proportion of the industrially important heterogeneous processes take place at the gas-solid interface. Working in the gas phase enables one to independently vary the temperature and the chemical activities of reactants and products over broader ranges than can be achieved in liquid solutions. The kinetics of diffusion, which are often limiting in electrochemical processes, are faster in the gas phase. Some of the problems involved in gas-solid endergonic photoprocesses related to the high free energies of desorbed ionic intermediates have already been discussed. This section will give a brief overview of the structural and energetic differences between the gas-solid and liquid-solid interfaces and their probable effects on the kinetics of interfacial photoprocesses.

Direct experimental comparisons of the chemisorption of atoms from aqueous electrolytes with their adsorption from the gas phase are few and far between. The best-studied system to date is that of hydrogen on Pt. Ross³⁸ has measured zero-coverage enthalpies and entropies of adsorption, corresponding to the reaction



For the (111) surface $\Delta H_{\text{ads}}^{\circ} = -46.8$ kJ/mole H_2 and $\Delta S_{\text{ads}}^{\circ} = -55.8$

J/mol-K. The heat of adsorption is very close to that measured by Christmann and Ertl³⁹ for adsorption of gas phase H₂ at very low pressures:



$\Delta H_{\text{ads}}^{\circ} = -41.2$ kJ/mole. While no single-crystal results for $\Delta S_{\text{ads}}^{\circ}$ on Pt are available, Behm et. al.⁴⁰ have measured $\Delta S_{\text{ads}}^{\circ}$ for H₂ on Pd(100) of -260 J/mol-K, while Ross' figure for H₂ on Pt(100) is -53.1 J/mol-K. The similarity in heats of adsorption of H₂ on Pt from gas and from electrolyte shows that the presence of water has little effect on the strength of the Pt-H bond, in agreement with results of thermal desorption studies⁴¹ which demonstrate that water is bound very weakly to Pt. Photoemission and thermal desorption studies⁴² have shown that molecular water is similarly bound very weakly to SrTiO₃; on a stoichiometric crystal no water sticks at room temperature. Only when a high concentration of Ti³⁺ is initially present does water vapor bind to the surface, and this water appears to be a dissociated form. The tremendous differences in $\Delta S_{\text{ads}}^{\circ}$ for H₂ adsorption on Pt in aqueous electrolyte as opposed to H₂ adsorption from the gas phase onto Pd shows the importance of the partial ordering of the water structure at the interface. Adsorption of H₂ on Pt causes an lesser decrease in system entropy in acidic electrolyte as opposed to in the gas-solid case, in part due to disruption of the water structure in the double layer by adsorbed hydrogen. These large entropy effects seem to have general significance in electrochemical phenomena, for activated complexes as well as for equilibrium chemisorbed states. While processes which are slow at the gas-solid interface generally have high enthalpies of activation, many

slow electrochemical processes, such as oxygen reduction on Pt, have low (10-15 kcal/mol)⁴³ activation energies but also have very low pre-exponential factors indicative of unfavorable activation entropies. Thus the presence in liquid water of short-range order, while unlikely to significantly change the most probable energies of the fluid-phase electron acceptor and donor states, can drastically alter the kinetics of the chemical steps in water dissociation through entropy effects.

Though the most probable energies of the fluid-phase electron acceptor and donor states would seem largely insensitive to the presence or absence of liquid water, the density of states distributions would be broader with liquid water present due to fluctuations in solvation energies. Broader state distributions should lead to faster charge transfer from the surface by an elastic tunneling mechanism, due to better density of states overlap with a semiconductor band edge or surface state whose energy does not align perfectly with the most probable energy in the fluid-phase state distribution.

As noted in Section II-2-6, Williams and Nozik¹⁶ have argued that charge transfer at the semiconductor-electrolyte interface is essentially irreversible because solvent relaxation times are faster than the characteristic tunneling times. At the gas-solid interface there is no solvent relaxation to remove the initial alignment of states in the semiconductor and electrolyte which permits elastic tunneling. Thus back-tunneling should be as rapid as charge transfer in the forward direction. Since charge transfer is not expected to be irreversible at the gas-solid interface, provision of conditions to allow rapid, irreversible chemical reaction of the adsorbed charge acceptor is more critical

to the attainment of high quantum efficiencies than at the liquid-solid interface.

A large number of questions need be answered before the arguments given above can be put in more substantive terms. First, is the critical electron transfer step that between the semiconductor and an adsorbed species or that between the semiconductor (or an adsorbed species) and an entity in the gas or electrolyte phase? If the former, to what extent does an adsorbed species feel solvent fluctuation effects? In water dissociation it seems most likely that the critical charge transfer must be between the semiconductor and an adsorbed species, since the half-cell reactions require multiple electron transfer, bond scission, and bond formation all of which should proceed most rapidly when catalyzed by the surface. Whether a chemical or a charge-transfer step is rate limiting in electrochemical oxygen evolution or reduction is still a topic of debate. The present theory of heterogeneous charge transfer is sorely lacking in its ability to describe solvent fluctuation effects (or even simple effective dielectric constants) in the neighborhood of the surface, and admixture of catalytic steps is beyond its grasp. All that one can say is that the presence of liquid water should broaden the hole-acceptor distribution of states by somewhere between 0 and 0.5 eV. If an electron-transfer step is critical to the evolution of oxygen on n-type semiconductors, this broadening should accelerate the kinetics of water photodissociation at the aqueous electrolyte-semiconductor interface relative to those expected at the water vapor-semiconductor interface.

The foregoing paragraphs have concentrated on the rates of reactions between the semiconductor and the gas or liquid phase. Charge transfer is probably faster in the presence of liquid water due to solvation broadening of acceptor states. Chemical steps, on the other hand, may be slower with liquid water present due to higher entropies of activation. Let us now consider what differences would be expected in band-bending at the gas-solid and liquid-solid interfaces. Chemisorption and band-bending unfortunately lead one rapidly into chicken-or-egg causal relationships.

In Section II-2-3 the model of depletion layer formation by analogy to metal-semiconductor Schottky junctions was discussed. The magnitude of the band-bending was taken as the differences in the energies measured from the Fermi level to common vacuum level for the electrolyte and the semiconductor. Charge transfer occurs between the two phases until Fermi levels are aligned, causing formation of an asymmetrical double layer. The electrolyte side of this double layer is an inner Helmholtz layer consisting, for an oxide in basic or acidic electrolyte with no other electroactive species, of adsorbed H^+ and OH^- ions and water molecules. In this simple, "non-chemical", Schottky treatment, all charge in the inner Helmholtz layer arises from charge transfer from the semiconductor due to the initial mismatch in the Fermi level of the two phases. The H^+/OH^- ratio on the surface is directly related to the redox potential (or work function) of the semiconductor before contact with the electrolyte. In such a treatment the Usanovich view of acid-base chemistry⁴⁴ is taken to an extreme - redox reactions alone control the surface acid-base chemistry. A less extreme, more chemical view of the interaction allows partial electron transfer similar to that in a

Lewis-type acid-base interaction.

This determination of surface excess charge (i.e. charge in the Helmholtz layer) by electron transfer describes to first order conditions at the water vapor-semiconductor interface, where only neutral molecules impinge upon the semiconductor surface and gaseous ions are unlikely to desorb. The absolute surface concentrations of H^+ and OH^- will vary with the saturation coverage of water and the equilibrium between molecular and ionized water on the surface, but the excess of OH^- over H^+ (for an n-type semiconductor) will correlate directly with the extent of band-bending. Unfortunately the magnitude of this band-bending is difficult to predict. Some of the problems of the concept of the "Fermi level of the electrolyte" were discussed in Section II-2-2. The "Fermi level of a gas" is an even more specious proposition. The gas, a collection of widely-spaced, noninteracting local centers, cannot be viewed as a matrix for a delocalized sea of free electrons. The actual bending achieved will depend upon the local chemistry of charge transfer into the adsorbed molecules. Chung³⁵ and Lo⁴⁵ have published absolute measurements of band-bending upon adsorption of H_2O on TiO_2 and $SrTiO_3$, but their calculation made use of an electrochemically derived flatband potential and ignored the contribution of the electrolyte Helmholtz layer to the latter. Accurate determination of band-bending at the gas-surface interface will require use of a Kelvin probe. It is to be expected that smaller densities of negative charge (lower surface excess hydroxide ion concentration) can be developed at the gas-solid interface than at the liquid-solid interface due to the lack of a dielectric solvating medium.

At the electrolyte-solid interface ionic species, as well as neutral molecules, impinge upon the surface; and ions can be desorbed into the electrolyte as low-energy solvated species. Specific adsorption of ions due to Bronsted and Lewis-type effects can lead to large excess surface charges without a redox reaction between electrolyte and semiconductor; the extent of these specific interactions can be gauged through measurements of the point of zero zeta potential. Thus, quite different distributions of charge in the first adsorbed layer and the semiconductor depletion layer can be expected at the solid-liquid and solid-gas interfaces due to the different types of acid-base chemistry involved.

In Section II-2-2 (deuces wild) it was argued that for PEC cells the hydrogen evolution potential, rather than some "Fermi level of the electrolyte", should be considered to pin the Fermi level of the semiconductor once water-splitting has commenced. During hydrogen evolution the platinum electrode or platinum coating on the semiconductor serves as a "dynamic hydrogen electrode".⁴⁶ The effective pressure of hydrogen used for the calculation of the hydrogen evolution potential is the pressure of gas over the electrolyte minus the vapor pressure of water, and the potential will be stable and very close to that of the standard hydrogen electrode (with external hydrogen source) as long as the photocurrent is $\sim 0.1 \text{ mA/cm}^2$ or greater.

In a gas-phase reaction no bubbles of hydrogen form, and the activity of hydrogen is determined by the partial pressure of hydrogen, not the total pressure of gas. There is no multilayer reservoir of hydrogen at the Pt surface to pin the Fermi level of the system by serving as a reversible source or sink of electrons. Photo-oxidation or

reduction of the near-surface region of the semiconductor could then drive the E_F of the semiconductor to unanticipated levels.

One final major experimental difference between studies of the gas-semiconductor and liquid-semiconductor interfaces is the relative ease with which an external potential can be applied to modify the semiconductor band-bending. In liquid electrolyte the semiconductor Fermi level can be potentiostated at any desired value with respect to the hydrogen evolution potential; the applied potential falls across the semiconductor depletion layer. Although this does not change the relative energies of states in the electrolyte and at the semiconductor surface, at least to first order, it does allow the band-bending, and thus the rates of recombination processes, to be varied in a controlled manner. Water splitting can be studied on materials with electron affinities too great to allow spontaneous evolution of hydrogen.

Since the gas phase is not an electrically conductive medium, analogous potentiostating at the gas-solid interface is impossible. It would be possible to induce an electric field in the near-surface region of the semiconductor by placing the semiconductor wafer between the plates of a capacitor, but the potentials required to induce field strengths comparable to those in the depletion layer in PEC cells far exceed the dielectric strength of water vapor.

Throughout this discussion it has been assumed that only one or a few monolayers of water were present at the water vapor-solid interface. As the water vapor pressure approaches the equilibrium vapor pressure a thick film of water hundreds or thousands of monolayers thick will form. This layer will then have solvent properties very similar to those of

liquid water. Oxygen electro-reduction proceeds readily on Pt coated with electrolyte films $\sim 5000 \text{ \AA}$ thick.⁴⁷ The viscous boundary layer through which electroactive species must diffuse rather than be carried by convective mixing is somewhat thicker.⁴⁸ The films of water formed at near-equilibrium pressures are likely to have solvent properties typical of bulk liquid water but have somewhat different mass transport properties.

In summary, the gas-solid and liquid-solid interfaces differ in many ways which, as of yet, are inadequately quantified by experiments. Entropy effects are more important to the kinetics of chemical processes at the liquid interface. Solvent fluctuation broadens the electronic state distributions involved in charge transfer in liquids, probably increasing forward and decreasing back-transfer rates in photoelectrolysis. Acid-base chemisorption and surface charge-balance differ at the two interfaces. The ability of liquid electrolytes to support ionic currents allows facile transport of ionic photochemical intermediates and allows independent control of band-bending through potentiostating with respect to a reference electrode.

II-5 The Solar Resource and Quantum Conversion

Sunlight provides a diffuse and intermittent but inexhaustible source of energy. In the United States, the annual mean daily solar irradiation onto a horizontal surface varies from 260 w/m^2 at El Paso, Texas to 100 w/m^2 at Point Barrow, Alaska. New York receives 140 w/m^2 and Los Angeles about 220 w/m^2 .⁴⁹ To readily contrast the diffuse nature of solar energy to the concentration of energy in fossil fuels,

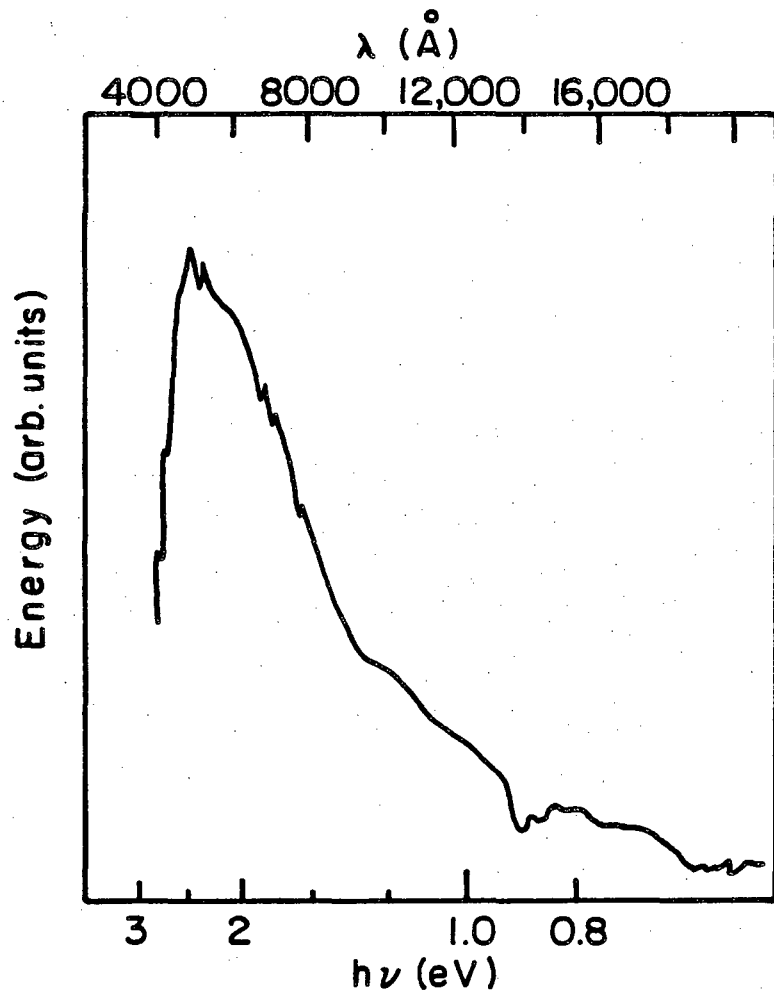
one can calculate the thickness of films of various fuels which would have the same heat content as one hour's sunlight impinging on a flat horizontal surface at a mean insolation of 150 w/m^2 . These thicknesses are $1.5 \times 10^{-3} \text{ cm}$ for gasoline and 4.4 cm for gaseous hydrogen at 1 atm and 25°C . At 10% conversion efficiency, one could then produce 4.4 liters of gaseous $\text{H}_2/\text{hr-m}^2$ (or $1.5 \text{ ml gasoline/hr-m}^2$) from mean annual sunlight, water and, in the case of gasoline, pure gaseous CO_2 . The highly diffuse nature of the solar resource presents scientists and engineers with the specific challenge of producing energy collection systems with very low costs per unit area.

Quantum converters, such as photocatalysts, PEC cells, and photovoltaics, can utilize only a fraction of the solar spectrum. Photons with energies smaller than the semiconductor bandgap will produce essentially no quantum effect since the probability of multiphoton excitations is too low to be significant with solar photon fluxes. For a solid absorber in the absence of major hot carrier effects only part of the energy of a photon with $h\nu > E_g$ will go into quantum excitation; the excess energy $(h\nu - E_g)$ will be thermalized. In a liquid or gaseous absorber an overly energetic photon may pass through without causing any quantum excitation. The maximum possible quantum excitation efficiency for an absorber with a single threshold energy E_g is then given by:

$$X(E_g) = \frac{\int_{E_g}^{\infty} I(h\nu) E_g (h\nu)^{-1} d(h\nu)}{\int_0^{\infty} I(h\nu) d(h\nu)} \quad (\text{II-11}())$$

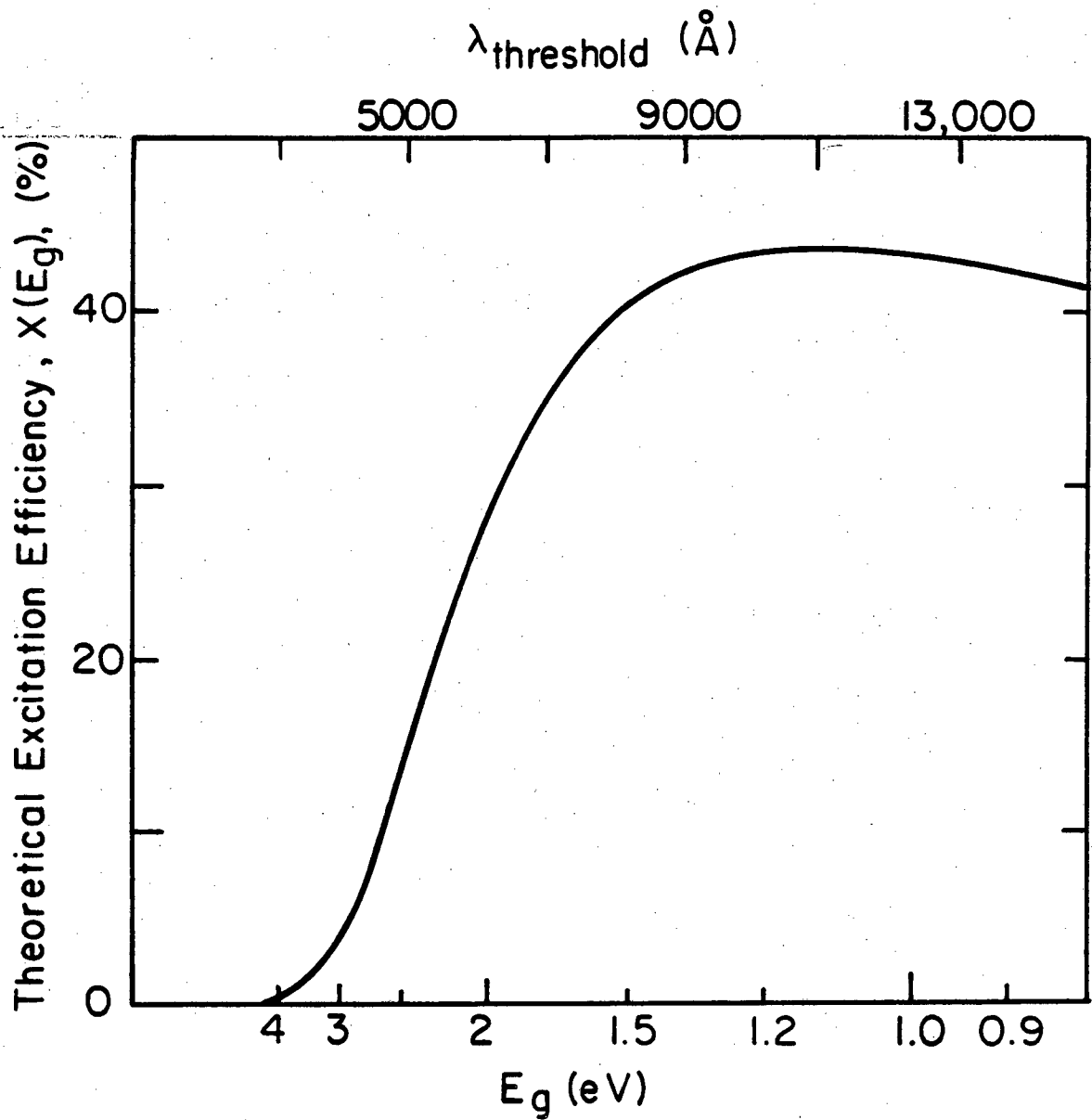
where $X(E_g)$ is the ratio of energy going into quantum excitation to total

incident energy and $I(h\nu)$ is the intensity of sunlight with photon energy $h\nu$. Figure II-8 shows the AM1 (high noon, clear sky, sea level) solar spectral distribution.⁵⁰ Figure II-9 shows the excitation efficiency $X(E_g)$ as a function of bandgap for these conditions⁵⁰. $X(E_g)$ shows a maximum of 44% at an absorption threshold of 1.18 eV, corresponding to a wavelength of 10,000Å, in the infrared. It should be stressed that this 42% is the theoretical efficiency of quantum excitation, not the efficiency of the total device. The generally-quoted theoretical maximum conversion efficiency of 29% for a single-junction photovoltaic device takes into account a potential gradient in the junction region required for efficient carrier separation. This and related losses are likely to be somewhat different for photochemical devices than for photovoltaics. It should be noted that the potential required for the electrolysis of liquid water, 1.23 V, lies very close to the maximum of the $X(E_g)$ curve, i.e. a theoretical loss-free conversion of 43% for sunlight to water is thermodynamically possible. However, the practical requirements for band-bending (at least 0.1 V), activation overpotentials (0.3 - 0.7 V), and system resistance indicate that semiconductors with bandgaps in the range of 1.7 - 2.0 eV are likely to be needed for water photolysis. This bandgap range leads to $X(E_g)$'s of 36 - 28% and maximum conversion efficiencies of 26 - 17%. Taking into account losses in the absorber and optimistic activation energies for chemical reactions, the most efficient solar photochemical storage system would involve a reaction with a ΔG somewhat smaller than that for water and an absorber with $E_g \sim 1.5\text{eV}$.



XBL 818-6330

Fig. II-8. Solar spectral distribution. Noon on a clear day at sea level.



XBL818-6331

Fig. II-9. Maximum excitation efficiency for a single-threshold quantum absorber as a function of threshold energy (bandgap).

REFERENCES

1. H Gerischer, in Physical Chemistry, an Advanced Treatise, Vol. 9A, H. Eyring, ed., Academic Press, New York, 1970.
2. F. Lohmann, Z. Naturforsch., 22a, 843, 1967.
3. N.F. Mott, Proc. R. Soc. London A171, 27 (1939).
4. W. Schottky, Z. Phys., 118, 539 (1942).
5. A.J. Nozik, Annu. Rev. Phys. Chem., 29, 196 (1978).
6. M.A. Butler and D.S. Ginley, J. Electrochem. Soc., 125, 228 (1978).
7. A.J. Nozik, Annu. Rev. Phys. Chem., 29, 189 (1978).
8. J.M. Bolts and M.S. Wrighton, J. Phys. Chem., 80, 2641 (1976).
9. N.W. Ashcroft and N.D. Mermin, Solid State Physics, Holt, Rinehart and Winston, New York, 1976, p. 357.
10. S.R. Morrison, J. Vac. Sci. Technol., 15, 1417 (1978).
11. R.A. Marcus, Ann. Rev. Phys. Chem., 15, 155 (1964).
12. H.. Gerischer, Photochem. and Photobio. 16, 243 (1972).
13. H. Gerischer, Surface Science, 18, 97 (1969).
14. J. O'M. Bockris and S.U.M. Khan, Quantum Electrochemistry, Plenum Press, New York, 1979, p. 173.
15. C.B. Duke, Tunneling in Solids, Academic Press, New York, 1969.

16. F. Williams and A.J. Nozik, *Nature*, 271, 137 (1978).
17. T. Freund and S.R. Morrison, *Surf. Sci.*, 9, 119 (1968).
18. R. Memming and G. Schwandt, *Electrochim. Acta*, 13, 1299 (1968).
19. M. Nishida, *Nature*, 277, 202 (1979).
20. M.S. Wrighton, A.B. Bocarsly, J.M. Bolts, M.G. Bradley, A.B. Fischer, N.S. Lewis, M.C. Palazzotto, and E.G. Walton, in Interfacial Photoprocesses: Energy Conversion and Synthesis, M.S. Wrighton, ed., *Adv. in Chem. Series No. 184*, 1980, p. 269.
21. H. Reiss, *J. Electrochem. Soc.*, 125, 937 (1978).
22. D. Laser and A.J. Bard, *J. Electrochem. Soc.*, 123, 1833 (1976).
23. M.S. Wrighton, A.B. Ellis, P.T. Wolczanski, D.L. Morse, H.B. Abrahamsson, and D.S. Ginley, *J. Am. Chem. Soc.*, 98, 2774 (1976).
24. C.N. Sayers and N.R. Armstrong, *Surf. Sci.*, 77, 301 (1978).
25. M. Tomkiewicz, *J. Electrochem. Soc.*, 126, 1505 (1979).
26. R.H. Wilson, L.A. Harris, and M.E. Gerstner, *J. Electrochem. Soc.*, 126, 844 (1979).
27. B.A. Parkinson, A. Heller, and B. Miller, *J. Electrochem. Soc.*, 126, 954 (1979).
28. D. Redfield and W.J. Burke, *Phys. Rev. B*, 6, 3104 (1972).
29. M. Cardona, *Phys. Rev.*, 140, A651 (1965).

30. B.A. Parkinson, A. Heller and B. Miller, *J. Electrochem. Soc.*, 126, 954 (1979).
31. A.J. Bard, A.B. Bocarsly, F.F. Fan, E.G. Walton, and M.S. Wrighton, *J. Am. Chem. Soc.*, 102, 0 (1980).
32. J.A. Turner, J.A. Manassen, and A.J. Nozik, in Photoeffects at Semiconductor-Electrolyte Interfaces, A.J. Nozik, ed., ACS Symposium Series No. 146, 1981.
33. B. Kraeutler and A.J. Bard, *J. Am. Chem. Soc.*, 100, 5985 (1978).
34. M.S. Wrighton, P.T. Woczanski, and A.B. Ellis, *J. Solid State Chem.*, 22, 17 (1977).
35. Y.W. Chung, Ph.D. Thesis, U. Calif, Berkeley, 1977, p. 135.
36. H. Van Damme and W.K. Hall, *J. Am. Chem. Soc.*, 101, 4373 (1979).
37. M. Grätzel, *J. Am. Chem. Soc.*, 102, 2461 (1980).
38. P.N. Ross, Jr., *Surf. Sci.*, 102, 463 (1981).
39. K. Christmann and G. Ertl, *Surf. Sci.*, 60, 365 (1976).
40. R.J. Behm, K. Christmann, and G. Ertl, *Surf. Sci.*, 99, 320 (1980).
41. G.B. Fisher and J.L. Gland, *Surf. Sci.*, 94, 446 (1980).
42. S. Ferrer and G.A. Somorjai, *Surf. Sci.*, 94, 41 (1980).
43. P.N. Ross, Jr., Proceeding Electrochem. Soc. Meeting, Minneapolis, May 1981, and LBL report No. 11891.

44. M. Usanovich, Zhur. Obschei Khim., 9, 182 (1939).
45. W.J. Lo, Ph.D. Thesis, U. Calif. Berkeley, 1978.
46. J. Giner, J. Electrochem. Soc., 111, 376 (1964).
47. R.H. Müller, Proc. Electrochem. Soc. Meeting, Toronto, May 1964.
48. N. Ibl and R. Müller, Z. für Elektrochemie, 5, 671 (1955).
49. F. Kreith and J.F. Kreider, Principles of Solar Engineering, McGraw-Hill, Washington, p. 73.
50. K.I. Zamaraev and V.N. Parmon, submitted to Cat. Rev.

Chapter III Selective Review of the Photoelectrochemical and Photocatalytic Experimental Literature

The photoelectrochemical literature has been extensively reviewed (see, for example, Nozik,¹ Memming² and Heller³). This being the case, this chapter will not attempt an exhaustive review. Rather, an outline of the main lines of research being pursued in the field, especially those of possible interest to a scientist pursuing heterogeneous photocatalysis, will be given. Particular attention will be paid to observed trends which may guide the selection of future semiconductor materials. Photosynthetic cells for water dissociation, CO₂ reduction, and for certain various organic reactions will be considered. Although liquid-junction solar cells lie outside the scope of this research effort, some developments in this field will be discussed due to their important materials innovations. Results from heterogeneous photocatalytic experiments will be compared and contrasted with photoelectrochemical results.

III-1 Photosynthetic Cells

III-1-1 PEC Cells for Water Photoelectrolysis

The first PEC cells for photoelectrolysis of water, reported by Fujishima and Honda,⁴ used a TiO₂ photoanode in basic solution and a Pt counterelectrode in acid. Although no externally applied potential was needed for efficient operation, the pH difference between the anolyte and catholyte provided a free energy boost equivalent to an applied potential of 0.8 V. The success of Honda's cell led to the investiga-

tion of a large number of oxide semiconductors for use as photoanodes in water photoelectrolysis. The majority of these materials have also required an external potential: SnO_2 ,⁵ WO_3 ,⁶ Fe_2O_3 ,⁷ FeTiO_3 ,⁸ V_2O_5 ,⁶ PbO ,⁶ CdO ,⁹ and YFeO_3 ;¹⁰ their flatband potentials lie anodic (more positive on the electrochemical scale) to the hydrogen redox potential. Recent work¹¹ using an equivalent circuit model to extract the true depletion layer capacity from the measured differential capacitance has shown that the flatband potential of TiO_2 lies ~150 mV cathodic of the hydrogen couple; water splitting at zero applied potential should be possible on TiO_2 , but at a slow rate as band-bending will be very small.

A second class of oxide semiconductors have flatband potentials cathodic to the hydrogen potential and thus can split water without an applied potential: KTaO_3 ,¹² SrTiO_3 ,^{13,14} BaTiO_3 ,¹⁵ Ta_2O_5 ,⁹ and ZrO_2 .⁹ The first three materials have band gaps of 3.4 - 3.5 eV; the latter two have bandgaps of 4.0 and 5.0 eV, respectively. The large bandgaps of these materials lead to low solar energy conversion efficiencies, as only about 2 - 5% of the energy of sunlight reaching the earth is in photons with energies greater than 3.4 eV.¹⁶ The maximum solar conversion efficiency obtained to date is only about 1%¹⁴ due to recombination losses at zero applied potential. Except for its large bandgap, SrTiO_3 has proven an excellent material for photoanodes. In basic solution it is highly resistant to photocorrosion¹⁴, though at high current densities in acidic electrolytes corrosion can be severe.¹⁷ It has sufficient catalytic activity for oxygen evolution that quantum yields of 100% can be obtained, at least when an anodic potential > 1 V is applied¹⁴.

The large bandgap of SrTiO_3 makes it impractical for any solar conversion scheme, as 1% solar conversion will scarcely give enough economic yield to amortize a sheet of plate glass. Unfortunately, the oxides with smaller bandgaps, such as Fe_2O_3 , require a larger applied potential for hydrogen evolution (this correlation is discussed in greater detail in Section VII-5). A number of research groups have investigated mixed oxides or mixtures of oxides in an attempt to attain in one material the small bandgap of Fe_2O_3 and the low electron affinity of SrTiO_3 . Ghosh and Maruska¹⁸ have doped single crystals of TiO_2 and SrTiO_3 with a series of transition metal ions which have absorptions in the visible: V, Cr, Mn, and Fe. Although the oscillator strengths for these ions in the host lattices are quite large, the solubility is quite small (crystals doped with > 0.5 wt % could not be grown) so the total visible response is small. The ions which gave the largest visible response (Cr and Mn) also served to decrease the near-UV response, apparently due to decreased hole diffusion lengths. Rauh *et. al.*¹⁹ report similar results with mixed perovskites - addition of ions which should be responsive to visible light yields slight photoactivity in the visible but also a great reduction in UV response, leading to an overall decrease in solar conversion efficiency. The visible absorption seems to be by local centers, rather than by a delocalized band within the bandgap of the host. These local centers also serve as efficient sites for carrier recombination. Mavroides²⁰ and Dwight and Wold²¹ have found a related perversity in other mixed oxides. The flatband potential of the ternary system is almost identical to that of the binary component with the less favorable flatband potential. While some bright points, such as an increase in hole diffusion length (but not visible

response) upon doping SrTiO_3 with Al, are found in the studies of these doped and mixed systems, the overall results are not encouraging.

Favorable bandgaps and favorable flatband potentials seem to be mutually exclusive properties of oxides, due to the tendency of all valence bands derived largely from O 2p orbitals to lie about the same distance from the vacuum level⁹. There is a host of sulfide, selenide, telluride, and phosphide semiconductors with bandgaps in the 1.4 - 2 eV range and with conduction bands closer to the vacuum level than the hydrogen redox couple. Unfortunately, no non-oxide semiconductor has been found which can evolve oxygen from aqueous solution without itself being oxidized into a soluble corrosion product or a passivating layer. Most of the chalcogenides yield as corrosion products the elemental chalcogen or an oxidized polychalcogenide. Tributsch²² has investigated the photoelectrochemistry of a number of layered chalcogenides (MoS_2 , MoSe_2 , et. al.) in which the top of the valence band is derived from nonbonding metal d orbitals rather than from chalcogenide p-orbitals. Since photoexcitation does not involve direct oxidation of chalcogenide ions, no elemental chalcogen is formed as a corrosion product. Nor, sorry to say, is oxygen the major anodic product; most photogenerated holes lead to photocorrosion in the form of chalcogenates or chalcogenous acids. The evolution of these particular products shows that an adsorbed atomic oxygen species is probably formed as an intermediate, and a slight yield of O_2 has been measured on MoS_2 . Suggestions for further experiments with these compounds are made in Section VII-5. Attempts to stabilize non-oxide semiconductors with oxide overlayers have either failed (thin oxide films) or have led to photoresponse spectra characteristic of the larger bandgap oxide.

Wrighton's group has succeeded in derivitizing Si²³ and GaAs²⁴ so that they are capable of carrying out electrochemistry impossible on the bare semiconductor, but as of yet the charge transfer kinetics tend to be very slow, and no derivitized surface has been found which is stable at oxygen evolution potentials.

In the forgoing discussion it has been stressed that the semiconductor must be able to evolve oxygen without corroding. This is not necessary if a p-type semiconductor is used as a photocathode. Although a number of p-type semiconductors have been used for water photoelectrolysis, most have required large applied potentials. For operation at zero applied potential the flatband potential of a photocathode must lie anodic (positive) of the oxygen evolution potential. GaP is the most frequently used photocathode. P-type semiconductors have proven to be poor catalysts for hydrogen evolution, and a substantial overvoltage is required. Nakato²⁵ and Metee²⁶ have decreased the required overvoltages through the addition of hydrogen evolution catalysts.

p/n photoelectrochemical cells employing n-type photoanodes and p-type photocathodes are, in theory, very attractive for the photodissociation of water. Although the 1.23 eV/electron required for water photolysis very nearly matches the 1.2 eV bandgap corresponding to the highest excitation efficiency for a single threshold device using solar light, losses for band-bending and kinetic overpotentials indicate that a bandgap of 1.8 - 2 eV is probably necessary for efficient water electrolysis using a single semiconductor. By using two semiconductors of smaller bandgap in series, one can hope for a better match to the solar spectrum and thus for a higher conversion efficiency. Since the anode

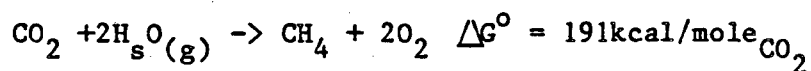
and cathode can, in effect, supply an applied potential to each other, the flatband potential requirements for operation with no external applied potential are less stringent than those for cells using a single semiconductor. The flatband potentials should not lie too far within the bounds of the hydrogen and oxygen couples however, lest larger portions of the photovoltage be expended in this biasing, thereby requiring two semiconductors with large bandgaps. Despite this partial relaxation of the flatband potential requirement, discovery of a suitable photoanode poses considerable, and as of yet unresolved, materials problems. Most p/n photoelectrolysis cells reported to date have used SrTiO_3 or TiO_2 anodes, yielding solar conversion efficiencies (0.25%²⁷ to 0.67%)²⁸ no better than those for SrTiO_3/Pt cells. Metee et. al.²⁶ have studied a p/n cell using p-GaP ($E_g = 2.3$ eV), the established p-type electrode with a plausible flatband potential, and n- Fe_2O_3 ($E_g = 2.2$ eV), one of the few stable photoanodes with $E_g < 3$ eV. The maximum value of the sum of the band-bending magnitudes for the n and p-type semiconductors in a short-circuited p/n cell is given by $U_{fb}(p) - U_{fb}(n)$. For GaP/ Fe_2O_3 this is only ~ 0.1 V, and band-bending with no external potential is marginal. This low band-bending, the low catalytic activity of H_2 evolution on GaP, and recombination at local centers and phase boundaries ("n- Fe_2O_3 " is actually $\alpha\text{-Fe}_2\text{O}_3$ + magnetite) all probably contributed to the observed low quantum efficiencies of 0.02 - 0.1% (solar conversion being even smaller). Thus while p/n cells are theoretically attractive, they are to date even less efficient in practice than simple n-type/Pt cells.

Materials problems have severely limited the solar conversion efficiencies which have been achieved in water photoelectrolysis cells. If

a number of photoanodes which yield dissolved corrosion products rather than oxygen upon illumination in water could be used, higher conversion efficiencies might result. Such semiconductors might be stable against photocorrosion at the gas-solid interface. Part of the rationale for the work undertaken here was to determine the details of water photodissociation at the vapor interface with semiconductors such as SrTiO₃ known to be photoactive in aqueous electrolytes, with the hope of extending this chemistry to the smaller bandgap semiconductors.

III-1-2 PEC Cells for CO₂ Reduction

Carbon dioxide is another interesting starting material for artificial photosynthetic systems. Although present in the modern atmosphere to the extent of only 330 ppm, it is present to much higher concentrations in exhaust gases from combustion. A synthetic photoprocess to yield CH₄ in large quantities from CO₂ and H₂O would be very exciting. Although the overall ΔG° for such a reaction,



is quite large, averaged out over the eight electrons formally transferred the free energy change corresponds to 1.04 eV per electron, less than the 1.23 eV per electron required for liquid water splitting. However, it is doubtful that all eight electrons could be transferred with this same moderate potential requirement. For example, the ΔG° for the two-electron reduction of formate to formaldehyde corresponds to 1.6 eV per electron. Russell *et. al.*²⁹ have studied the (non-photo) electrochemical reduction of CO₂, formic acid, and formaldehyde in aqueous

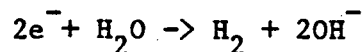
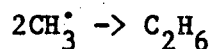
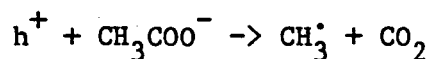
solution with an eye towards conversion of CO_2 to methanol. CO_2 reduction occurs on metals with high hydrogen overpotentials: Pb, Sn, Zn, and amalgams. The major product is formic acid or formate ion (in basic solution). Although E^0 for this reaction lies lightly anodic to the hydrogen evolution potential, a substantial overvoltage (~ 1 V) is required.³⁰ The highest current efficiency for CO_2 reduction is obtained in nearly neutral solutions²⁹. Formate/formic acid reduction occurred most readily in acidic solutions, and methanol was the only product. The reductions occurred in a narrow potential band .25 - .53 V cathodic of the hydrogen evolution potential, with maximum current densities of ~ 5 μA (corresponding to ~ 100 monolayers/hr). Based on the overall reaction an overvoltage of $\sim .3$ V is required; however, the reduction proceeds at a voltage very close to reversible potential for the formate-formaldehyde reaction.

Quite different electrolyte pH's are needed to optimize the CO_2 -formic acid and formic acid-methanol reductions, though similar catalysts (Pb, Sn) were effective. Optimal electrochemical reduction of methanol to methane is likely to require still different conditions. The prospects for a 1-step electrochemical process for reducing CO_2 to CH_4 using water at the hydrogen source thus appear somewhat dim.

The reduction of CO_2 with a PEC cell has been reported by Halmann³¹ using a p-GaP photocathode and a C anode. Application of a substantial (-1.0 V SCE) cathodic potential was required. Formic acid and lesser amounts of formaldehyde and methanol were produced.

Although endergonic electrochemical reduction of CO_2 to alcohols or hydrocarbons and oxygen has proven difficult, facile electrochemical and

photoelectrochemical catalysis of the exergonic Kolbe disproportionation of carboxylic acids to hydrocarbons and CO_2 has been demonstrated. ³² Since the carboxylic acid used must contain at least two carbon atoms, this process cannot be used in the direct reduction of CO_2 to methanol or methane. In a n-TiO₂/Pt PEC cell, acetate was disproportionated to CO_2 , C_2H_6 , and H_2 :



At zero applied potential in deoxygenated solution the reaction proceeded very slowly due to the small band-bending. Other acids gave analogous decarboxylation, simply splitting off the $-\text{COOH}$ group as CO_2 . Although the Kolbe reaction is not suitable for energy storage, it points the way towards the use of surface photochemistry in highly specific organic reactions.

III-2 Liquid Junction Solar Cells

The successful stable water photoelectrolysis cells all use semiconductors with such wide bandgaps that only a very small proportion of solar light can be absorbed. The corrosion problems encountered in using semiconductors with smaller bandgaps for water electrolysis have already been outlined. It has been found, however, that addition to the

cell of a species more easily oxidized than hydroxide ion can in some cases halt this corrosion. Thus photoelectrolysis of the hydrogen iodides, bromides, and chlorides to H_2 and X_2 may be possible. However, the cost (both in dollars and in energy expended in manufacture), low boiling points, and corrosive nature of these compounds have made photoelectrolysis cells for anhydrous hydrogen halides less attractive than their soggy cousins. Similarly, the development of photolysis cells for the other anhydrous hydrogen chalcogenides present a smelly, unrewarding challenge; though if coupled with a fuel cell, these obnoxious devices could provide an efficient means of storing sunlight for later use as electricity. Texas Instruments³³ is developing such an HBr-based technology using a unique blend of silicon p-n photovoltaic technology and electrochemistry.

Although these HX and H_2 Ecchs photolysis cells are possible, the great mass of experimentation on chalcogenide and halide redox couples as corrosion suppressants has centered on liquid junction solar cells. No net chemistry occurs in such cells - the energy output is not a fuel, but rather electric power. The corrosion suppressor (Se^{2-} for a CdS or CdSe electrode) is oxidized to selenium or polyselenide at the photoanode, then reduced back to selenide at the conterelectrode. Though there is no net chemistry to attract the attention of catalysis scientists, these cells provide an excellent means of determining the electronic and electrocatalytic properties of new materials. A large number of surface chemical effects found in such cells await elucidation. The most efficient liquid junction solar cells reported to date is a (n-GaAs | 0.8 M K_2Se - 0.1 M K_2Se_2 - 1 M KOH | C) arrangement reported by Heller and Miller.³⁴ Such cells are stable for at least two months, and

solar-to-electrical conversion efficiency of 12% has been obtained through several tricks.* One of these is the adsorption of Ru^{3+} ions, which are thought to split a surface state, thereby reducing a shunting current (see Section VII-1). This explanation for the Ru-enhancement of the photocurrent has not yet been adequately tested through detailed surface studies. As will be discussed later, such shunting effects could be important in photocatalysis.

The d-band layered semiconductors introduced by Tributsch²² show promise in liquid junction cells, although Lewerenz et. al.³⁵ have shown that facile recombination at layer edges may cripple the solar conversion efficiency on such materials. Photocorrosion in aqueous solutions can be suppressed by the addition of the I_3^-/I^- couple. Such cells have yielded solar conversion efficiencies up to 5%, with lifetimes primarily limited by the tendency of evolved iodine to eat away metallic structures. The I_3^-/I^- couple has also proven useful with other semiconductors with filled metal d-states, such as Fe_2O_3 .³⁶ Detailed surface studies of the adsorption of iodine on the layered semiconductors and Fe_2O_3 could bring to light important details of d-state to adsorbate hole transfer. Although no d-band semiconductor has been found which can continuously dissociate water, this class of materials may be useful in future photocatalytic and photosynthetic devices.

III-3 Photocatalytic Systems - Catalytic Criteria

In evaluating "photocatalytic" systems, criteria must be established to distinguish between reactions which are truly catalytic with respect to the solid surface and those which in reality constitute a

stoichiometric consumption of previously adsorbed surface moieties. Ideally, one should continue the reaction until the number of moles of products exceeds the number of moles of all species in the system except for the reactant(s) consumed. Unfortunately, at the slow rates typical of photocatalytic systems, evolution of the amount of products needed to exceed the moles of all catalysts present can take months, if not years. One must then fall back to a less stringent operational criterion for catalysis.

The atomic density of solid surfaces is on the order of 10^{15} cm^{-2} . This will be the approximate concentration of an impurity adsorbed to a monolayer coverage. If the photoreaction has yielded many times this number of product molecules, say 10^{17} per cm^2 of catalyst area, if the reaction shows no signs of tapering off, as would be expected for a reaction consuming some species in the near-surface region of the semiconductor, and if no change in the catalyst concomitant with the magnitude of the product yield can be detected, the reaction should be considered catalytic rather than stoichiometric. Though this standard cannot be considered highly rigorous, it should be noted that a number of reports of "photocatalytic" reactions do not meet these criteria.

An interesting distinction between photocatalysis and normal heterogeneous catalysis is that in the former the overall rate of reaction may be almost independent of the catalyst surface area, since light cannot penetrate all of the nooks and crannies. It is reasonable, then, to calculate rates in terms of $(\text{molecules})(\text{time})^{-1}(\text{illuminated cross-sectional area})^{-1}$ rather than to normalize to the total area of the catalyst. However, since the entire surface may serve as a reservoir

for a previously adsorbed reactant, catalytic criteria should be based upon the total surface area. In comparing the efficiency of catalytic systems, the quantum yield $[(\text{molecules product yield}) \times (\text{photons per equivalent}) \div (\text{incident photons})]$ is the best measure.

III-4 Photocatalysis at the Liquid-Solid Interface

In photocatalytic systems there are no physically distinct anodes and cathodes connected by an external circuit. The photocatalyst may consist of two phases in physical contact, or may be composed of a single phase. Both types of photocatalysts have been shown to be effective for a variety of reactions in liquid electrolytes.

The two-phase photocatalysts have been named "photochemical diodes" by Nozik²⁷. His diode consisted of a single crystal of n-TiO₂ in ohmic contact (through a Ga-In eutectic) with a p-GaP wafer. Upon illumination of both sides of the diode, hydrogen was evolved from the GaP while O₂ bubbled off of the TiO₂, in strict analogy to a short-circuited p/n PEC cell. Although it was argued that the operation of such a structure is independent of size, considerable losses were found unless ohmic contacts were provided through the Ga-In eutectic.³⁷ Provision of this contact complicates the device, leaving it with few advantages over the analogous PEC cell.

Wrighton et. al.³⁸ have reported the catalytic decomposition of water from aqueous electrolytes when a n-SrTiO₃ crystal whose back has been directly coated with platinum is illuminated with bandgap light. This system works without artificial provision of an ohmic contact, albeit with somewhat reduced efficiency, so that use of a simple

suspension of platinized SrTiO_3 powder is possible.

Although the two photocatalytic systems discussed above give behavior equivalent to the analogous PEC cells, Bard et. al.³² have noted differences in the product distribution of the photo-Kolbe reaction when performed in a TiO_2/Pt PEC cell or on a platinized TiO_2 powder photocatalyst. In the PEC cell the major reduced disproportionation product of formate is ethane, while on the photocatalyst it is methane. In the PEC cell oxidation of the formate ion on TiO_2 leads to adsorbed methyl radicals which, in the absence of other reductants, combine to form ethane while hydrogen is evolved from the distant Pt cathode. On the photocatalyst the methyl radicals adsorbed on TiO_2 can react with H_2 or H from the proximal Pt sites, yielding CH_4 as the major product. The interspersion of the oxidative and reductive centers thus can lead to unique chemistry on photocatalysts. Photocatalysts can also make use of materials which cannot be made sufficiently conductive for service as photoelectrodes. For example, Bulatov and Khidekel³⁹ and Sato and White⁴⁰ have reported the photocatalytic decomposition of liquid water over platinized powders of the anatase phase of TiO_2 , though the catalytic nature of these results is unproven. Anatase has also proven more photoactive than rutile in other applications³².

A number of other multiphase photocatalytic systems for aqueous solutions have been developed. Among the most complex and intriguing is a homo-heterogeneous scheme for catalytic water photolysis reported by Grätzel et. al.⁴¹ Illumination causes electron transfer from aqueous $\text{Ru}(\text{bpy})_3^{3+}$ to a C_{14} alkyl derivative of the methyl viologen dication. The resulting $\text{Ru}(\text{III})$ complex reacts with water on the surface of

suspended RuO_2 particles to yield oxygen. Micellization extends the lifetime of the $\text{C}_{14}\text{MV}^{+1}$ moiety, which reacts with water on colloidal Pt to yield hydrogen. Quantum yields are still low because the excited state lifetimes, while greater than those in purely homogeneous systems, are still far too short (20 - 30 msec) for efficient operation. These combined homo-heterogeneous systems gain some of the charge separation properties of heterogeneous systems while partially circumventing the fundamental problems facing systems in which the metallo-organic photoreceptor is bound to a semiconductor surface - the inability of a monolayer to absorb more than 1% of incident light and the low conductivities of thicker layers.

Single-phase photocatalysts in liquid electrolytes

A fair number of reactions, some exergonic and some endergonic, have been studied using liquid phase reactants on single phase photocatalysts, i.e. non-platinized semiconductor powders. Both oxidation and reduction have been observed on metal-free n-type semiconductors. Frank and Bard⁴² found that TiO_2 and some other n-type materials were effective photocatalysts for the oxidation of SO_3^{2-} and CN^- . Watanabe *et. al.*⁴³ have correlated the photocatalytic reduction of methylene blue on TiO_2 suspensions with similar chemistry in n- TiO_2/Pt PEC cells. A number of metal ions have been photocatalytically reduced on oxide semiconductor powders and/or single crystals: Ag^+ ,^{44,45} Au(III) ,⁴⁶ Cu^{2+} ,^{38,47} Pd^{2+} ,^{48,49} and Pt(IV) .⁵⁰ The significance of this work is that it shows that photo reductions can occur on the surfaces of n-type semiconductors. This is somewhat at odds with first-order photoelectrochemical theory.

Inoue et. al. ⁵¹ have reported the photoreduction of CO₂ on aqueous suspensions of TiO₂, ZnO, CdS, GaP, and SiC. Formic acid, formaldehyde, methanol and a trace of methane were produced, with a quantum efficiency of $\sim 5 \times 10^{-4}$ for formaldehyde. Quantitative determination of formic acid was precluded by the gas chromatographic means of analysis used. Though no surface areas of the catalysts were reported, the maximum product yields correspond to ~ 10 monolayers assuming a typical surface area for the semiconductor powders of 5 m²/g. This yield is probably, though not unambiguously, indicative of a catalytic reaction. Although the reaction is definitely a photoeffect, there was no definite proof of CO₂ as the source of carbon in the final products.

A fair number of photocatalytic reactions have thus been reported at the liquid-solid interface. Some of the two-phase photocatalysts achieve quantum efficiencies roughly equivalent to those obtained in the analogous PEC cell. Aside from the reductions of aqueous metal ions, the reactions on single-phase photocatalysts proceed at very low quantum yields. At least to the knowledge of these authors, no unambiguously sustainable hydrogen photoproduction from water on platinum-free semiconductors had been attained prior to the work reported in this thesis.

III-5 Photocatalysis at the Gas-Solid Interface

Photoeffects at the gas-solid interface have been studied for many years. The simplest chemical effects involve photodesorption of molecules adsorbed in the dark or photocatalyzed adsorption. Photodesorption has been reported both on semiconductors or oxides and on metals, but the data of Koel et. al. ⁵² indicate that most "photo"

desorption from metals, at least at wavelengths above the vacuum UV, are due to localized heating rather than to quantum effects. Impure surfaces of materials such as CdS, ZnO, ⁵³ TiO₂, and oxidized stainless steel tend to give as desorption products CO₂ and, to a lesser extent, atomic O when illuminated by bandgap radiation. CO₂ photodesorption is believed to proceed through capture of a photogenerated hole by an adsorbed CO₂⁻ species. ⁵⁴ The group of Munuera ⁵⁵ have studied the photoadsorption and photodesorption of oxygen on TiO₂ powders and have correlated these effects with the degree of hydroxylation of the surface, as will be discussed in Chapter VII. Ferrer ⁵⁶ has studied oxygen adsorption and photodesorption on clean, single-crystal SrTiO₃ under UHV conditions. Oxygen uptake is related to the concentration of a surface Ti³⁺ species present on reduced and/or argon-sputtered surfaces. Adsorption of oxygen quenches the Ti³⁺, which reappears upon photodesorption of the oxygen using bandgap radiation. Although no net chemistry takes place during photodesorption studies, the photoinduced charge transfer steps which occur may be similar to those essential to photocatalytic reactions.

Both endergonic and exergonic reactions have been reported at the illuminated gas-solid interface. Freund and Gomes ⁵⁷ have reviewed early work on exergonic reactions. All of these reactions are oxidations or isotopic exchanges: oxidations of CO, alcohols, and alkanes; H₂-D₂ and O₂¹⁶ - O₂¹⁸ exchange. Reports of reductive photochemistry are more rare.

Boonstra and Mutsaers ⁵⁸ observed the photohydrogenation of acetylene on TiO₂ powders. The reaction ceased with time, giving a maximum

product yield less than that corresponding to monolayer coverage of the powders. When thermally dehydroxylated powders were used no photoactivity was seen. The reaction therefore involved a stoichiometric consumption of surface hydroxyl groups, rather than a sustainable photocatalytic effect. Schrauzer and Guth⁵⁹ reported the photodissociation of water and the reduction of N_2 to NH_3 using water as the hydrogen source over TiO_2 and $TiO_2-Fe_2O_3$ powders. These reactions stopped in time, an effect ascribed by the authors to a facile back-reaction, though no efficient water-forming catalyst was present. Using the high end of their reported 0.5 - 1 μ particle size range and assuming spherical particles it can be calculated that their maximum hydrogen accumulation corresponded to ~ 2 monolayers. Since the actual surface area was undoubtedly greater than that estimated with the assumption of spherical particles, their results are consistent with a stoichiometric consumption of a surface species. Van Damme and Hall⁶⁰ attempted to repeat Schrauzer and Guth's results using a flow system in which no back reactions could occur and detected no significant H_2 production. Thus this reaction also appears to have been the stoichiometric consumption of an adsorbed species rather than true photocatalysis. The issue of back reactions is dealt with in some detail in Chapter V.

Recently Kawai and Sakata⁶¹ and Sato and White⁶² have reported the reaction of water vapor and "active carbon" to yield H_2 and CO_2 on illuminated TiO_2/RuO_2 on TiO_2/Pt catalysts. In both cases catalytic yields of hydrogen were observed. The ΔG° for this reaction is +63 kJ/mole, assuming that the photoactive part of the active carbon is in fact graphite. The use of "active" carbon raises questions as to whether this reaction is in fact a disproportionation of carboxylate or

other oxidized surface moieties analogous to the photo-Kolbe reaction rather than an oxidation of graphite. This reaction proceeded more rapidly in water vapor than on Pt/TiO₂ powders covered with liquid water. The ready photoactivity of carbonaceous species with water and the ubiquitous presence of C impurities on powders draw attention to the need for strict catalytic criteria for the evaluation of photocatalytic reactions.

Most recently, Kawai and Sakata⁶³ have reported the photocatalytic decomposition of gaseous water over mixtures of TiO₂ and RuO₂ powders. They report catalytic yields after one week's operation. The rate of hydrogen production was ~0.5 monolayers/hr (11 μ mole D₂ in 20 hr on 80 mg TiO₂ with surface area 0.1 m²/100 mg) corresponding to a quantum yield of approximately 0.02% (20 cm² exposed cross-section, 500 W Hg lamp). This rate of H₂ production is one order of magnitude smaller than the minimum detectable significant rate using single crystals and the experimental apparatus employed in the studies reported here. Thus, while photocatalytic decomposition of gaseous water at room temperature has now been demonstrated, it proceeds at much lower turnover frequencies and at lower quantum efficiency than the photocatalysis in thin films of aqueous alkaline electrolytes reported here.

The photodecomposition of water occurs rapidly and with good quantum yields (for bandgap radiation) in PEC cells and on some two-phase photocatalysts operating in aqueous electrolytes. Although various exergonic oxidations can be run photocatalytically at the gas-solid interface with fair yields, the photocatalytic decomposition of water vapor has historically eluded demonstration. Even now that it has been demonstrated,

the efficiency at room temperature is much lower than that which can be achieved in aqueous electrolyte. The experiments to be described in the next several chapters in part attempted to discern the critical differences between the gas-solid and liquid-solid interfaces which lead to this great disparity in photoactivity. A number of gas-solid and liquid-solid systems have been investigated, and the semiconductor surface compositions before and after reactive and unreactive illumination have been determined. Though the results are not entirely conclusive, they do indicate that (1) photoreduction as well as photo-oxidation of water can occur on n-type semiconducting oxides, and (2) differences in the nature of surface hydroxylation at the gas-solid and liquid-solid interfaces may be in large part responsible for the great differences in photocatalytic activity seen at the gas-solid and liquid-solid interfaces at room temperatures.

III-6 Surface States in Photoelectrochemistry and Photocatalysis

The "surface state" has played the role of the philosopher's stone in much of the photoelectrochemical literature. Although many anomalous effects have been ascribed to these entities, with few exceptions no actual determination of the actual chemical identity of these surface states has been achieved. The usage of the term "surface state" has been much broader than the definition commonly adhered to in the literature of solid state physics. A "surface state" may be intrinsic to the termination of the bulk semiconductor, or may be induced in the semiconductor by chemisorption of an external species. The local states of an adsorbed molecule are also considered a surface state. Even the local states of a material intentionally attached to the (derivitized) surface

may be thought of as surface states.

Much of the impetus for the invocation of surface states in photoelectrochemistry has arisen from the widespread acceptance of the quantum mechanical treatment of charge transfer at the semiconductor-electrolyte interface espoused by Gerischer inter alia.⁶⁴ Efficient charge transfer across the interface can occur only by an elastic tunneling process between states of equal energy, whereas charge transfer between a delocalized band of the bulk semiconductor and a localized surface state can occur efficiently through inelastic processes. The E° for the O_2/OH^- couple lies within the bandgap of the semiconductors used in water photoelectrolysis. If this E° level is naively considered as the hole acceptor level of the electrolyte, a surface state at this level needs be invoked to account for efficient hole transfer. In reality, solvent fluctuations are likely to sufficiently broaden the distribution of hole acceptor states in the electrolyte so that direct hole injection from the valence band into the electrolyte is possible. Photoemission studies⁶⁵⁻⁶⁷ have yet to identify any surface state at the energy of the O_2/OH^- formal redox potential. Though surface states are thus not necessary for theoretical consistency on oxygen evolution, the complex four-electron oxidation undoubtedly takes place through a series of adsorbed intermediates. Wilson⁶⁸ has measured a dark cathodic current on TiO_2 ascribed to reduction of one of these species after its formation during illumination. Identification of these intermediates is the fundamental question in modern electrocatalysis research, a question which is still far from being resolved.

Schwerzel et. al.¹⁷ have ascribed the rapid photocorrosion of SrTiO_3 under high bias in certain acidic electrolytes to the presence of surface states within the bandgap. Though their analysis suffers from the aforementioned problem of the identity of E^0 values with actual acceptor state energies, their predicted surface state energies correlate well with the Ti^{3+} level reported by Lo⁶⁷, Chung⁶⁶, Ferrer⁵⁶, and Henrich⁶⁵ on argon-bombarded SrTiO_3 in vacuo. Wilson⁶⁸ has developed in some quantitative detail a surface state model for the photoreduction of CdS .

Carrier recombination via surface states has been demonstrated. Beckmann and Memming have observed luminescence on GaP due⁶⁹ to such recombination. Heller et. al.³⁴ have ascribed the improvement in photocurrents in GaAs cells upon chemisorption of Ru^{3+} to suppression of recombination at surface states. Attempts to test this hypothesis through photoemission work were frustrated by impurities and overlapping emissions.⁷⁰

Surface states have been used to explain photoelectrochemistry involving redox couples which lie outside the semiconductor band edges as determined by flatband potential and bandgap measurements. The effect, known as Fermi level pinning,⁷¹ also explains why liquid junction solar cells using identical electrodes but different redox couples with widely disparate redox potentials sometimes yield the same photovoltages. If a sufficiently high density of surface states exists these states can play the role of the metal in Schottky-barrier formation. If these surface states are kinetically inert with respect to the electrolyte, the band-bending will be determined by bulk semiconductor-surface state charge transfer and not by bulk semiconductor-electrolyte charge

transfer. With band-bending fixed by the surface state, an applied potential will appear across the electrolyte Helmholtz layer instead of across the semiconductor depletion layer. The applied potential then shifts the relative energies of the band edges and the acceptor states in the electrolyte, and "supra-bandgap" electrochemistry can result. Fermi level pinning becomes important only when the total charge in the surface state exceeds that in the depletion layer. This is most likely when (1) the concentration of surface states is high, (2) the doping level of the semiconductor is low and (3) the dielectric constant of the semiconductor is low. These requirements are met for largely covalent semiconductors such as Si, GaAs, and probably the molybdenum and tungsten sulfides and selenides. For semiconductors with moderate doping levels ($\sim 10^{15} \text{ cm}^{-3}$) surface state densities as low as 1% of a monolayer can cause Fermi level pinning. For the highly doped ($\sim 10^{19} \text{ cm}^{-3}$) oxide semiconductors commonly used in water photoelectrolysis cells, however, surface state concentrations greater than 100% of a monolayer would be required. In fact, no photoelectrochemical evidence for Fermi level pinning on TiO_2 or SrTiO_3 has been reported.

Nozik et. al. ⁷² have an alternate explanation for supra band-edge photoelectrochemistry in their postulate of hot carrier injection. This theory also requires the presence of surface states, as discussed in Chapter VII. An alternative explanation for the apparent shift in band edges with applied potentials, this one involving no surface states, has been advanced by Turner et. al. ⁷³

Direct spectroscopic detection of surface states on photocatalysts and photoelectrodes has been rather unusual, and direct correlation of

surface states with photochemical activity has proven still more elusive. Using UPS and low resolution electron loss spectroscopy, Chung⁶⁶ has detected a surface species ascribed to Ti^{3+} 0.6 eV below the Fermi level on certain vacuum-prepared (100) surfaces of TiO_2 (rutile). On Ti^{3+} -rich surfaces water adsorbes dissociatively, while on Ti^{3+} -poor surfaces water is adsorbed as intact molecules. A similar Ti^{3+} state was found on $SrTiO_3$ by Henrich⁶⁵ (on the (001) surface), Lo⁶⁷ (111), and Ferrer (111)⁵⁶. Oxygen diffusion appears to be less rapid in $SrTiO_3$ than on TiO_2 , as the Ti^{3+} induced by argon bombardment cannot be as easily quenched by annealing in vacuo. Ferrer⁵⁶ has found that exposure of a Ti^{3+} -containing surface to H_2O , O_2 , H_2 , or background gases yields a hydroxylated surface typified by UPS emissions 4.6, 6.4, and 11.8 eV below the Fermi level - all well below the valence band edge and below the conceivable hole acceptor levels in aqueous electrolytes or in water vapor.

A few other moderately detailed surface analyses of photoelectrodes have been performed. Sayers and Armstrong⁷⁴ using XPS, showed that the near-surface region of an n- TiO_2 photocathode was slowly oxidized during use in a water photoelectrolysis cell. Tench and Raleigh⁷⁵ found Sr depletion in the near surface region of $SrTiO_3$ upon contact with water, again by XPS. Cahen et. al.⁷⁶ and Noufi et. al.⁷⁷ used XPS to study S substitution for Se upon illumination of CdSe in electrolytes containing S^{2-} . All of these efforts were hampered by the necessity of transferring the sample from the electrochemical cell to the vacuum chamber through a glovebox or room air, with inevitable contamination.

Techniques based upon electron energy analysis cannot be used for in situ studies of surface states in PEC cells. Tomkiewicz,⁷⁸ using detailed impedance vs. applied potential measurements, has mapped out the distributions of surface states on TiO_2 due to alkylsilane derivatizing agents. More detailed in situ analysis awaits the development of advanced optical techniques. Although surface states play major roles in the operation of PEC cells and photocatalysts, much research remains to be done to specify the chemical nature of such surface states and to test the theories of charge transfer and depletion layer formation presently flying about unpinned by any direct spectroscopic evidence. The results contained in this thesis underline the need for further study of surface hydroxyl groups and other intermediates in the oxygen evolution reaction at both the liquid-solid and gas-solid interfaces.

REFERENCES

1. A.J. Nozik, *Ann. Rev. Phys. Chem.*, 29, 189 (1978).
2. R. Memming, *Electrochimica Acta*, 25, 77 (1980).
3. A. Heller and B. Miller, *Electrochimica Acta*, 25, 29 (1980).
4. A. Fujishima and K. Honda, *Bull. Chem. Soc. Jpn.*, 44, 1148 (1971),
5. J.M. Bolts, M.S. Wrighton, *J. Phys. Chem.*, 80, 2641 (1976).
6. K.L. Hardee, A.J. Bard, *J. Electrochem. Soc.*, 123, 1683 (1976).
7. R.K. Quinn, R.D. Nasby, R.J. Baughman, *Mater. Res. Bull.*, 11, 1011 (1976).
8. D.S. Ginley and M.A. Butler, *J. Appl. Phys.*, 48, 2019 (1977).
9. H.H. Kung, H.S. Jarrett, A.W. Sleight, A. Ferretti, *J. Appl. Phys.*, 48, 2463 (1977).
10. M.A. Butler, D.S. Ginley and M. Eibschutz, *J. Appl. Phys.*, 48, 3070 (1977).
11. M. Tomkiewicz, *J. Electrochem. Soc.*, 126, 1505 (1979).
12. A.B. Ellis, S.W. Kaiser, M.S. Wrighton, *J. Phys. Chem.*, 80, 1325 (1976).
13. J.G. Mavroides, J.A. Kafalas and D.F. Kolesar, *Appl. Phys. Lett.*, 28, 241 (1976).
14. M.S. Wrighton, A.B. Ellis, P.T. Wolczanski, D.L. Morse, H.B.

- Abrahamson and D.S. Ginley, *J. Am. Chem. Soc.*, 98, 2774 (1976).
15. R.D. Nasby and R.K. Quinn, *Mater. Res. Bull.*, 11, 985 (1976).
 16. K.I. Zamaraev and V.N. Parmon, submitted to *Cat. Rev.*
 17. R.E. Schwerzel, E.W. Brooman, H.J. Byker, E.J. Drauglis, D.D. Levy, L.E. Vaaler and V.E. Wood, in Photoeffects at Semiconductor-Electrolyte Interfaces, A.J. Nozik, ed., ACS Symposium Series No. 146, 1980.
 18. A.K. Ghosh and H.P. Maruska, *J. Electrochem. Soc.*, 124, 1516 (1977).
 19. R.D. Rauh, J.M. Buzby, T.F. Reise, and S.A. Alkaitis, *J. Phys. Chem.*, 83, 2221 (1979).
 20. J.G. Mavroides, J.C. Fan and H.J. Zeiger, in ref. 17, p. 217.
 21. K. Dwight and A. Wold, in ref. 17, p. 13.
 22. H. Tributsch, *J. Electrochem. Soc.*, 125, 1086 (1978).
 23. N.S. Lewis and M.S. Wrighton, in ref. 17, p. 37.
 24. J.M. Bolts and M.S. Wrighton, *J. Am. Chem. Soc.*, 101, 6179 (1979).
 25. Y. Nakato, S. Tonomura and H. Tsubomura, *Ber. Bunsenges. Phys. Chem.*, 80, 1289 (1976).
 26. H. Metee, J.W. Otvos and M. Calvin, *Solar Energy Mat.*, 4, 443 (1981).
 27. A.J. Nozik, *Appl. Phys. Lett.*, 30, 567 (1977).

28. K. Ohashi, J. McCann and J. O'M. Bockris, *Nature*, 266, 610 (1977).
29. P.G. Russell, N. Kovac, S. Srinivasan and M. Steinberg, *J. Electrochem. Soc.*, 124, 1329 (1977).
30. K.S. Udupa, G.S. Subramanian and H.V.K. Udupa, *Electrochim. Acta*, 16, 1593 (1977).
31. M. Halmann, *Nature*, 275, 155 (1978).
32. B. Kraeutler and A.J. Bard, *J. Am. Chem. Soc.*, 100, 5985 (1978).
33. J.S. Kilby, J.W. Lathrop, W.A. Porter, U.S. Patent 4,021,323.
34. B.A. Parkinson, A. Heller and B. Miller, *J. Electrochem. Soc.*, 126, 954 (1979).
35. H.J. Lewerenz, A. Heller, H.J. Leamy, and S.D. Ferris, in ref. 17, p. 17.
36. J.H. Kennedy, R. Shinar and J.P. Ziegler, *J. Electrochem. Soc.*, 127, 2307 (1980).
37. A.J. Nozik, personal communication.
38. M.S. Wrighton, P.T. Wozanski and A.B. Ellis, *J. Solid State Chem.*, 22, 17 (1977).
39. A.V. Bulatov and M.L. Khidekel, *Izv. Akad. Nauk SSSR, Ser Khim*, 1902 (1976).
40. S. Sato and J.M. White, *Chem. Phys. Let.*, 72, 83 (1980).
41. M. Grätzel, *J. Am. Chem. Soc.*, 102, 2461 (1980).

42. N. Frank and A.J. Bard, *J. Phys. Chem.*, 81, 1484 (1977).
43. T. Watanabe, T. Takizawa and K. Honda, *J. Phys. Chem.*, 81, 1845 (1977).
44. E. Bauer and A. Perrett, *Helv. Chim. Acta*, 7, 919 (1924).
45. H. Janker, C.J. Dippel, J.H. Houtman, C.J.G.F. Janssen, and L.K.H. van Beek, *Phot. Sci. Eng.*, 13, 1 (1969).
46. A.K. Bhattacharya and N.R. Phari, *J. Indian Chem. Soc.*, 4, 299 (1926).
47. H. Reiche, W.W. Dunn and A.J. Bard, *J. Phys. Chem.*, 83, 2248 (1979).
48. H. Jonker, C.J.G.F. Janssen, C.J. Dippel, T.P.G.W. Thigssens and L. Postma, *Phot. Sci. Eng.*, 13, 45 (1969).
49. F. Möllers, H.J. Tolle and R. Memming, *J. Electrochem. Soc.*, 121, 1160 (1974).
50. B. Kraeutler and A.J. Bard, *J. Am. Chem. Soc.*, 100, 4317 (1978).
51. T. Inoue, A. Fujishima, S. Konishi and K. Honda, *Nature*, 277, 637 (1979).
52. B.E. Koel, J.M. White, J.L. Erskine, and P.R. Antoniewicz, in Interfacial Photoprocesses: Energy Conversion and Synthesis, M.S. Wrighton, ed., *Adv. in Chem. Series No. 184*, p. 27.
53. Y. Shapira, S.M. Cox and D. Lichtman, *Surf. Sci.*, 50, 503 (1975).

54. Y. Shapira, S.M. Cox and D. Lichtman, *Surf. Sci.*, 54, 43 (1976).
55. G. Munuera, V. Rives-Arnau and A. Saucedo, *J. Chem. Soc. Faraday Trans. I*, 75, 736 (1979).
56. S. Ferrer and G.A. Somorjai, *Surf. Sci.*, 94, 41 (1980).
57. T. Freund and W.P. Gomes, *Cat. Rev.* 3, 1 (1969).
58. A.H. Boonstra and C.A.H.A. Mutsaers, *J. Phys. Chem.*, 79, 2025 (1975).
59. G.N. Schrauzer and T.D. Guth, *J. Am. Chem. Soc.*, 99, 7189 (1977).
60. H. Van Damme and W.K. Hall, *J. Am. Chem. Soc.*, 101, 4373 (1979).
61. T. Kawai and T. Sakata, *Nature*, 282, 283 (1974).
62. S. Sato and J.M. White, *Chem. Phys. Lett.*, 70, 131 (1980).
63. T. Kawai and T. Sakata, *Chem. Phys. Lett.*, 72, 87 (1980).
64. H. Gerischer, in Physical Chemistry, an Advanced Treatise, Vol 9A, H. Eyring, ed., Academic Press, New York, 1970.
65. V.E. Henrich, G. Drsselhaus, and H.J. Zeiger, *Phys. Rev. B*, 17, 4908 (1978).
66. W.J. Lo, Y.W. Chung, and G.A. Somorjai, *Surf. Sci.*, 71, 199 (1978).
67. W.J. Lo and G.A. Somorjai, *Phys. Rev. B*, 17, 4942 (1978).
68. R.H. Wilson, in ref. 17, p. 103.

69. K.H. Beckmann and R. Memming, *J. Electrochem. Soc.*, 127, 840 (1980).
70. Gary Schwartz, personal communication.
71. A.J. Bard, A.B. Bocarsly, F.F. Fan, E.G. Walton and M.S. Wrighton, *J. Am. Chem. Soc.*, 102, 0 (1980).
72. D.S. Boudreaux, F. Williams and A.J. Nozik, *J. Appl. Phys.*, 51, 2158 (1980).
73. J.A. Turner, J. Manassen, and A.J. Nozik, in ref. 17, p. 253.
74. C.N. Sayers and N.R. Armstrong, *Surf. Sci.*, 77, 301 (1978).
75. D.M. Tench and D.O. Raleigh, in Electrocatalysis on Non-Metallic Surfaces, NBS Spec. Pub. 455, 1976, p. 229.
76. D. Cahen, G. Hodes and J. Manassen, *J. Electrochem. Soc.*, 125, 1623 (1978).
77. R.N. Noufi, P.A. Kohl, J.W. Rogers, Jr., J.M. White and A.J. Bard, submitted to *J. Electrochem. Soc.*
78. M. Tomkiewicz, *J. Electrochem. Soc.*, 127, 1518 (1980).

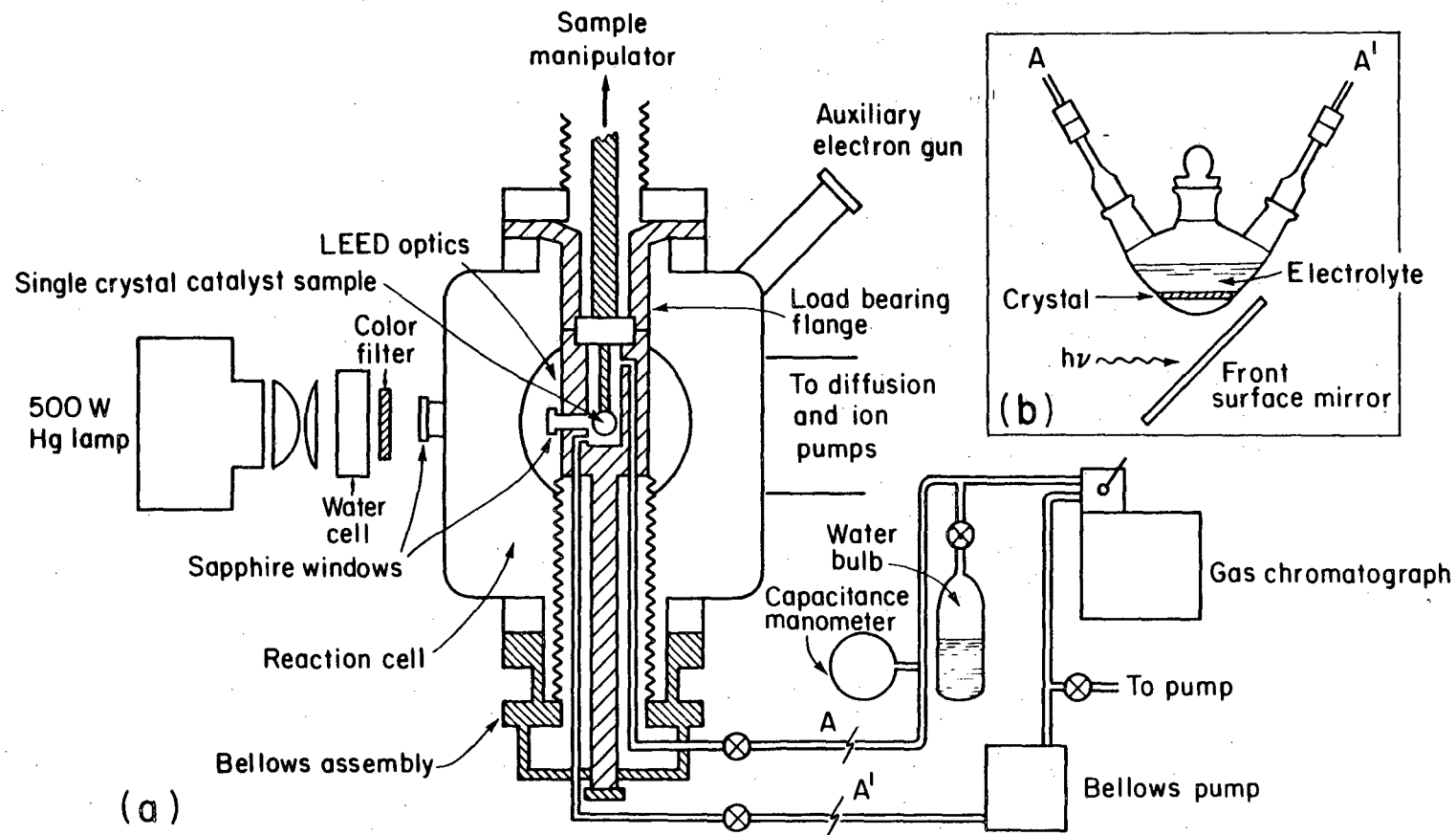
Chapter IV: Experimental

A diversity of apparatus was used in the surface analytical and photochemical experiments described in this report. In some cases surface analysis was performed in conjunction with photochemical reaction studies in a unified apparatus; at other times the two types of studies were carried out separately. In this chapter all of the apparatus, catalyst samples, and reagents employed are described in detail. The equipment used in individual experiments will be briefly outlined in the results chapters.

IV-1 Reaction Vessels for the Study of Heterogeneous Photochemistry

IV-1-1 Unified Surface Analysis-Photoreaction Chamber

Figure VI-1A shows a schematic diagram of the apparatus for the study of gas-phase photoreactions on well-characterized single crystal surfaces. The framework is a standard ultra-high vacuum chamber equipped with four-grid electron optics for analysis of surface composition by Auger electron spectroscopy (AES) and for determination of ordered surface structure by low energy electron diffraction (LEED). Auger signal detection was through a combination of Vacuum Generators, Varian, and home-grown electronics and a PAR JB-4 lock-in detector. An argon ion sputter gun allowed for mechanical cleaning of the surfaces; chemical cleaning could be achieved by resistive heating of a platinum or gold foil sample holder in 10^{-6} torr oxygen. The system was pumped to a post-bake base pressure of $\sim 5 \times 10^{-9}$ torr by a 110 l/s ion pump and a LN_2 -trapped 4" oil diffusion pump.



XBL7910-4558

Fig. IV-1. Apparatus used in photocatalysis studies.

After preparation and analysis of the surface, a bellows-mounted isolation cell could be raised around the crystal and sealed against the top plate with a gold or viton O-ring. The cell and outer chamber were equipped with sapphire windows to allow illumination of the sample. The isolation cell was part of a closed gas circulation loop encompassing the cell, a sampling valve for a gas chromatograph, and a manifold for pumping and the admission of high-purity gases and vapors. The circulation loop could be roughed out by a LN_2 -cooled sorption pump and/or a LN_2 -trapped rotary mechanical pump and could also be pumped into the main vacuum chamber prior to experimental runs. Research-grade gases were admitted through copper or stainless steel lines. Vapors of water and piperidine could be admitted from a glass bulb containing high purity liquids degassed through repeated freeze-pump-thaw cycles. The operating volume of the circulation loop in this configuration was 100 ml.

This apparatus was used in both gas-surface photochemical experiments and in experiments in which a thin film of liquid electrolyte coated the sample. The latter experiments were carried out by removing the sample from the apparatus, dipping it and a vycor glass rod holder in an aqueous solution of a deliquescent salt, and drying the film with hot air. The coated sample was placed in the reaction cell which was then evacuated and backfilled with water vapor, saturating the coating. The presence of the insulating film precluded the use of electron-beam analysis techniques to determine the structure and composition of the underlying sample. The mean thickness of the applied film could be controlled by applying the initial electrolyte solution with a microliter pipette rather than by dipping the crystal. Mean film thicknesses of

basic compounds could be determined after the experiment by titration of the sample with HCL.

IV-1-2 Photocatalytic Experiments in Bulk Liquid Electrolytes

The photoactivity of samples in bulk liquid electrolytes of known composition were studied by inserting the borosilicate reaction vessel shown in Figure IV-1B into the circulation loop in place of the bellows-mounted cell. The sample was supported by the cell walls; no metallic components were used in the reaction cell. 5 or 10 ml of electrolyte was brought into the vessel to cover the sample. After outgassing of the electrolyte the circulation loop was evacuated (to the vapor pressure of the electrolyte) and sealed. The sample was illuminated from below using a front-surfaced mirror. The volume of the circulation loop with this reaction vessel in place was 170 ml.

IV-1-3 Photoelectrochemical Measurements

In some experiments an electrochemical cell with discrete electrodes was operated within the reaction vessel described in IV-1-2. In this case teflon-insulated platinum leads ran through a vacuum feedthrough to the vessel exterior. Cell currents were determined by measuring the voltage drop across a 11 ohm resistor with a digital millivoltmeter. Frequent current readings allowed accurate integration of photocurrent for comparison with simultaneous gas chromatographic measurement of hydrogen production.

Measurements of the effects of temperature and light-intensity on photocurrent were carried out in a non-evacuatable borosilicate vessel

purged with argon. The cell was mounted in an ethylene glycol bath heated by a stirring hotplate, and the electrolyte was stirred by a teflon-coated magnet.

IV-2 Gaseous Product Detection

A gas chromatograph was used to analyze the products of heterogeneous photoreactions. The argon-purged stainless steel and teflon sampling valve fitted with a 0.25 ml sampling loop was an integral part of the circulation loop; 100% of the flow passed through it. Each operation of the sampling valve injected 0.25 ml of the argon carrier gas at about 30 psi into the reaction loop. Blank experiments showed that no impurities in the argon were important to the observed photochemistry, either as reactants or as pseudoproducts.

Two detectors and three column systems were used with the gas chromatograph. A thermal conductivity detector (TDC) and a molecular sieve 5A column formed the basis of the analysis system for the water photodissociation experiments. The sensitivity of the chromatograph was determined by admitting low pressures of known gases to the circulation loop and then sampling. This technique was checked by direct injection of submicroliter amounts of known gases at atmospheric pressure into the chromatograph through a septum. The two methods gave sensitivity calibrations agreeing within a factor of about 2; the results of the low pressure sampling were more reproducible and were considered more accurate. The minimum number of hydrogen molecules in a sample detectable at a signal:noise ratio of about 1:1 was 3×10^{13} . Since the ratio of total circulation loop volume to sampling loop volume was 400, the above

detection limit corresponds to the production of 1×10^{16} molecules H_2 in the circulation loop. This corresponds to a hydrogen partial pressure of 5×10^{-8} torr. Dilution experiments showed that the detector showed good linearity for the detection of hydrogen in the pressure range from ~ 2 torr to the detection limit. The absolute calibration of sensitivity for hydrogen is good to about a factor of two.

The detection of oxygen proved more problematic. The sensitivity of a TCD operating with an argon carrier gas is inherently lower for oxygen than for hydrogen due to the smaller difference between the thermal conductivities of oxygen and argon. Extrapolation of the oxygen detection sensitivity in the torr region to zero pressure implied a detection limit for oxygen in the circulation loop of 1×10^{17} molecules. However, dilution experiments showed a marked nonlinearity in oxygen sensitivity, with the sensitivity dropping at lower pressure. A time dependence of oxygen partial pressure in the circulation loop was noted, as oxygen appeared to slowly displace water vapor from the circulation loop walls or to otherwise react with portions of the plumbing.

The system sensitivity to nitrogen in the torr range was $\sim 1/2$ that for oxygen. Nonlinearity and time-dependent effects were smaller than those for oxygen. Other gases, such as CO , CO_2 , and CH_4 were detectable, but at lower sensitivities. Water adsorbed on the molecular sieve 5A column and gave no detector signal. Elution times for various gases are listed in Table IV-1.

TABLE IV-1

Retention Times on Molecular Sieve 5A at 110°C	
Gas	Time (sec)
H ₂	79
O ₂	120
N ₂	168
CH ₄	250

Attempts at periodic sampling of the product gases for mass spectroscopic analysis led to overall lower sensitivity levels than could be achieved chromatographically, even after water vapor was trapped out with liquid nitrogen.

At the water vapor pressures used in these experiments hundreds of data points could be gathered before water vapor adsorption noticeably changed the column characteristics. The column could then be regenerated by operation at 200°C for 1/2 hour. However, when experiments were run with mixtures of water vapor with ammonia or piperidine vapors the molecular sieve column deteriorated rapidly. A Chromosorb 104 column and a series bypass valve were then added to the system. After sampling, the light gases were allowed to run through the Chromosorb 104 column into the molecular sieve 5A. The sieve column was then switched out of the carrier flow and the water and basic vapors allowed to elute out of the chromosorb through the detector, enabling quantitative measurement. The molecular sieve column was then switched back online and good separation of light gases was obtained. The long static residence time in the sieve column further hampered the detection of low levels of

oxygen. Hydrogen sensitivity was reduced by about a factor of two in this mode due to longer retention times and peak broadening. Typical elution times and a valve switching schedule for this detection system are listed in Table IV-2.

TABLE IV-2: Retention times and switching schedule

for 12 ft Molecular Sieve 5A + 6 ft Chromosorb 104 at 130°C,

18 ml/min Ar carrier

<u>Time (sec)</u>	<u>Switching Schedule</u>
0	sample
80	switch MS5A column offline
150	NH ₃ elutes
250	switch MS5A column online
340	H ₂ elutes
380	O ₂ elutes
415	N ₂ elutes
450	switch MS5A offline
550	H ₂ O elutes

Highly sensitive detection of methane and other hydrocarbons, and somewhat less sensitive detection of alcohols and aldehydes was made possible by a flame ionization detector (FID) used with a Chromosorb 102 column. The presence of as few as 2×10^{14} molecules of methane in the circulation loop could be detected with this system. Relative sensitivity factors for the detection of a wide range of molecules by a FID have been given by Dietz. ¹ Elution times for various molecules; and

this system are listed in Table IV-3.

TABLE IV-3

Retention times on the Chromosorb 102 Column at 115^oC, 25 ml/min
Ar carrier flow, flame ionization detector

Gas	Retention Time (sec)	Notes
CO	30	
H ₂ , Air	30	small negative signal
CH ₄	38	
CO ₂	42	small negative signal
C ₂ H ₆	48	
C ₂ H ₄	53	
H ₂ O	80	small signal, see text
H ₂ CO	120	
CH ₃ OH	145	
CH ₃ CH ₂ OH	275	

It should be noted that, although the FID gives no direct response to water vapor, a signal corresponding in time to the elution of water vapor was observed. The intensity of this signal correlated with the the extent of carbonization of he detector by the previous passage of hydrocarbons and/or alcohols through it. The signal due to water was probably due to steam hydrogenation of the carbon deposits in the detector. The fact that water, rather than some impurity therein, produced this signal was determined by substituting the TCD for the FID and injecting water vapor. At equal carrier flow rates the huge TCD signal

due to water come at the same elution time as the enigmatic FID water signal. The FID has negligible sensitivity to hydrogen and could not be used in water dissociation experiments.

IV-3 Light Source

Light was provided by 500 W high-pressure mercury lamps provided by Osram or Advanced Radiation Laboratories. The lamp was mounted in a water-cooled housing with a light-path distance to the sample of 38 cm. A 2 cm water cell absorbed much of the infrared radiation. A fused quartz lens system provided a concentration factor of about 5 at the sample region. The total irradiance at the sample was 23 mV/cm^2 as measured with an Eppley thermopile.

The spectral distribution of the lamp's output in the wavelength range 2200-6000 Å was measured with a Heath EU-701 monochromator and a photomultiplier tube of response type S-5. 57% of the energy of the lamp in this region is in photons with energy greater than the bandgap of SrTiO_3 (3.2 eV). A bit more than half of these bandgap photons are in an emission peak centered around 3.4 eV ($\lambda = 3650 \text{ Å}$). The other half have photon energies exceeding 3.7 eV, chiefly in a series of emissions around 3.9 eV (3150 Å). The total flux of bandgap photons to the crystal was typically $2 \times 10^{16} \text{ cm}^{-2} \text{ sec}^{-1}$.

Colored glass filters² were used to select parts of the spectral output of the lamp so that quantum and thermal effects could be distinguished. 96% of the energy transmitted through the Corning 7-51 (UV-pass) filter in the wavelength range 2200-6000 Å (total irradiance at crystal 4 mW/cm^2) was in photons with $h\nu > 3.2 \text{ eV}$. The higher energy

component of the bandgap radiation was attenuated more strongly by the 7-51 filter than was the peak at 3.4 eV. The Corning 7-54 filter passed 80% of both the 3.4 and 3.9 eV components. An irradiance of 13 mW/cm^2 at the sample was obtained through the Corning 3-74 (visible pass) filter. Less than 1% of the energy transmitted by this filter in the wavelength 2200-6000 Å was in photons with $h\nu > 3.2 \text{ eV}$. Neither the sapphire windows nor the borosilicate glass vessels used in these studies caused significant absorptive loss of light intensity,³ though reflective losses of approximately 6% per gas/glass interface occur.⁴

To test the crystal heating effects of the light, a thermocouple was wired into a crystal mounted within the gas reaction cell. The cell was evacuated and backfilled with water vapor at 20 torr. When only the water filter was used the crystal temperature reached 95°C upon illumination. Adding the UV-pass filter decreased the temperature to 32°C . Upon replacing the UV-pass with the visible-pass filter, the temperature rose to 65°C . With only the water filter in place the bulk liquid electrolyte reaction vessel operated at 44°C .

IV-4 Sample Preparation

SrTiO_3 single crystal boules were obtained from National Lead and from Commercial Crystal Laboratories. Spark-source mass spectrometry kindly performed on the NL boule by Daniel Levy at Battelle Columbus Laboratories showed the following impurities: barium (10ppm), iron (3.0ppm), sulfur (1ppm), and tantalum (>30 ppm). The CCL boule was intentionally doped to a nominal 100 ppm with tantalum. Until recently, tantalum doping of SrTiO_3 boules was a manufacturing necessity to allow

the highly strained, highly reduced boules produced by the flame fusion method to be annealed and oxidized back to stoichiometry at an adequate rate. ⁵ Although modern procedures have obviated the necessity of tantalum doping, most of the crystals whose use has been reported in the literature have probably been tantalum-doped.

Wafers approximately 1 mm thick were cut from the boules with a low-speed diamond saw. The wafers were oriented to within 1° of the (111) plane as determined by Laue back-reflection X-ray diffraction. Crystals destined for ultra-high vacuum experiments and for some reaction studies were polished to a mirror finish with 1 μ diamond paste. Some crystals, if properly oriented, were left with the finish imparted by the diamond saw or were ground with 600 grit SiC paper. Wafer frontal areas varied from 50 to 250 mm².

In ultra-high vacuum experiments the diamond-polished crystals were rinsed in alcohol, then water; and were mounted in the chamber. Cleaning by ion bombardment was followed by annealing at high temperature to remove the structural damage from the near-surface region. Some crystals for liquid-phase experiments were given a chemical etch to remove surface mechanical damage. The etch consisted of a 3 minute immersion in molten NaOH pellets held in a gold-lined porcelain crucible. For experiments where metallic contamination of the crystal could be critical, the wafers were then soaked in aqua regia, rinsed in ultra-pure water, rinsed in high purity (Apache ^{SP7329}) 35% NaOH solution, and again rinsed in ultra-pure water. The etch treatment was highly oxidizing; previously reduced, conducting samples turned clear and insulating during etching. During the etching a yellow-orange color indicative of

the formation of peroxotitanium complexes⁶ was observed. The yellow color was completely removed by washing away the NaOH with water.

"Pre-reduced" crystals were treated in flowing hydrogen at 1000°C for four hours. Such treatment typically results in an n-type carrier concentration of 10^{19} cm^{-3} .⁷ These crystals showed good conductivity, and were generally blue-black and opaque. However, some crystals which were highly conducting were light blue and nearly transparent. No differences in activity between these two types of crystals were noted, in agreement with the results of Schwerzel et al.⁸

"Platinized" crystals were coated in one of three different ways. Thermal decomposition of chloroplatinic acid sprayed through an atomizer at a crystal heated in a porcelain crucible gave the most adherent films; adherence was improved if the crystal was not polished. In vacuo evaporation of platinum from a hot tungsten wire gave films with a metallic luster but poor adherence. Pre-reduced crystals could be electroplated from a solution of aqueous 3% $\text{H}_2\text{PtCl}_3 \cdot 6\text{H}_2\text{O}$, 0.1% $\text{Pb}(\text{CH}_3\text{COO})_2$. This method allowed good spatial control of the deposit through application of the plating solution and anode to a limited area of the surface.

Parts of SrTiO_3 crystals for photocatalytic experiments could be masked from electrolyte contact with Torr-Seal UHV-compatible epoxy. Although the epoxy discolored somewhat under UV illumination, no hydrogen was evolved from the epoxy.

SrTiO_3 anodes for photoelectrochemical cells were prepared from polished, etched, and pre-reduced wafers. To ensure an ohmic contact, Ga-In eutectic was rubbed on the back of the crystal and a platinum or

copper wire was attached with conducting silver epoxy.⁹ The wire was insulated with teflon tubing, and all surfaces except the clean SrTiO₃ front of the crystal were covered with insulating Torr-Seal epoxy. Platinized-platinum counterelectrodes were prepared by cathodic polarization of Pt foils in 3% H₂PtCl₆·H₂O, 0.1% Pb(CH₃COO)₂.

TiO₂ crystals were cut from boules supplied by National Lead. Wafers were oriented to the (110) or (750) planes using Laue diffraction. The surface normal to the (750) plane (i.e. the [750] direction in this tetragonal crystal system) lies 9.48° towards [110] from [110]. Crystals were polished in diamond paste and rinsed in ethanol. "Pre-reduced" TiO₂ crystals were heated in ultra-high vacuum rather than in hydrogen.

α-Fe₂O₃ crystals were obtained from Atomergic in the form of small flakes. The predominant exposed face as determined by Laue back-diffraction was the (0001) basal plane of the corundum-type structure. Attempts to induce n-type conductivity in samples by hydrogen reduction led to metallic iron and/or magnetite. Mavroides¹⁰ has noted that one cannot produce a single n-type α-Fe₂O₃ phase through simple reduction.

Corundum crystals oriented to the (0001) and (1102) faces were obtained with a proprietary surface finish from Union Carbide. These crystals were etched in a melt of 1:1 potassium persulphate and boric acid. 11

IV-5 Gases and Reagents

The carbon dioxide used in these studies was of Matheson research grade. The argon used as gas chromatographic carrier and for crystal sputtering was standard LBL grade containing the following maximum impurity levels: 2 ppm O₂; 5 ppm N₂; 1.5 ppm H₂O; 1 ppm H₂; 0.5 ppm CO₂; 0.5 ppm HC; and 0.8 ppm hydrocarbons. The hydrocarbon impurity level is such that at the end of a typical experiment, when there would be ~100 torr of argon carrier gas in the reaction cell, there would be ~3x10¹⁴ molecules of hydrocarbon (as methane) in the cell due to this impurity. For any catalytic reaction producing many monolayers of product (1 monolayer = 10¹⁵ molecules for a 1 cm² catalyst) this impurity level is insignificant.

Electrolytes of several different levels of purity were employed. Most solutions were prepared from reagent grade materials and deionized water. The reagent grade NaOH used in these experiments was listed as containing 0.2% Na₂CO₃, 40 ppm NH₄OH, 10 ppm Cl⁻, 4 ppm Fe, 4 ppm Ni, and 1 ppm heavy metals. One ppm of Pt in crystalline NaOH would lead to 10¹⁶ atoms Pt in 10 ml of 10 M aqueous NaOH. If all of this impurity were plated onto a catalyst of area 1 cm², a layer about 10 monolayers thick would develop. NaOH solutions of higher purity were also used. The Alfa ultrapure 30% NaOH was handled in an Ar-filled glovebag and is reputed to be the purest available commercially. The metallic elements reported in this solution are Mg (<.1 ppm), Ca (< 1 ppm), Ba (< 5 ppm), and K (< 1 ppm). Sought but not detected were Hg, Pb, Ni, Co, Fe, Zn, Cd, Al, Mn, Th, and Sr. Experiments with these ultrapure solutions were carried out in glassware previously soaked in 1:1 conc. H₂SO₄:H₂NO₃ as

recommended by Huang¹² and rinsed in ultrapure water (Harleco 64112).

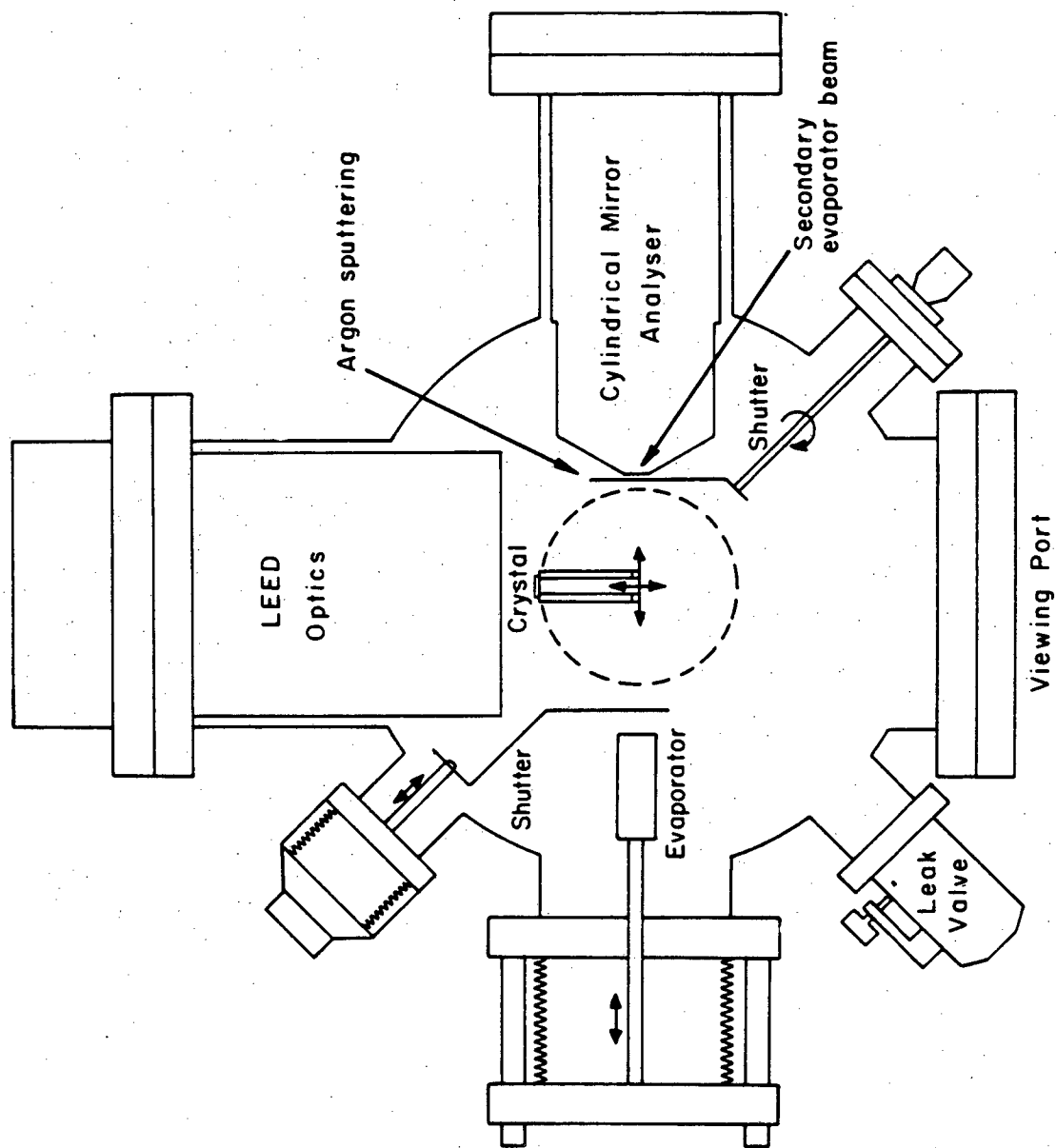
IV-6 Other Surface Analysis Equipment used in Photochemical Studies

Two Auger spectrometers were used for the analysis of SrTiO_3 crystals used in liquid-phase photocatalysis experiments. A Physical Electronics 590 scanning Auger microprobe was used to search for locally reduced areas on photocatalysts. The high current densities inherent in the submicron beam size, however, led to some electron beam damage of the surface. This problem was minimized in the other system, equipped with a Varian 2707 cylindrical mirror analyzer and a glancing incidence electron gun with a beam size of ~ 1 mm. Both Auger systems were equipped with turbomolecular-pumped sample introduction locks. Samples were removed from the reaction vessel, rinsed in ultrapure water, and placed on stainless steel carriers for insertion into the Auger apparatus.

IV-7 Apparatus for Deposition and Characterization of Thin Metal Films

Figure IV-2 gives a schematic view of the vacuum apparatus for the study of metal films on oxides. The system was pumped to a base pressure of 2×10^{-10} torr by a 400 l/s ion pump. A Physical Electronics single-pass cylindrical mirror analyzer (resolution = 0.5%) with coaxial electron gun allowed for Auger analysis of surface composition. Surface structure was monitored with a Physical Electronics LEED optics unit activated by a Varian control unit modified to provide the 3A direct current required by the thoriated iridium cathode and the higher focusing voltages. Oxide crystals were mounted on resistively heated

Fig. IV-2. Ultra-high vacuum apparatus used in thin film studies.



XBL 781-4468

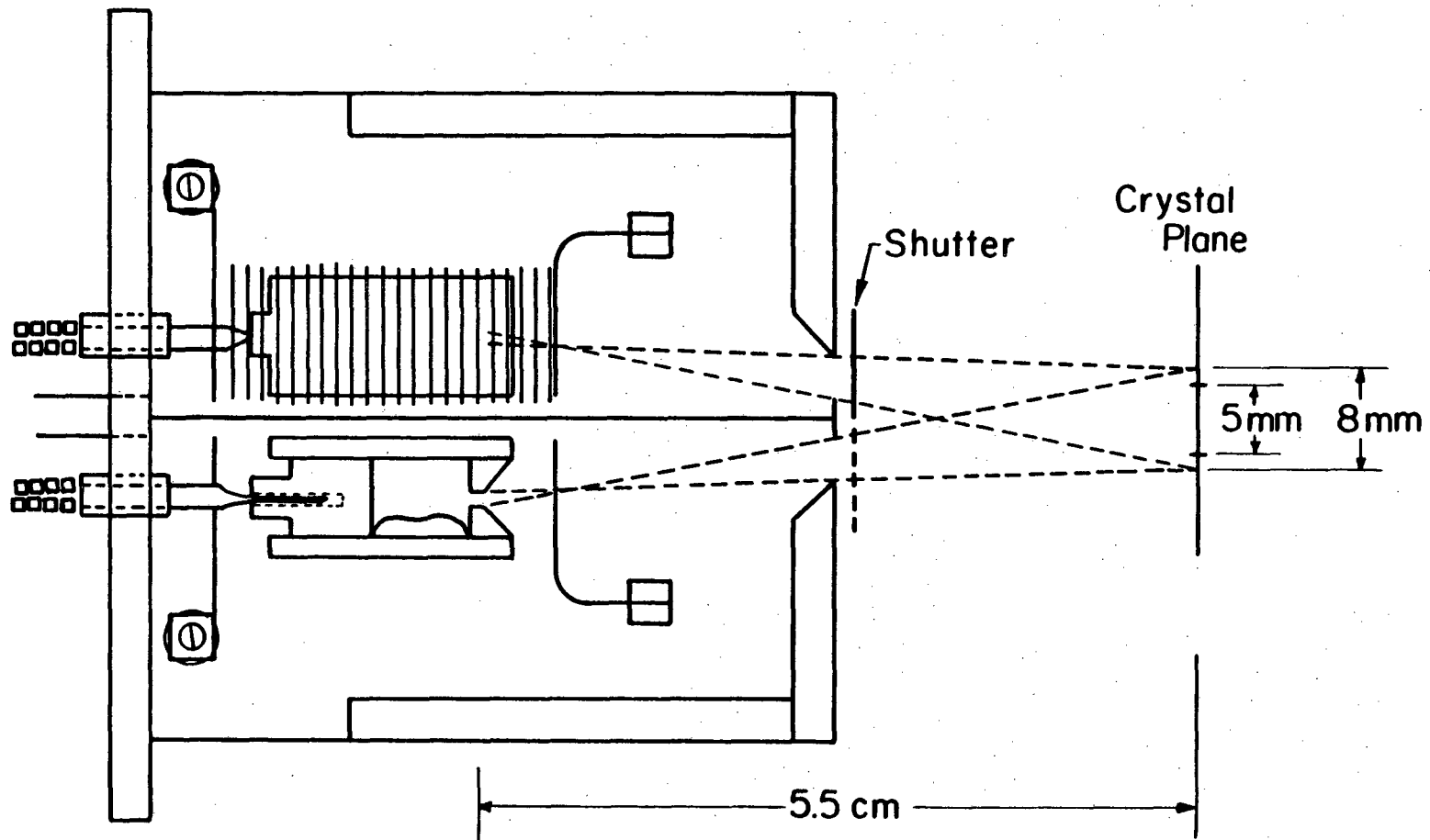
tungsten foils, and the approximate crystal temperature was monitored by a Pt - Pt 10% Rh thermocouple clamped between the foil and the crystal. The oxide samples were cleaned by cycles of argon bombardment and heating in 10^{-6} torr oxygen until the crystal could be annealed at $\sim 800^{\circ}\text{C}$ in vacuo without any diffusion of impurities to the surface. A shutter prevented sputtered metals from depositing onto and shorting out insulators in the CMA.

Films of palladium and gold were evaporated from the effusive sources shown in Figure IV-3. The effusion cells were formed from tubes of Coors AD-998 high-density alumina tubing press-fitted with machined plugs of graphite and charged with ~ 100 mg of Marz-grade gold or palladium. The front plug was countersunk and drilled to give an opening 1 mm in diameter and 1/2 mm long, to allow effusive behavior. The rear plugs were drilled to accept W-25% Re/W-3% Re thermocouples. The high density alumina tubes are mechanically stable to 1950°C .¹³ No evidence of reaction between the graphite and alumina or tungsten and alumina was observed as Al in the beam or as visible degradation of the C- Al_2O_3 or W- Al_2O_3 interfaces. An earlier design using mullite tubes showed severe degradation around the heating coils.

The effusion cells were heated by coils of 0.020" tungsten wire wrapped directly around the alumina tubes. Molybdenum radiation shielding was installed. About 9A, 15 V DC was required to evaporate Pd. During evaporations the system pressure was in the 10^{-9} torr range.

The intensity of the vapor fluxes from the effusion sources should fall off with the cosine of the angle from the orifice axis¹⁴ and so will be essentially constant for small deviations from the axis. The

TWO-SOURCE EVAPORATOR



XBL 781-4463

Fig. IV-3. Metal evaporator used in thin film studies.

evaporator output was collimated with stainless steel apertures to yield a beam umbra size (region of constant beam intensity) of 5x5 mm and a penumbra size of 8 x 8 mm at the target position. A shutter mounted on a linear feedthrough enabled either, neither, or both of the metal beams to impinge upon the target with both effusion sources heated. Palladium fluxes of 0 - 1/3 monolayers/minute (i.e. $0 - 2 \times 10^{13}$ atoms $\text{cm}^{-2} \text{s}^{-1}$) could be maintained with good stability over many hours. Evaporation of Au and Pd from non-equilibrium sources such as baskets and hairpin turns of tungsten wire had been tried earlier, but these sources did not give sufficient beam stability at high evaporation rates to allow the whole range of film thickness from 0.1 to 30 monolayers to be studied.

The thickness of evaporated films was estimated using Auger electron spectroscopy. A discussion of quantitative Auger work and criteria for gaining information on film morphology from Auger data are given in Appendix I. The stability of the Auger apparatus was such that measurements of peak intensities from clean surfaces prepared on different days varied by about 10%.

Effusive sources were used partly so that evaporator fluxes could be calculated from vapor pressure data. However, the fluxes calculated from the temperatures measured by the W-Re thermocouples were much lower than those determined by Auger spectroscopy. This was probably due to heat loss along the overly thick thermocouple wires. No thinner W-Re wire was available and other thermocouple wires had an inadequate temperature range.

References for Chapter IV

1. W.A. Dietz, Jour. Gas Chromatography, Feb., 1967.
2. R.C. Weast, ed., CRC Handbook of Physics and Chemistry, Chemical Rubber Co., Cleveland, 1969, pp.E-228 - E-244.
3. Pub. VAC 2322, "Sapphire Optical Window Assemblies", Varian Assoc., Palo Alto, 1967.
4. A.B. and M.P. Meinel, Applied Solar Energy, Addison-Wesley, Reading, Mass., 1977, p. 231.
5. Michael Urbanik, Commercial Crystal Laboratories, personal communication.
6. E. Knecht and E. Hibbert, J. Soc. Chem. Ind. 30, 396 (1911).
7. H. Yamada and G.R. Miller, J. Solid State Chem. 6, 169 (1973).
8. R.E. Schwerzel, E.W. Brooman, H.J. Byker, E.J. Drauglis, D.D. Levy, L.E. Vaaler, and V.E. Wood, Photoeffects at Semiconductor-Electrolyte Interfaces, A.J. Nozik, ed., ACS Symposium Series #146, 1981, p. 193.
9. M.S. Wrighton, A.B. Ellis, P.T. Wolczanski, D.L. Morse, H.B. Abrahamson, and D.S. Ginley, J. Am. Chem. Soc. 98, 2774 (1976).
10. J.G. Mavroides, J.C. Fan, and H.J. Zeiger, in ref. 8, p. 217.
11. J.M. Charig and D.K. Skinner, in G.A. Somorjai, ed. The Structure and Chemistry of Solid Surfaces, John Wiley and Sons, N.Y., 1969, p. 34-2.

12. C.J. Huang, Ph.D. Thesis, Case Western Reserve University, 1976.
13. Adolph Coors Co., product literature.
14. N.F. Ramsey, Molecular Beams, Oxford University Press, 1956.

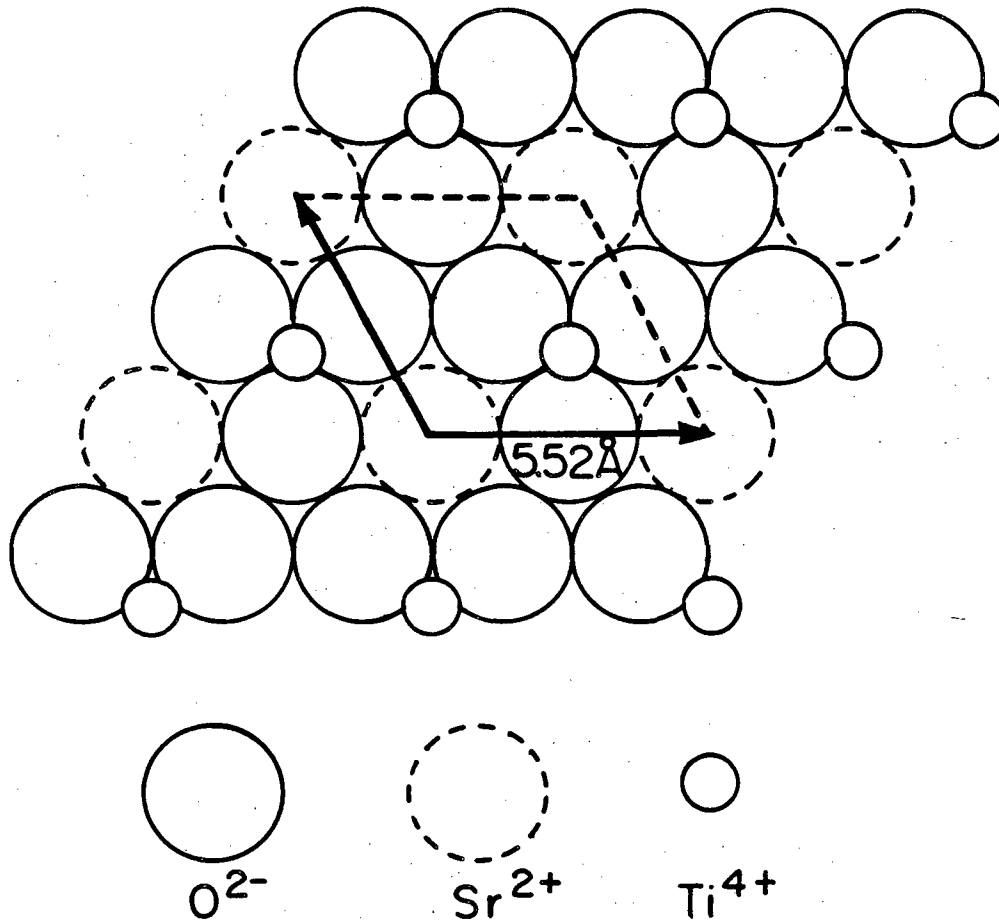
Chapter V: Photochemical Results

V-1 The Structure and Chemical Composition of the SrTiO₃ (111) Surface

V-1-1 The (111) Termination of the SrTiO₃ Bulk Structure

Strontium Titanate has a cubic perovskite structure with a unit cell length of 3.905 Å. Ti^{4+} ions lie at each vertex of the cube, O^{2-} ions bisect each edge, and a Sr^{2+} ion lies at the cube center. Alternatively, one can consider the Sr^{2+} ions at the vertices, the O^{2-} ions at the face centers, and Ti^{4+} at the cube center. Natural cleavage occurs along the (100) plane,¹ but the (111) is the most densely packed low index surface.

SrTiO₃ is a largely ionic material. Its cubic structure, somewhat unusual for a substance with a pentatomic stoichiometric formula, arises in part from the nearly equal ionic radii of Sr^{2+} and O^{2-} . Along the [111] direction, SrTiO₃ is composed of planes of Ti^{4+} ions alternating with nearly closest-packed layers of composition SrO₃ (Figure V-1). The Ti occupies octahedral holes surrounded entirely by O. The separation of the SrO₃ planes is 2.26 Å with Ti planes lying halfway between. Both SrO₃ and Ti planes are packed ABCABC, for an overall packing of AaBbCc. The unit mesh vectors of the unreconstructed SrTiO₃ (111) surface are 5.52 Å long with an enclosed angle of 120°. The surface has 3-fold symmetry as can be clearly seen when the positions of the Ti ions are taken into consideration.

SrTiO_3 (111)

XBL818-6317

Fig. V-1. (111) surface termination of the SrTiO_3 bulk structure.

V-1-2 Unit Mesh of the SrTiO₃ (111) Surface

LEED patterns were obtained for a SrTiO₃ (111) surface by annealing a pre-reduced crystal at high temperature (~1200°C.) Figure V-2 shows the LEED pattern from SrTiO₃ (111) at a beam energy of 41.5 eV. Comparison of LEED patterns of SrTiO₃ (111) with those taken of Pt(111) on the same apparatus for calibration shows that the SrTiO₃ (111) surface has the same periodicity as the unreconstructed termination of the bulk structure; that is, the surface exhibits a primitive 1x1 structure.

Exposure of this surface at room temperature up to several thousands of Langmuirs (1 L = 10⁻⁶ torr·sec) of O₂, H₂O, or H₂O + NH₃ caused no diminution of LEED spot brightness or appearance of new spots. Heating the crystal to around 500°C in 10⁻⁶ torr O₂ caused a gradual disappearance of the LEED spots.

V-1-3 Compositional Changes with Surface Pre-Treatment

SrTiO₃ surfaces for ultra-high vacuum studies were cleaned by a repetitive process of sputtering with 1.5 keV Ar⁺ ions, heating in 10⁻⁶ torr O₂, and heating in vacuum. Argon sputtering removed impurities such as K, Ca, Cl, and S; but sputtering in the high-pressure/low-pressure apparatus led to the deposition of carbon due to high background levels of CO. In the other vacuum systems carbon deposition during sputtering was less prevalent. Heating to c. 700°C in oxygen removed carbon, but encouraged the accumulation of oxidizable impurities such as K and Ca at the surface. Heating in vacuo minimized the segregation of these elements but at times led to sulfur accumulation on SrTiO₃.

SrTiO₃ (111)



42 eV

XBB 819-8420

Fig. V-2. LEED pattern of SrTiO₃ (111) surface.

The effects of sputter and heat treatments on surface composition were observed with AES in two vacuum chambers. In the high pressure/low pressure chamber with a retarding field analyzer both freshly sputtered surfaces and crystals heated in oxygen gave O (510 eV) / Ti (380 eV) peak ratios of 1.4. This value was obtained for both stoichiometric and pre-reduced crystals. Heating to $\sim 800^{\circ}\text{C}$ in vacuo at times reduced the O (510 eV)/Ti (380 eV) peak ratio to 1.1. This effect was most pronounced when sulfur was present on the surfaces. Several authors have commented on the sensitivity of the rates of in vacuo reduction of SrTiO_3 and TiO_2 to the composition of the background gases.² Calculated from standard heats and free energies of formation, the equilibrium oxygen pressures above rutile (TiO_2) at 25°C and 800°C are 10^{-147} torr and 10^{-32} torr, respectively, well below the oxygen pressure in UHV chambers. The composition of TiO_2 heated in vacuum is thus determined by the relative kinetics of the reduction of TiO_2 and the $\text{Ti}_n\text{O}_{2n-1}$ Magnelli phases.³ TiO_2 is much easier to reduce in bulk than is SrTiO_3 , for which there are no analogs to the Magnelli phases.

In very clean vacuum ($< 10^{-9}$ torr) sputtering SrTiO_3 at room temperature or annealing it at $\sim 900^{\circ}\text{C}$ causes no significant change in the O/Ti Auger peak ratio for either stoichiometric or pre-reduced crystals. This is in contrast to TiO_2 , which shows strong evidence of reduction upon Ar^+ -bombardment, both in the O (507 eV)/Ti (380 eV) and the Ti (380 eV)/Ti (414 eV) peak ratios (see Chapter VI).

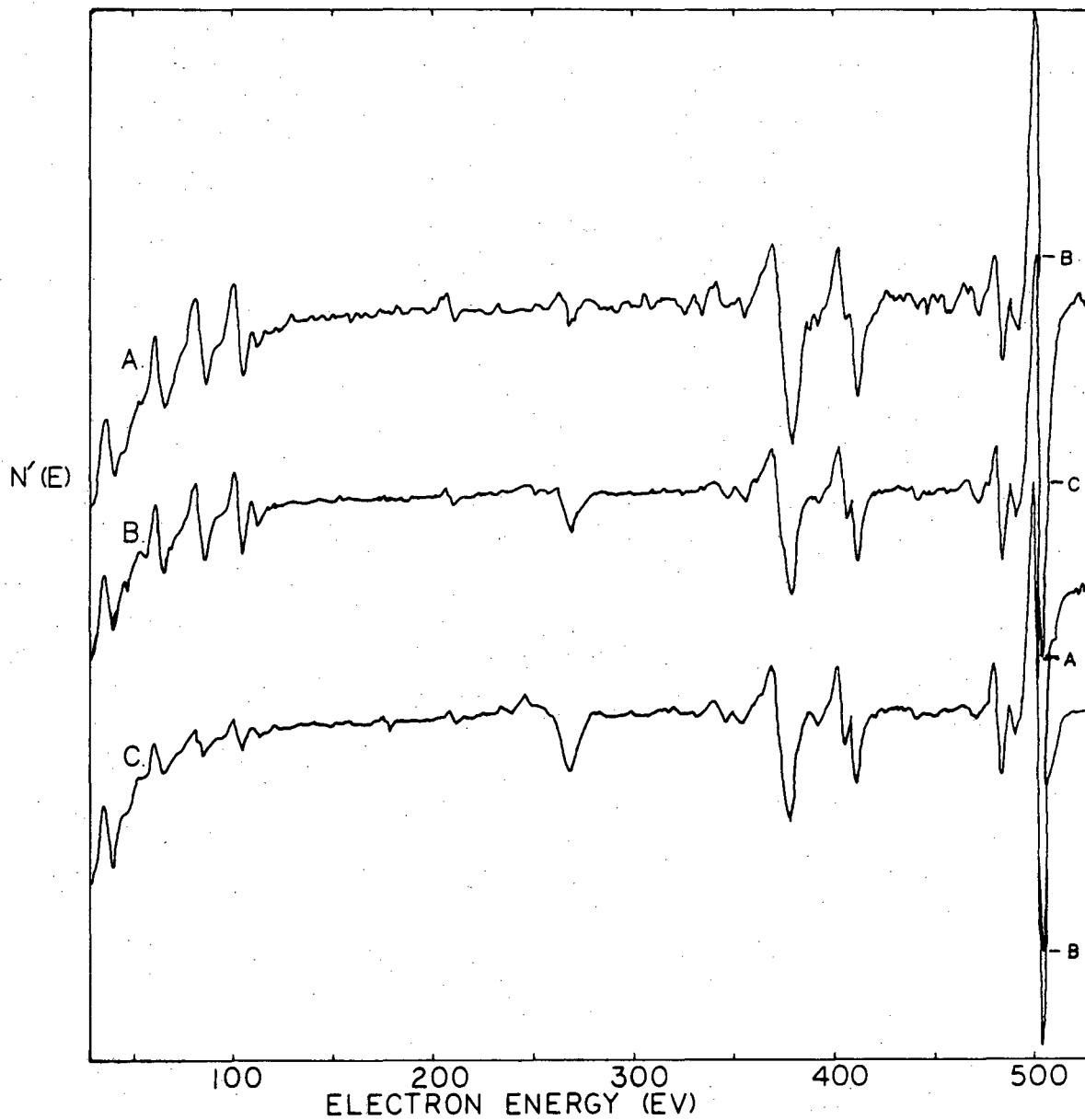
No gross electron-beam reduction of the surface occurs with the glancing incidence electron guns used in two of the vacuum systems, but the highly focused beam of the scanning Auger microprobe can cause sig-

nificant reduction of SrTiO_3 even at moderate beam intensities. Argon sputtering of SrTiO_3 at room temperature increases the Sr (66 eV)/Ti (380 eV) peak ratio as measured with the single-pass CMA and glancing incidence electron gun (Table V-1). When SrTiO_3

TABLE V-1 Auger peak ratios for SrTiO_3 surfaces

	O (507 eV)/ Ti (380 eV)	Ti (380 eV)/ Ti (414 eV)	Sr (66 eV)/ Ti (380 eV)
Ar-sputtered, room temp	3.3	1.2	0.47
Ar-sputtered, c. 800°C	3.9	1.3	0.64
Annealed 900°C	3.1	1.3	0.03
Rinsed with water	2.6	1.4	0.19

is sputtered at higher temperature an even greater enhancement of the Sr/Ti ratio occurs, with a lesser increase in O/Ti. When the sputtered crystal is removed from ultra-high vacuum, rinsed in high purity liquid water, and returned to vacuum for analysis the surface is depleted in Sr, even with respect to the well-annealed surface (Fig. V-3). Due to the uncertainty in Auger sensitivity factors, it is not clear which of these surfaces most closely approximates the stoichiometry of SrTiO_3 . The high temperature annealed surface, which is the only surface which gives a LEED pattern, has a unit mesh consistent with the bulk structure. UPS and XPS data,⁴ which are much more sensitive to subtle changes in oxidation state than Auger, show that the high-temperature annealed surface has no detectable Ti^{3+} . This surface would then appear to be closest to SrTiO_3 in stoichiometry. The Ar-sputtered surface is Sr rich, and the surface exposed to liquid electrolyte is Sr-deficient. Tench and Raleigh,⁵ using XPS, have shown that rinsing in water also



XBL 806-10538

Fig. V-3 Auger spectra of SrTiO_3 . (A) Freshly Ar^+ -sputtered surface; (B) A. exposed to room air 2 min.; (C) A. exposed to liquid 7 M- water for 1 min.

removes Sr from SrTiO_3 cleaved in air. As will be discussed in more detail later, changes in Sr concentration at the surface can alter the relative energies of the SrTiO_3 valence and conduction bands vis-a-vis the energy levels of reactants in the gas or liquid phase.

V-2 Photocatalytic Activity of Clean SrTiO_3 and SrTiO_3/Pt
with Water Vapor and Other Gases

V-2-1 Water Vapor and CO_2

Illumination of room-temperature SrTiO_3 in water vapor at 5-20 torr pressure produced no detectable hydrogen. Experiments were carried out with crystals cleaned in UHV as well as with samples exposed to air. Pre-reduced as well as stoichiometric crystals were used, as were both metal-free and platinized samples. The same crystals, when coated with a layer of aqueous alkaline electrolyte and illuminated, evolved catalytic amounts of hydrogen as will be discussed in section V-3.

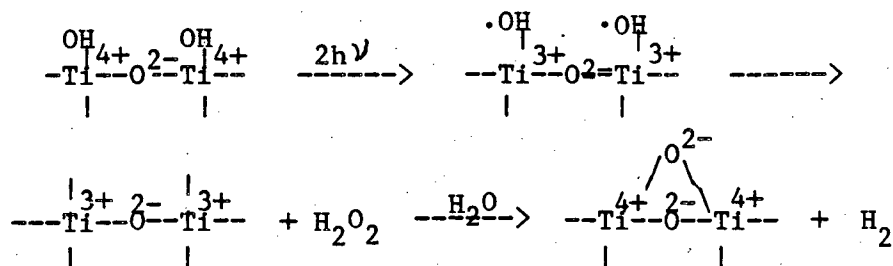
Previous workers^{6,7} had reported the photogeneration of methane upon illumination of a Pt-SrTiO_3 sandwich in a mixture of water vapor and CO_2 . Upon repetition of these experiments the production of monolayer amounts of methane was observed; however, the correlation of methane production with illumination was found to be much less strong than had originally been believed. Trace amounts (but still equivalent to thousands of monolayers) of ethanol, methanol, and other small organic molecules were detected in the reaction loop and these compounds, rather than CO_2 , may have been the source of carbon for the small amounts of methane formed. Methane formation by such a path is not

significantly endergonic. Intentional addition of ethanol to the water vapor source increased methane formation greatly. Some formaldehyde was also formed, suggesting that at least part of the methane produced was due to the disproportionation $\text{CH}_3\text{CH}_2\text{OH} \rightarrow \text{CH}_4 + \text{H}_2\text{CO}$ ($\Delta G^\circ = 1.9$ kcal/mol). When the Pt and SrTiO_3 foil was heated to $\sim 150^\circ\text{C}$ this reaction proceeded rapidly even without illumination, and the photo and thermal effects could not be adequately separated. Pt at room temperature has been shown to adsorb ethanol dissociatively, though the fragment observed was CO, not H_2CO .⁸ After it was found that hydrogen could be photogenerated from water on NaOH-coated platinized SrTiO_3 , experiments were run to determine whether methane could be photogenerated from water vapor and carbon dioxide on NaOH-coated crystals. No methane production above background was observed. Mass spectrometry showed that some CO_2 remained in the gas phase, and wet chemical analysis indicated that not all of the NaOH had been converted to the bicarbonate or carbonate by reaction with CO_2 .

V-2-2 SrTiO_3 in Mixed Vapors of Water and Volatile Bases

While SrTiO_3 or SrTiO_3/Pt illuminated in water vapor at room temperature evolved no detectable hydrogen, SrTiO_3 illuminated in films of basic aqueous electrolytes yielded catalytic amounts of hydrogen, as will be shown in Section V-3. Since only basic electrolytes proved effective, it was hypothesized that the lack of a basic catalyst, rather than fundamental differences in the gas-solid and liquid-solid interfaces, caused the absence of photoactivity at the gas-solid interface. One mode through which a basic catalyst might operate arises from Van Damme and Hall's⁹ proposed mechanism for a stoichiometric

photoconsumption of hydroxyl groups to yield H_2 and O_2 :



The final surface product here involves a bridging oxide similar to the siloxane linkages common on dehydrated silica gel. To return to the hydroxylated starting material and thereby get catalytic activity, the "titanoxane" linkage must be hydrolysed. This might be done through general base catalysis, but also might require a specific base-hydroxide. Peri¹⁰ has shown that adsorption of ammonia breaks some siloxane linkages, yielding adsorbed OH and NH_2 moieties. Experiments were therefore carried out to see if volatile bases could catalyze the photodissociation of water vapor on $SrTiO_3$.

Some hydrogen photogeneration was observed in water-ammonia gas mixtures, as shown in Figure V-4. In this experiment with a platinized pre-reduced crystal no hydrogen generation was observed in the dark or under illumination through the 3-66 filter ($h\nu < 2.4$ eV for light passed). Slight activity may have been observed with the 3-74 filter ($h\nu < 3.1$ eV). With the 7-51 filter rates of hydrogen production up to 20 monolayers per hour were observed. In subsequent experiments the background production of hydrogen on the cell walls grew.

Figure V-5 compares rates of hydrogen accumulation during sub-bandgap and bandgap illumination. Extended dark periods gave nearly the same slope as subbandgap illumination. When a platinized Pt foil

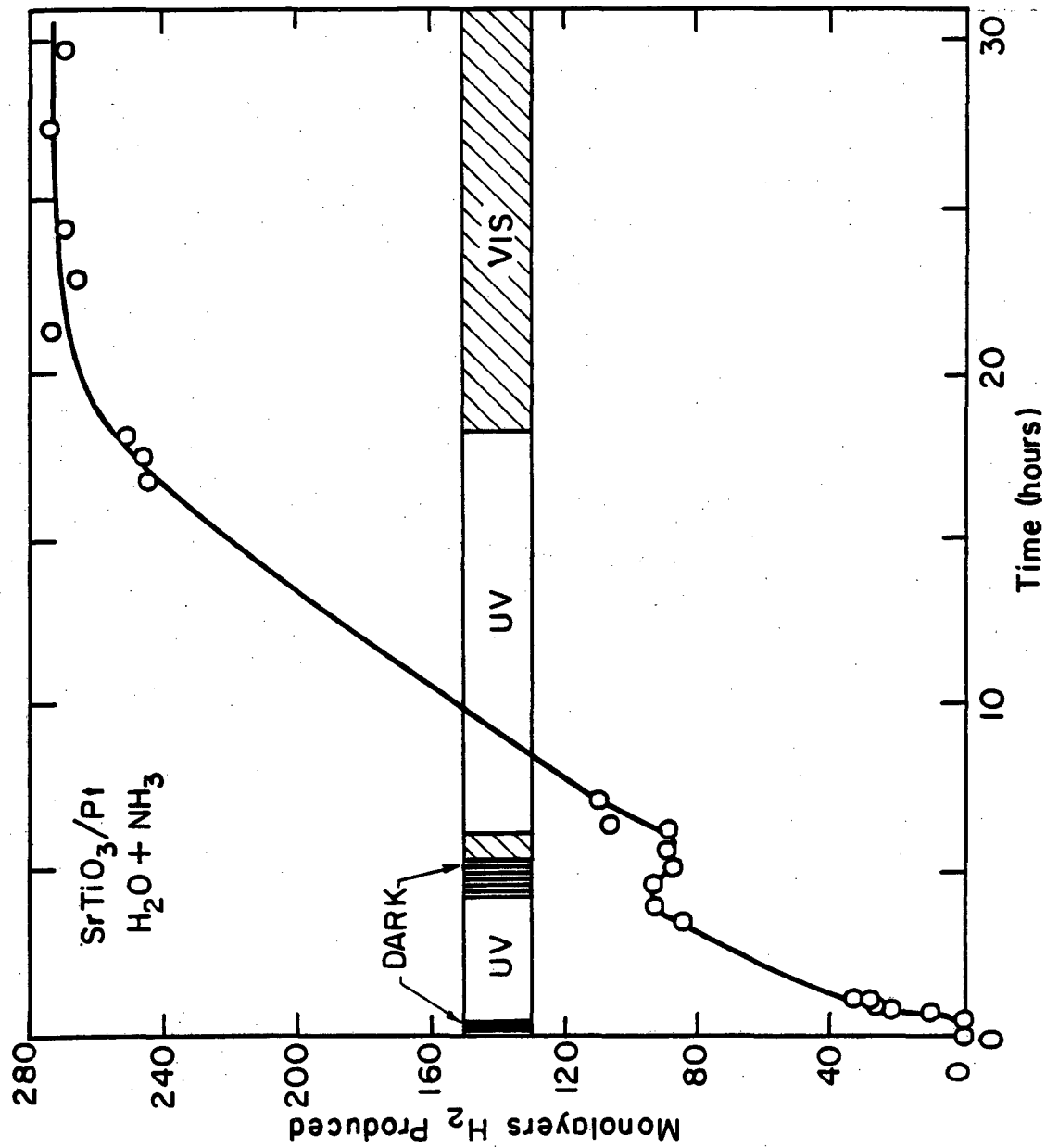
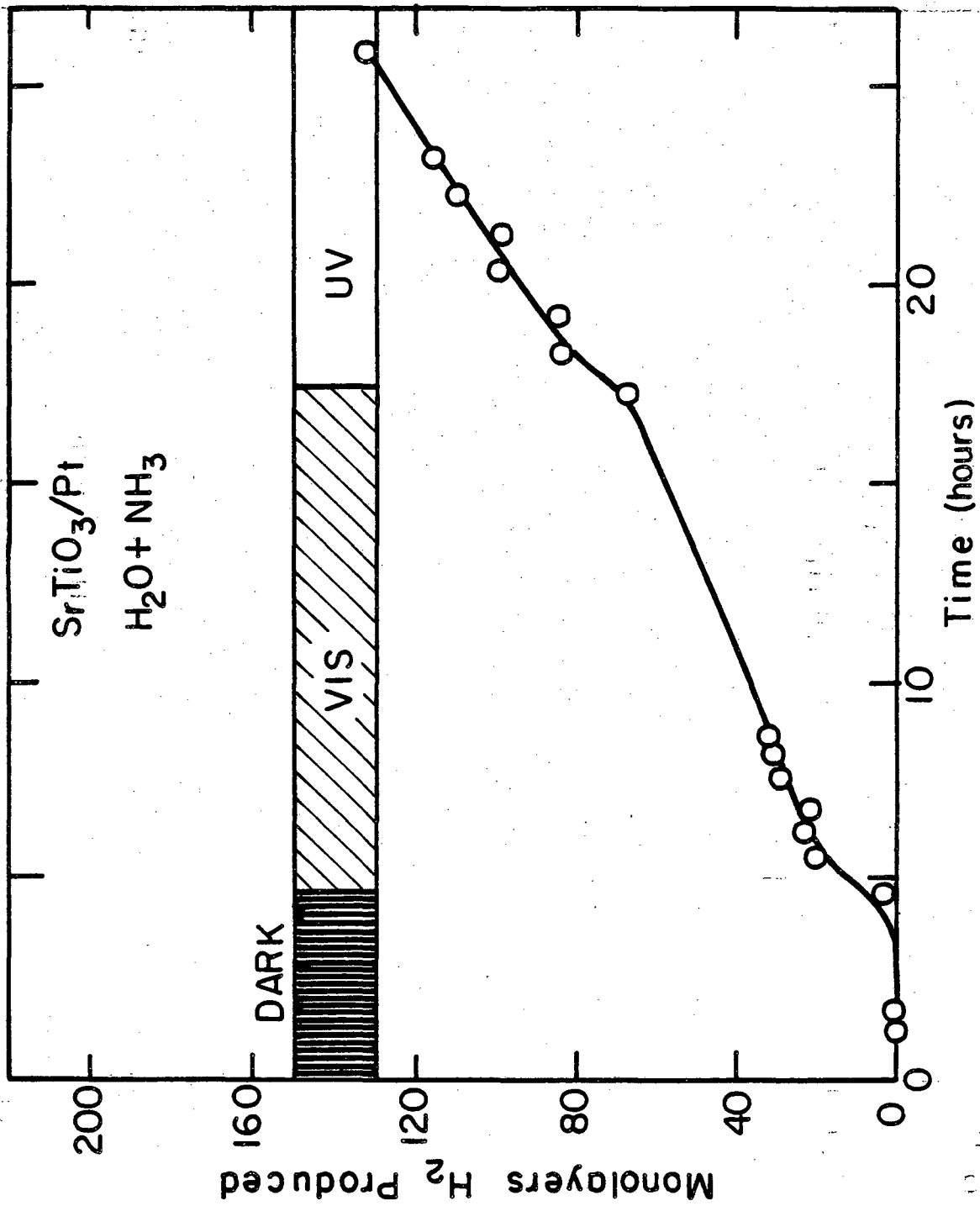


Fig. V-4. H_2 generation on $SrTiO_3/Pt$ in water vapor-ammonia mixture.



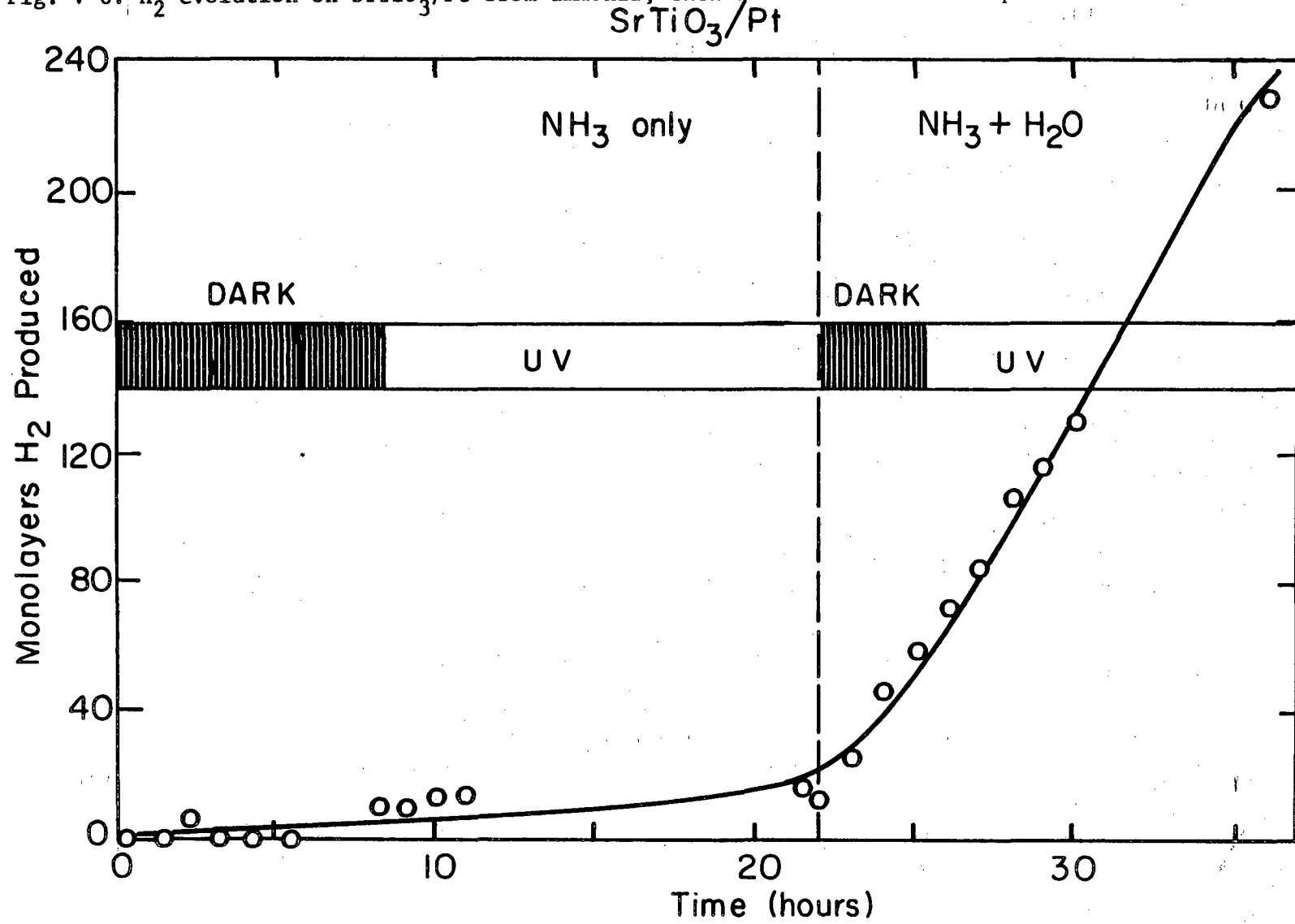
XBL 818-6324

Fig. V-5. H₂ production on SrTiO₃/Pt from water vapor-ammonia mixture.

replaced the platinized SrTiO_3 crystal, a different pattern of response to light was observed. Upon illumination the H_2 level jumped, probably as the warming foil desorbed hydrogen. The steady state rate of hydrogen generation under illumination was, however, less than or equal to that seen in the dark. Background reactivity became especially troublesome after the experiment shown in Figure V-6, in which anhydrous ammonia gas was admitted over platinized SrTiO_3 . No significant hydrogen production was observed in either dark or illuminated conditions. However, when water vapor was admitted to the cell along with the ammonia, hydrogen production commenced at a rate independent of illumination. This light-independent component of hydrogen production occurred whether or not SrTiO_3 and/or Pt were in the cell. It would appear that the anhydrous ammonia broke through the passivating oxide film on some of the metal components of the circulation loop. The background reactivity could be removed only after extensive rinsing of the circulation loop with nitric acid.

As the experiments progressed ammonia adsorbed on the column and detector of the gas chromatograph. The resulting instrumental instability made measurement of hydrogen difficult and identification of heavier product molecules impossible, even after extended bakeout of the gas chromatograph. With the addition of a series bypass valve and a Chromosorb 104 column the ammonia and water vapor could be routed around the molecular sieve 5A column, mitigating the instrumental instability. However, this method entailed several minutes extra residence time for the light gases in the molecular sieve. This broadened the peaks and decreased the sensitivity of the system for hydrogen by about threefold. Since hydrogen photogeneration in ammonia-water vapor mixtures was

Fig. V-6. H₂ evolution on SrTiO₃/Pt from ammonia, then ammonia and water vapor.



XBL 818-6323

barely detectable in the original system, this loss of sensitivity was crucial. The gain in instrumental stability still did not allow for the detection of oxidized products to determine whether the photogenerated hydrogen arose from water or from ammonia. Although anhydrous ammonia underwent no photocatalyzed decomposition on SrTiO_3/Pt , water vapor might play a catalytic role in the decomposition of ammonia rather than vice-versa as originally postulated. Although the standard free energy change for the dissociation of gaseous ammonia to hydrogen and nitrogen is $+3.976$ kcal/mol,¹¹ under our reaction conditions the dissociation of 0.33 atm of ammonia to yield 200 monolayers (4.8×10^{-5} atm) of hydrogen and 1.6×10^{-5} atm of nitrogen is exergonic: $\Delta G = -7.61$ kcal/mol. Thus hydrogen production from ammonia under these conditions requires no thermodynamic assist from light, while water photodissociation must be light-driven.

The rate of hydrogen photogeneration in ammonia-water vapor mixtures was too slow and the background reaction too fast to allow the photochemical reaction to be identified. Even after the reaction cell was coated with gold, the background reaction severely hindered experiments. Ammonia is a weak base, with $K_b = 1.8 \times 10^{-5}$.¹² A search was made for other volatile bases of greater strength. Piperidine (hexahydropyridine) with a K_b of 1.3×10^{-3} ¹² and a vapor pressure at room temperature of ~ 20 torr, seemed most promising.

Piperidine itself decomposed yielding hydrogen when illuminated through a 7-54 filter. This filter passed photons with energies up to 3.9 eV. When the 7-51 filter, which transmitted photons only up to 3.4 eV, was substituted no hydrogen-releasing reaction occurred. 7-51 fil-

tered illumination of platinized SrTiO_3 in 20 torr H_2O + 20 torr piperidine produced no hydrogen. The products of (base pressure) $\times K_b$, a rough measure of base activity, for the ammonia-water and piperidine-water mixtures were nearly equal. The lack of hydrogen production in piperidine-water lends some support to the idea that the photogeneration of hydrogen in the ammonia-water mixture was due to a water-catalyzed decomposition of ammonia or a specific water-ammonia reaction, rather than to a general base-catalyzed decomposition of water vapor.

V-2-3 H_2 Production from Reduced SrTiO_3 at Elevated Temperatures
in Room Temperature Water Vapor

Hydrogen was evolved when a reduced SrTiO_3 crystal held at elevated temperature ($\sim 160^\circ\text{C}$) in water vapor was illuminated with bandgap radiation. The crystal was mounted on a Pt foil which was heated resistively. Elevated temperature, light, and water vapor were all required for continuous hydrogen production (Fig. V-7). No similar photoeffect was seen on stoichiometric crystals, and reproducibility with other pre-reduced crystals was not good. The efficacy of the reduced crystal decreased in subsequent experiments and the color characteristic of the reduced crystal also bleached out. It thus appeared that the reaction may not have been catalytic with respect to the SrTiO_3 . Rather, it constituted a stoichiometric reaction of previously reduced centers in the n-type SrTiO_3 with water to produce hydrogen or light controlled diffusion of hydrogen from the crystal bulk.

Light would appear to perform a gating role, speeding the reaction of adsorbed water with the reduced centers. It should be noted that

n-SrTiO₃/Pt (160°C) + 19 Torr H₂O(g)

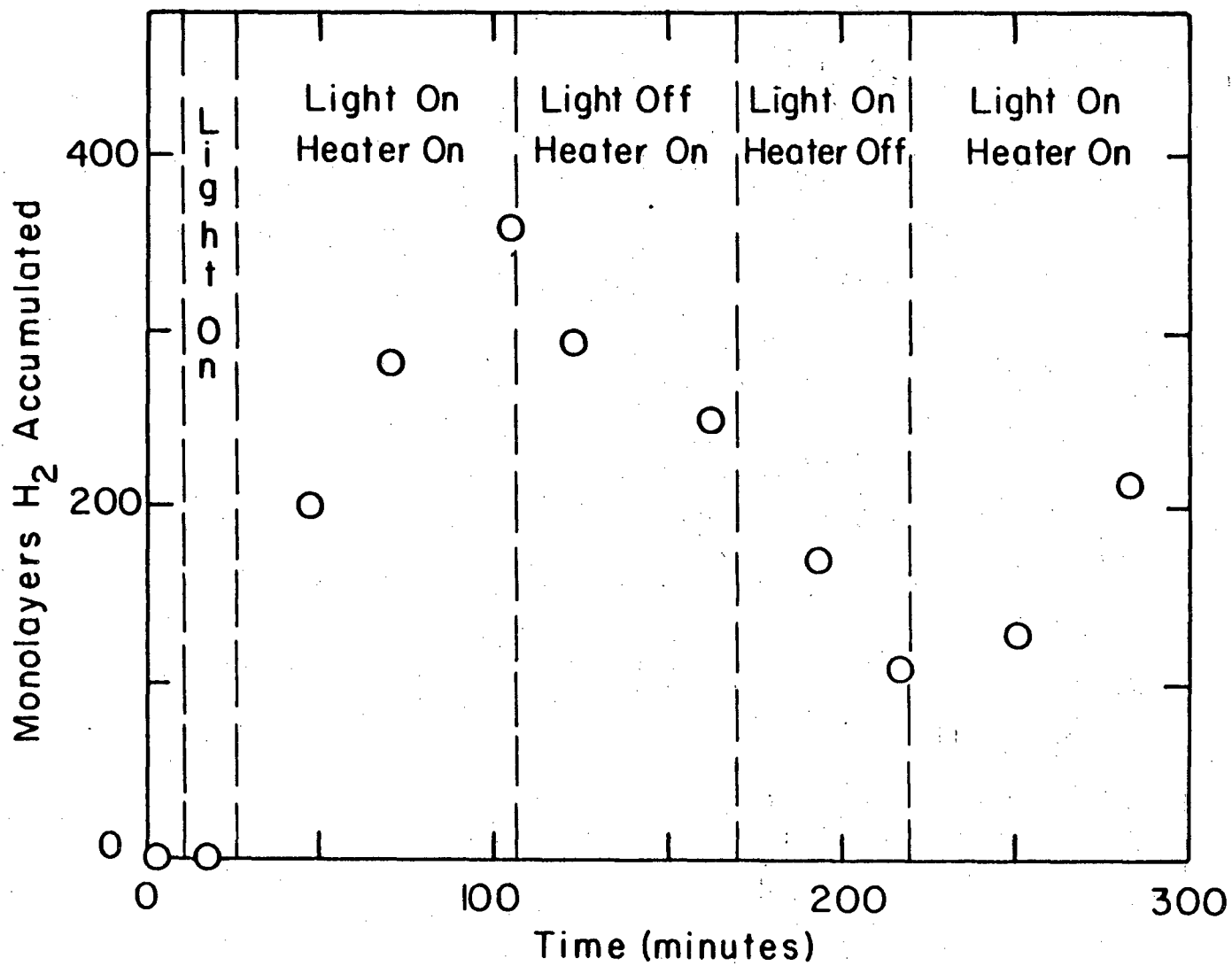


Fig. V-7. H₂ above SrTiO₃/Pt as modulated by bandgap light and XBL 802-4699 sample temperature.

during these experiments a viton O-ring in the cell closure was being radiatively heated. Above 150°C viton has been shown to decompose.¹³ When the Pt crystal holder was heated above 200°C hydrogen was evolved even in the absence of water vapor or light. The results in Figure V-7 may involve a photoreaction of a viton decomposition product (or out-gassed CO) rather than simple water photodissociation.

A similar hydrogen generation effect has been observed in ultra-high vacuum by Ferrer.¹⁴ When a pre-reduced SrTiO_3 crystal at or above 200°C was illuminated in 10^{-7} torr H_2O , hydrogen evolved at a rate of 3 monolayers/hr, accompanied by a decrease in the reduced Ti^{3+} surface species as monitored by the 1.6 eV electron energy loss peak. No such activity was seen on a stoichiometric crystal lacking Ti^{3+} centers. No production of gas-phase oxygen was observed, though the sensitivity of the mass spectrometer to oxygen would have been sufficient to pick up the level of oxygen associated with water dissociation. Paladino et al.¹⁵ have measured the rate of oxygen diffusion in SrTiO_3 by a radiotracer method. Extrapolating his data to 400°C , one obtains a diffusion coefficient of $7 \times 10^{-12} \text{ cm}^2 \text{ s}^{-1}$. This diffusion coefficient implies that a flux of 3×10^{13} oxygen vacancies $\text{cm}^{-2} \text{ s}^{-1}$ would reach the surface from the interior of a crystal with a bulk vacancy concentration of 10^{19} cm^{-3} . This flux is adequate to explain the lack of gaseous oxygen production if water molecules donate oxygen to the vacancies as hydrogen is liberated.

The observed decrease in the surface concentration of Ti^{3+} upon illuminating pre-reduced SrTiO_3 in water vapor is of interest in determining the mechanism of the reaction. If photogenerated Ti^{3+} were the

reductant which produced hydrogen from water, illumination of a crystal held in water vapor would be expected to increase the Ti^{3+} concentration. In reality, a decrease was seen, suggesting that the Ti^{3+} was quenched by photogenerated oxygen and that the actual reduction of water vapor to hydrogen was accomplished by electrons photoinjected into the conduction band, which lies 0.6 eV cathodic to the Ti^{3+} level (see Figure VII-5). Light with $2.8 \text{ eV} < h\nu < 3.2 \text{ eV}$, which could promote electrons from the valence band to the Ti^{3+} level but not to the conduction band, caused hydrogen generation in neither the low-pressure, stoichiometric reaction nor the catalytic reaction in aqueous electrolytes.

Ti^{3+} then may play a critical role in this reaction, but not as a photogenerated reductant. It may serve to bind water to the surface¹⁶ and promote the incorporation of oxygen from adsorbed water into the crystal lattice under conditions where the kinetics of the production of gas phase molecular oxygen are not favorable.

V-2-4 Back Reactions

It should be noted that Pt is an excellent catalyst for possible back-reactions involving the oxidation of hydrogen and hydrocarbons. Hanson and Boudart¹⁷ have measured pseudo first-order rate constants for hydrogen-oxygen combination on silica-supported platinum. In excess oxygen recombination followed a rate equation of $r = kS_{Pt}(H_2)$ where S is the Pt surface area in cm^2 and (H_2) is the hydrogen density in $\text{micromoles-cm}^{-3}$. They determined a rate constant at 303°K varying from $3 \times 10^{-3} \text{ cm-s}^{-1}$ to $4 \times 10^{-3} \text{ cm-s}^{-1}$ depending on catalyst loading. In our

experimental apparatus, assuming 1 cm^2 Pt area, a rate constant of $3.5 \times 10^{-3} \text{ cm-s}^{-1}$ would correspond to an instantaneous recombination rate of 120 monolayers/hr when 1000 monolayers of hydrogen are present in the circulation loop with excess oxygen. The observed rates of hydrogen oxidation on platinized SrTiO_3 at room temperature were considerably lower than this, even after cleaning the crystal in UHV.

When 14 torr of water vapor, 9 torr of hydrogen, and 130 torr of air were admitted to the circulation loop with a platinized crystal the hydrogen pressure dropped 0.5 torr in 46 hours, corresponding to $k = 6 \times 10^{-5} \text{ cm-s}^{-1}$. When the crystal was heated the hydrogen pressure dropped very rapidly, corresponding to $k = 0.20 \text{ cm-s}^{-1}$. Whereas at low temperature hydrogen-oxygen recombination does not severely hamper experiments in the photodissociation of water vapor, at higher temperature measures must be taken to prevent back-reaction.

With a constant hydrogen production rate and a H_2 -pressure dependent back reaction (assuming, for the moment, that air leaks provide excess oxygen) a steady state hydrogen pressure will be reached. The evolution of hydrogen molecular density with time is given by

$$H(t) = \frac{r_f}{k_b S_{\text{Pt}}} (1 - e^{(-r_b t)})$$

where H is the hydrogen density in $\mu\text{mol-cm}^{-3}$, r_f is the forward reaction rate in $\mu\text{mol-s}^{-1}$, k_b is the recombination rate constant in cm-s^{-1} and S the Pt surface area in cm^2 . The steady state ($t \rightarrow \infty$) hydrogen density is:

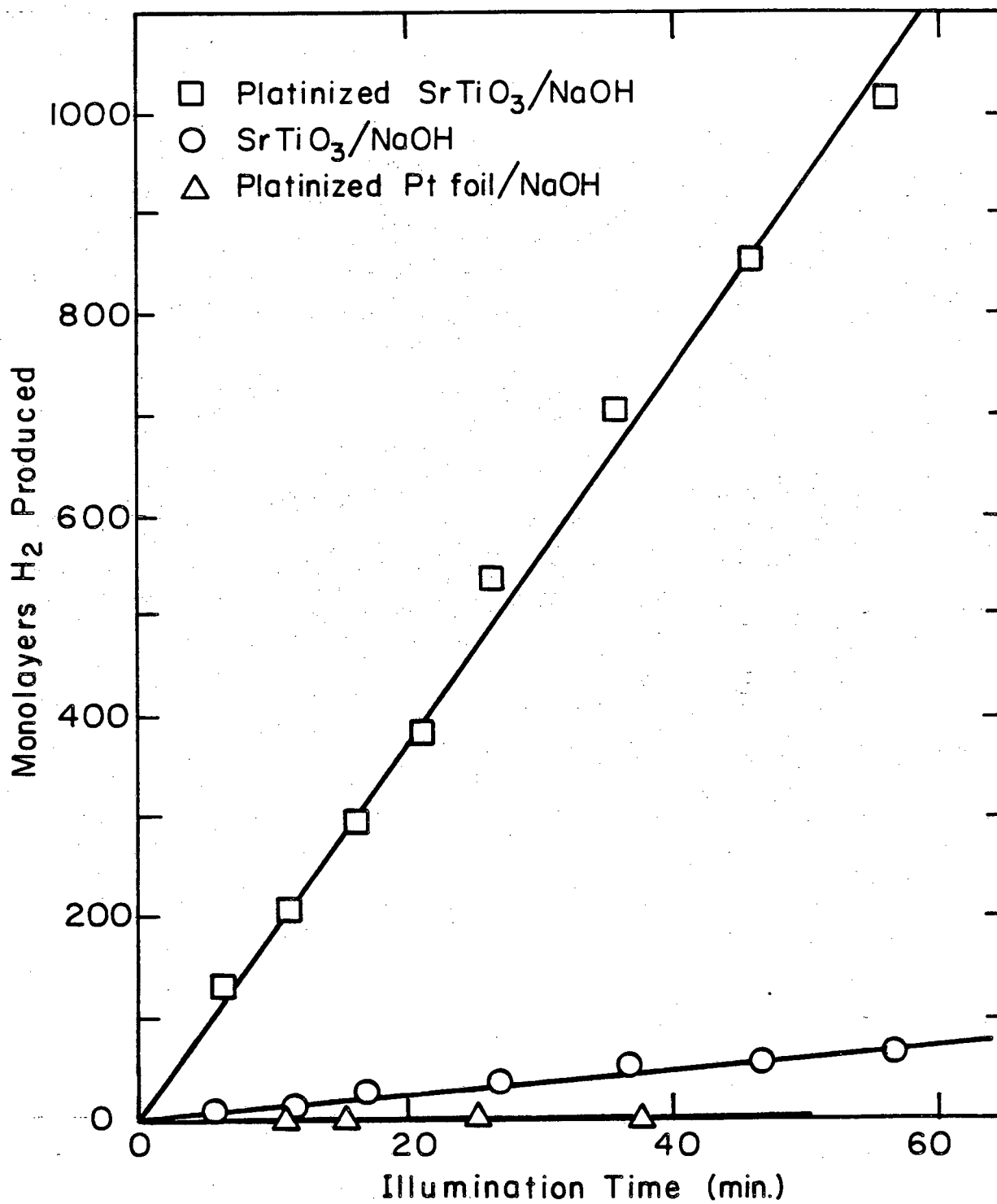
$$H(\infty) = \frac{r_f}{k_b} S_{Pt}$$

It is of interest to calculate the minimum forward rate which would yield a steady state hydrogen density sufficiently large to unambiguously indicate the catalytic nature of the surface reaction, say 100 monolayers (10^{17} molecules) of hydrogen in the gas phase. Using Boudart's $k_b = 3.5 \times 10^{-3} \text{ cm-s}^{-1}$ and a Pt surface area of 1 cm^2 , a forward rate of 7 monolayers H_2/hr would give an unambiguous hydrogen accumulation. Assuming a roughness factor of 10 for the Pt coatings used increases the required rate to 70 monolayers/hr for a platinized crystal. This figure should be compared with the actual rates of hydrogen production observed on platinized crystals in aqueous electrolyte films of over 1000 monolayers/hr. While back-reactions could play a major role in limiting the total yield in a room temperature water vapor surface photolysis experiment, the lack of any observed hydrogen photo-production from water vapor at room temperature on clean SrTiO_3/Pt would appear to be due not just to the rate of back-reaction but to a fundamental limit to the rate of the forward reaction as well.

V-3 Photoactivity of NaOH-coated SrTiO_3

V-3-1 Photoactivity of NaOH-coated Platinized SrTiO_3

SrTiO_3 , either platinized or metal-free, when coated with NaOH and illuminated in water vapor, yielded hydrogen in catalytic amounts (as shown in Figure V-8). The crystal was placed in an open-framed holder made of vycor glass rod and dipped in a concentrated aqueous NaOH



XBL7910-7181

Fig. V-8. H₂ photogeneration on SrTiO₃ coated with NaOH, in 20 torr water vapor.

solution. The crystal was then dried in a blast of hot air, leaving an adherent film of NaOH. The crystal holder was then mounted in the high-pressure reaction cell of the high pressure/low pressure apparatus and the cell was evacuated to 10^{-6} torr. The cell and circulation loop were sealed, and a stopcock was opened to allow the cell walls, crystal, and NaOH to equilibrate with the vapor over a pool of high purity water. The water was often heated slightly to speed the rate of equilibration. The circulation pump was started to force the vapor past the crystal and through the sampling valve of the gas chromatograph. Periodic sampling measured the accumulation of hydrogen and other gases in the closed circulation loop. Although these experiments were carried out in the high-pressure/low-pressure apparatus, the crystals were prepared ex-situ and the presence of the NaOH layer precluded the application of surface analytical techniques to the SrTiO_3 .

As shown in Figure V-8 platinized, pre-reduced crystals produced hydrogen at rates exceeding 1000 monolayers (10^{18} molecules) per hour. The crystal was platinized by thermal decomposition of H_2PtCl_6 . Although most Pt was applied to the back face of the crystal, with this technique deposition of some Pt onto the front face also occurred.

When an NaOH-coated platinum foil was substituted for the platinized SrTiO_3 no hydrogen production above background was observed. The foil had been previously platinized (cathodically polarized in 3% aqueous chloroplatinic acid containing 0.2% of lead acetate) to give a black surface which would more closely approximate the light absorption properties of the SrTiO_3 . The presence of the semiconductor thus is required for photoactivity; platinum alone is not sufficient. However, NaOH-

coated SrTiO_3 crystals without platinum did show moderate photoactivity, as will be discussed in section V-3-2.

Oxygen is produced along with hydrogen on platinized crystals, as shown in Figure V-9. It appears that somewhat less than stoichiometric amounts of oxygen are accumulated, even at the high level of photoactivity shown here. This is probably due to oxygen adsorption on and absorption in various components of the walls of the circulation loop. When small amounts of oxygen were introduced into the circulation loop, the oxygen pressure in the loop decreased with time, even in the absence of hydrogen. This effect precluded the measurement of oxygen production at rates less than ~ 200 monolayers/hour.

The crude wavelength response of hydrogen production from a NaOH-coated, platinized pre-reduced crystal is shown in Figure V-10. "UV" means illumination through the water and 7-51 filter. "Visible" denotes illumination through water and 3-74 filters. Details of the spectral distribution of the various filtered lights have been given in Chapter IV. It should be recalled that the 7-51 filter passes photons with energies greater than the bandgap of SrTiO_3 , while photons passing through the 3-74 filter have sub-bandgap energies. Hydrogen is produced only during illumination with bandgap radiation. The jumps in hydrogen pressure in the system denoted by dashed lines in Figure V-10 accompany 2 torr changes in total pressure and are probably due to thermal adsorption-desorption effects. However, the total energy flux into the system during "visible" illumination is greater than that during "UV" illumination. Thus the decrease in hydrogen pressure during visible illumination is not due to simple adsorption of hydrogen onto a cooling

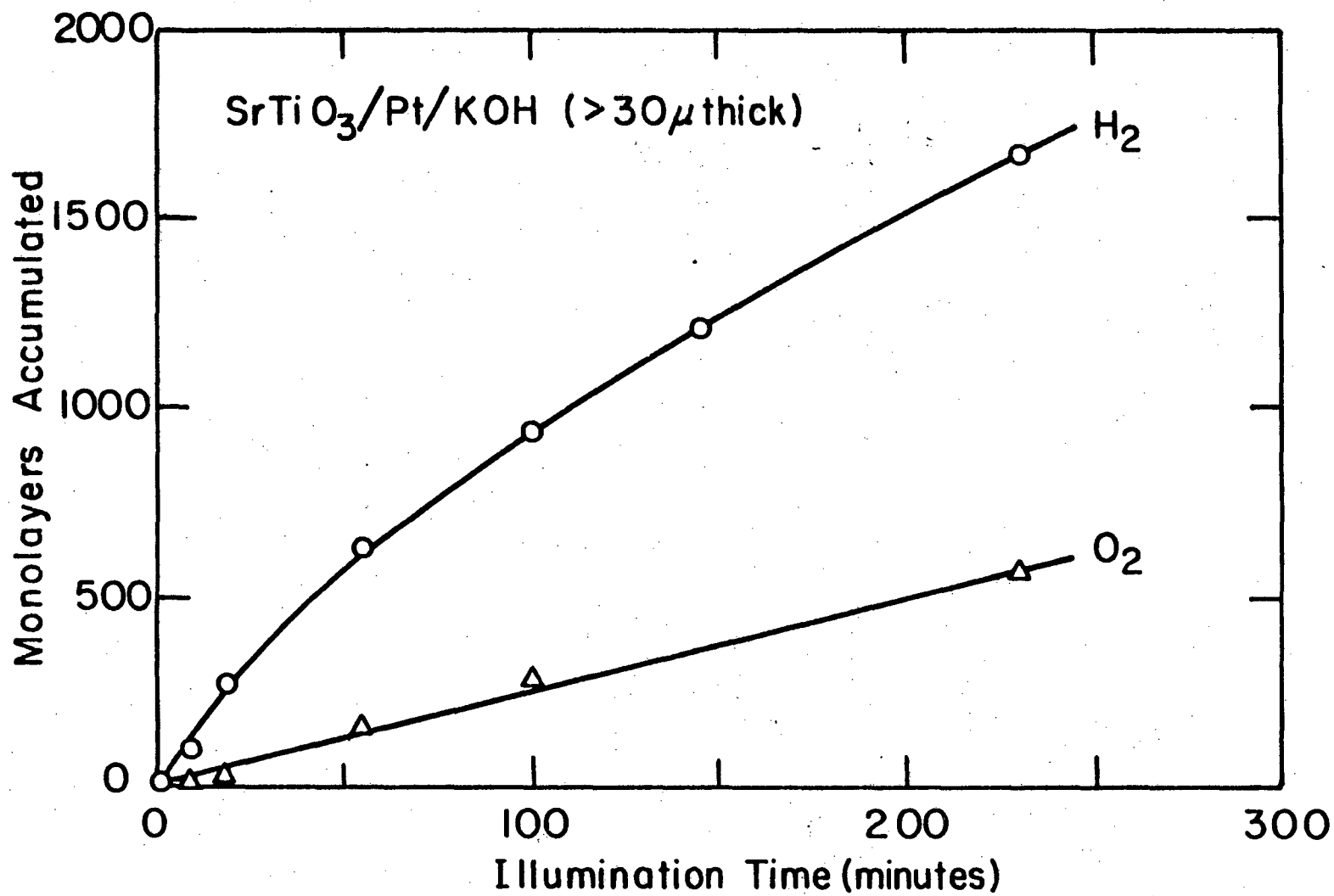


Fig. V-9. H₂ and O₂ photogeneration on hydroxide-coated SrTiO₃/Pt in water vapor.

XBL 799-7069

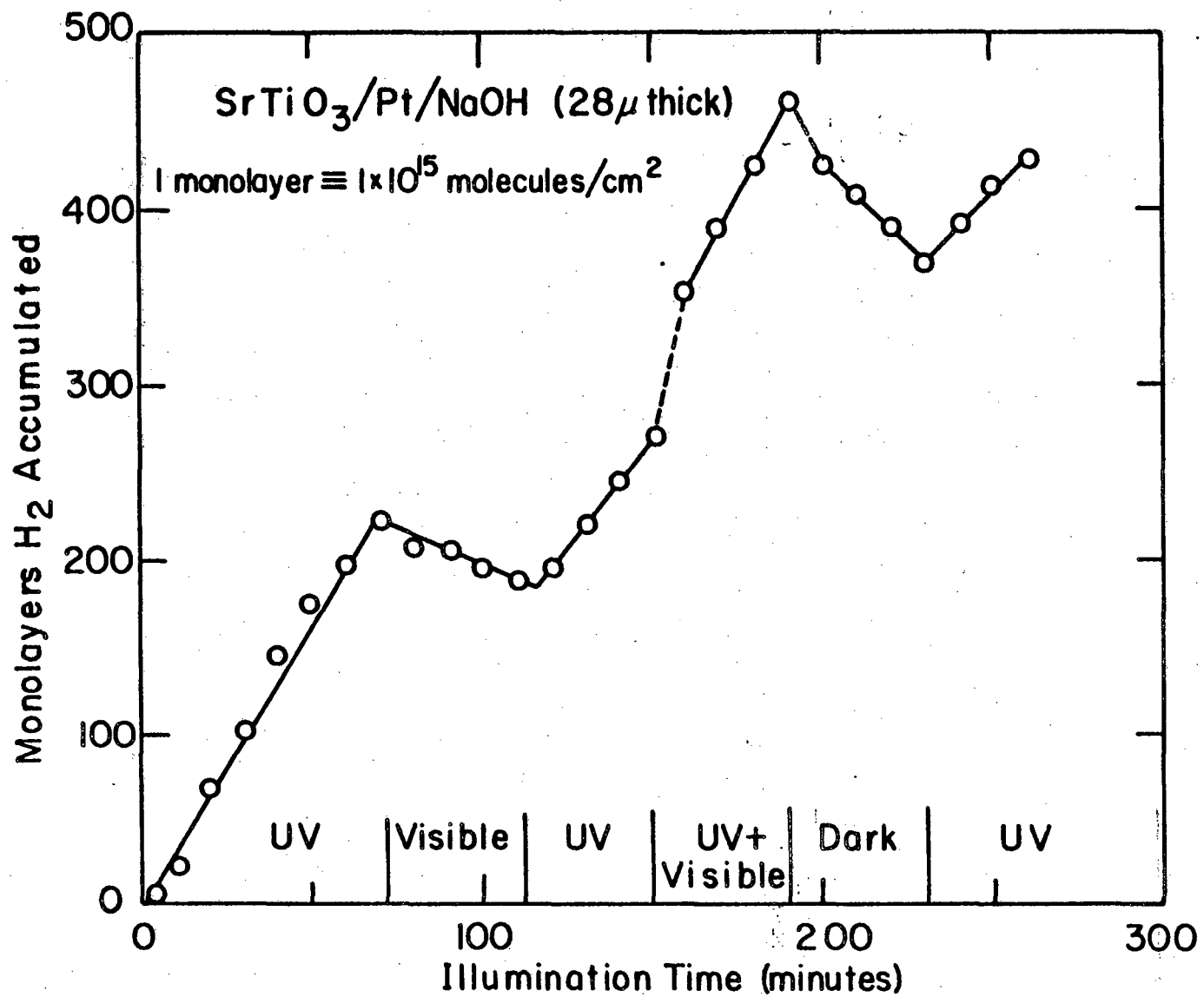


Fig. V-10. Coarse wavelength dependence of H₂ photogeneration on XBL 799-7067 NaOH-coated SrTiO₃/Pt in water vapor.

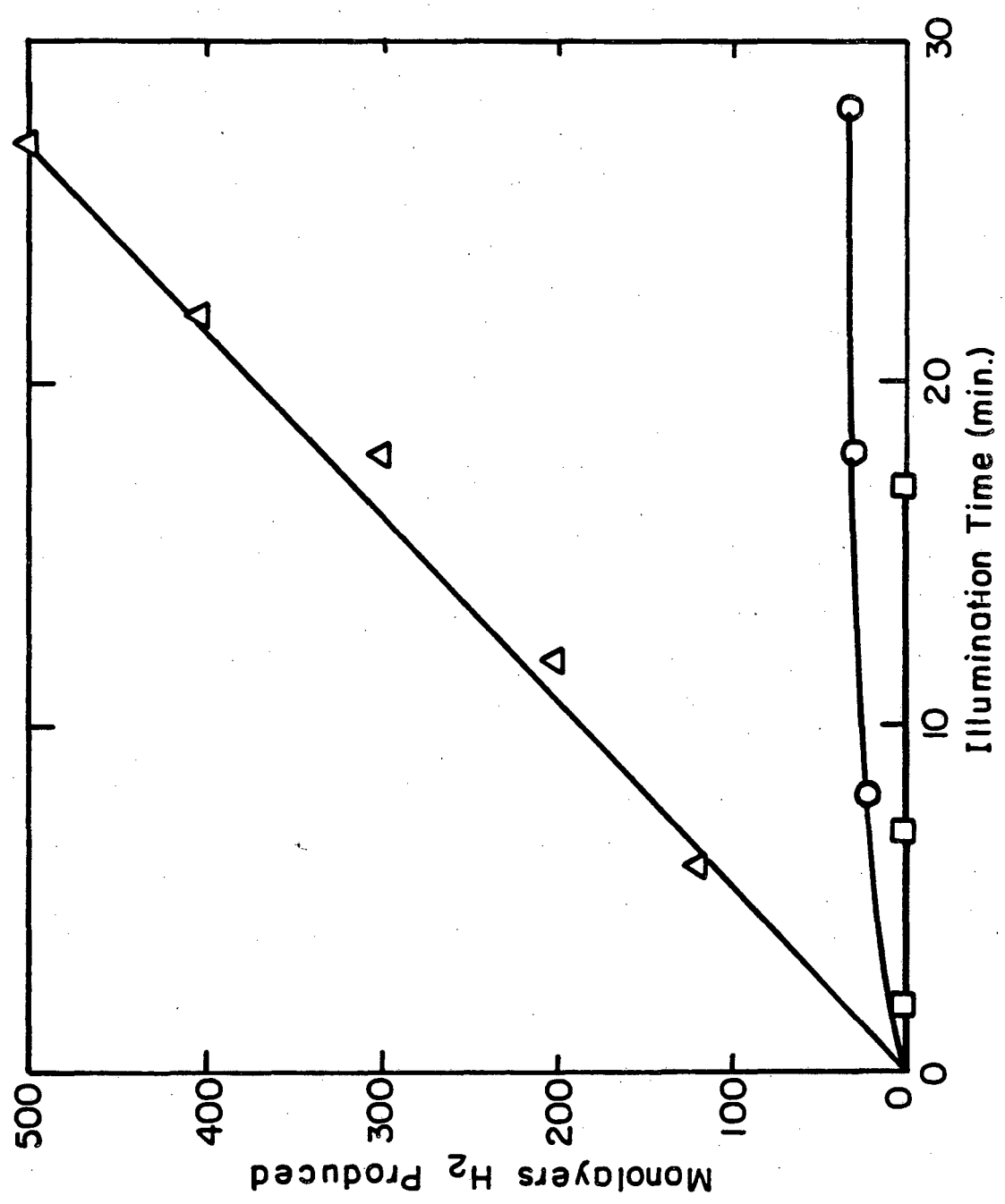
crystal and walls, but rather to a back reaction. From the downward slopes in this figure, and assuming an excess of oxygen from slight air leaks during this experiment and a Pt area of 1 cm^2 , a quasi first-order rate constant of $5 \times 10^{-3} \text{ sec}^{-1}\text{-cm}$ is calculated. This compares well with the $3\text{-}4 \times 10^{-3} \text{ sec}^{-1}\text{-cm}$ found by Hanson and Boudart¹⁷ and is higher than the recombination rate measured in this apparatus for H_2 and O_2 on clean platinized SrTiO_3 . These results indicate that the water-saturated NaOH film does not severely inhibit the recombination of H_2 and O_2 .

Figure V-11 shows the effect of changing the amount of water vapor admitted to the cell containing an NaOH-coated, platinized SrTiO_3 crystal. No activity was observed when water vapor was admitted briefly to a maximum pressure of 10 torr(squares). When the water bulb was sealed off the pressure dropped below 4 torr, as water was absorbed by the NaOH crust, which remained chalky white throughout the experiment, but did not completely obscure the SrTiO_3 and Pt from view.

When water vapor was admitted for a longer time to a maximum of 18 torr before sealing the bulb, some activity was observed(circles). A small translucent spot was observed in the NaOH film, indicating inhomogeneous absorption of water. Much higher photoactivity was obtained when the vapor above the liquid water was allowed to equilibrate with the NaOH layer at ~ 20 torr, with the NaOH layer becoming fully transparent. The small activity denoted by the circles may be due to local saturation of a small part of the NaOH layer.

Figure V-12 shows the dependence of hydrogen production on the average dry thickness of the NaOH film, as calculated from the known number of micromoles of NaOH spread evenly over the surface. Hydrogen

Fig. V-11. Water vapor pressure dependence of H₂ photogeneration on NaOH-coated SrTiO₃. Details of key in text.



XBL 818-6322

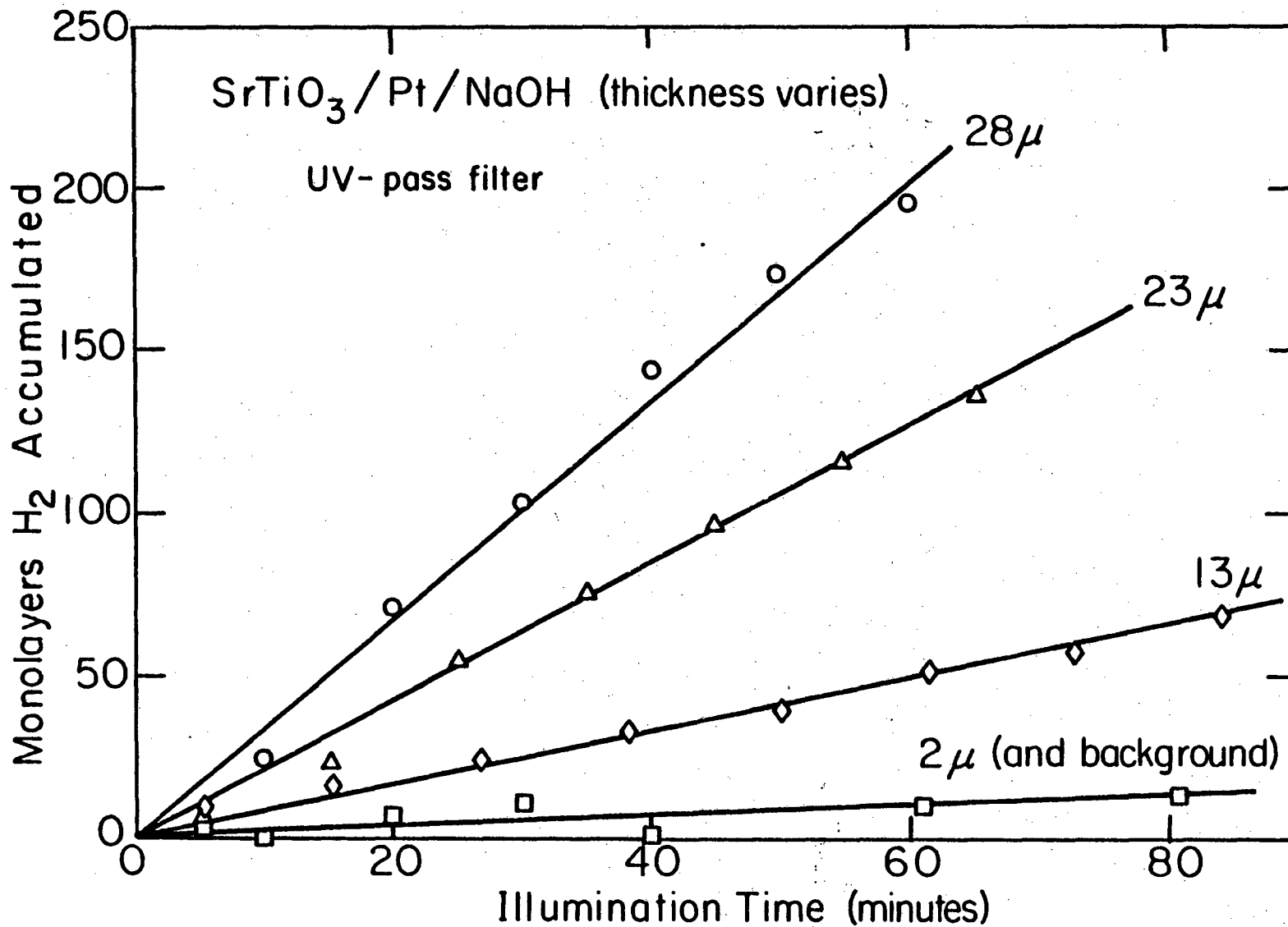


Fig. V-12. NaOH crust thickness dependence of SrTiO₃ hydrogen photogeneration activity in 20 torr water vapor.

XBL 799-7070

production decreases as the thickness of the NaOH film is made smaller. The hydrogen production rate for the 2μ film is indistinguishable from the background hydrogen obtained with no crystal or NaOH present. The data was obtained in random order of NaOH thicknesses. The back of the crystal employed had been electroplated with platinum. A cutoff in hydrogen production at around 2μ NaOH thickness was also observed on crystals which had been platinized by vacuum evaporation of the metal and which showed higher overall hydrogen production activity.

The preceding two Figures indicate that rapid hydrogen photogeneration on platinized SrTiO_3 required both a rather thick layer of NaOH and admission of sufficient water vapor to saturate the alkali. Sodium hydroxide is a deliquescent material; it absorbs enough water from moist air to form an aqueous solution. To determine whether the only role of the NaOH coating was to allow the formation of a layer of aqueous electrolyte around the crystal, crusts of other ionic compounds were tried. Some of these others were also deliquescent and formed liquid layers. Others were hygroscopic and picked up some water but not enough to form a free-flowing electrolyte. The results of these experiments are summarized in Table V-2.

Sodium and potassium hydroxides gave similar activity. Cesium hydroxide gave appreciable, though somewhat smaller, activity probably due to the lower viscosity of the saturated electrolyte and greater loss of film thickness through dripping off the crystal. No hydrogen activity was seen in films of LiCl and CaCl_2 , both deliquescent materials. In such electrolytes production of chlorine as well as oxygen might be expected, but hydrogen evolution should be unaffected by the chloride. Cesium carbonate, another basic deliquescent material, was active while sodium

TABLE V-2: The Hydrogen photoproduction activity of water vapor saturated ionic compound films on a platinized, pre-reduced SrTiO₃ (111) crystal.

	H ₂ produced	no H ₂ produced	
NaOH,d	X		
KOH,d	X		
CsOH,d	X		
CsCl,h		X	
CaCl,h		X	
LiCl,d		X	
CaCl ₂ ,d		X	
Na ₂ CO ₃ ,h		X	d= deliquescent h= hygroscopic, but not deliquescent
Cs ₂ CO ₃ ,d	X		

carbonate, basic but not deliquescent, was not. An effective coating must both hold substantial quantities of water and be basic. This latter point was somewhat surprising in light of the body of literature which indicates that water photolysis cells utilizing n-SrTiO₃ or n-TiO₂ photoanodes can operate successfully in both basic and acidic electrolytes. ¹⁸ The theory which implies that changes in electrolyte pH should have no effect on such cells has been reviewed in Chapter II. This unexpected enhancement of activity by basic materials led to the studies of photoactivity in bulk electrolyte reported in section V-4.

V-3-2 Hydrogen Photogeneration on NaOH-coated, Metal-free SrTiO₃

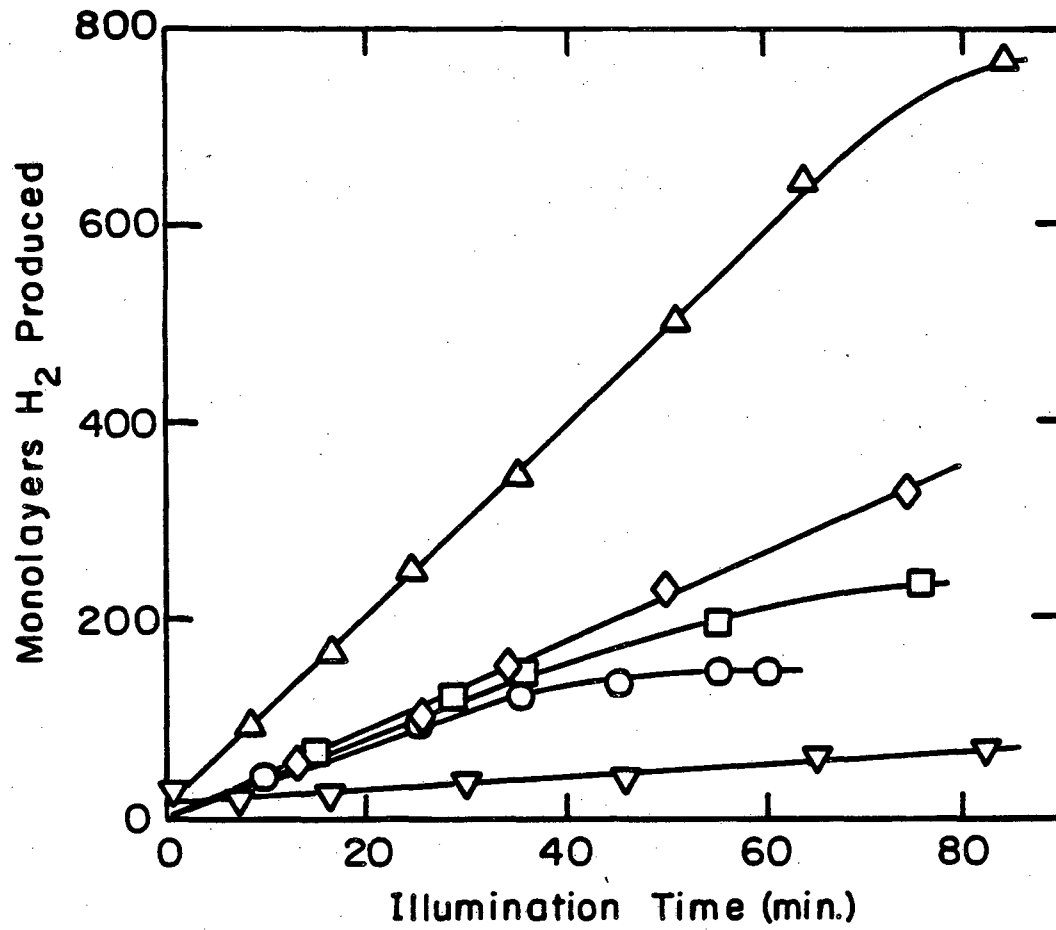
Metal-free, as well as platinized, SrTiO₃ proved effective for hydrogen photogeneration when coated with NaOH and illuminated with bandgap radiation in an atmosphere of water vapor (Figure V-8). The SrTiO₃ crystals were held in an open basket of vycor glass rod mounted so that neither the crystal nor the NaOH film were in contact with any metallic surface. Photoactivity was seen even when the crystal and holder were etched in concentrated nitric acid or aqua regia prior to the experiment to remove any metallic impurities which might have been picked up during handling. No photoactivity was seen with NaOH-coated blanks of ground glass or α-alumina.

The photoactivity of metal-free surfaces, while less than that of platinized crystals, is of interest because it runs counter to the expectations of simple photoelectrochemical theory and gives hope for the development of photocatalytic processes outside the realm of electrochemistry. According to standard paradigms, only oxygen is produced

on the illuminated surface of an n-type semiconductor because the electric field in the semiconductor depletion layer drives photogenerated free electrons away from the surface. Photoactivity of a metal-free crystal is unexpected because the identical band-bending on all surfaces would preclude efficient separation of photogenerated charge carriers and prevent photogenerated electrons from reaching the surface. Hydrogen and oxygen evolution from distinct surfaces of a metal-free crystal might be explained by the differences in surface band bending caused by nonequivalent illumination of the faces. The generation of both hydrogen and oxygen on the the same surface might be indicative of a more local photocatalytic process which could not be explained by the simple band-bending model.

Figure V-13 summarizes the results of an experiment designed to investigate the locus of hydrogen evolution on platinized and metal-free SrTiO_3 . The same (111) SrTiO_3 was used for all of the data on this figure. All edges of the crystal were covered with Varian Torr-Seal UHV-compatible epoxy, and one edge was attached to a vycor glass support rod. In each case the crystal was dipped in 10 M NaOH, the resulting film was dried, and the crystal was illuminated with the water-filtered output of the mercury lamp in an atmosphere of saturated water vapor. After each run the crystal was rinsed in distilled water. After each application of epoxy the crystal was set in an oven to cure per Varian instructions. The experimental runs summarized in Figure V-13 are as follows:

- 1) (Circles). Both sides of the crystal were open, with a continuous film of NaOH covering the crystal faces and extending over the epox-



XBL818-6321

Fig. V-13. Effect of blocking non-illuminated (or platinized) face of NaOH-coated SrTiO₃. Key in text.

ied edge.

- 2) (Squares).. Same as 1), except that the back (nonilluminated) surface was blocked with epoxy.
- 3) (Triangles, point up). Same as 2), except that a spot of Pt was electroplated onto the front surface. Electroplated platinum showed poor adhesion and generally exhibited lower activity than platinum derived from thermal decomposition of H_2PtCl_6 , but plating with the "electrochemical pencil" allowed better control over the area plated.
- 4) (Diamonds). Same as 3), except that the Pt spot was covered with epoxy.
- 5) (Triangles, point down). Same as 4), except that the crystal was rotated so that the open face of the crystal was away from the light. This run measures the combined effect of hydrogen evolution from the epoxy and reactivity due to light reflected from the back of the stainless steel cell.

The results indicated that sealing off the back side of a Pt-free crystal had no significant effect on the rate of hydrogen generation. The hydrogen is thus generated on the illuminated surface in contrast to the situation in $SrTiO_3$ -Pt photoelectrochemical cells, where only oxygen is evolved from the illuminated surface in measureable quantities. A process is involved here which apparently does not require two separate regions with grossly different surface band-bending properties. The reaction here involves more local separation of photogenerated charge carriers - either on an atomic scale or on the scale of the remaining

structural heterogeneities of the the surface.

More detailed studies of hydrogen evolution from metal-free SrTiO_3 were made in bulk aqueous electrolyte and are discussed in section V-4. Discussion of possible mechanisms whereby photo-generated electrons reach the illuminated SrTiO_3 surface can be found in Chapter VII.

V-4 Photoactivity of SrTiO_3 in Bulk Aqueous Electrolyte

V-4-1 Platinized SrTiO_3 in Aqueous Electrolytes

The requirement of a basic coating on SrTiO_3 in the experiments of the previous chapter led to the desire for a more quantitative measure of the effect of hydroxide concentration on the photoactivity of SrTiO_3 . This required that experiments be run in aqueous electrolytes of known concentration. The experimental apparatus was modified to allow the crystal to be immersed in a pool of electrolyte held within a borosilicate reaction vessel. The circulation pump and gas chromatograph enabled the hydrogen pressure in the vapors circulating over the electrolyte to be measured. The reaction vessel was agitated periodically to dislodge bubbles forming on the crystal.

Wrighton, Wolczanski, and Ellis¹⁹ had reported the photoelectrolysis of water on platinized SrTiO_3 in NaOH solutions, but no mention was made of other electrolytes. Wrighton *et. al.*²⁰ found no significant change in photocurrent with NaOH concentration for a SrTiO_3/Pt cell operated at 2.8 V applied potential over a hydroxide concentration range of 0.025-9.1 N. Nozik and Chance²¹ found that the photoefficiency of TiO_2 -Pt cells, of necessity operated with an anodic potential applied to

the TiO_2 , was independent of the electrolyte pH. Thus photoelectrochemical cells, at least those operated with high applied potentials, had given results seemingly at variance with our observations of the need for a coating of a basic material to give photoactivity in water vapor at room temperature.

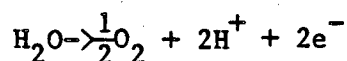
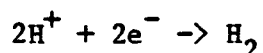
Table V-3 gives a go-no go summary of our results for hydrogen photogeneration on a platinized, pre-reduced crystal in various electrolytes.

TABLE V-3: H_2 Photogeneration on SrTiO_3/Pt in various electrolytes

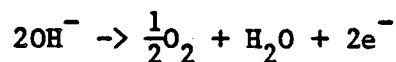
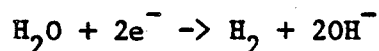
Electrolyte		H_2 Produced	H_2 Not Produced
.001-20N	NaOH	X	
1-10N	HClO_4		X
10N	H_2SO_4		X
1N	NaClO_4		X
1N	NaF		X
10N	LiCl		X
18N	NH_3	X	

Measureable hydrogen production was observed in sodium hydroxide solutions with concentrations as low as 10^{-3} M. No hydrogen evolution was observed in any acidic solutions. Perchloric acid was chosen because

perchlorate shows little if any specific adsorption effects on Pt. ²²
 No photoactivity was observed in sulfuric acid. Normal electrolysis of water driven entirely by an external potential proceeds most efficiently in acidic or alkaline electrolytes where there is an adequate concentration of one of the two electroactive ions (H^+ or OH^-) which carry the majority of charge between the anode and cathode. In acid H^+ (or H_3O^+) is the carrier ion:



While in basic solutions OH^- carries charge:



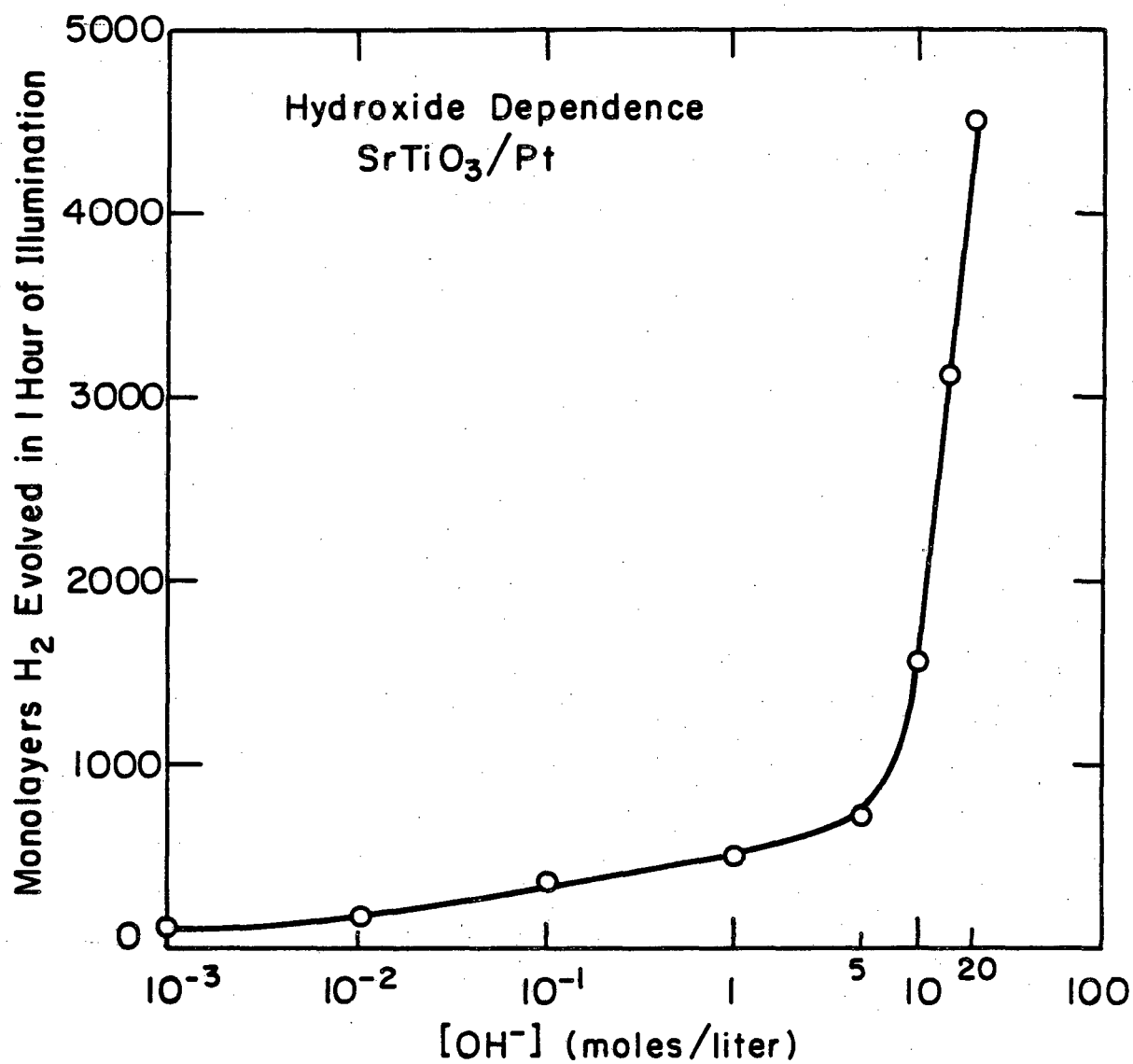
On platinized $SrTiO_3$ the acidic mechanism is apparently inoperative.

No photoactivity was observed in neutral solutions of $NaClO_4$ or $LiCl$, even with the latter in high concentration. Prof. Metiu of UCSB proposed that the size of the anion was critical - only very small anions could produce a high enough charge density in the inner Helmholtz layer to ensure sufficient band-bending to efficiently separate photo-generated electrons and holes. ²³ The Yatsimirskii thermochemical radius of OH^- is 1.40 Å while that for sulfate is 2.30 Å, with perchlorate at 2.36 Å. ²⁴ The solid state radius of F^- (1.36 Å) ²⁵ is even smaller.

than the quoted OH^- radius. No photoactivity was seen in 1 N NaF, showing that small ionic size was not a sufficient condition for photoactivity. The use of solid-state radii in a discussion of the liquid-solid interface is of course dangerous, since the true effective radius of an adsorbed ion probably lies between the radii of its solid-state and fully hydrated forms. F^- shows no specific adsorption effects on Pt even at potentials where the surface is oxidized²², while OH^- shows strong specific interactions with oxides. Specific ion effects, rather than simply ionic size, appear important. Since HF is a weak acid, 1 N NaF should be slightly basic ($[\text{OH}^-] < 10^{-5}$ moles/liter), but no photoactivity was seen. H_2 production was seen in more basic solutions (.001 N NaOH and in 18 M NH_3 where $[\text{OH}^-] = 10^{-2}$).

The variation of the photoactivity of a platinized, pre-reduced SrTiO_3 single crystal with the concentration of the sodium hydroxide electrolyte is shown in Figure V-14. Below 5 N the rate of hydrogen production increases less than two-fold per decade increase in $[\text{OH}^-]$. Above 5 N the dependence is much more striking. The data in Figure V-14 were gathered in random order of concentration with the electrolyte at 44°C . These results will be discussed in Chapter VII.

Since relatively small amounts of hydrogen are evolved in the experiments discussed here, the greater solubility of hydrogen in less concentrated electrolytes²⁶ might have some effect on the amount of hydrogen detected in the vapor circulating above the electrolyte pool. To test this possibility, and to compare results from platinized SrTiO_3 with those from a SrTiO_3/Pt electrochemical cell with discrete electrodes, the experiments summarized in Figure V-15 were performed. n- SrTiO_3 and



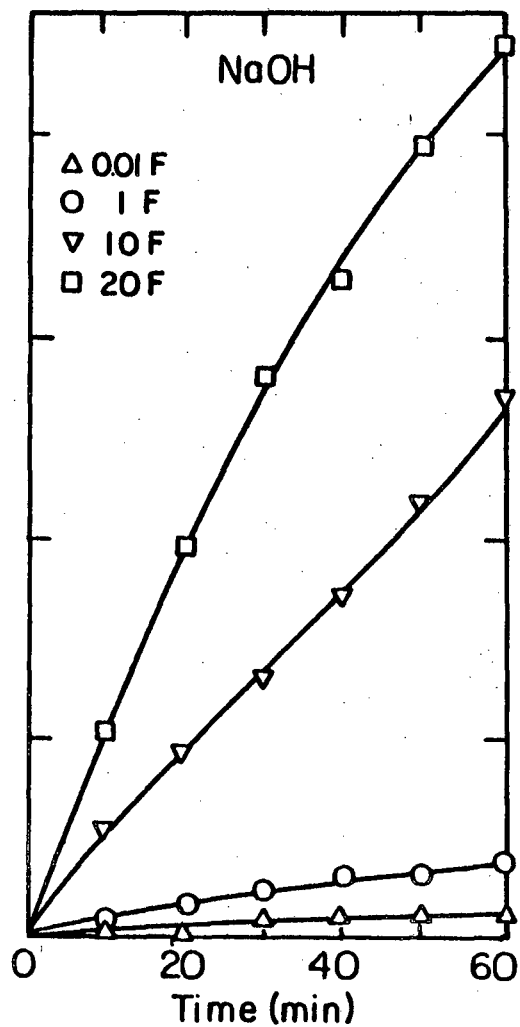
XBL799-7068

Fig. V-14. Hydrogen generation activity on SrTiO₃/Pt as a function of concentration of aqueous NaOH electrolyte.

platinized platinum electrodes were mounted on a vacuum feedthrough and inserted into the reaction vessel so that photocurrents and hydrogen pressures over the electrolyte could be measured simultaneously. The results are plotted as monolayers H_2 where one monolayer = 3.2×10^{-4} coulomb/cm². Qualitative agreement is seen between the two measurements. Increasing the electrolyte hydroxide concentration increases photoactivity as measured in either way. The overall hydroxide concentration dependence is thus not merely a hydrogen solubility effect. At low hydroxide concentrations coulometry shows somewhat higher activity than is indicated by the gaseous hydrogen accumulation. This effect may be an artifact of different hydrogen solubilities. The discrepancies between chromatography and coulometry at higher hydroxide concentrations are probably due to uncertainties in the calibration of the chromatograph. The hydroxide concentration dependence of photoactivity is seen both for platinized $SrTiO_3$ crystals and for this $SrTiO_3/Pt$ electrochemical cell with discrete electrodes. These electrodes were connected by an 11 ohm resistor. With the photocurrents observed, the potential of the $SrTiO_3$ electrode was at most 20 mV anodic to the Pt electrode. The latter, since hydrogen was being evolved, was at very close to the reference hydrogen potential.

Measurements of photoactivity vs. light intensity can indicate the relative importance of recombination phenomena. An augmented light level increases the concentrations of photogenerated electrons and holes in the semiconductor bulk and at the surface. If recombination is fast compared to the rates of the spatial separation of electrons and holes and of the catalytic reactions at the surfaces, then the photoactivity vs. light intensity curve should level off at high light intensities

A. Gas Chromatography



B. Coulometry

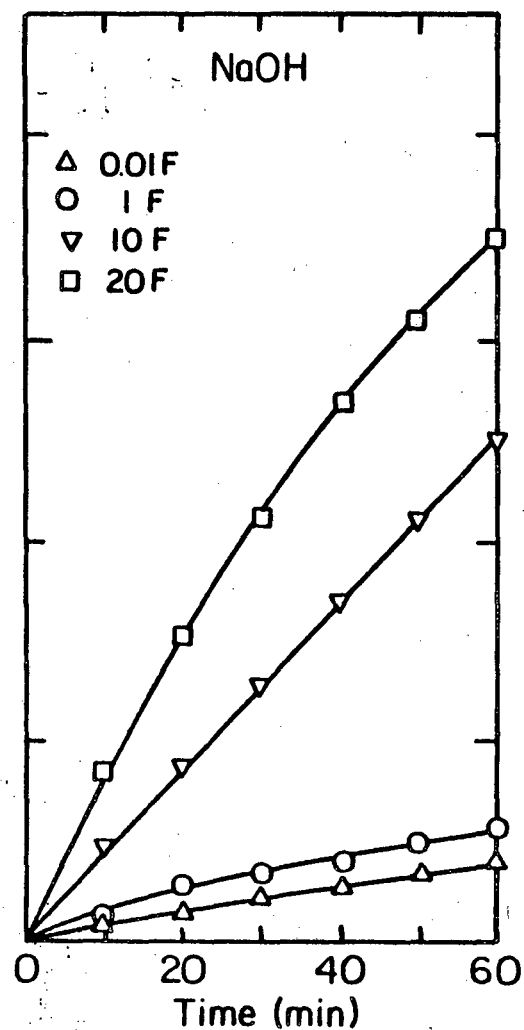
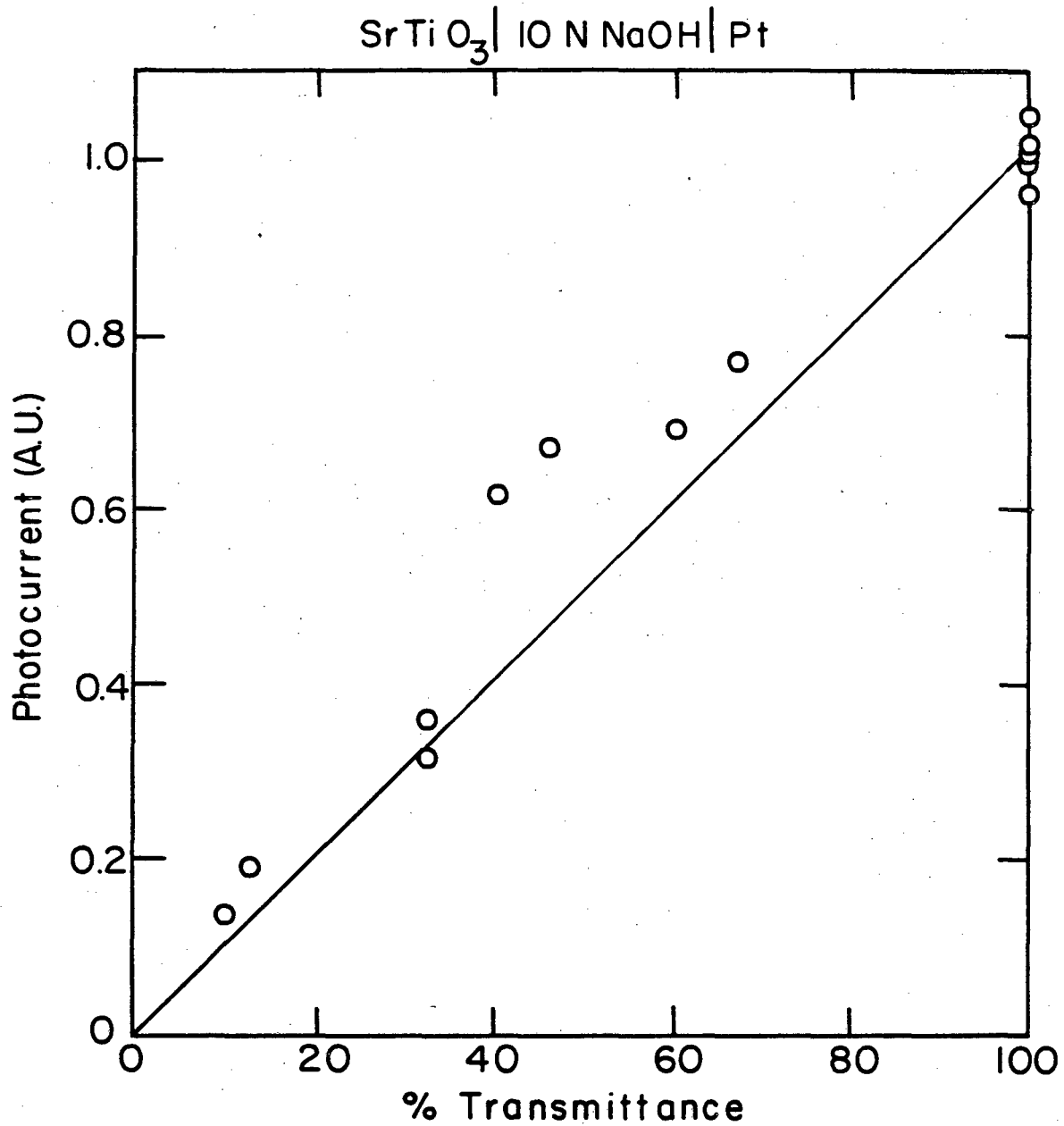


Fig. V-15. Simultaneous gas chromatographic and coulometric measurements of H_2 photogeneration in a $SrTiO_3$ -Pt PEC cell at zero applied potential. Effect of NaOH electrolyte concentration.

XBL 805-5064

where more photogenerated carriers are lost to recombination. In Figure V-16 the photocurrent (normalized to that obtained at the full illumination of 2×10^{16} suprabandgap photons $\text{cm}^{-2} \text{sec}^{-1}$) is plotted as a function of the transmission of the screens placed in front of the light source. Measurements were made over a flux range of 2×10^{15} - 2×10^{16} photons $\text{cm}^{-2} \text{sec}^{-1}$. Although some downward concavity is seen, it does not appear that the reaction is severely limited by recombination in concentrated electrolytes. This is consistent with the high quantum yield of 0.4 for the cell operating in 10 F NaOH.

The results obtained with the photoelectrochemical cell operated at zero applied potential (i.e. with the SrTiO_3 electrode a maximum of 20 mV anodic to the Pt electrode) correlate with those obtained on platinized SrTiO_3 crystals in bulk electrolyte and in thin electrolyte films. In all cases photoactivity increases with increased hydroxide concentration in the electrolyte. The photoactivity of the cell with discrete electrodes was about four times that seen for platinized crystals. In the photoelectrochemical cell a gallium-indium eutectic is spread over the back of the SrTiO_3 crystal to assure an ohmic contact. The expectation is that, since indium has a smaller electron affinity than SrTiO_3 , any electron flow upon equilibration will be into the SrTiO_3 and no rectifying depletion layer will form in the semiconductor (accumulation layers are thinner than depletion layers and can generally be tunneled through with high efficiency). The work function of Pt, on the other hand, is larger than that of SrTiO_3 , and depletion layer formation is expected. This depletion layer would form a barrier to the passage of electrons from the SrTiO_3 to the Pt, thereby lowering cell efficiency.



XBL802-4702

Fig. V-16. Photocurrent for a SrTiO_3 -Pt PEC cell with zero applied potential as a function of light intensity.

Neville and Mead²⁷ have measured surface barrier energies for metals on strontium titanate in vacuum by measuring photoresponse, forward current vs. voltage, and thermal activation. They conclude that indium (electronegativity = 1.7 eV) yields a barrier of 0.90 ± 0.02 eV) while gold, with an electronegativity of 2.4 eV (similar to that of platinum) gives a surface barrier of 1.23 ± 0.07 eV. Since either of these barriers is larger than the band-bending in a SrTiO_3 -Pt cell at zero applied potential²⁰ and should therefore preclude photoactivity in such cells, it is not yet clear how these solid-state measurements relate to the photochemistry.

The hydroxide concentration effect raises many questions. Is it associated with the evolution of hydrogen or of oxygen? Are there permanent changes in surface compositions associated with it? What does it portend for photocatalytic reactions? These questions will be dealt with in the next section, and in Chapter VII.

V-4-2 Photoactivity of Pt-free SrTiO_3 in Aqueous Electrolytes

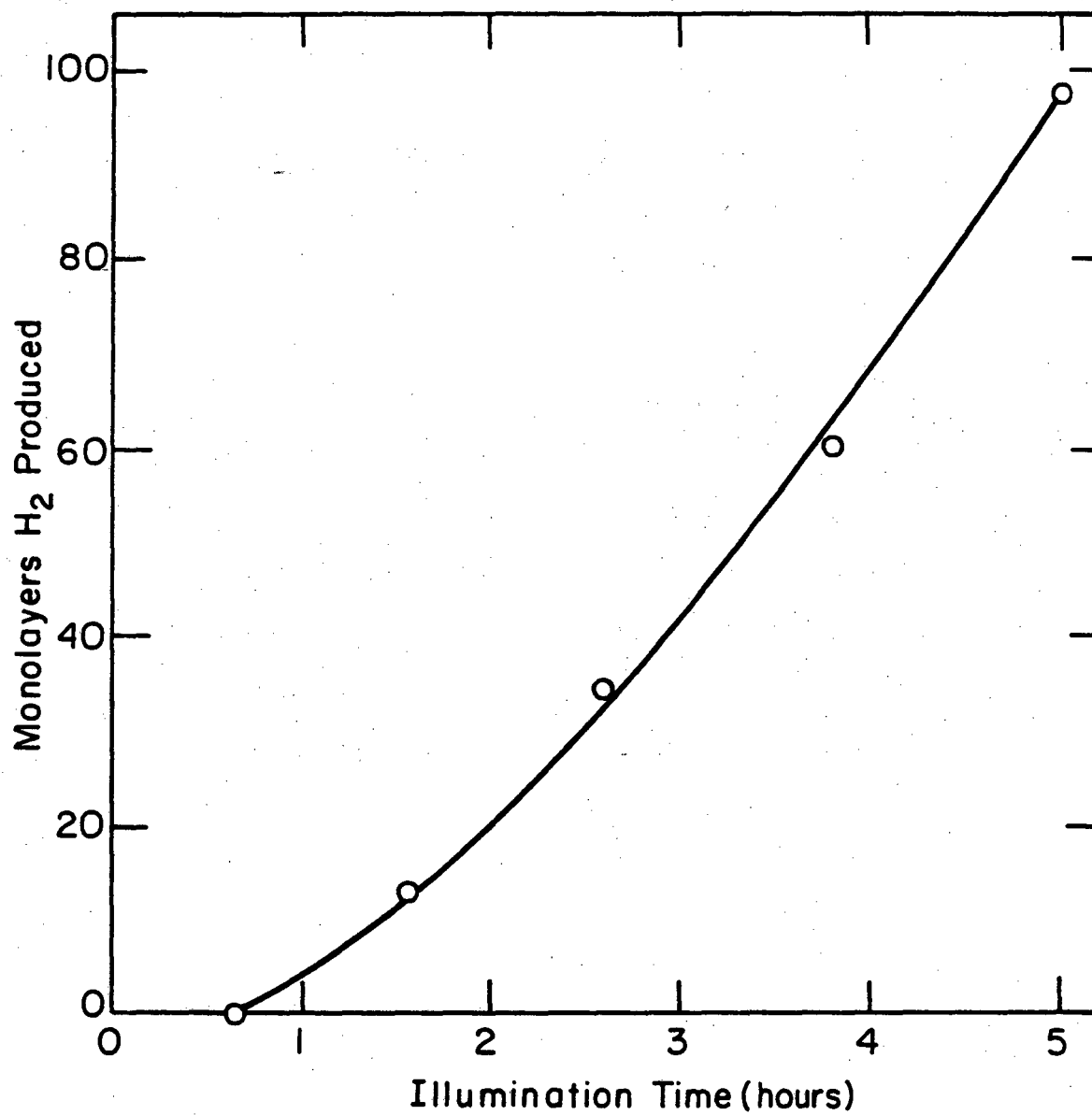
As shown in Figure V-8, NaOH coated SrTiO_3 was active for photogeneration of hydrogen from water vapor even when no platinum was present. In this section further experiments in bulk aqueous electrolytes, in some cases coupled with post-reaction surface analysis, are described. The experiments sought to somewhat elucidate the enhancement of SrTiO_3 photoactivity at high hydroxide concentrations and to gain further understanding of how reducing power can be generated at the surface of this n-type semiconductor. Most experiments were performed on stoichiometric, rather than hydrogen pre-reduced, crystals so that the

hydrogen produced could be unambiguously linked to photoactivity.

Figure V-17 shows the accumulation with time of hydrogen above an illuminated stoichiometric SrTiO_3 crystal in 29 M aqueous NaOH. The average yield in this experiment of 20 monolayers/hr corresponds to a quantum efficiency for bandgap electrons of 0.05%. As shown in Figure V-18, only photons with $h\nu > 3.2$ eV were effective for hydrogen production. The degree of upward concavity in the accumulation curve varied in different experiments. This concavity may arise from several sources:

- 1) solubility of H_2 in the electrolyte
- 2) trapping of hydrogen bubbles on the crystal surface during the initial stages of the experiment
- 3) induction time for the formation of an active surface species.

Previously colorless stoichiometric crystals took on a slight bluish cast indicative of slight reduction of the crystal as experiments proceeded, but there was no detectable decrease in the resistivity of the crystal. Pre-reduced crystals gave similar hydrogen production behavior. When ground-glass or α -alumina blanks were substituted for SrTiO_3 , hydrogen production was below 4 monolayers/hr. Intentional additions to the electrolyte of acetone or ethanol, which were used to clean the crystal in early experiments, did not increase hydrogen production. Intentional admixture into the electrolyte of the halocarbon grease which sealed ground glass joints in some experiments also had no significant effect.



XBL 801 4602

Fig. V-17. H₂ photogeneration from Pt-free, stoichiometric SrTiO₂ in 29M NaOH.

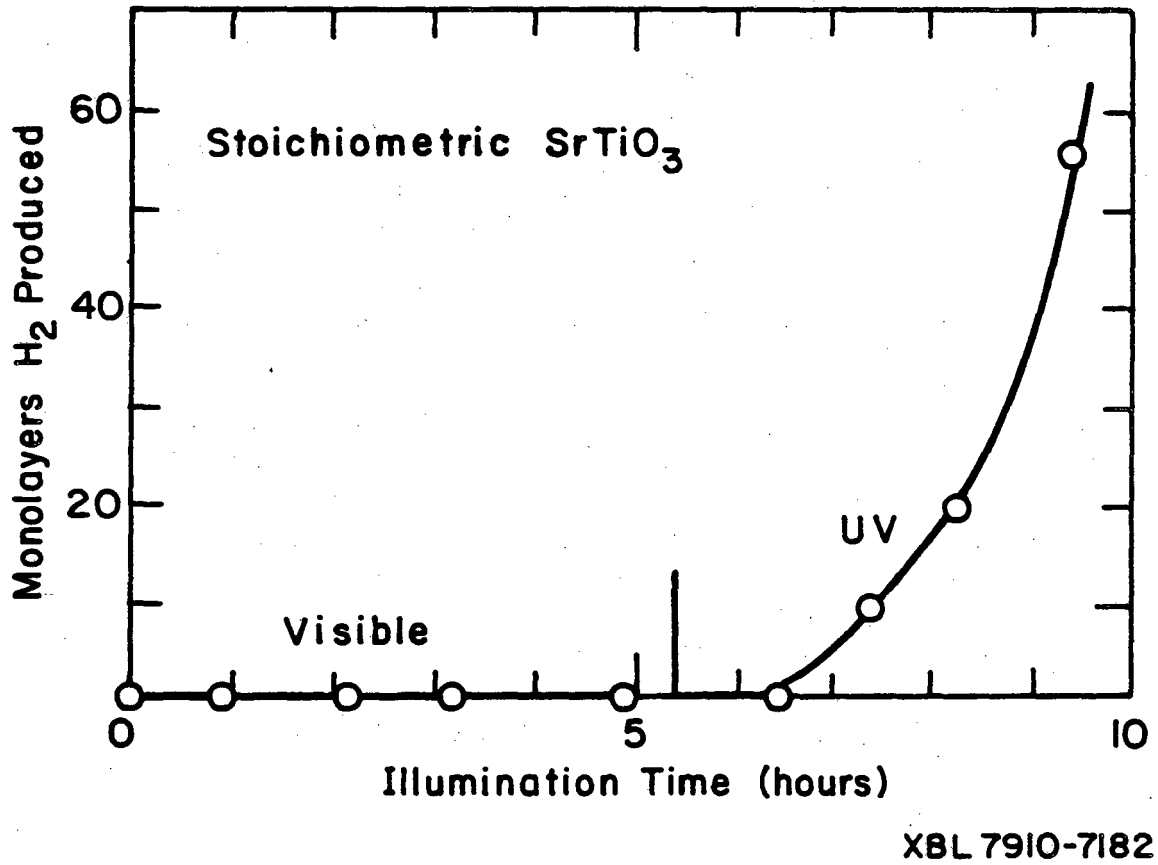


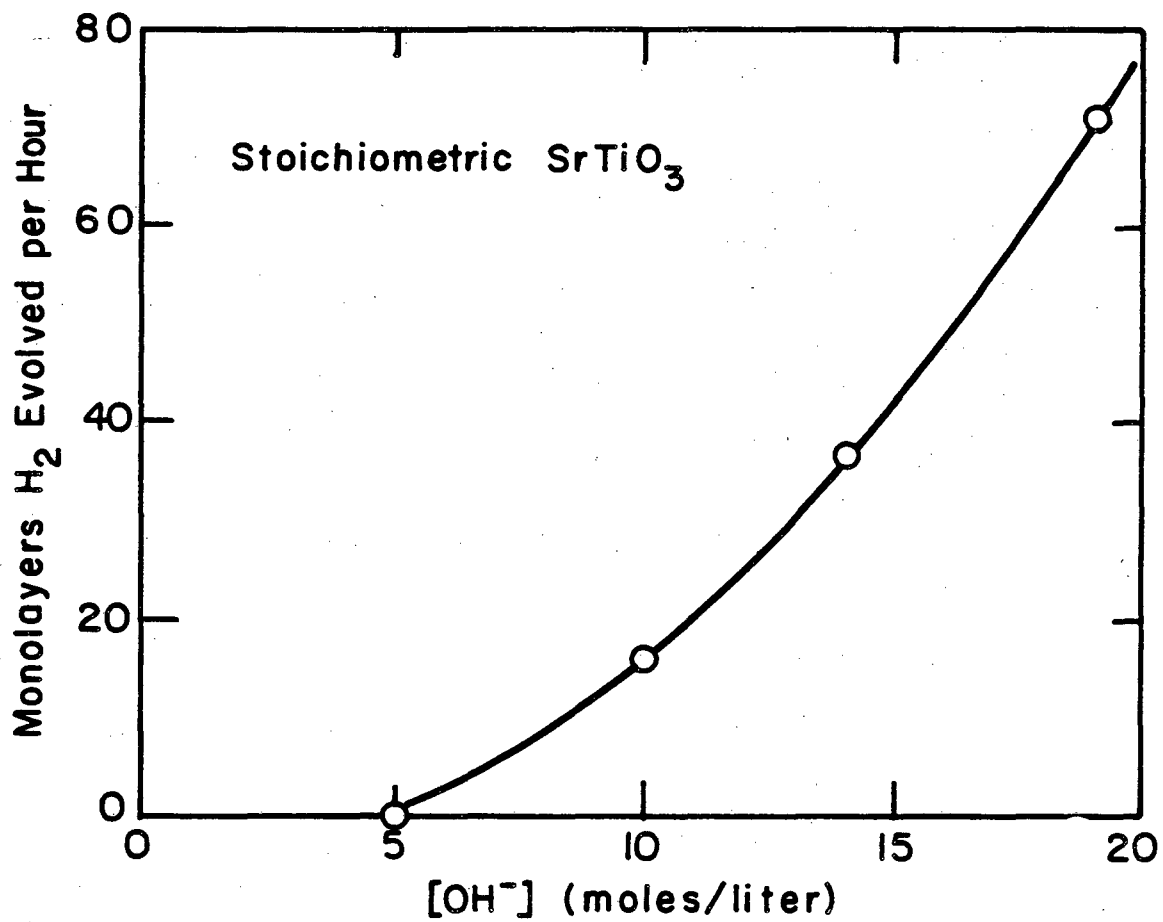
Fig. V-18. Coarse wavelength dependence for photoactivity on Pt-free stoichiometric SrTiO₃.

Hydroxide Dependence

The hydroxide concentration dependence of H_2 photogeneration from a single stoichiometric metal-free $SrTiO_3$ crystal is shown in Figure V-19. A linear concentration scale is used rather than the logarithmic scale used in Figure V-14. The points were taken in random order of concentration, with the crystal and cell being thoroughly rinsed in deionized water between runs. As in the case with platinized $SrTiO_3$, hydrogen photogeneration increases at higher OH^- concentrations.

Pertitanates and soluble titanium

Fusion of titanium-containing minerals with molten NaOH has been shown to form water-soluble pertitanate species.²⁸ Especially in light of the inability to confirm O_2 as the oxidized product in these experiments, it was important to determine whether peroxotitanate production was responsible for the higher photoactivity in highly alkaline solutions. After an extended hydrogen-producing run the electrolyte was slowly acidified to $pH < 2$ with HNO_3 . Aqueous hydrogen peroxide was added, and the absorbance around 410 nm was scanned.²⁹ This procedure is sensitive to general soluble titanium. No absorbance around 410 nm was seen to a noise-limited sensitivity of 10^{-3} optical density units. This sensitivity would correspond to about five monolayers of soluble titanium produced, assuming Beer's law holds. Extraction of the $SrTiO_3$ crystal with 1 N HNO_3 followed by addition of H_2O_2 to the extract also yielded no absorbance at 410 nm. This indicates that no multilayer of stable titanium peroxide insoluble in basic solution had formed as the oxidation product of the photoreaction. Addition of H_2O_2 to a nitric



XBL 7910-7183

Fig. V-19. NaOH concentration dependence of H₂ photogeneration on Pt-free, stoichiometric SrTiO₃.

acid solution containing the crystal did produce highly visible orange peroxotitanium species. Thus, neither soluble titanium nor surface peroxy species were produced in multilayer quantities during hydrogen photogeneration in concentrated aqueous NaOH. The enhanced photoactivity at high $[\text{OH}^-]$ is not due to an onset of oxidative photocorrosion.

Other Concentrated Electrolytes

At the high NaOH concentrations employed here the activity of water itself is depressed. To determine whether this factor, rather than specific properties of hydroxyl solutions, were primarily responsible for the effect, experiments were run in other concentrated electrolytes. As was shown in Table V-3, 10 N HClO_4 , 10 N H_2SO_4 , and 10 N LiCl had not yielded hydrogen with an illuminated platinized crystal. The two former solutions are strongly acidic, and the latter contains chloride, which is known to adsorb strongly on Pt and which might provide a competitive oxidation reaction. Metal-free crystals were also tried in 10 M aqueous NaClO_4 . At least at low concentrations, ClO_4^- interacts weakly with Pt, and the salt is unusually soluble. The perchlorate ion is thermodynamically unstable with respect to chloride throughout the entire $\text{pH}-E_h$ region of stability for water, but except in the concentrated acid in the presence of organic material the perchlorate ion is thought to be kinetically stable against electrochemical reduction. ³⁰ No hydrogen photogeneration was seen in the neutral perchlorate solutions. A summary of results on stoichiometric metal-free crystals in various electrolytes is seen in Table V-3.

Electrolyte Purity

Most of the experiments described to this point employed electrolytes compounded from deionized water and reagent-grade chemicals. At the high solute concentrations used here, trace impurities could have a drastic effect upon the interfacial chemistry. It has been suggested³¹ that the $[\text{OH}^-]$ concentration effect and the photoactivity of metal-free surfaces could be accounted for by the photoreduction of heavy metal impurities onto the SrTiO_3 surface. Bard and coworkers³² have shown that photoelectroplating of metals can occur even from exceedingly dilute solutions. That such photoplatinization can greatly modify the catalytic properties of a semiconductor surface is made clear in Table V-3. Intentional addition of platinum (IV) up to a concentration of $4 \times 10^{-4} \text{ M}$ increased the photoactivity of a stoichiometric SrTiO_3 crystal in 30% (10 M) NaOH more than ten-fold. As determined by AES, some platinum was deposited thinly over the entire surface, but there was a visible deposit around a hydrogen bubble which had been trapped beneath the crystal. Platinization of the unilluminated surface of a stoichiometric SrTiO_3 crystal had caused no increase in the hydrogen evolution rate; interdispersion of Pt and SrTiO_3 on the illuminated surface appears necessary for increased activity on insulating stoichiometric crystals. On conducting pre-reduced crystals platinization of either front or back was effective.

A $4 \times 10^{-4} \text{ M}$ Pt (IV) concentration corresponds to 2400 monolayers platinum in solution. The reagent grade NaOH used was certified to contain 1 ppm total heavy metals impurities (as Ag). If all of this impurity were actually Pt there would be 12 monolayers Pt in the 10 M NaOH elec-

trolyte aliquots. In the thin NaOH films which yielded similar results there would be 2% of a monolayer of Pt. Even assuming that all of the heavy metal impurities were Pt or a similarly active metal and that all the impurity available plated out, it seems unlikely that two experimental conditions with such disparate amounts of Pt available would yield such similar results (Table V-4) if all hydrogen evolution took

TABLE V-4: Hydrogen Photogeneration on Metal-free SrTiO₃ in Various Electrolytes

Electrolyte	Run duration (hr)	Normalized H ₂ yield (monolayers)	Average yield (monolayers/hr)
30% reagent NaOH	12	1300	110
30% ultra-pure NaOH	17	940	55
30% high purity NaOH, acetate added to 8×10^{-2} M	18	1250	70
30% reagent NaOH Pt(IV) added to 4×10^{-4} M	12	19,200	1600
10M reagent NaClO ₄	24	0	0
7M-Omega water	13	36	3
1M H ₂ SO ₄	15	0	0
40% reagent NaOH*	10	600	60

* pre-reduced crystal

place on photoplated platinum. No photoactivity was seen in 10 M NaClO₄ compounded from a reagent containing 5 ppm heavy metals, a higher metal content than found in the NaOH solutions used.

To further investigate the possible role of impurities, experiments were performed under cleaner conditions earlier described in the experimental section. Commercial ultra-pure NaOH solutions were used. Glassware was soaked several days in nitric-sulfuric acid²² then rinsed in spectroscopic or electronic grade water, followed by the electrolyte to be used. Crystals were also etched and rinsed in ultra-pure electrolyte before use. As seen in Table V-3, experiments under these cleaner conditions gave hydrogen yields within the range of the earlier experiments. It is impossible to totally disprove the presence of <1% metallic impurities on the surface as the means by which photogenerated electrons can reach the electrolyte, but the experiments just described, as well as the results of Auger analysis which follow, indicate some residual hydrogen evolution activity for the metal-free surface. Much of the consciousness of the importance of Pt impurities in electrolyte arises from an erroneous report of high oxygen reduction electrocatalytic activity on sodium tungsten bronzes.³³ Weber,³⁴ who found that the high activity was due to Pt contamination, derived a Tafel plot for hydrogen evolution on the clean sodium tungsten bronze (which is a perovskite as is SrTiO_3). On this material currents equivalent to hydrogen photoproduction on metal-free SrTiO_3 ($\sim 2\mu\text{A}$) required an overpotential of 150 mV. As this is less than the difference between the flatband potential of SrTiO_3 and the hydrogen redox level²⁰, slow hydrogen production on metal-free SrTiO_3 should be energetically possible even according to the simple photoelectrochemical paradigm.

Several authors^{35,36} have reported photoassisted reactions on titanium oxides between carbon and water yielding some hydrogen and CO_2 . Hydrogen-producing photo-Kolbe disproportionations of carboxylates have

also been demonstrated.³⁷ However, neither addition of acetate to 0.08 M nor unintentional gross contamination of the 10 M NaOH electrolyte with charred epoxy residue caused significant acceleration of hydrogen production in our experiments. Schwerzel et al.³⁸ have also found zero activity for the photo-Kolbe reaction on SrTiO₃ in basic solution. Though the lack of the ability to detect oxygen production precludes proving that our photogeneration of hydrogen does in fact constitute a photodissociation of water, the most probable alternative reactions do not seem to occur under our experimental conditions. The evolution of many tens of monolayers of hydrogen indicates that the reaction is catalytic with respect to the surface and does not simply constitute the stoichiometric consumption of a surface adsorbed species, as is probably the case with some reports of photocatalysis on powders.^{39,40}

Photochemistry on other oxides

TiO₂, α-Al₂O₃, and α-Fe₂O₃ were also investigated as possible photocatalysts for H₂ evolution in concentrated aqueous NaOH. As expected, no photoeffects were seen on α-Al₂O₃, which is transparent to all of the incident light. Platinized, pre-reduced TiO₂ yielded H₂ at rates approximately equal to those seen on metal-free SrTiO₃. No hydrogen production was observed on as-received α-Fe₂O₃, with or without platinum. When Fe₂O₃ was reduced in a hydrogen furnace and placed in concentrated NaOH, hydrogen was evolved. However, this was a dark reaction due to the reduction of Fe₂O₃ to reactive magnetite or metallic iron.

These results show that the correlation of flatband potentials negative of RHE with hydrogen photogeneration at zero applied potential

seems to hold for photocatalytic, as well as for photoelectrochemical, systems. SrTiO_3 , whose flatband potential lies negative of RHE, evolves hydrogen photocatalytically even in the absence of platinum. TiO_2 , whose flatband potential lies, by the latest measurements,⁴¹ a mere 150 mV negative of RHE, does evolve H_2 slowly when platinized, but the rate on metal-free TiO_2 lies below the detection capabilities of the apparatus used here. Fe_2O_3 , with a flatband potential fully 690 mV positive of RHE,⁴² evolves no hydrogen, even when platinized.

Post-reaction Surface Analysis

The photogeneration of hydrogen on SrTiO_3 and its dependence on the composition and concentration of the electrolyte raise many questions about the composition of the semiconductor surface. Does a change in surface composition accompany hydrogen photogeneration? Or conversely, is photoactivity seen only under conditions where no change in surface composition occurs? What impurities are found on the surface in various electrolytes? How does the composition of the surface in contact with aqueous electrolytes compare to that of a clean surface prepared in ultra-high vacuum? What surface states are present on the semiconductor, and to what extent do their energies overlap with the states available in adsorbed species or in the electrolyte bulk? To attempt to answer these questions several electron spectroscopies have been brought to bear.

In recent years considerable progress has been made with various techniques for in-situ examination of the solid-liquid interface: surface enhanced Raman, FTIR, multiple-pass reflectance IR, optical reflec-

tance spectroscopy, spectroscopic ellipsometry, and the like. However, none of these techniques has the sensitivity for elemental composition of Auger electron spectroscopy nor provides the detail of surface electronic structures obtainable through photoelectron spectroscopies. The interfacing of these vacuum techniques with liquid-solid systems poses many problems which are being attacked aggressively by several groups. 43-45

The results described here were obtained with a primitive interfacing technique (transfer through air). They indicate the level of data which can be obtained before clean transfer methods and their application to semiconductor systems can be perfected.

The effects of the various steps in the transfer process are shown by the Auger spectra in Figure V-3. Spectrum A is for a SrTiO_3 surface cleaned by Argon-ion sputtering in vacuo. The only impurities seen are Ar (215 eV) and a very small amount of carbon. $\text{C (272 eV)/Ti (383 eV) = .15}$. The Sr 68 eV/Ti 383 eV peak height ratio is 0.5. This is lower than reported in earlier work ⁴⁶ due to different mode of electron energy analysis. In this work the cylindrical mirror analyzer was used in the standard variable resolution mode in which the intensity of lower energy peaks is suppressed. In the earlier work energy analysis was by a retarding grid with the CMA held at a constant pass energy. The O/Ti (383 eV) peak ratio in this spectrum is 3.4. In agreement with earlier work in clean vacuum, annealing an Ar-sputtered crystal in vacuo to -800°C caused no change in the O/Ti ratio. This is in marked contrast to the behavior of TiO_2 , for which the O/Ti ratio of the annealed surface is higher (see section VI-4-2).

Spectrum B was taken after the Ar-sputtered surface was exposed to room air for two minutes. The crystal was transferred to the turbomolecularly-pumped transfer lock, which was backfilled with nitrogen. The crystal was removed from the lock, held in air 2 minutes, and returned to the lock. After the lock was turbopumped to 10^{-7} torr the crystal was transferred back to the UHV chamber. There is no significant change in the Sr/Ti ratio. The O/Ti ratio has increased to 4.7 which is unusually high. The C/Ti ratio increased somewhat to 0.28. Exposure to air causes no gross contamination of the surface, though the Ar-sputtered surface does pick up a fair amount of oxygen.

The Auger spectrum of a crystal transferred through air and rinsed 1 minute in electronic-grade water is shown in Figure V-3-C. The most striking result is that the Sr (68 eV)/Ti (383 eV) ratio has decreased to 0.2. The C/Ti ratio has increased to 0.5 and a well-defined peak shape characteristic of graphitic or partially hydrogenated overlayer appears. The O/Ti ratio is essentially the same (4.5) as for the air-exposed crystal. A very small Cl(181 eV) impurity is visible.

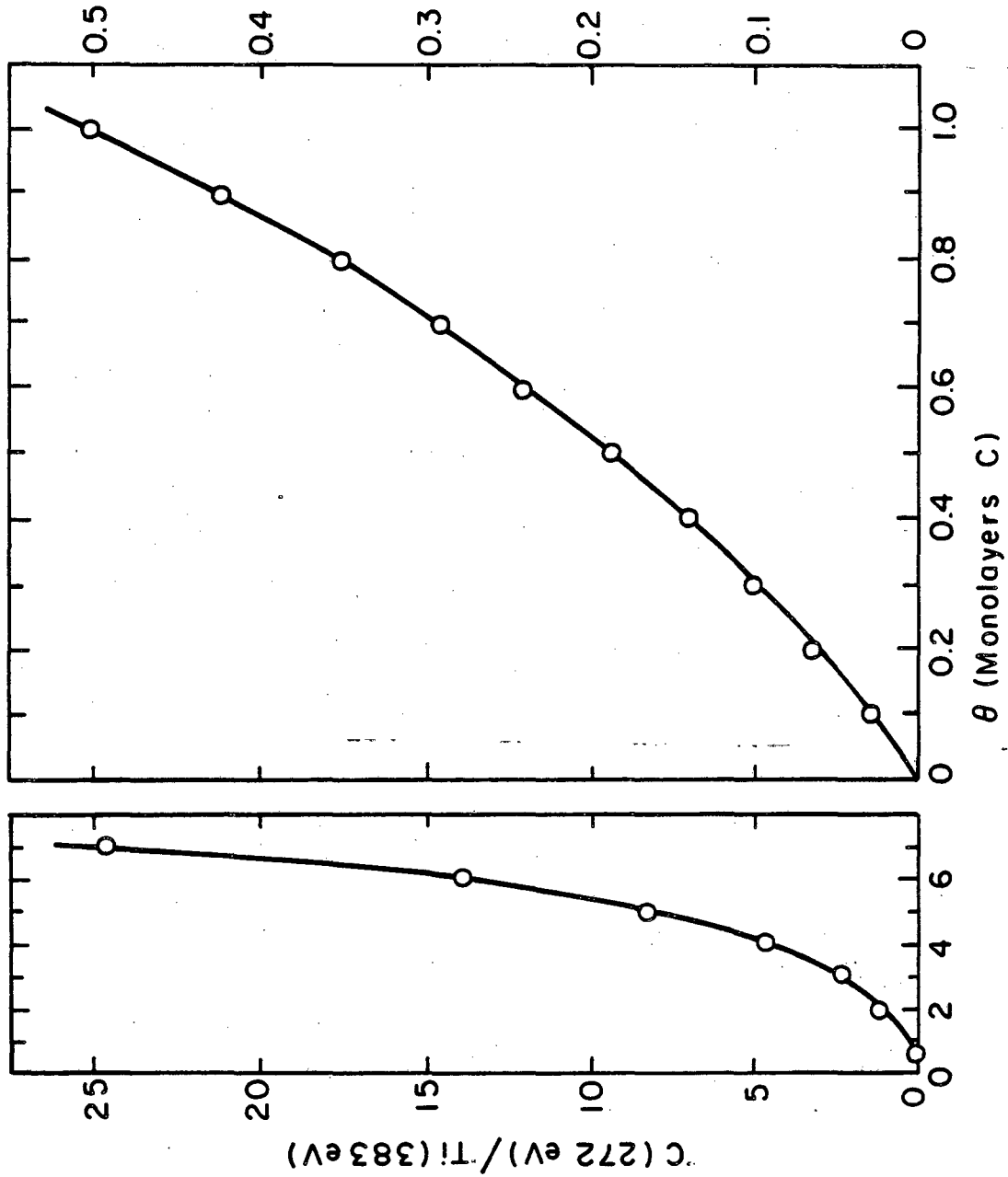
It is of some importance to gain an estimate of the carbon coverage corresponding to a given C/Ti ratio. Since both the Auger peak shape and sensitivity for Ti change upon oxidation, simple use of standard Auger spectra of the elements will lead to a poor estimate. During the work described in Chapter VI Auger spectra of clean TiO_2 and thick Au overlayers were taken at equal sensitivities. This allows the calibration of the Auger yield of oxidized Ti against standard elemental spectra. Cylindrical mirror analyzers and the same modulation energies were used for all spectra in this calibration. The use of TiO_2 rather than

SrTiO_3 in the calibration probably leads to an error of ~30%. The ratio of the Auger intensity expected from a monolayer of a substance to that from the bulk substance is given by the following equation (see Appendix):

$$\frac{I_1}{I_{00}} = 1 - \exp(-d/\lambda \cos 42^\circ)$$

where d is the interlayer spacing ($(2/3)^{-0.5}$ x nearest neighbor spacing for closest-packed layers), λ is the attenuation length of the Auger electrons, obtained from a universal curve,⁴⁷ and 42° is the acceptance angle of the CMA. One monolayer of carbon should yield 39% of the signal from bulk graphite. Combining this figure, the calculated attenuation of the Ti signal by 1 monolayer carbon (0.61) and the relative Auger yields of the bulk materials (corrected for oxidation of Ti), one estimates that the C(272 eV)/Ti (383 eV) ratio corresponding to 1 monolayer carbon on SrTiO_3 is 0.5. The calculated intensity corresponding to different coverages of C on TiO_2 are shown in Figure V-20. By a similar treatment, one calculates that a monolayer of carbon would decrease the Sr (68 eV)/Ti (383 eV) by a factor of 0.7 due to the shorter mean free path of Sr Auger electrons. The calculations indicate that ~1 monolayer of C is present on the SrTiO_3 surface in spectrum C. Since the Sr/Ti ratio in spectrum C is less than 40% of that in spectrum A, it appears that some Sr has in fact been removed from the surface. The carbon coverages calculated by the method of the previous paragraph seem high in light of experience with the attenuation of Ti and O signals by various levels of C contamination.

Fig. V-20. C/Ti Auger ratio as a function of C coverage on SrTiO₃.
Details of calculation in text.

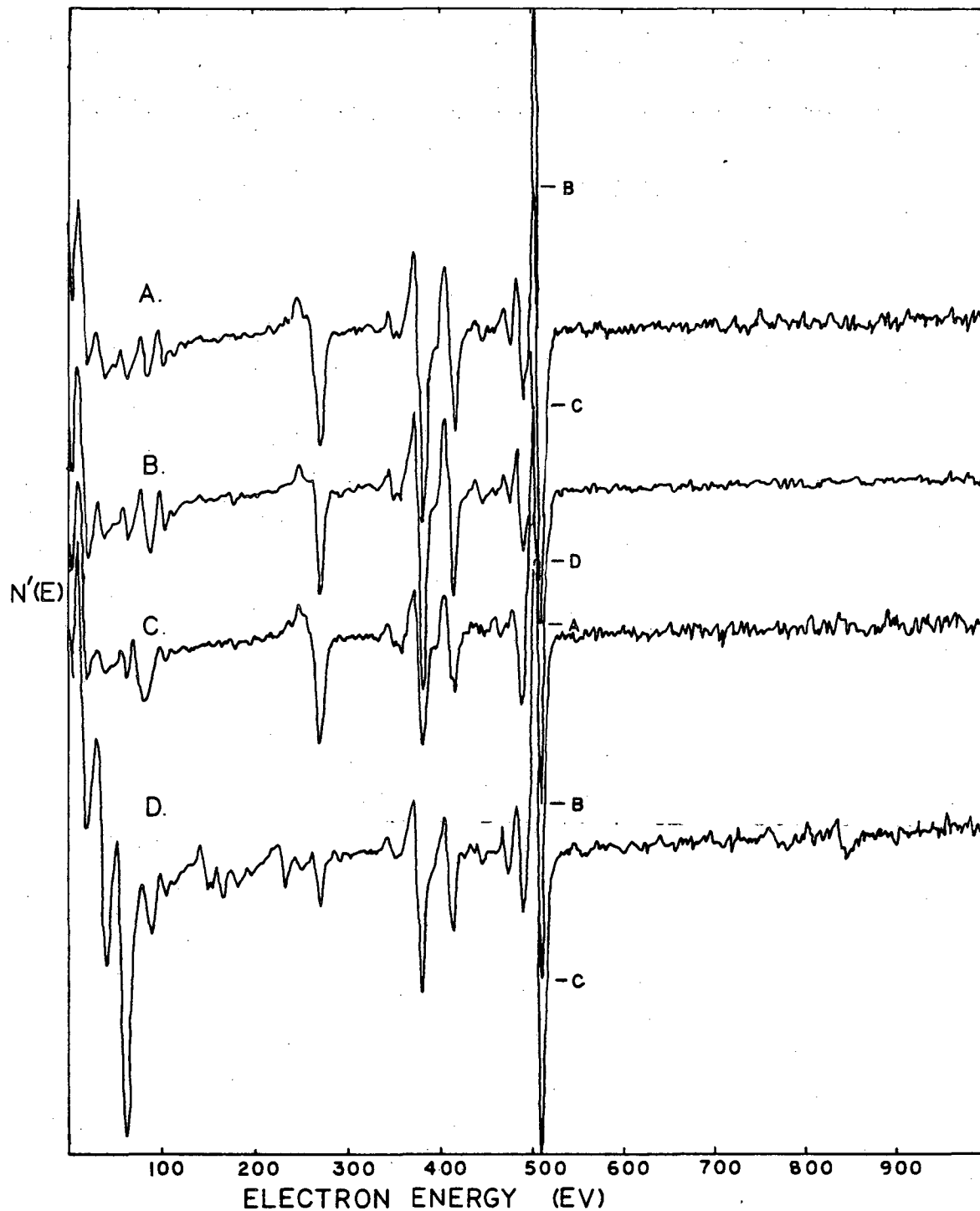


XBL 818-6320

Figure V-3 showed the effects of pure water on a clean SrTiO_3 surface. The surface compositions of crystals used in photochemical experiments in various electrolytes are shown in Figure V-21. These spectra were obtained in the Scanning Auger Microprobe using moderate electron beam current densities capable of reducing the surface. The O/Ti ratios in these measurements are, therefore, suspect. The high current densities were used to allow detection of trace impurities. Spectrum A is from a crystal given the pretreatment described in Chapter IV. The Sr/Ti ratio is similar to that of the water-dipped crystal of Figure V-3. The C/Ti (383 eV) ratio is 0.6, corresponding to ~ 1.5 monolayers according to the all-Auger estimate. Aside from carbon no impurity elements are evident. The carbon peak shape is more characteristic of graphite or a partially hydrogenated overlayer than of a carbide,⁴⁸ and is too intense to be due to a carbonate, even of great thickness.^{49,50}

Spectrum B shows the composition of a SrTiO_3 crystal after hydrogen-producing illumination in 10 M reagent-grade NaOH. The crystal was rinsed with electronic-grade water before being placed in the SAM. The only change evident is an increase in intensity of the middle "Sr" peak (78 eV). This is due to the presence of oxidized silicon on the surface, as confirmed by the presence of an Auger signal at 1606 eV. No large irreversible change in the Sr/Ti stoichiometry of the surface has occurred and no metallic impurities are evident. Similar results were obtained after illumination in H_2SO_4 or pure water, in which significant hydrogen generation was not seen.

Spectrum C was taken from a surface illuminated in 10 M NaClO_4 and rinsed in water prior to insertion in the SAM. No hydrogen production



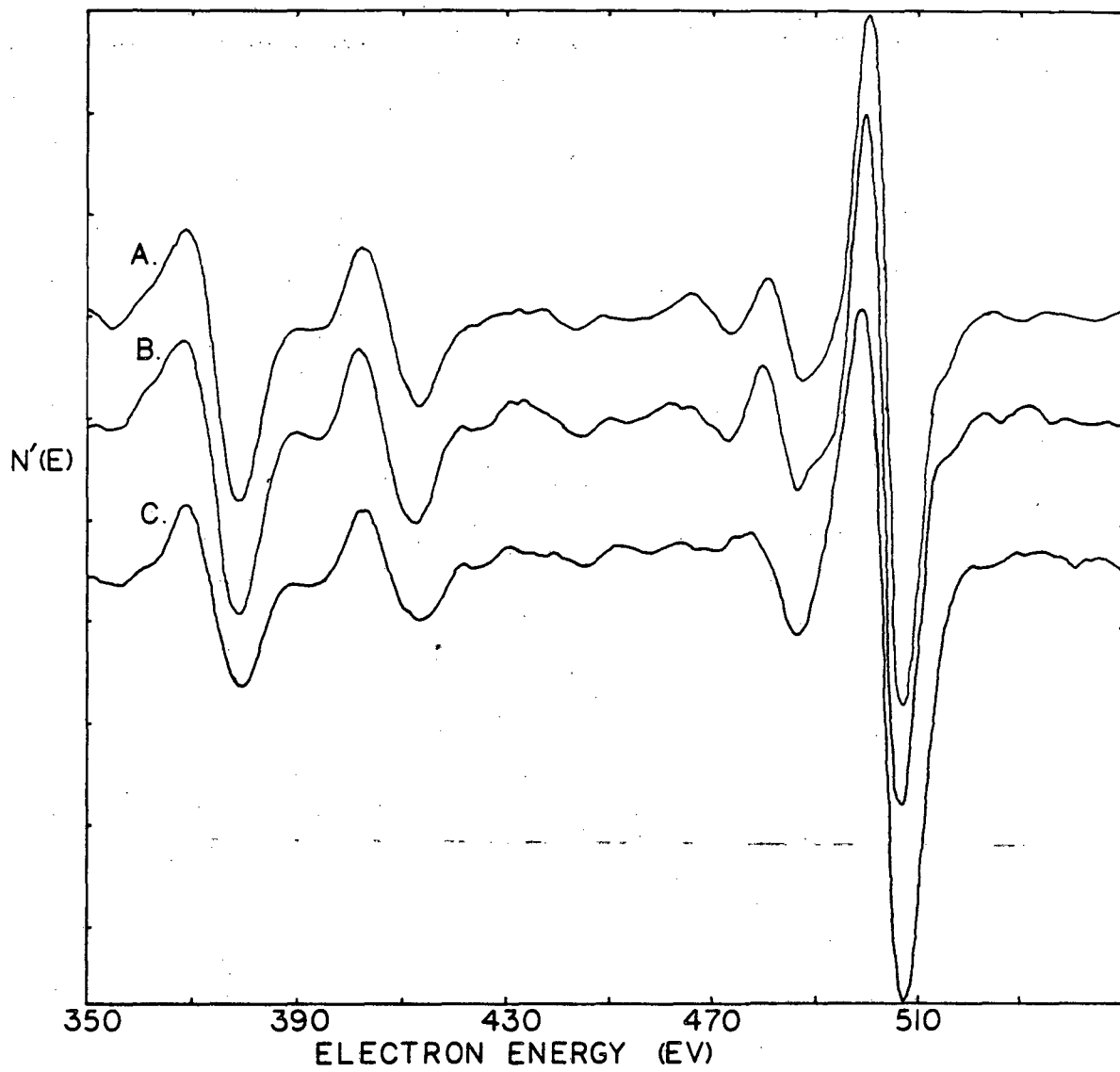
XBL 806-10539

Fig. V-21. Auger spectra of SrTiO_3 A) Before illumination,
 B) After hydrogen-producing illumination in 10 M NaOH,
 C) After non-hydrogen-producing illumination in 10 M NaClO_4 ,
 D) After illumination in 10 M NaOH + 4×10^{-4} M H_2PtCl_6

was observed in this electrolyte. Even more silica is seen on this surface than was found after illumination in NaOH. Thus leaching of the glass reaction vessel walls and deposition of the leachate onto the SrTiO_3 is not the path by which high NaOH concentrations enhance photoactivity. The middle and high-energy Sr peaks are largely obscured by the Si, but the size of the 66 eV Sr peak indicates that the Sr/Ti ratio was not changed greatly.

Spectrum D shows a SrTiO_3 crystal Pt-plated by addition of Pt(IV) to the 10 M NaOH to 4×10^{-4} molar during illumination. This spectrum was taken in the high Pt region which had formed around a hydrogen bubble. The impurity peaks correspond to Pt (64 eV), C, and a small amount of Cl. The carbon peak height has been reduced relative to that found on metal-free surfaces. Platinum may catalyze a carbon-scavenging reaction, or platinum may selectively deposit on carbon. The titanium peak shape on this surface is characteristic of an oxide rather than of the metal or of an intermetallic compound (see Chapter VI). This surface gave hydrogen photogeneration rates more than 100 times those seen on metal-free surfaces.

Details of the Ti/O Auger spectra for cases A, B, and C are shown in Figure V-22. These spectra were taken with a 10 V peak-to-peak modulation, a low beam current, ($< 0.1 \mu\text{A}$) and defocused beam before the survey spectra in Figure V-21 were obtained. The spectra taken before and after hydrogen-producing illumination in 10 M NaOH (A and B) are identical with the possible exception of the strength of the Ti feature at 420 eV. The crystal illuminated in 10 M NaClO_4 exhibits a higher O/Ti ratio (3.8 vs. 2.5) and a different O peak shape. The latter effect is



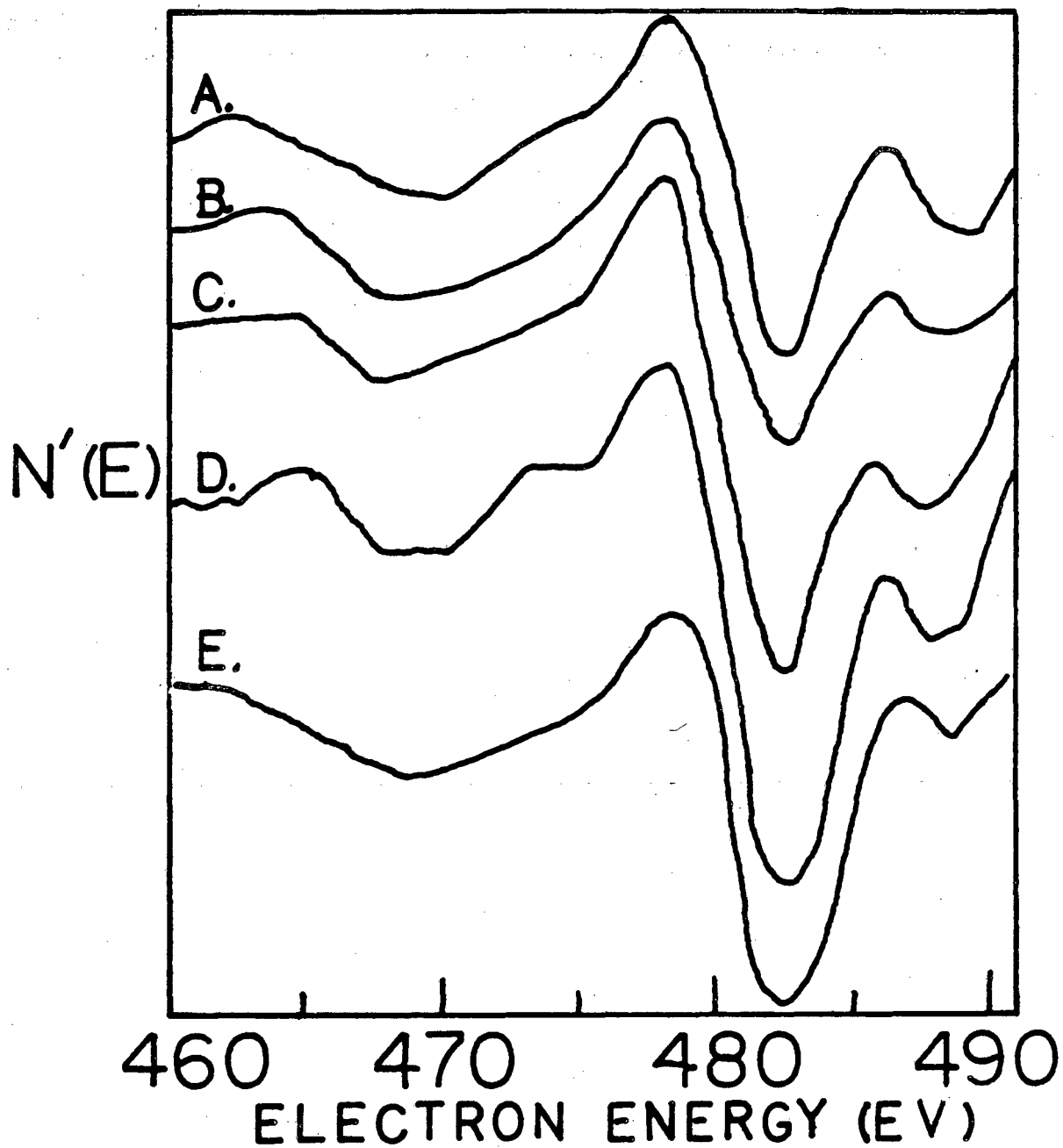
XBL 806-10540

Fig. V-22. Details of Ti-O Auger features for cases A, B, and C of Fig. 21.

visible as the decreased upward peak at 478 eV. Details of the oxygen peak shape are given in the spectra of Figure V-23; taken with a 2 V p-p modulation. The unique oxygen feature of the perchlorate-illuminated surface is the upward peak at 473 eV. This feature is even more evident in N (E) spectra. Knotek⁵¹ has reported a similar peak shape on a TiO₂ surface exposed to water vapor and aged in vacuo. However, the added O signal in the perchlorate-illuminated surface is in approximately the same proportion to the silicon signal as is found in published spectra of SiO₂.⁵² Legaré et. al.⁵³ reported a strikingly similar oxygen peak shape in an Auger spectrum of air-oxidized silicon. They ascribed the unusual peak to a bulk plasmon in SiO₂.

Photocatalytic systems have been described in analogy to photoelectrochemical cells with separate parts of the catalyst serving as anode and cathode. In the absence of metallic surface impurities the possible composition of the cathodic regions on SrTiO₃ is unclear. Small portions of the surface which are unusually highly reduced could allow photogenerated electrons to tunnel through the thinner depletion layer and reduce species in the electrolyte. A Scanning Auger Microprobe map of the oxygen concentration of a crystal which had been illuminated in 10 M NaOH showed no such localized gross reduction of the surface, with a spatial resolution of ~3 μ .

The presence of carbon contamination on SrTiO₃ surfaces raises the question of whether a carbonaceous species, rather than water, is oxidized during hydrogen photogeneration on Pt-free crystals, where difficulties with detection of slow oxygen production and the low photoactivity leave the issue unresolved. However, as stated before, addition



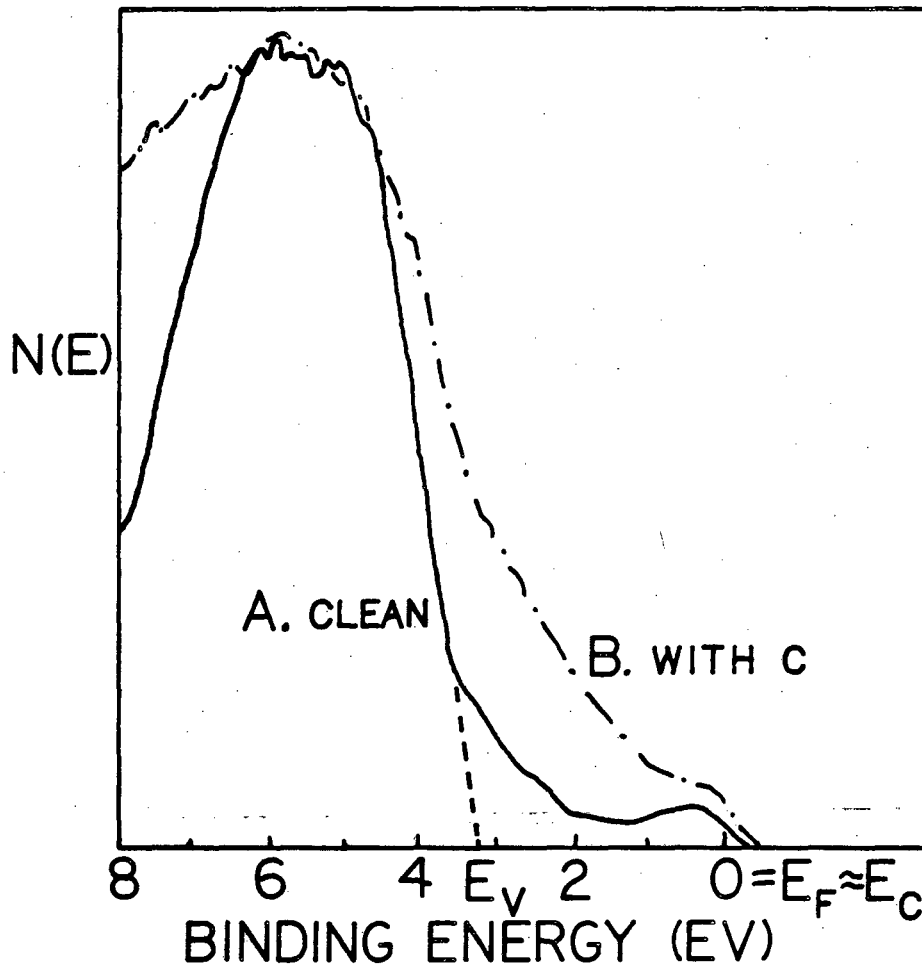
XBL 808-11545

Fig. V-23. Details of low energy portion of oxygen Auger spectrum of SrTiO₃ crystals; A) Ar⁺ sputtered, B) illuminated in 7 M-water, C) illuminated in 30% NaOH, D) illuminated in 10 M NaClO₄, E) illuminated in 1 M H₂SO₄. Inflection point of main oxygen peak at 501 eV.

of likely carbonaceous species to the electrolyte caused no significant acceleration of hydrogen production. The presence of carbon monolayers on SrTiO_3 shows the need for caution in evaluating photoreactions where the total product yield is on the order of one monolayer or less.

Carbon may play the role of a catalyst, instead of a reactant, in some photoassisted reactions on titanium oxides. Frank *et. al.*⁵⁴ have reported evidence that a state lying about 1.2 eV above the valence band mediates electron transfer from TiO_2 electrodes to certain redox couples. Photoelectron spectroscopy⁵⁵ has detected only one surface state within the energy gap on clean TiO_2 surfaces. This state, ascribed to Ti^{3+} , lies 0.6 eV below the conduction band (see Figure VII-5), too cathodic to perform the chemistry reported by Frank. Figure V-24 shows the UPS spectrum of Ar-sputtered SrTiO_3 before and after contamination with ~1 monolayer (by Auger) carbon through pyrolysis of acetylene. The carbon layer leads to considerable emission within the bandgap, implying the existence of filled states. The spectrum is relatively formless, and the vacuum-prepared carbon layer may be quite different from that which forms in aqueous solution. However, in light of the ubiquity of carbonaceous species on water-exposed SrTiO_3 and the lack of photoemission evidence for other surface states in the proper energy range to explain Frank's chemistry, electron transfer in that case may proceed through a carbonaceous surface species.

The results of the Auger analyses are essentially negative - no detectable change in surface composition correlates with photoactivity for hydrogen production or the lack thereof. This indicates that the effects of high hydroxide concentrations in augmenting photoactivity are



XBL 808-11544

Fig. V-24. Effect of C contamination on UPS spectrum of SrTiO_3 .

due to the electronic structure of the electrolyte itself or to surface modifications undetectable by Auger such as specific types of hydroxylation. The limitations of the techniques used here must be kept in mind. Auger spectroscopy is not as sensitive to subtle changes in surface oxidation states as are photoelectron spectroscopies. The transfer of the crystals through air may have obscured oxidation state changes. The necessity of rinsing the crystals prior to Auger analysis may have obliterated significant changes in stoichiometry. To properly utilize surface analytical techniques one should study photoactivity at the gas-solid interface. However, no activity was seen for the dissociation of water vapor on NaOH-free SrTiO_3 at room temperature. The results listed here do, however, raise some possibilities of improving the yield of gas-surface photoreactions as will be noted in the General Discussion.

REFERENCES

1. V.E.Henrich, G. Dresselhaus, and H.J. Zeiger, Phys. Rev. B 17, 1908 (1971).
2. H.H. Kung, H.S. Jarrett, A.W. Sleight, and A. Ferretti, Jour. Appl. Phys. 48, 2463 (1977).
3. M.Marezio, D. Tranqui, S. Lakkis and C. Schlenker, Phys. Rev B 16, 2811 (1977).
4. S. Ferrer and G.A. Somorjai, Surf. Sci., 94, 41 (1980).
5. D.M. Tench and D.O. Raleigh, in Electrocatalysis on Non-metallic Surfaces, NBS Spec. Pub. 455, 1976, p. 229.
6. J.C. Hemminger, R. Carr, and G.A. Somorjai, Chem. Phys. Lett. 57, 100 (1978).
7. J.C. Hemminger, R. Carr, W.J. Lo, and G.A. Somorjai, in Interfacial Photoprocesses: Energy Conversion and Synthesis, M.S. Wrighton, ed., Advances in Chem. Series No. 184, 1980.
8. H.J. Krebs and J. Lueth, Ber. Kernforschungsanlage Jülich [Conf], Jül-Conf-26, 135 (1978).
9. H. Van Damme and W.K. Hall, J. Am. Chem. Soc., 101, 4373 (1979).
10. J.B. Peri, J. Phys. Chem., 70, 2937 (1966).
11. R.C.Weast, ed., Handbook of Chemistry and Physics, Chemical Rubber Co., Cleveland, 1969, p. D-61.

12. R.B. Fischer and D.G. Peters, Quantitative Chemical Analysis, W.B. Saunders, Philadelphia, 1969, pp. 834-5.
13. R.N. Peacock, *J. Vac. Sci. Technol.* 17, 330, (1980).
14. S. Ferrer and G.A. Somorjai, submitted to *Phys. Rev. Lett.*
15. A.E. Paladino, L.G. Rubin, J.S. Waugh, *J. Phys. Chem. Solids* 26, 391 (1965).
16. Y.W. Chung, Ph.D. Thesis, U.C. Berkeley, 1977.
17. F.V. Hanson and M. Boudart, *J. Catal.* 53, 56, (1978).
18. A.J. Nozik, *Ann. Rev. Chem.* 29, 189 (1978).
19. M.S. Wrighton, P.T. Wolczanski, and A.B. Ellis, *J. Solid State Chem.* 22, 17 (1977).
20. M.S. Wrighton, A.B. Ellis, P.T. Wolczanski, D.L. Morse, H.B. Abrahamson, and D.S. Ginley, *J. Am. Chem. Soc.* 98, 2774 (1976).
21. A.J. Nozik and R.R. Chance, personal communication.
22. C.J. Huang, Ph.D. Thesis, Case Western Reserve University, 1976.
23. H. Metiu, personal communication.
24. K.B. Yatsimirskii, *Izvest. Akad. Nauk SSSR, Otdel. Khim. Nauk*, 453 (1947), 398 (1948).
25. L. Pauling, The Nature of the Chemical Bond. 3rd ed., Cornell Univ. Press, Ithaca, 1960, p. 514.

26. E.W. Washburn, ed. Int. Crit. Tables, McGraw-Hill, N.Y., 1928, p. III-273.
27. R.C. Neville and C.A. Mead, *J. Appl. Phys.* 43, 4658 (1972).
28. E. Knecht and E. Hibbert, *J. Soc. Chem. Ind.*, 30, 396 (1911).
29. J. Muhlebach, K. Müller, G. Schwarzenbach, *Inorg. Chem.* 9, 2381 (1970).
30. M. Pourbaix, Atlas of Electrochemical Equilibria in Aqueous Solutions, Pergamon Press, 1966.
31. M.S. Wrighton and J.M. Bolts, personal communication.
32. H. Reiche, W.W. Dunn, and A.J. Bard, *J. Phys. Chem.* 83, 2248 (1979).
33. D.B. Sepa, A. Damjanovic, and J. O'M. Bockris, *Electrochim. Acta* 12, 746 (1967).
34. M.F. Weber, Electrocatalytic Activity and Surface Properties of Tungsten Bronzes, Ph.D. Thesis, Iowa State University, 1977, p. 76.
35. S. Sato and J.J. White, *J. Phys. Chem.*, 70 131 (1980).
36. T. Kawai and T. Sakata, *Nature*, 282, 283 (1979).
37. B. Kraeutler and A.J. Bard, *J. Am. Chem. Soc.*, 100, 5985 (1978).
38. R.E. Schwerzel, E.W. Brooman, H.J. Byker, E.J. Drauglis, D.D. Levy, L.E. Vaaler, and V.E. Wood, in Photoeffects at

Semiconductor-Electrolyte Interfaces, A.J. Nozik, ed., ACS Symposium Series #146, 1981, p. 191.

39. A.H. Boonstra and C.A.H.A. Mutsaers, *J. Phys. Chem* 79, 2025 (1975).
40. G.N. Schrauzer and T.D. Guth, *J. Am. Chem. Soc.* 99, 7189 (1977).
41. M. Tomkiewicz, *J. Electrochem. Soc.* 126, 1505 (1979).
42. M.A. Butler and D.S. Ginley, *J. Electrochem. Soc.* 125, 228 (1978).
43. E. Yeager, W.E. O'Grady, M.Y.C. Woo, and P. Hagans, *J. Electrochem. Soc.*, 125, 348 (1978).
44. A. Hubbard, R. Ishikawa, J. Katekaru, *J. Electroanal. Chem.*, 86, 271 (1978).
45. P.N. Ross, Jr. *Surf. Sci.*, 102, 463 (1981).
46. W.J. Lo, Ph.D. Thesis, U. Calif., Berkeley (1978).
47. F.J. Szalkowski, Ph.D. Thesis, U. Calif., Berkeley, 1973, p. 66.
48. T.W. Haas, J.T. Grant, G.J. Dooley III, *J. Appl. Phys.*, 43, 1853 (1972).
49. R.E. Weber, *R-D Magazine*, Oct. 1972.
50. P.N. Ross, Jr., unpublished data.
51. M.L. Knotek, in "Proc. Symp. on Electrode Materials and Processes for Energy conversion and Storage", eds. J.D.E. McIntyre, S. Srinivasan, and G. Will (Proceedings, Vol. 77-6, The Electrochem.

Soc., Princeton, NJ, 1977).

52. Handbook of Auger Electron Spectroscopy, 2nd ed., Physical Electronics Industries, Eden Prairie, Minn., 1976.
53. P. Legaré, G. Maire, B. Carrière, J.P. DeVille, Surf. Sci., 68, 348 (1977).
54. S.N Frank and A.J. Bard, J. Am. Chem. Soc., 97, 7427 (1975).
55. Y.W. Chung, Ph.D. Thesis, Univ. Calif. Berkeley, 1977.

Chapter VI: LEED-Auger Studies of Ultra-Thin Pd and Au Films on Graphite, α -Al₂O₃, and TiO₂. Film Structure and Thermal Intermetallic Compound Formation.

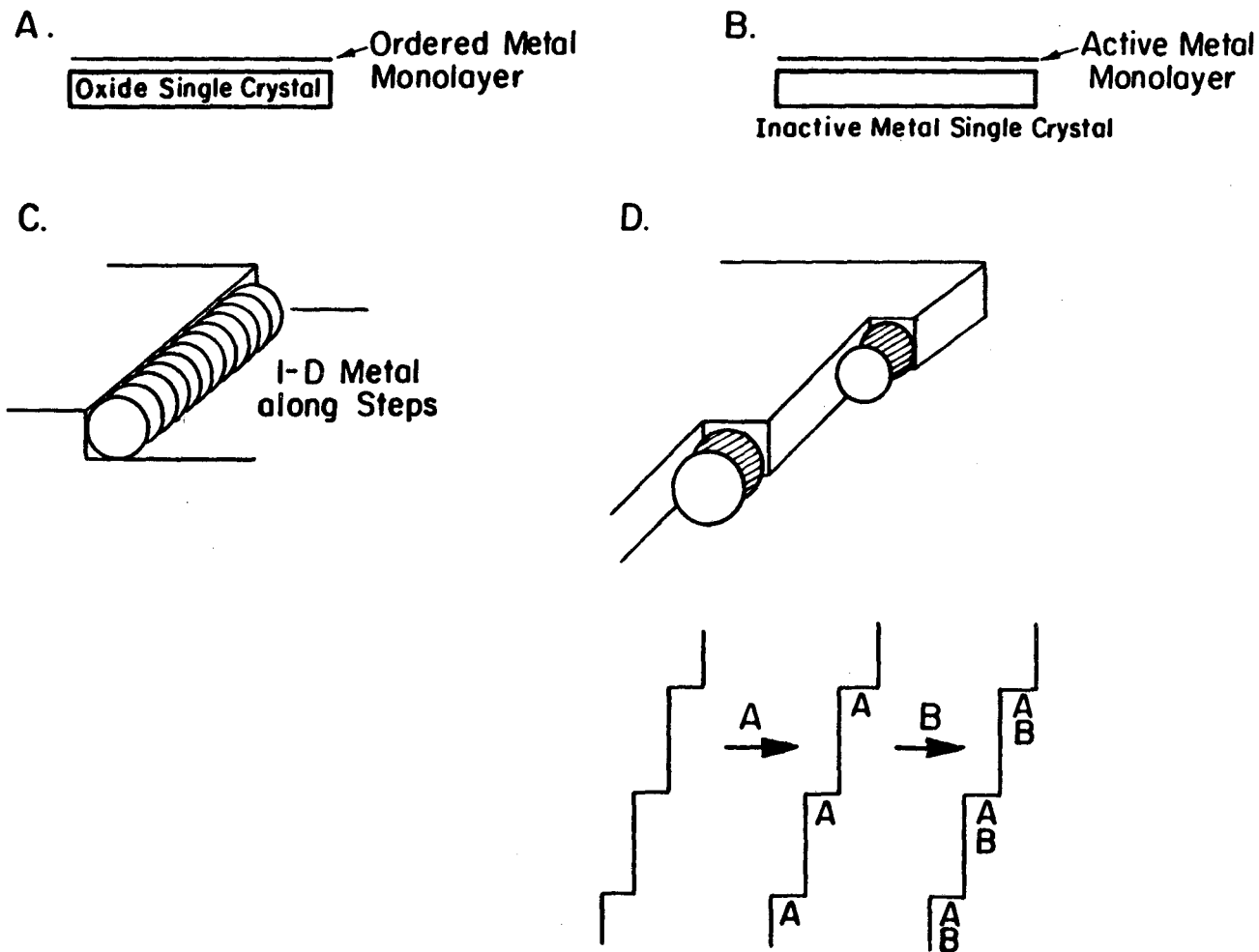
VI-1 Introduction

In recent years scientists investigating heterogeneous catalysis by metals have followed two major experimental paths. Some have worked with actual industrial supported catalysts consisting of sub-micron diameter metal particles dispersed over porous pellets of alumina or silica. Others have studied reactions on model catalysts consisting of single crystals of catalytically active metals. Those working on metal single crystals cannot control the types of atomic-scale defect sites present on their catalysts. Those working on metal single crystals must consider the question of just how well their model represents real supported catalysts. In some instances ^{1,2} the choice of oxide substrate has been shown to have a profound influence on the chemisorption and catalytic activity of supported metal particles. Both metal-metal oxide chemistry and morphology appear to play a role in the substrate dependence. Even when supports are chemically inert, differences between the electronic structures of small metal particles, metal monolayers, and large metal single crystals may be of catalytic significance. Some types of catalysis require both metal and oxide sites. As shown in the previous chapter, addition of noble metals to photoactive oxides can increase their photactivity manyfold. Other dual-functional catalysts are of great technological importance for catalytic hydrocracking. The need for well-characterized metal-on-oxide model catalysts is clear.

The work to be described in this chapter was part of an effort to grow ordered supported model catalysts. Several ideal types of model catalysts are shown in Figure VI-1. In types A and B well-ordered monolayers of active metals are grown on single-crystal substrates. In types C and D one hopes to use enhanced binding of metal atoms to step and kink sites on the substrate to grow metal particles with well defined geometries. The postulated ultimate in catalyst control is illustrated in Figure VI-1-D. Here sequential deposition of two metals would lead to highly dispersed bimetallic clusters. Comparison of the chemistry of kink-A-B and kink-B-A clusters would do much to clarify the effects of metal-supported and metal-metal interactions.

While Figure IV-2 showed the types of film geometries desired for catalytic studies, Figure VI-2 summarizes three models for the actual growth of evaporated films on uniform substrates. All three assume that surface diffusion is sufficiently rapid compared to the deposition rate that equilibrium surfaces will be achieved. Under these conditions the growth mode will be governed by the relative surface free energies (excess free energy required to produce a given area of new surface from bulk material) of the substrate and deposit and by the strength of interaction between the two materials and their degree of lattice mismatch. If the surface free energy of the deposit material is low and there is close lattice matching, layer-by-layer (Frank-Van der Merwe)³ growth can occur. This mode is also possible with a high surface free energy deposit if the interaction energy between the substrate and deposit is strong and attractive. If the deposit surface free energy is high and the interaction is weak, island growth (Volmer-Weber mode)⁴ is expected. A somewhat intermediate (Stranski-Krastanov)⁵ mode can occur

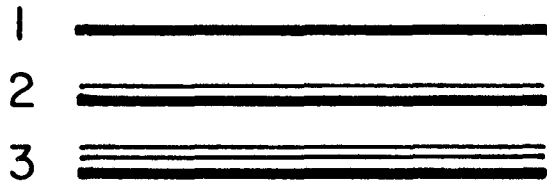
Fig. VI-1. ORDERED SUPPORTED CATALYSTS



XBL 78I-4457

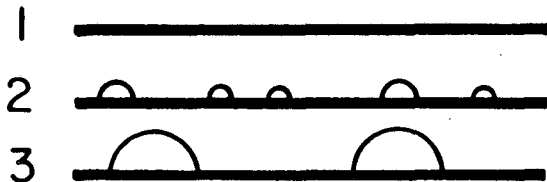
Fig. VI-2. MODES OF FILM GROWTH

A. Layer by Layer (Frank-Van der Merwe)



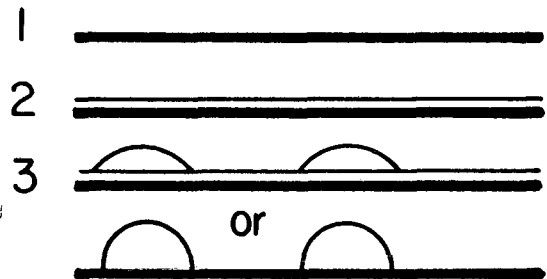
$\sigma_{\text{dep}} < \sigma_{\text{sub}}$
 and/or
 σ_{sd} large and negative,
 close match between substrate
 and deposit crystal lattices

B. Island Growth (Volmer-Weber)



$\sigma_{\text{dep}} > \sigma_{\text{sub}}$
 σ_{sd} small

C. Stranski-Krastanov



σ_{sd} large and negative,
 lattice mismatch induces
 strain

XBL 781-4456

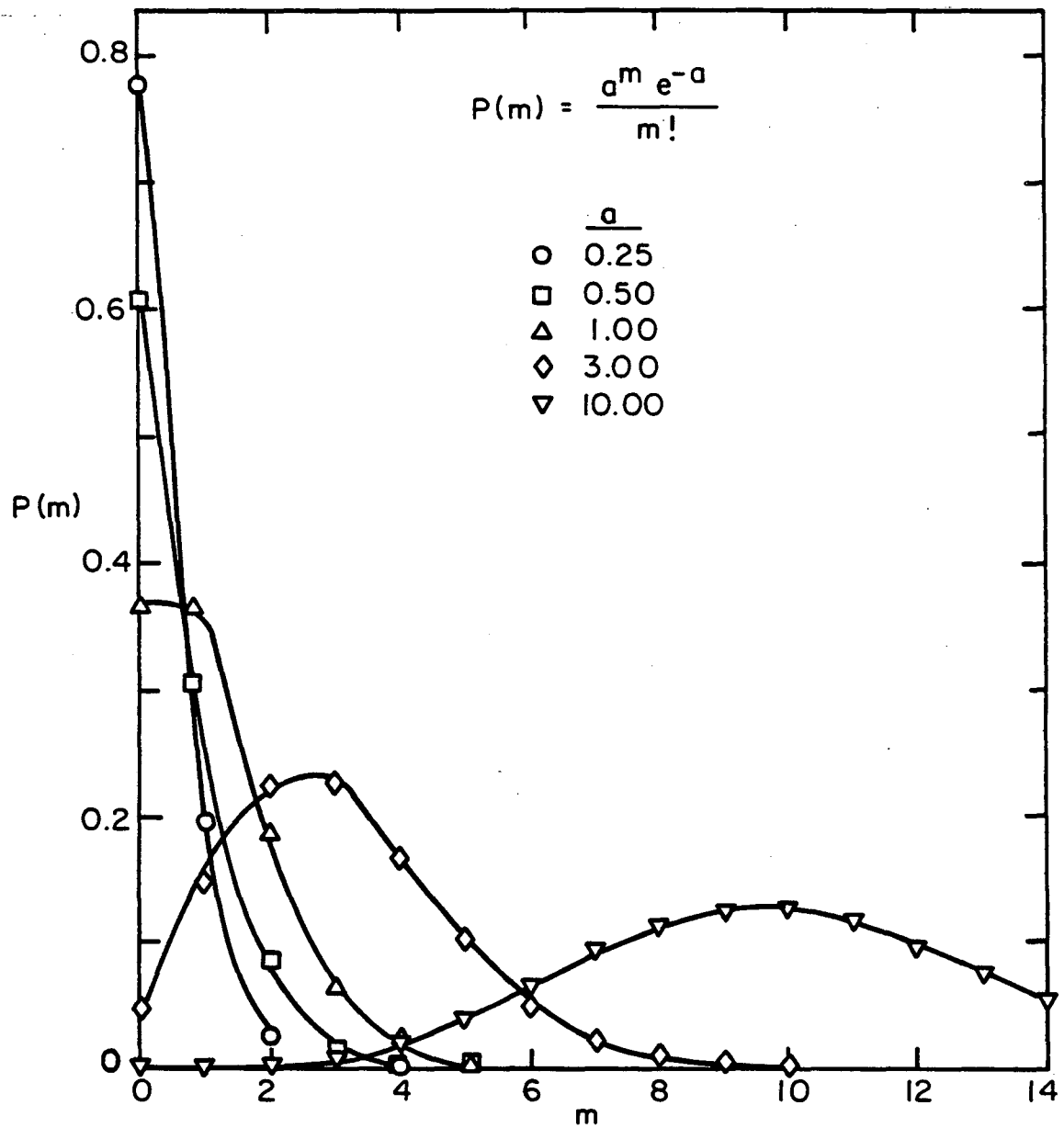
if the interaction is strong but the lattice mismatch is fairly large. In this case a monolayer may form in which the deposit takes on the unit mesh of the substrate surface structure. Continued growth of this pseudomorphic form to greater thicknesses would result in a severe lattice strain, and subsequent growth leads to island formation on top of the monolayer or even to island growth with breakup of the original monolayer. Numerous examples for each growth mode can be found in the literature, and Biberian⁶ has written an extensive review. Hydrocarbons, with very low surface free energies, tend to form ordered monolayers which give beautiful LEED patterns. Soft metals, such as Pb, tend to form ordered monolayers on other metals.⁷ Noble metals on refractory metals often give at least one smooth, ordered layer. Paraschevov et. al.⁸ have found that Pd on W(110) grows layer-by-layer with a surface temperature of 300° K but follows a Stranski-Krastanov mode at 840° K. The data for many metal-on-metal systems unambiguously indicates layer-by-layer growth, as clear breaks in slopes of Auger intensity vs. mass of metal deposited area observed (see Appendix I). Schmeisser et. al.⁹ have claimed monolayer growth of Ni on ZnO. However, the model by which they treated their data cannot adequately distinguish between different modes of film growth.

The three models discussed in the preceding section all assume that surface diffusion is rapid and equilibrium is reached. It is instructive to consider the opposite extreme where no diffusion occurs: "hit-and-stick" film growth. At room temperature growth of real films will lie between these extremes.

If one assumes a uniform flux of deposit molecules onto the substrate surface (which is achieved over ~80% of the deposit area formed by the evaporator used here) the probability of a deposit atom hitting a given binding site is equal for all binding sites and is independent of whether that site is empty, singly occupied, or multiply occupied. Under these conditions a Poisson distribution defines the number of sites with a given level of occupancy.^{10,11} The general Poisson distribution is

$$P(m) = [a^m e^{-a}] / m!$$

$P(m)$ is the probability of an event occurring m times. $a=np$, where p is the probability of a given event and n is the number of trials. In film formation, an "event" is a deposit atom hitting a particular surface site. Assuming a unit sticking coefficient, n is the total time integrated flux of atoms to the surface, and $p=(\text{number of surface sites})^{-1}$. Therefore a is the average number of monolayers which would be present on the surface if layer-by-layer growth occurred; it is also the number of monolayers which would be calculated using a mass measurement from a quartz crystal oscillator film thickness monitor or a calculation based on the flux from an effusion cell. Figure VI-3 shows the thickness distributions of hit-and-stick films with mean thicknesses from 1/4 to 10 monolayers. At a mean thickness of one monolayer the vacant sites and those with one adatom would be equal in number, and more than half this number of sites would have two adatoms. Pure Poisson distribution behavior is not to be expected for deposition onto surfaces at room temperature. Electron microscopy and associated diffraction studies have shown that surface diffusion is sufficiently rapid



XBL 818-6332

Fig. VI-3. Thickness distributions for random films of mean thickness a .

even at very low temperatures to allow some crystallinity in the deposit.¹² With a single crystal substrate above 300°C, films thicker than 100 Å often show excellent long-range order -- equilibrium morphology prevails at these temperatures and coverages. Over a substrate temperature range of 77-373°K micropoly-crystalline films with high surface areas tend to form in a compromise between equilibrium morphology and nucleation kinetics. Films grown at liquid helium temperature are highly disordered but show crystallinity on a very fine scale. A pure "hit-and-stick" mode of film growth thus never appears to occur in vacuum-grown films, but the Poisson limit is approached at lower substrate temperatures, and the model provides a good test for the ability of Auger analysis to distinguish between growth modes.

The surface free energies of metals exceed those of oxides by about 10 kcal/surface mole of metal atoms. In the absence of specific metal-metal oxide interactions one would expect evaporated films to grow primarily by island formation, in agreement with results from electron microscopy for most metal oxide systems. In a few systems, such as Os on silica,¹³ formation of very thin raftlike islands has been reported. The results presented here allow comparison of the behavior of Al₂O₃ (a stable, rather unreactive compound) and TiO₂ (rutile, an easily reduced oxide), with Au (a rather inert metal) and Pd (a more easily oxidizable metal and one very susceptible to the formation of intermetallic compounds).

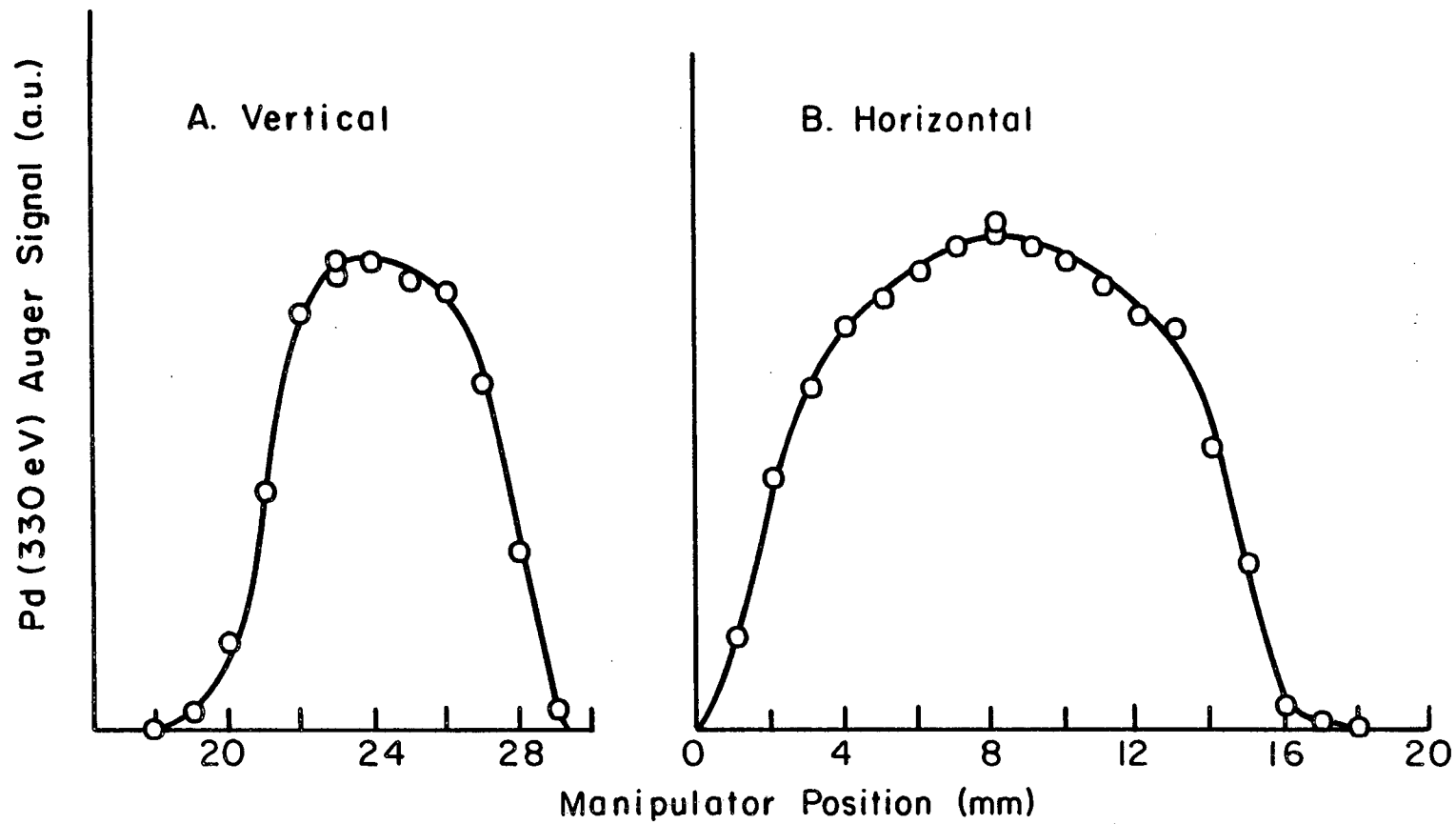
VI-2 Deposition of Pd and Au on Graphite: Particle Size Effects

Highly oriented pyrolytic graphite, (HOPG), obtained through the generosity of Dr. A. Moore at Union Carbide, Parma, Ohio, served as the film substrate during the initial testing of the evaporator. The material could be easily cleaned in vacuo and, following deposition of thick layers of metal, the substrate could be removed from vacuum and the surface layer peeled off to expose a fresh substrate without demounting the target heater assembly. Only the c-axis of HOPG is highly oriented,¹⁴ i.e. the graphite planes are strictly parallel. There is considerable disorder in the A,B-axis orientation. LEED patterns obtained from HOPG sputter-cleaned and annealed in UHV showed only a ring structure with no spots of higher intensity along the ring. Such spots of intensity would be indicative of partial ordering of the A-B axes over the range of the coherence width of the LEED beam, approximately 100Å.

Vertical and horizontal profiles of the Pd spot thrown by an evaporator are shown in Figure VI-4. This evaporator used a tungsten basket instead of an effusive source, but employed the same collimators incorporated in the final design. After deposition of Pd, the graphite substrate was moved within the analysis plane of the CMA and the Pd Auger peak-peak height plotted against the sample position. Although the design goal of a central region of absolutely constant flux was not achieved, within the central 50% of the spot along either axis the Auger peak height ratio varied by 10% or less.

No order was observed by LEED for Pd or Au films grown on graphite, either before or after annealing. Film thicknesses varied from 1/10 to

Fig. VI-4. Profiles of evaporated Pd spot.

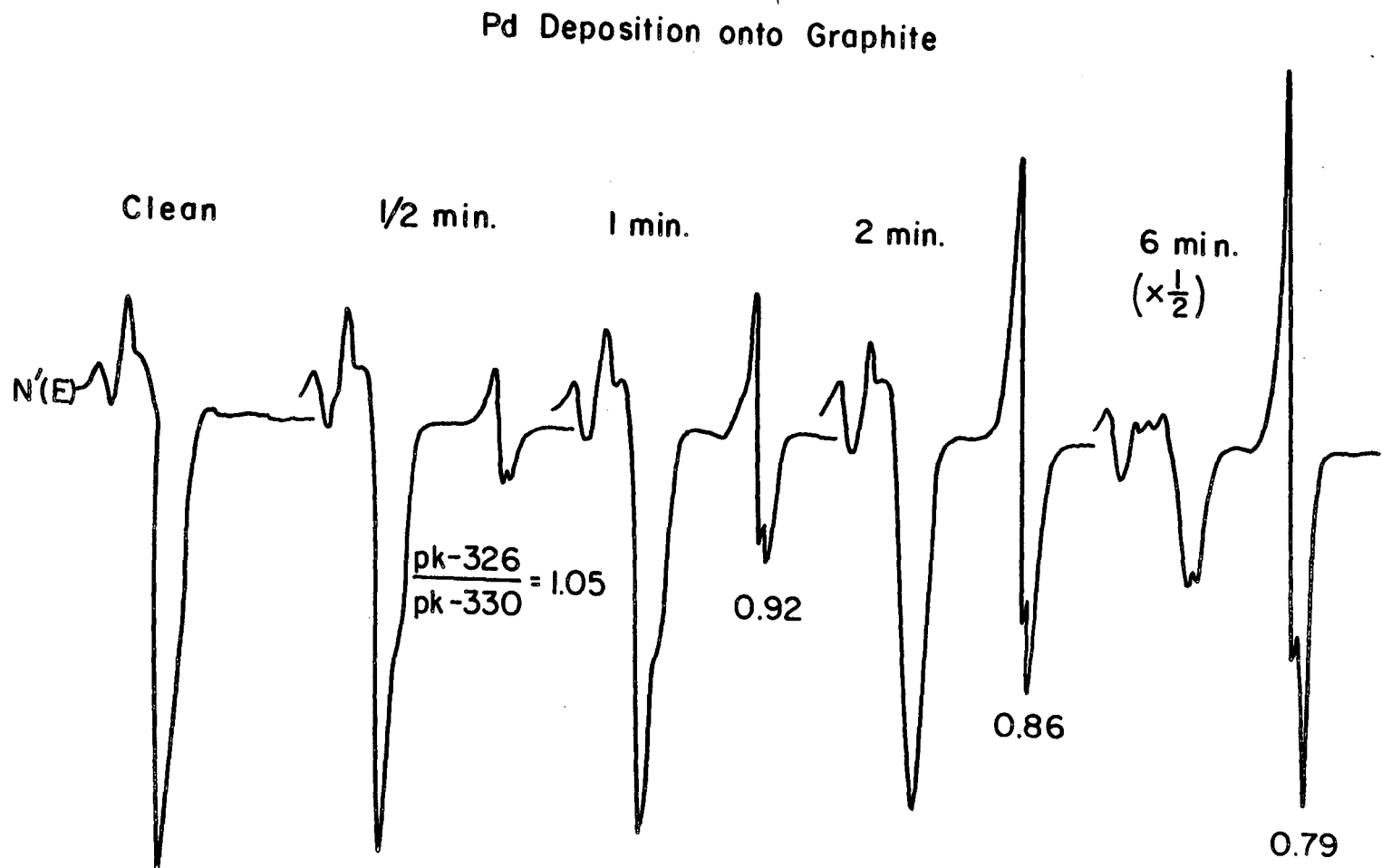


XBL 818-6333

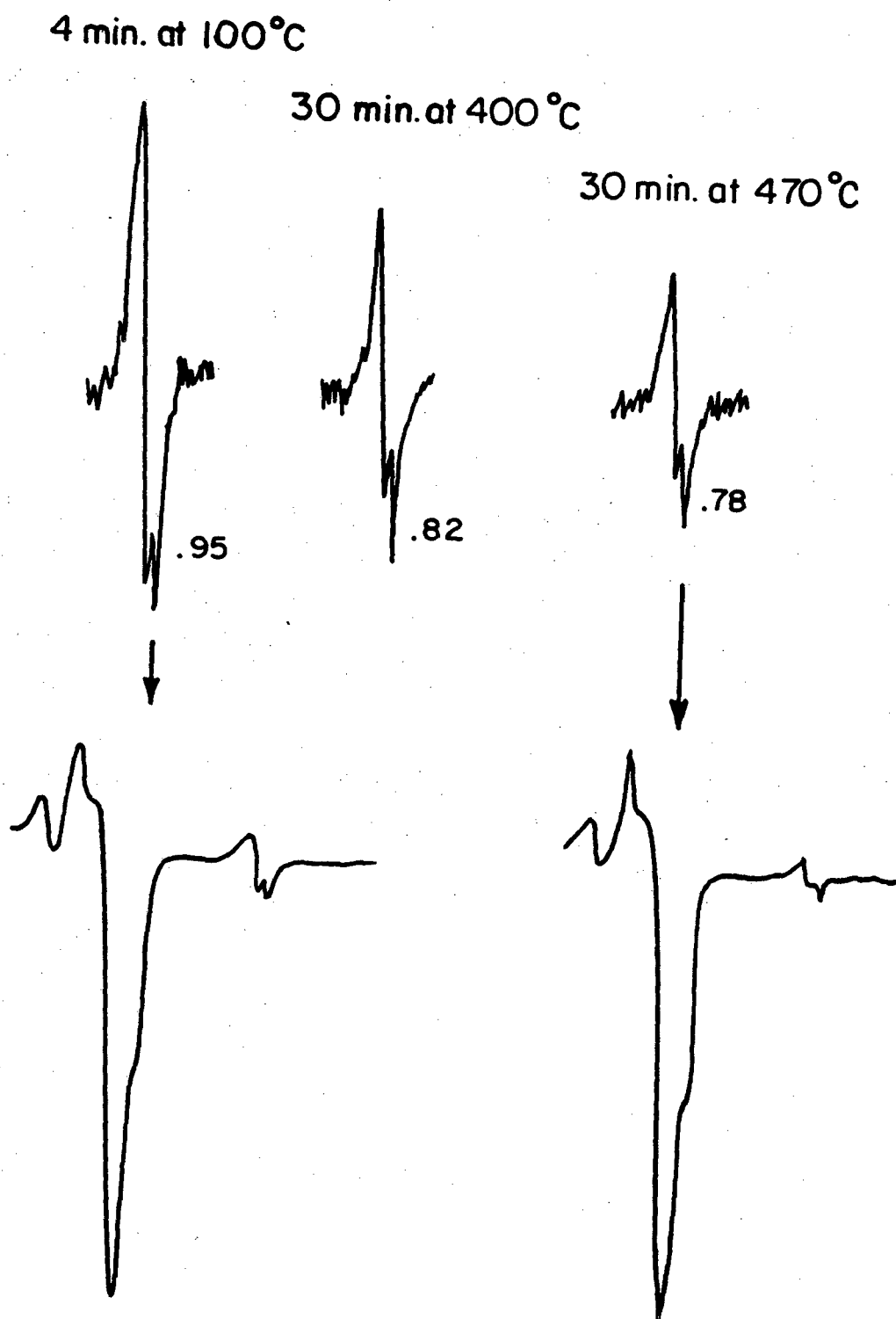
several monolayers, estimated by comparison of the Pd signal intensity with that obtained from a Pd foil standard. A palladium Auger peak at 279 eV overlaps with the C 272 eV peak, making determination of film thickness by attenuation of the substrate Auger peak well-nigh impossible at Pd coverages $> \sim 0.5$ monolayers.

The shape of the Pd (330 eV) $M_{5N_{4,5}}N_{4,5}$ Auger peak changed (1) with the amount of Pd deposited onto the surface (Figure VI-5) and (2) with the thermal treatment of the deposit (Figure VI-6). The change is most easily seen as the shift in the vertical position of the local minimum (tweak) of the $N'(E)$ curve at ~ 4 eV lower kinetic energy than the overall minimum at 330 eV. This can be numerically represented as the ratio of the distances from the maximum to the local minimum and to the absolute minimum, i.e. the peak-to-tweak to peak-to-peak height in Figure VI-7. This ratio varied from 1.05 for $\sim 2\%$ of a monolayer Pd to 0.75 for thick deposits and for the pure Pd foil. The effect was not instrumental in nature - the time constants in the electronics used were sufficiently small that no amplitude-dependent modification of peak shape occurred. Changing the electron multiplier gain to change the signal reaching the lock-in amplifier had no effect on the peak shape change. The effect was also shown not to be the result of electron-beam induced modification of the deposit. Similar results were obtained when one spot in the center of the deposit was monitored as successive doses of Pd were added to the surface (squares in Fig. VI-7) or when the edge of a thick deposit was studied in several places which had received different total Pd doses (circles in Fig. VI-7).

Fig. VI-5. Variations of Pd Auger peak shape with deposition time.



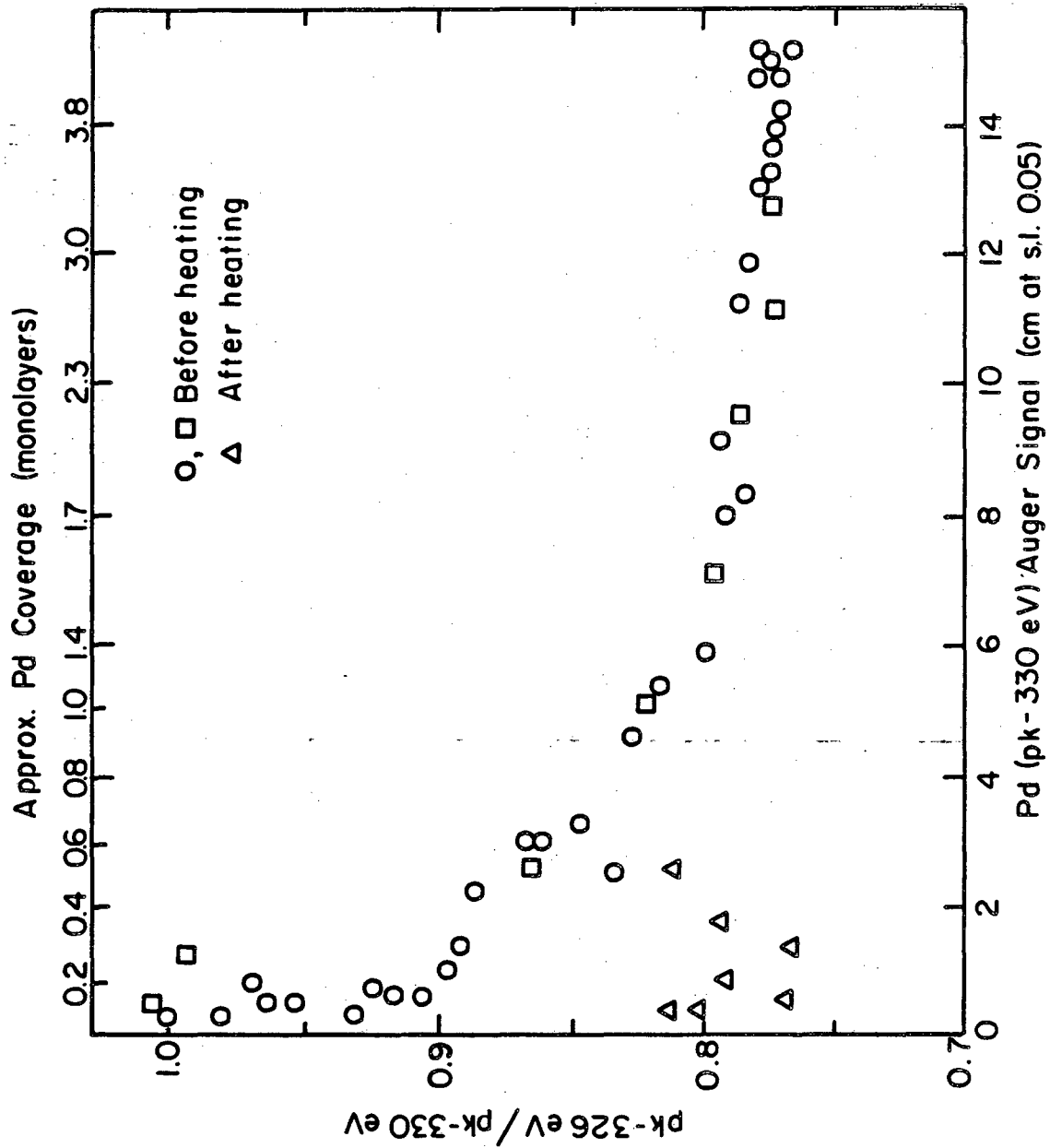
XBL 818-6334



XBL 818-6335

Fig VI-6. Change of Pd Auger peak shape upon annealing Pd film on graphite.

Fig. VI-7. Peak-to-tweak ratio as a function of total Pd Auger signal. Details of key in text.



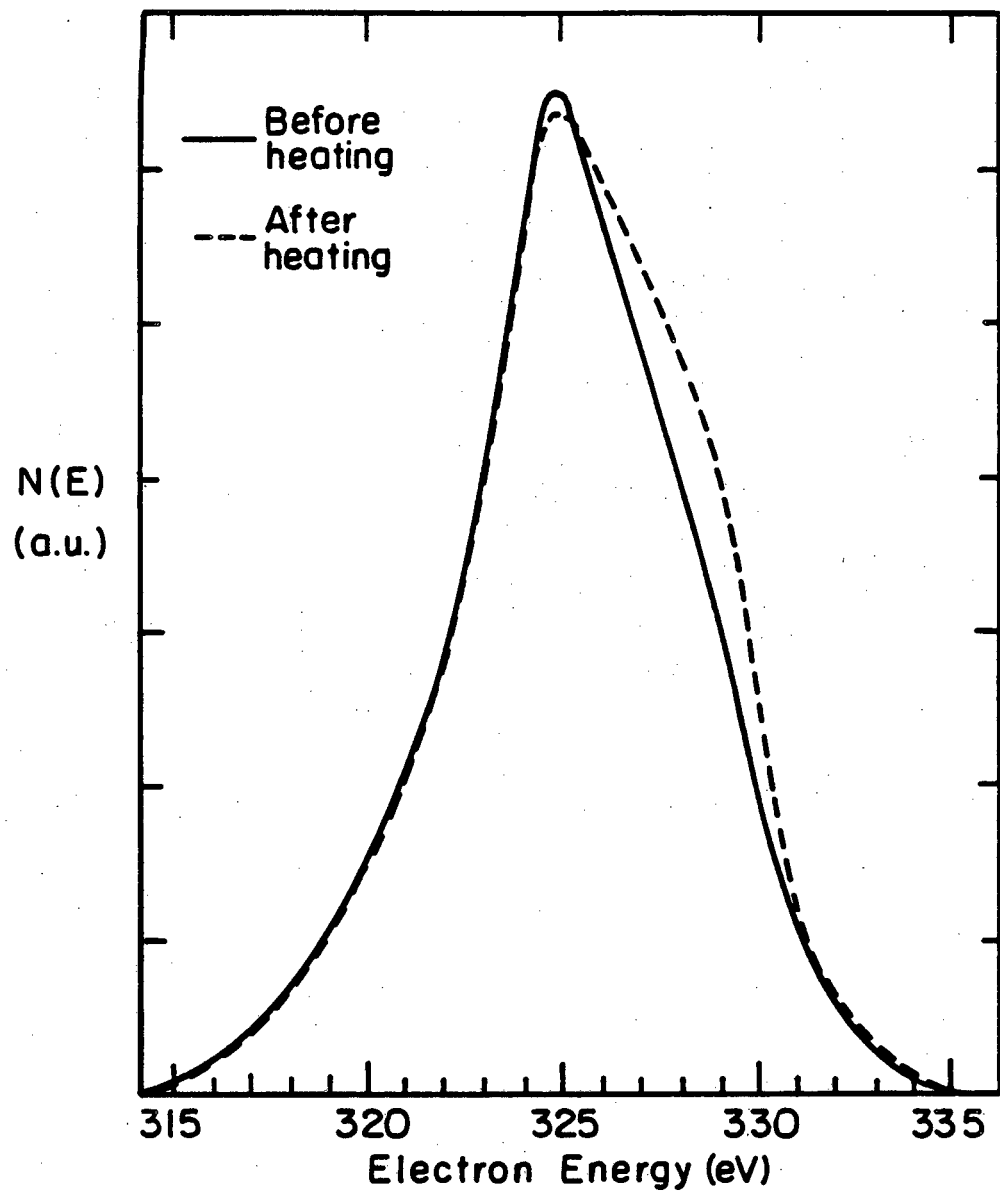
XBL 818-6318

Figure VI-6 shows the effect of heating on the Pd peak shape. After the Pd was deposited at room temperature and Auger spectra were taken the graphite block was radiatively heated by the tungsten holder. The sample was then cooled to room temperature and Auger spectra were taken. Heating to 300°C for four minutes caused a small change (from 1.0 to 0.95) in the tweak-to-peak ratio. After 1/2 hour at 470°C the ratio had dropped to 0.78 at the same spot on the surface, almost to the bulk Pd value. As shown in Figure VI-7, the tweak-to-peak ratio for a given peak-to-peak height is also considerably lower after heating. The 1/2 hour anneal at 470°C also reduced the Pd peak-to-peak height at a given location to 60% of its value before heating. Such behavior is consistent with the sintering of the Pd deposit into larger, isolated particles either through coalescence of small particles into larger ones or through Ostwald ripening (migration of individual atoms from smaller to larger particles).

The Pd peak shape change indicates a modification in the band structure of Pd as a function of its physical dispersion on graphite. Thick or highly annealed deposits show bulk behavior, while submonolayer films on room temperature graphite exhibit a unique Auger shape. While the tweak-to-peak ratio is a sensitive indicator of this phenomenon, it, being derived from a derivative curve, is of no immediately obvious physical meaning. The N(E) curves before and after annealing were therefore derived by graphical integration of the derivative curves which gave tweak-to-peak ratios of 0.97 and 0.76, respectively. The two curves were not taken on the same spot on the surface, rather, they are spots giving nearly equal peak-to-peak values. There was approximately 0.1 monolayer Pd at the point surveyed by the "before heating" spectrum.

The derivative spectra were graphically integrated, the downward-sloping background due to secondary electrons was subtracted, and the maximum values were normalized and brought to coincidence in energy to yield the results shown in Figure VI-8. The $N(E)$ spectrum taken before heating, which is characteristic of high tweak-to-peak ratios in the derivative spectrum, is almost symmetric and has a full width half maximum of 6.5 eV. The $N(E)$ spectrum taken after heating shows a pronounced shoulder on the high kinetic energy side and has a FWHM of 7.6 eV. Both spectra are considerably broader than either the modulation voltage used for phase-locked detection (2V p-p) or the CMA resolution (1.6 V at 330 eV).

The change in Pd derivative peak shape can be understood in terms of the broadening of the band structure as progressively larger aggregates of Pd atoms are formed. Since Auger electron emission is a three-level process, unambiguous correlation of peak shape changes with specific alterations in band structure are generally not possible. The " $M_5N_{4,5}N_{4,5}$ " Auger electron is emitted when a hole created in the band derived from $3d_{5/2}$ orbitals is filled by an electron from the band derived from 4d orbitals, with the resultant release of energy expressed by the ejection of an Auger electron from the latter band. Although the peak is labelled " $M_5N_{4,5}N_{4,5}$ ", the major splitting is due to some involvement of the M_4 sub-level, which lies 4.7 eV below the M_5 .¹⁵ The initial state of the Auger transition involves one hole. The final state involves two holes, and the interaction between these holes can remove degeneracies in the final state leading to very complex spectra. Since the strength of these interactions may be altered by the presence of neighboring atoms, one cannot conclude with certainty that a change in Auger peak shape corresponds to a change in the density of state



XBL 818-6319

Fig. VI-8. $N(E)$ Auger peaks for Pd on graphite before and after annealing.

distribution of the neutral metal or metal atom. Bearing this caveat in mind, one should consider the changes in band structure which might explain the observed Auger peak shape change. The centers of the M_4 and M_5 (3d) levels in Pd are split by 4.7 eV in the bulk metal¹⁵. Since these subshells lie 330 eV below the Fermi level, they will be less sensitive to chemical effects than the $N_{4,5}$ levels. The 4d band of bulk palladium has a width of 4eV.¹⁶ This broad bandwidth is due to splitting induced by spin-orbit and crystal field effects.¹⁷ The spin-orbit splitting decreases as one goes from bulk metal to free atom.¹⁸ The crystal field splitting will also in general decrease with decreasing particle size following the smaller proportion of fully coordinated atoms, but this splitting will depend rather strongly on the actual geometry of small particles. The width of the observed $N(E)$ Auger spectrum will be governed by the width of the self-convolution of the 4d-band, with the $M_5N_{4,5}N_{4,5}$ emission approximately twice as wide as the 4d band. The overlap of the $M_4N_{4,5}N_{4,5}$ transition will mix in a second peak of approximately the same width, but displaced ~5 eV towards higher energies. The double-involvement of the 4d band in the Auger emission smears out the actual structure of the d-band. Smaller contributions to the Auger width will come from the modulation voltage (2V), the analyzer resolution (1.6 eV), and interactions with the graphite substrate. Though the general broadening of the Auger emission from submonolayer Pd deposits agrees with expectations of band structure changes, one cannot obtain specific information about the shape of the d-band density of state curves. The Auger peak shape change, however, is a very convenient and sensitive fingerprint for the small-particle electronic structure which has been better defined by photoemission studies and

predicted by calculations.

The results of the SCF-X α -SW calculations of Messmer et. al.¹⁹ indicate that aggregates of more than 10 metal atoms should have essentially the same electronic structure as the bulk metal, and that even smaller particles (down to ~ 4 atoms) would have largely bulk-like behavior. However, the extended H \ddot{u} ckel and CNDO results of Baetzold et. al.²⁰ indicate that much larger particles, on the order of 100 atoms, are required before bulk-like electronic structure is obtained. They calculate a bulk 4d-bandwidth of 3.08 eV, and bandwidths of 2.65, 2.55, 2.42, 2.04, and 0.80 for clusters of 79, 67, 43, 19, and 2 atoms respectively. The same percentage of band narrowing, as seen in our Auger results, is calculated for a cluster of ~ 75 atoms, corresponding to a hemisphere ~ 16 Å in diameter, or ~ 6 atoms wide and three high. Since the Auger peak is broadened not only by the d-band width but by other factors, one would expect a smaller proportional broadening for the Auger peak than for the valence band photoemission peak for a given particle size. If so, the Pd particle size at 1/10 monolayer average deposition would be smaller than 16 Å in diameter.

Auger modeling of film morphology

Table VI-1 shows the percentages of the graphite surface covered by smooth Pd monolayers, 16 Å diameter Pd hemispheres, and 50 Å diameter Pd hemispheres which are consistent with the Pd 46 eV and Pd 330 eV peak heights and the attenuation of the C 272 eV peak as Pd is deposited onto the graphite (see Appendix I). The criterion for a good fit of the model surface morphology to reality is the consistency of coverages cal-

TABLE VI-1: Comparison of Monolayer and Island Models for Pd on Graphite

Dep. time	ml coverage		16A Islands % coverage			50A Islands % coverage			SD/mean			
	by		by			by			ml	o 16A	o 50A	
	Pd 46	C	Pd 330	Pd 46	C	Pd 330	Pd 46	C	Pd 330	ml	o 16A	o 50A
30 sec	.03	.14	.11	2.2	7	6.7	2.2	5	3	.61	.51	.42
1 min	.08	.38	.28	5.8	23	17.2	5.7	11.5	7.6	.62	.57	.36
2 min	.31	.67	.57	22	42	35	21	21	15	.36	.31	.18
										1.59	1.39	.96
4 min	.79		1.43	57		88	54		39	.41	.30	.23
6 min	1.16		1.73	84		106	74		47	.28	.16	.32
8 min	1.71		2.55	123		156	95		69	.28	.17	.22
										.97	.63	.77

culated from the Pd 46 eV, C 272 eV, and Pd 330 eV peaks, expressed as the ratio of the standard deviation to the mean of these values. None of the models gives a good fit, but the 50 Å diameter hemisphere model gives slightly more consistent results, even at the very low coverages where comparison of the Auger peak narrowing with Baetzold's calculations would indicate a smaller particle size. The Pd-C system is not very good for the determination of film morphology from Auger data. Overlap of C and Pd peaks makes C attenuation data unreliable at Pd coverages above $\sim 1/2$ monolayer. The 46 eV Pd peak is a $N_{4,5}N_{4,5}^0$ transition the intensity of which will depend very strongly upon the population of the 5s band. Baetzold's calculations indicate that the number of 5s electrons per atom is smaller for surface atoms than for those in the center of the cluster. One might then expect the Pd coverage calculated from the 46 eV peak height to be too low at low coverages. This is in fact found to be the case for treatment of the data, in all three models, but least so for the 50 Å model which gives the best fit.

Several photoemission studies support the contention that the Pd 4d-band of moderately large particles is narrower than that of bulk Pd. Eastman and Grobman,²¹ studying Pd films on silver, found bulk behavior for films of average thickness > 4 monolayers but pronounced narrowing of the d-band below 2 monolayers. Baetzold *et. al.*²⁰ found that the d-band width for Pd on amorphous carbon increased from 2.5 eV to 3.3 eV as the mean surface coverage increased from 5×10^{15} atoms/cm² to 10^{16} atoms/(cm² cross sectional area). These band widths are less than half the Auger peak widths reported here, and the change in width is larger in the photoemission work, indicating that the other factors do broaden the Auger peak substantially.

The photoemission results of others provide a much less ambiguous argument for band-narrowing at small particle sizes than do our Auger results. However, the Auger data does provide some new information. Our results are obtained on the smooth surface plane of highly oriented pyrolytic graphite rather than on the amorphous carbon films employed by Baetzold et. al.²⁰ In our experiments, interactions between the metal particles and substrate are thus likely to be much weaker, yet the d-band narrowing effect remains. The range of Pd atoms/(cm² cross sectional area) over which the tweak-to-peak Auger ratio changes is identical to the coverage range over which the d-band width changes on amorphous carbon despite the large difference in true surface area of the support. The Auger data show that sintering the deposit at moderate temperature causes a reversion to bulk-like behavior. The results indicate that specific binding of Pd to high energy sites on amorphous carbon is not necessary to the d-band narrowing and the production of highly dispersed Pd deposits on room-temperature carbon. The fact that an Auger peak shape change has been correlated with a well-documented change in d-bandwidth raises hope that studies of the catalytic consequences of the variable d-bandwidth can be carried out in a high pressure-low pressure system equipped with relatively inexpensive Auger apparatus rather than with the much more costly photoemission equipment. Pd and possible neighboring metals with similar Auger spectra such as Ag and Rh should be particularly suitable for such studies.

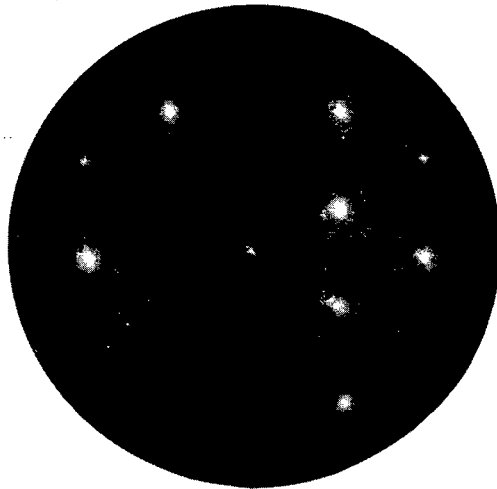
VI-3 Au and Pd on α -Al₂O₃

The basal (0001) plane termination of α -Al₂O₃ can thought of as an almost closest-packed plane of oxide ions with a nearest-neighbor

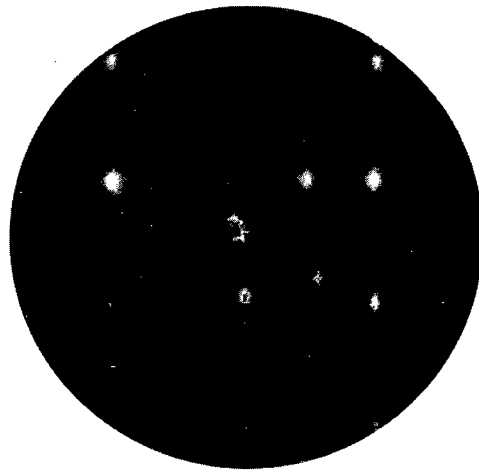
spacing of 2.75 Å. This distance is the same as the nearest-neighbor spacing in Pd (111). Al^{3+} ions fill 2/3 of the pseudo-octahedral holes. Due to the slight deviations from closest packing in the oxide ion layers, Al^{3+} reside on two planes between each pair of oxide planes, and there are two different Al-O bond lengths. One would expect that, in surface formation, the longer Al-O bonds would break, leaving half of the Al^{3+} associated with each ion layer. The (0001) $\alpha\text{-Al}_2\text{O}_3$ surface has 3-fold symmetry, with a unit mesh parameter of 4.76 Å. This is the spacing which would be expected to show up in low energy electron diffraction. For purposes of epitaxy the near-hexagonal net of oxygen ions spaced by 2.75 Å might be more important.

$\alpha\text{-Al}_2\text{O}_3$ is an electrical insulator, and electron-beam analysis technique can be used only if the yield of secondary electrons exceeds the incident beam current. The positive surface charging caused by excess secondary emission is self-limiting and causes few problems in analysis. When the primary beam energy drops below the secondary emission crossover point the negative surface charge deflects the probing beam, and analysis is impossible. The secondary crossover point of clean $\alpha\text{-Al}_2\text{O}_3$ was found to be about 80 eV, allowing LEED to be done with fair sensitivity to overlayer structures.

A LEED pattern for clean $\alpha\text{-Al}_2\text{O}_3$ (0001) is shown in Figure VI-9a. The unit mesh is consistent with the termination of the bulk structure. As had been reported by others,^{22,23} heating this surface above 900 °C caused the appearance of a $\sqrt{3}\times\sqrt{3}$ R 30° structure corresponding to an oxygen-poor surface. A LEED pattern for the $\alpha\text{-Al}_2\text{O}_3$ ($\bar{1}012$) surface is shown in Figure VI-9B. This surface has a quasi-rectangular unit mesh



A. (0001) 100 eV



B. ($\bar{1}012$) 190 eV

Fig. VI-9. LEED patterns for clean α - Al_2O_3 surfaces.

XBB 818-7906

with lattice parameters of $4.75 \times 5.2 \text{ \AA}$. Above $900 \text{ }^\circ\text{C}$ this surface develops a 1×2 structure, again due to oxygen loss.

Figure VI-10 shows the Auger spectrum of clean $\alpha\text{-Al}_2\text{O}_3$. No charging problems are seen on the clean surface. The Auger spectrum of alumina is theoretically favorable to the study of overlayer morphology because both a low-energy (54 eV)-short attenuation length ($\sim 5 \text{ \AA}$) and a high energy (1384 eV)-long attenuation length ($\sim 15 \text{ \AA}$) peak are present. In practice, the 54 eV peak is often obscured or severely distorted by nearby, more intense peaks from the overlayer metal. The $\alpha\text{-Al}_2\text{O}_3$ was very resistant to electron beam damage. Simultaneous mounting of Pd foil and $\alpha\text{-Al}_2\text{O}_3$ samples in the vacuum system allowed the determination of the relative Auger intensities of the two bulk materials. The Pd 330 eV peak had an intensity 1.54 times the O 503 eV peak of alumina. Taking an attenuation length of 9.5 \AA for Pd from the universal curve,²⁴ one calculates that one monolayer of Pd should yield 27% of the bulk Pd signal (Table VI-2). Such a calculation ignores the variation of the backscattering factor, which generally alters results by less than a factor of two. With an attenuation length of 12 \AA for the O (503) peak,²⁵ one monolayer of Pd should attenuate to 78% of the clean surface value. Ignoring corrections for backscattering factors, the Pd/O peak ratio for 1 even monolayer Pd on $\alpha\text{-Al}_2\text{O}_3$ should be 0.53.

Kuyers²⁵ has obtained a specific experimental value of 12 \AA for the attenuation length of the Pd 330 eV Auger electron in Pd. As will be seen, this value for λ gives a slightly better fit with experimental results and was used in section VI-2. With this value of λ , $\frac{I_1}{I_\infty}$ for Pd 330 eV = 22% and the Pd/O peak ratio expected for one monolayer Pd on $\alpha\text{-}$

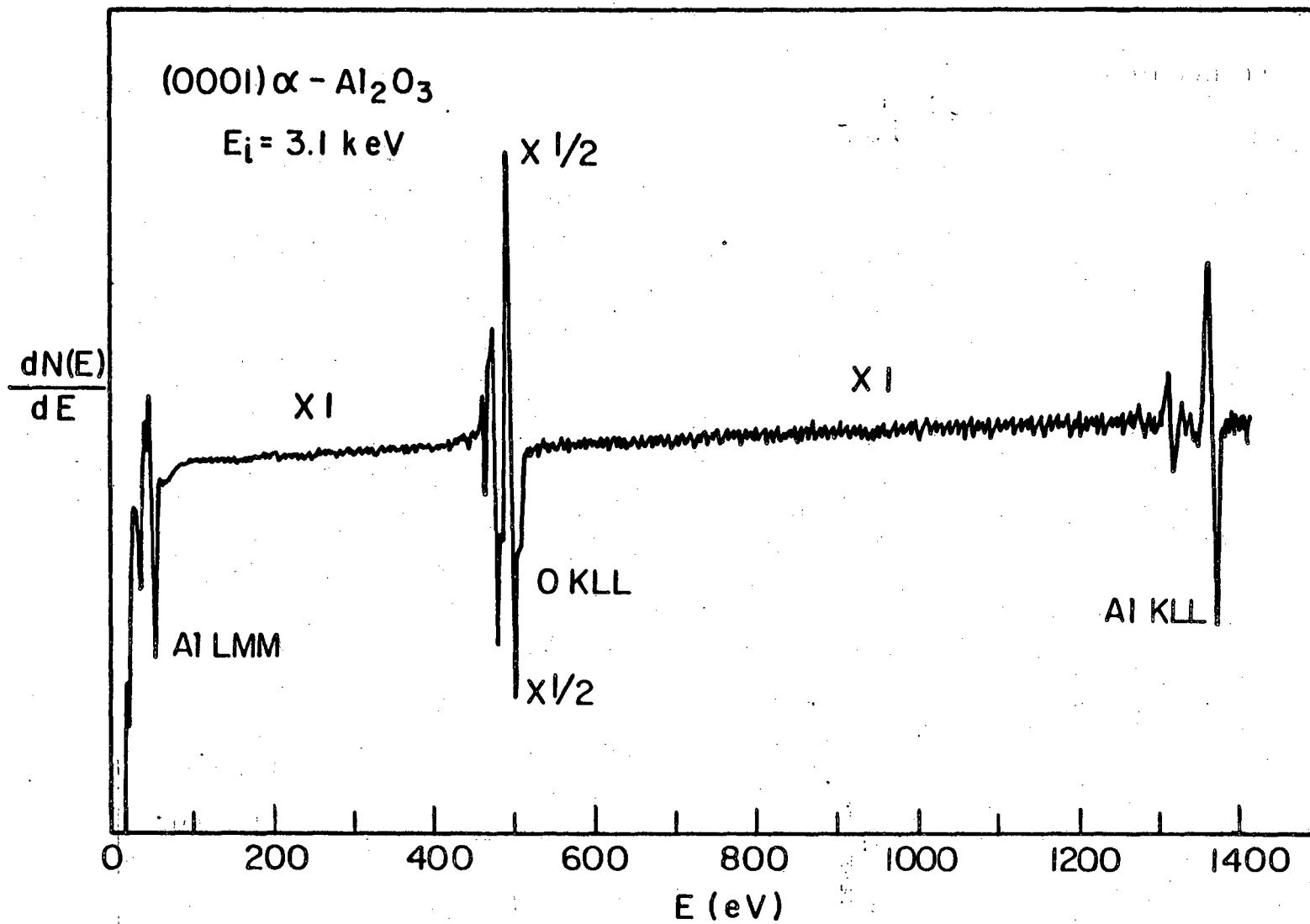


Fig. VI-10. Auger spectrum for clean α - Al_2O_3 .

XBL 781-4466

TABLE VI-2: Surface Sensitivity of Auger Electron Spectroscopy

$$I(E_A)_i = k(E)r(E)c_{Ai} \exp(-z_i/\lambda_E \cos\theta)$$

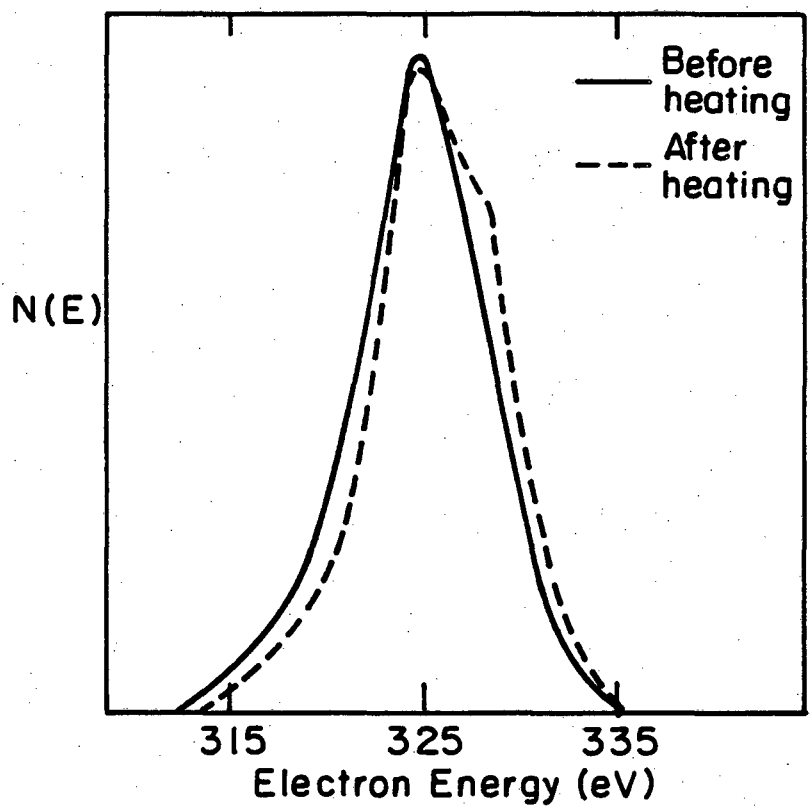
Pd 330 eV (Au 700eV)
 $\lambda = 9.5 \text{ \AA}$ $\alpha = .732$ ($\lambda = 5 \text{ \AA}$ $\alpha = .536$)

Atomic layer	% of bulk signal due to this layer	Cumulative %
1	27 (46)	27 (46)
2	20 (25)	47 (71)
3	14 (13)	61 (85)
4	10 (7)	72 (92)
5	8 (4)	79 (96)
6	6 (2)	85 (98)
7	4 (1)	89 (99)
8	3 (1)	92 (99)
9	2 (0)	94 (100)
10	2 (0)	96 (100)

Al_2O_3 is 0.43.

The Pd 330 eV peak shape seems to evolve upon evaporation of Pd onto $\alpha\text{-Al}_2\text{O}_3$ in a manner similar to that seen on graphite. However, the noise level for spectra on $\alpha\text{-Al}_2\text{O}_3$ is higher than that on graphite, probably due to slight fluctuations in the state of charge of the surface. This noise degrades the quality of data obtained for very low Pd coverages. Figure VI-11 shows $N(E)$ spectra for (a) ~ 1 monolayer Pd deposited onto $\alpha\text{-Al}_2\text{O}_3$ at 300°K and (b) a heavier deposit yielding about the same magnitude Pd signal after annealing to 1200°K for five minutes. The shoulder in the $N'(E)$ spectrum is less pronounced on the room temperature surface than on the annealed one. The room temperature $N(E)$ curve is more symmetric than that from the annealed surface which shows the high-energy shoulder typical of bulk Pd. The results here are much less dramatic than those in Figure VI-8, as would be expected for the thicker deposits used here.

Several models for the growth of Pd films on $\alpha\text{-Al}_2\text{O}_3$ are tested in Table VI-3. The measured attenuation values (with respect to the signals from bulk $\alpha\text{-Al}_2\text{O}_3$ and Pd) for the Al 54 eV ($\lambda = 5 \text{ \AA}$), 0 503 eV ($\lambda = 12 \text{ \AA}$), and Al 1380 eV ($\lambda = 17 \text{ \AA}$) are shown in the far right column for different amounts of Pd deposited and different levels of annealing. The Pd p-p height was used to calculate monolayer coverages assuming layer-by-layer growth taking the Pd self-attenuation length to be (1) 9.5 \AA , from the universal curve or (2) 12 \AA , from the results of Kuyers. The expected attenuation ratios of the three Al_2O_3 peaks were then calculated using these monolayer coverages and are listed in Table VI-3. The proportion of the alumina surface which must be covered by 50 \AA



XBL 818-6336

Fig. VI-11. $N(E)$ Pd Auger peaks for Pd on $\alpha\text{-Al}_2\text{O}_3$ (0001) before and after annealing at 1200°K .

TABLE VI-3: Comparison of measured Auger attenuation factors for Pd on Al_2O_3 with those predicted for monolayer and 50 Å hemisphere film morphologies.

Dep time	Substrate pk. attenuation factors calculated from coverages consistent with Pd signals												Measured attenuation factors		
	$\lambda_{\text{Pd}}=9.5 \text{ \AA}$						$\lambda_{\text{Pd}}=12 \text{ \AA}$								
	monolayer			50 Å hemisph.			ml			50 Å hemisph.					
	54 eV Al	503 eV O	1380 eV Al	54 Al	503 O	1380 Al	54 Al	503 O	1380 Al	54 Al	503 O	1380 Al	54 Al	503 O	1380 Al
4	.91	.95	.96	.94	.95	.96	.86	.91	.92	.94	.95	.96	.92	.91	.90
9	.80	.90	.92	.86	.89	.90	.75	.88	.91	.86	.88	.90	.81	.83	.83
19	.64	.83	.87	.77	.81	.83	.55	.78	.84	.74	.78	.81	.66	.75	.83
39	.47	.72	.80	.61	.67	.71	.38	.66	.75	.56	.63	.68	.51	.65	.79
39+	.30	.61	.71	.41	.51	.57	.22	.53	.64	.32	.43	.51	.38	.51	.57
heat	.64	.83	.87	.77	.81	.83	.54	.77	.83	.72	.77	.80	.68	.61	.66
+10	.26	.57	.67	.31	.43	.50	.36	.65	.74	.54	.61	.66	.45	.54	.55
+20	.33	.63	.72	.43	.52	.59	.23	.54	.65	.34	.45	.53	.34	.45	.44

diameter Pd hemispheres to give the observed Pd signal was also calculated using the two attenuation lengths, and the Al_2O_3 signal attenuations predicted by these models are also listed in Table VI-3. The set of predicted attenuation values which best agrees with the measured values for each Pd thickness is underlined. The 50 Å hemisphere model using the 12 Å attenuation length gives the best fit more times than all the other models put together, but the differences in fit are quite small.

No ordered LEED structures were seen upon evaporation of Pd or Au upon $\alpha\text{-Al}_2\text{O}_3(0001)$. Both the $p(1 \times 1)$ and the reduced $\sqrt{3} \times \sqrt{3} R30^\circ$ substrates were tried. Because of the near-perfect coincidence of the Pd(111) hexagonal mesh with the nearly hexagonal oxide ion net of $\text{Al}_2\text{O}_3(0001)$, the formation of a Pd(111) overlayer might be expected. This would be seen as an increase in the intensity of alternate spot in the $\alpha\text{-Al}_2\text{O}_3(0001)$ pattern as Pd was deposited since Pd(111) has real-space unit cell vectors 1/2 those of the substrate. No such effect was seen. Instead the intensity of substrate spots decreased uniformly and the diffuse background increased as Pd (or Au) was deposited, indicating a disordered overlayer. Films were evaporated onto substrates both at room temperature and at elevated temperatures. The room temperature deposits were annealed at temperatures up to 1200 °K, all without ordering. Pd films evaporated onto the substrate at 800 °K gave more pronounced shoulders on the Pd(330 eV) Auger peak than those formed at room temperature, thereby showing that larger Pd particle sizes were formed on the heated substrate.

LEED work became increasingly difficult as more metal was evaporated onto the alumina due to an increase in the secondary electron crossover energy. Deposition of ~2 average monolayers of metal caused the LEED electron beam to charge the surface and be deflected for beam energies below 200 eV. The sensitivity of LEED to overlayer superstructures decreases with increasing beam energy due to longer attenuation lengths. With more than ~5 monolayers of metal on the alumina even the higher energy beams used in Auger caused the surface to charge. The presence of isolated metal particles on the oxide apparently interferes with secondary electron emission without providing a conductive pathway to drain the charge. Metals are known to have lower secondary electron yields than oxides. ²⁶ An electron passing through a metal can lose energy in small increments through interactions with the free electron gas, with the result that most secondary electrons leave the surface with only a few eV kinetic energy. Interactions which can cause small incremental losses in the kinetic energy of an electron passing through oxides are much less probable than in metals, with the result that most secondary electrons come off of an oxide with an energy a bit greater than the band gap. Confirming this, $N'(E)$ secondary electron spectra from clean α - Al_2O_3 showed a high secondary electron yield at 10-15 eV. These electrons could be readily absorbed by the metal particles, thereby decreasing the overall secondary yield. In addition, charges residing on small metal particles of tight curvature could produce high fields which would play havoc with the incident electron beam.

Both Pd and Au are noble metals quite resistant to oxidation. The lack of ordering of Pd and Au films on α - Al_2O_3 can be understood in terms of a weak interaction between the metal and the oxide substrate.

In an attempt to study a system with stronger metal-oxygen interaction, Ni was evaporated onto the α -Al₂O₃ ($\bar{1}102$) surface. Deposition of small amounts of Ni onto the ($\bar{1}102$) 1×2 surface formed by annealing at 1300°K caused disappearance of the extra $1/2$ order spots. The 1×2 spots were quite sensitive to overlayers of any sort; their extinction may have been due to the pressure rise in the system during evaporation. No other LEED phenomena were observed.

The utility of Pt metals on alumina in industrial catalysis makes surface studies of these systems very attractive. The charging problems encountered here define an operational window of metal coverage available to electron beam techniques without the use of ion neutralization methods likely to increase surface contamination. No ordered monolayer or particle formation was seen within this operational window for the metals studied here. It is possible that other, more reactive, metals such as Ru, Rh, or Os would give ordered deposits at low coverage, though the results with nickel are discouraging. Further work with LEED on these systems may be warranted, though a coupling of photoemission techniques with local-structural and morphological information derived from extended X-ray absorption fine structure, X-ray diffraction, and electron microscopy would appear more likely to be fruitful.

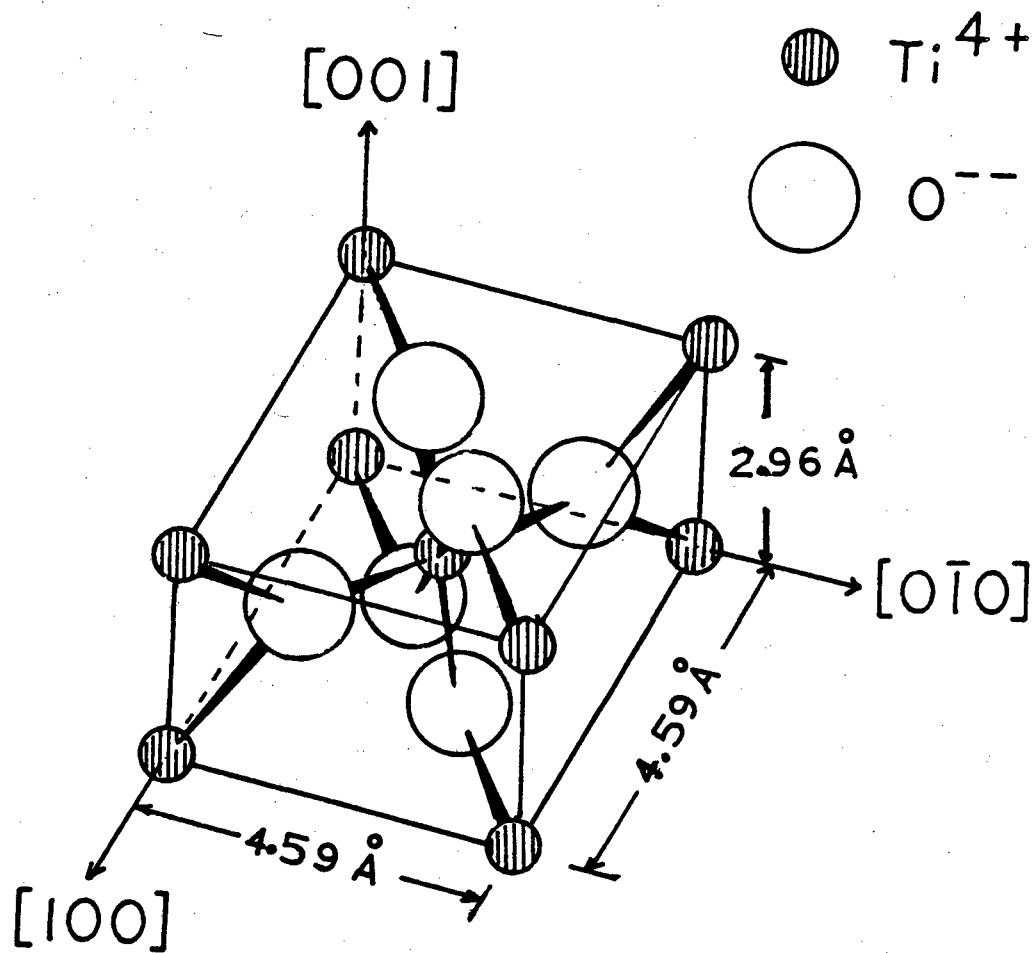
VI-4 Pd and Au on TiO₂

Titanium dioxide was chosen as a substrate for a number of reasons. It can be made conducting through a slight reduction so that metal films of all thicknesses can be studied with electron beam techniques. It shows photochemical activity similar to that of SrTiO₃ (though a higher

flatband potential prevents hydrogen evolution from water without an external potential). Although TiO_2 has seen little use as an industrial catalyst support, considerable research interest has developed in the strong metal support interactions (SMSI)^{1,2} which modify the catalytic properties of noble metals supported on titania. Stable surfaces of rutile have been identified and their interactions with small molecules have been followed by means of ultraviolet photoemission and low resolution electron energy loss spectroscopies.²⁷ Rutile is the high temperature phase of TiO_2 . The other major phase, anatase, has a more complex structure and in general appears to be somewhat more active chemically. Conventional means of TiO_2 powder production, such as hydrolysis of TiCl_4 followed by heat treatment, produce a mixture of anatase and rutile.

VI-4-1 The Structure of Clean Rutile Surfaces

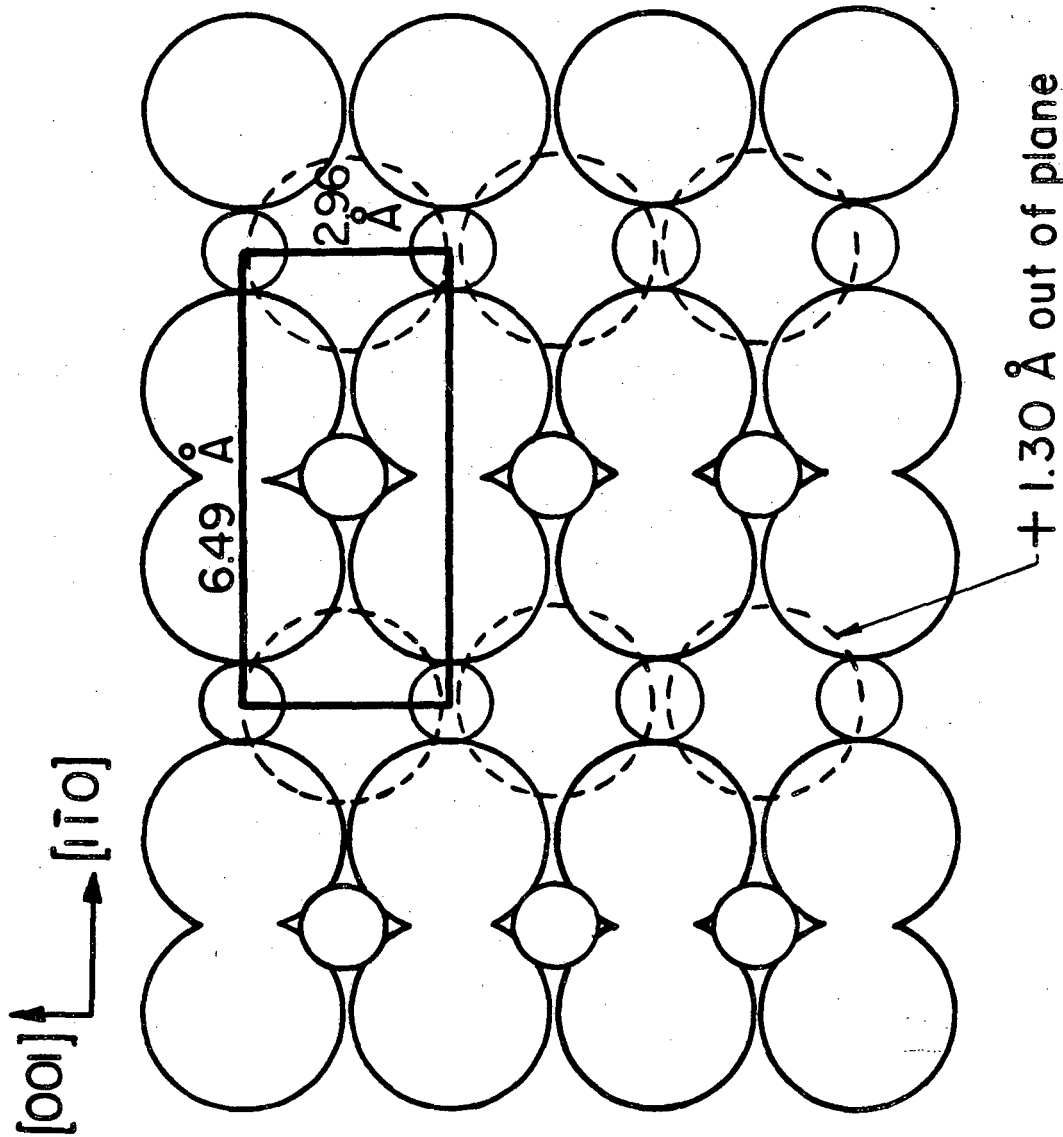
The bulk structure of rutile is shown in Figure VI-12. The crystal cleaves cleanly along the (110) plane,²⁸ one of the two surfaces chosen for study. The (110) termination of the bulk structure is shown in Figure VI-13, with large circles representing O^{2-} ions and small circles Ti^{4+} ions. The surface has a rectangular unit cell 6.49 Å (or about 2.3 Pd atom diameters) long in the [110] direction and 2.96 Å (1.08 Pd diameters) in the [001] direction. Such planes containing both Ti and O occur every 3.25 Å in a direction perpendicular to the plane of the figure, packed ABAB with each plane 1/2 unit cell length from the next one. Between these Ti-O planes lie two levels of oxygen ions, one of which is shown here in dotted circles. One might expect that upon cleavage the "interplanar" oxide ions would adhere to the closer Ti-O plane. The



XBL769-10513

Fig. VI-12. The TiO₂ (rutile) conventional unit cell.

Fig. VI-13. The (110) surface termination of the bulk rutile structure.

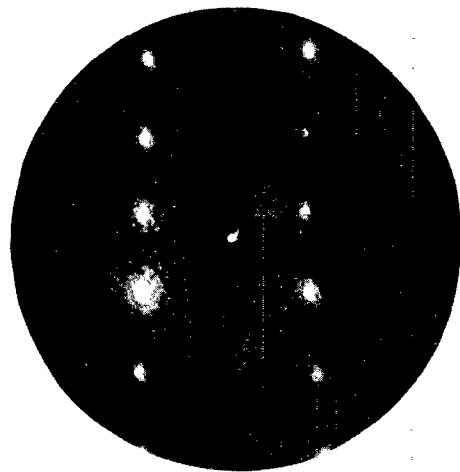


XBL 781-4458

actual arrangement of these "protruding" oxide ions on a polished, vacuum-annealed surface is not known, as the LEED intensity measurements and calculations required have not yet been done. Oxygen is readily removed from the surface by Ar^+ bombardment (Figure VI-17); part of the mechanism of reduction may be the dislodgement of these protruding oxygens. Figure VI-14 shows a LEED pattern from the clean TiO_2 (110) surface and its real-space interpretation. The LEED pattern is consistent with the unreconstructed termination of the bulk structure.

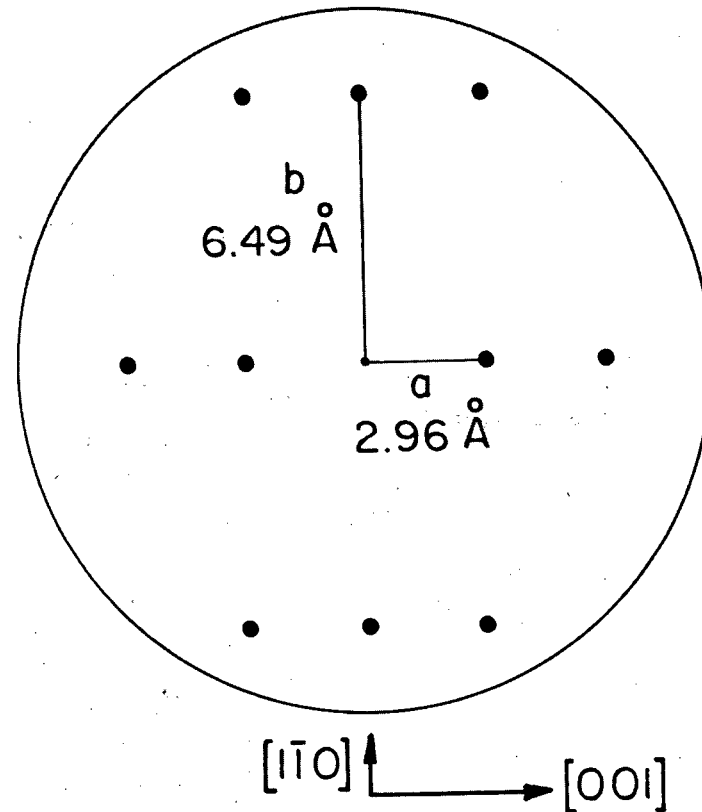
The second rutile surface to be investigated was that of a crystal cut $9\ 1/2^\circ$ from the (110) surface towards the [100] pole. This orientation corresponds to the (750) plane. The expected structure is shown in section at the top of Figure VI-15. It would have (110) terraces three unit cells long connected by (110) steps $1/2$ unit cells (or \sim one oxide ion) high. Because the terrace planes are packed ABAB, alternate, rather than adjoining, step faces would be equivalent; and the step periodicity seen by LEED would be 6, not 3, unit cells in the $[1\bar{1}0]$ direction. The actual LEED pattern observed, shown in the upper left corner of Figure VI-15, gave a periodicity of 2.5 unit cells in the $[1\bar{1}0]$ direction. If (110) terraces are maintained, this periodicity corresponds to the (320) surface shown in section at the bottom of Figure VI-15. Because this surface forms a higher angle (11.3°) to the (110) plane than does the macroscopic (750) surface plane which was cut, at least 17% of the real surface must have a step density lower than that of the ideal (320) surface. It seems most likely that there are domains of the flat (110) plane on the surface. If these domains were larger than the coherence width of the electron beam ($\sim 75\ \text{\AA}$) they would add weak spots with normal (110) spacing to the LEED pattern. Though no

TiO₂ (110)



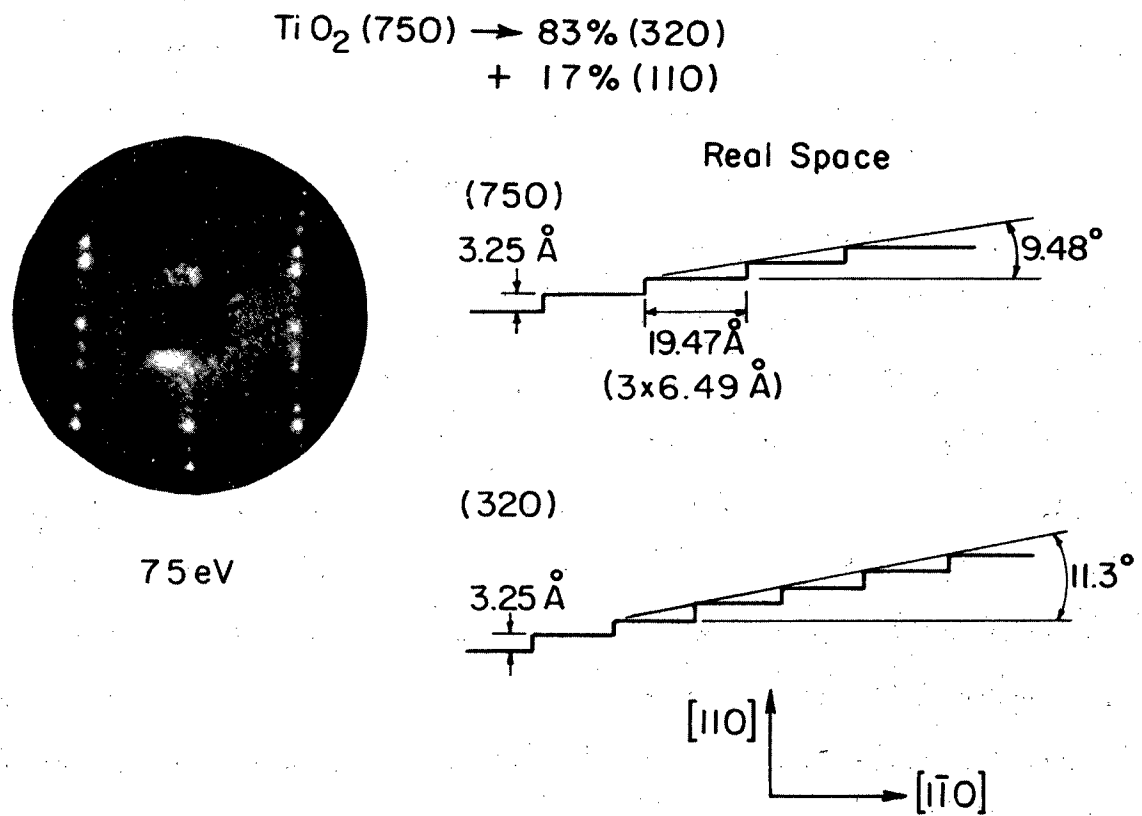
54 eV

Real Space



XBB 800-12373

Fig. VI-14. LEED pattern and real space interpretation for clean TiO₂ (110).



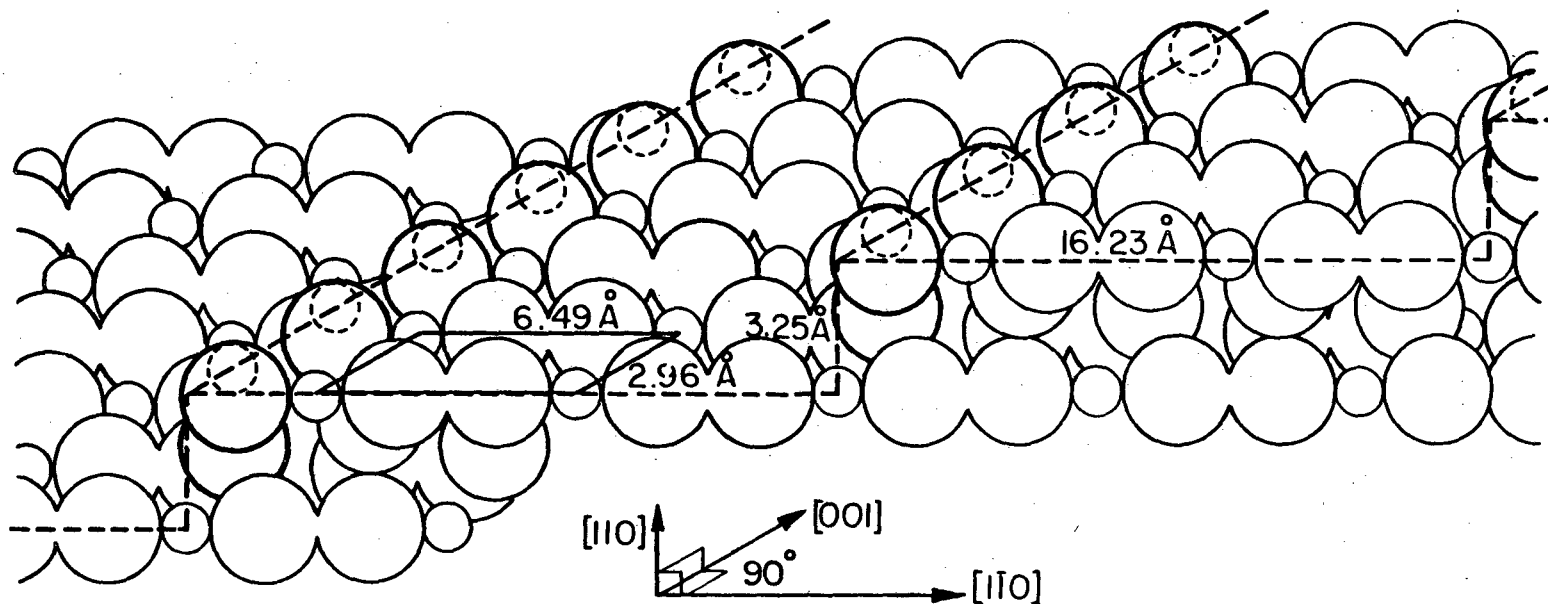
XBB 805-5987

Fig. VI-15. LEED pattern and interpretation for TiO_2 (750).

Parkinson et. al.¹ have invoked such a "shunting" mechanism to explain current losses in GaAs-based liquid junction solar cells and their mitigation through the adsorption of ruthenium ions. For such tunneling to occur with adequate probability several requirements must be met: (1) A surface state must lie between the surface conduction band edge (\sim at U_{fb} for a highly doped semiconductor) and the bulk position of the conduction band, and (2) the width of the depletion layer barrier at the energy of the surface state must be quite narrow to allow a sufficiently high probability of elastic tunneling. Condition (1) may be met on $SrTiO_3$. Although the major surface state identified on $SrTiO_3$ by photoelectron spectroscopy, a Ti^{3+} state 0.6 eV below the Fermi level, lies below (anodic of) the hydrogen couple and thus is an unlikely intermediate in hydrogen production, there is some evidence for states due to the ubiquitous carbonaceous impurities which lie in the proper energy range. However, condition (2) runs awry of experimental results, as equivalent rates of hydrogen photogeneration were seen on highly reduced and on stoichiometric crystals. The depletion layer barrier at a given energy is much narrower in the former, and any mechanism relying on tunneling through the surface barrier would be expected to proceed much more rapidly on the strongly doped crystal.

Another mechanism whereby photogenerated electrons could reach the semiconductor surface despite the depletion layer barrier is through hot carrier injection, a concept proposed in a photoelectrochemical context by Boudreaux et. al.² The principles of hot carrier injection from an n-type semiconductor are sketched out in Figure VII-3. When a photon with energy greater than the bandgap is absorbed, electrons and holes will be formed in states removed energetically from the conduction and

TiO₂ (rutile) (320)



XBL 78I-4467

Fig. VI-16. Isometric drawing of idealized TiO₂ (320) surface.

face at high temperatures. In contrast, the (001) surface facets and the (100) surface undergo several reconstructions (probably in conjunction with the formation of Magnelli phases) upon heating²⁷. The formation of some of the same overlayer structures on (110) and (750) surfaces (Section VI-4-4) lends some credence to the structure drawn in Figure VI-16.

VI-4-2 Auger Spectroscopy of Clean TiO₂

Figure VI-17 shows the Auger spectrum of a clean, well-ordered TiO₂ (110) surface. The main O (506 eV) and Ti (382 eV) peaks are too close in energy to allow overlayer film morphology to be well judged by differential attenuation. The peak at 40 eV overlaps with low energy Pd and Au transitions, further complicating attempts at quantitative analysis. The annealed (110) surface gives an O (506 eV)/Ti (382 eV) peak ratio of 2.3. The same ratio on the annealed (750) surface is 10% higher. This difference is a bit beyond the scatter in the measurements and is probably real. It may be due to a real difference in stoichiometry, but could also be explained by geometric effects. The Ti(382 eV)/Ti (414 eV) ratio on well-annealed surfaces is 1.4.

Sputtering the annealed rutile surfaces with Ar ions induces several changes in the Auger spectrum. The O (506 eV)/Ti (382 eV) peak ratio drops below 2.0. The most negative part of the derivative peak at 41 eV is chopped off, decreasing the TiO₂ (41 eV)/Ti (382 eV) peak-to-peak ratio (from 0.38 for the annealed surface) to 0.17. The shape of the Ti 414 eV ($L_3M_{2,3}M_{4,5}$ for the metal) peak is altered, while that of the 382 eV peak ($L_3M_{2,3}M_{2,3}$ for the metal) is relatively unchanged. The Ti (382

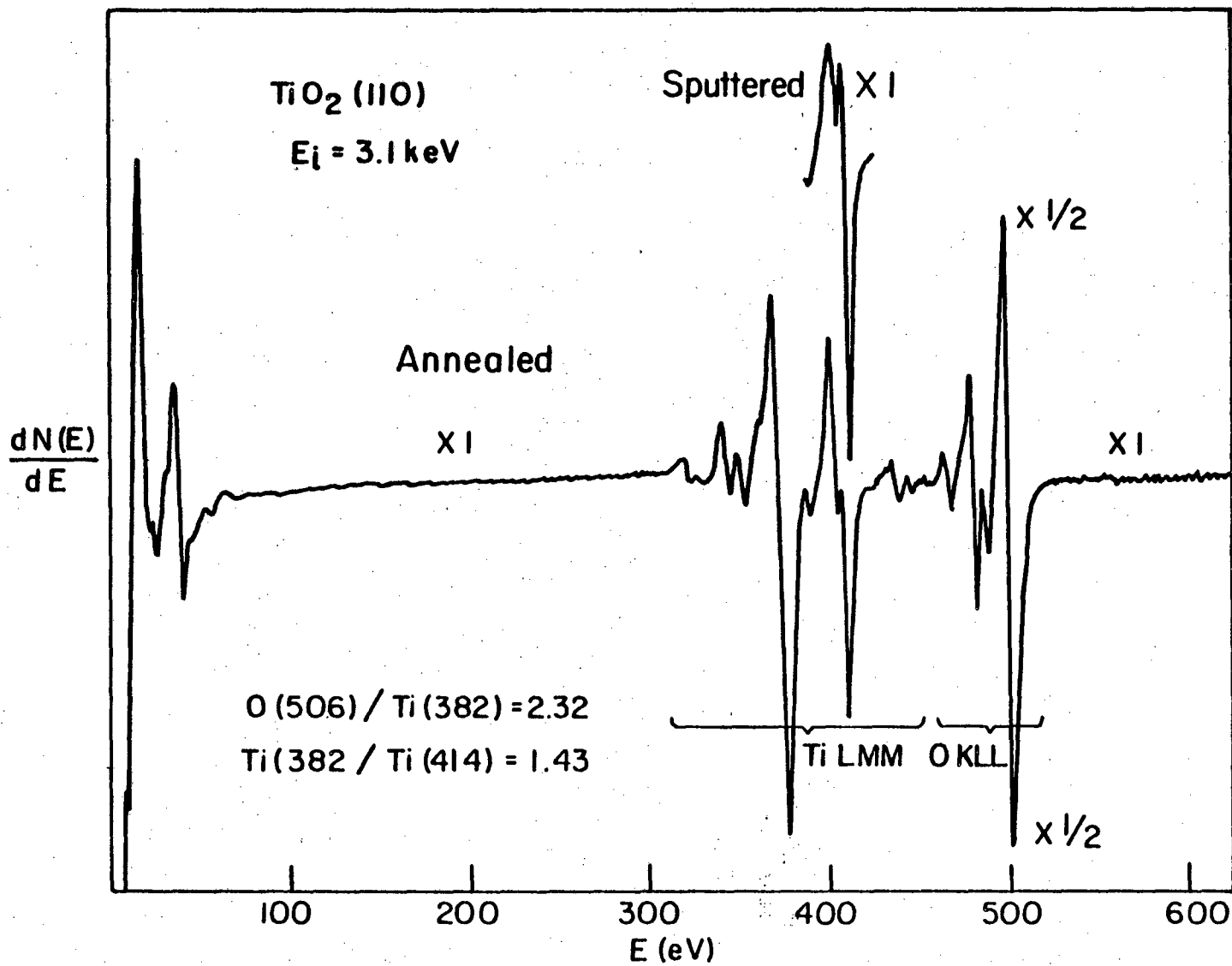


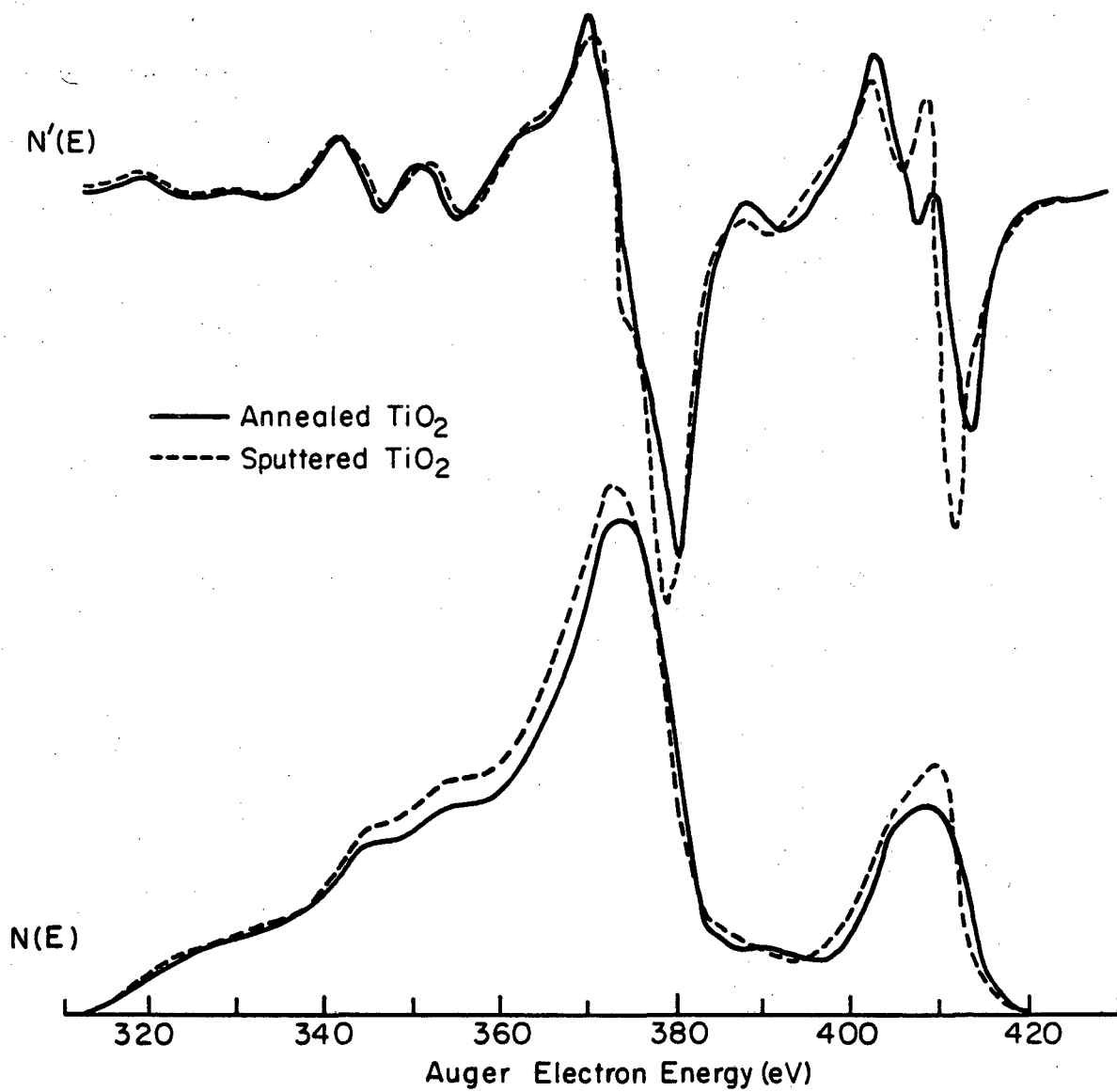
Fig. VI-17. Auger spectrum of clean annealed and sputtered TiO_2 (110) surfaces.

XBL 781-4465

eV)/Ti (414 eV) ratio decreases to 1.2 upon sputtering. Detailed $N'(E)$ and $N(E)$ Auger spectra (not normalized) for the TiL_{3MM} peaks are shown in Figure VI-18. The most obvious change in the $N'(E)$ spectrum (the change in the depth of the local minimum at ~ 407 eV) manifests itself in the $N(E)$ spectrum as slight additional intensity and peak skewing at the high-energy edge of Auger emission. Using UPS, Chung *et. al.*²⁷ have shown that sputtering TiO_2 surfaces causes the growth of an emission centered 0.6 eV below the Fermi level which has been ascribed to a Ti^{3+} state. The additional intensity at the high edge of the Auger spectrum is probably due to the presence of this Ti^{3+} . It is of interest to note that, in a pure ionic model, the 3d band of Ti^{4+} in TiO_2 should be completely empty. The emission around 414 eV, ascribed to the $L_{3M_{2,3}}M_{4,5}$ transitions, though requiring electrons in the 3d band, is seen in the oxide, albeit with altered shape and reduced intensity. The emission is probably due to the partial covalency of the Ti-O bond (i.e., the valence band has some Ti 3d, as well as O 2p, character) and possibly some population of the largely Ti 3d conduction band through reductive doping and interaction with the electron beam.

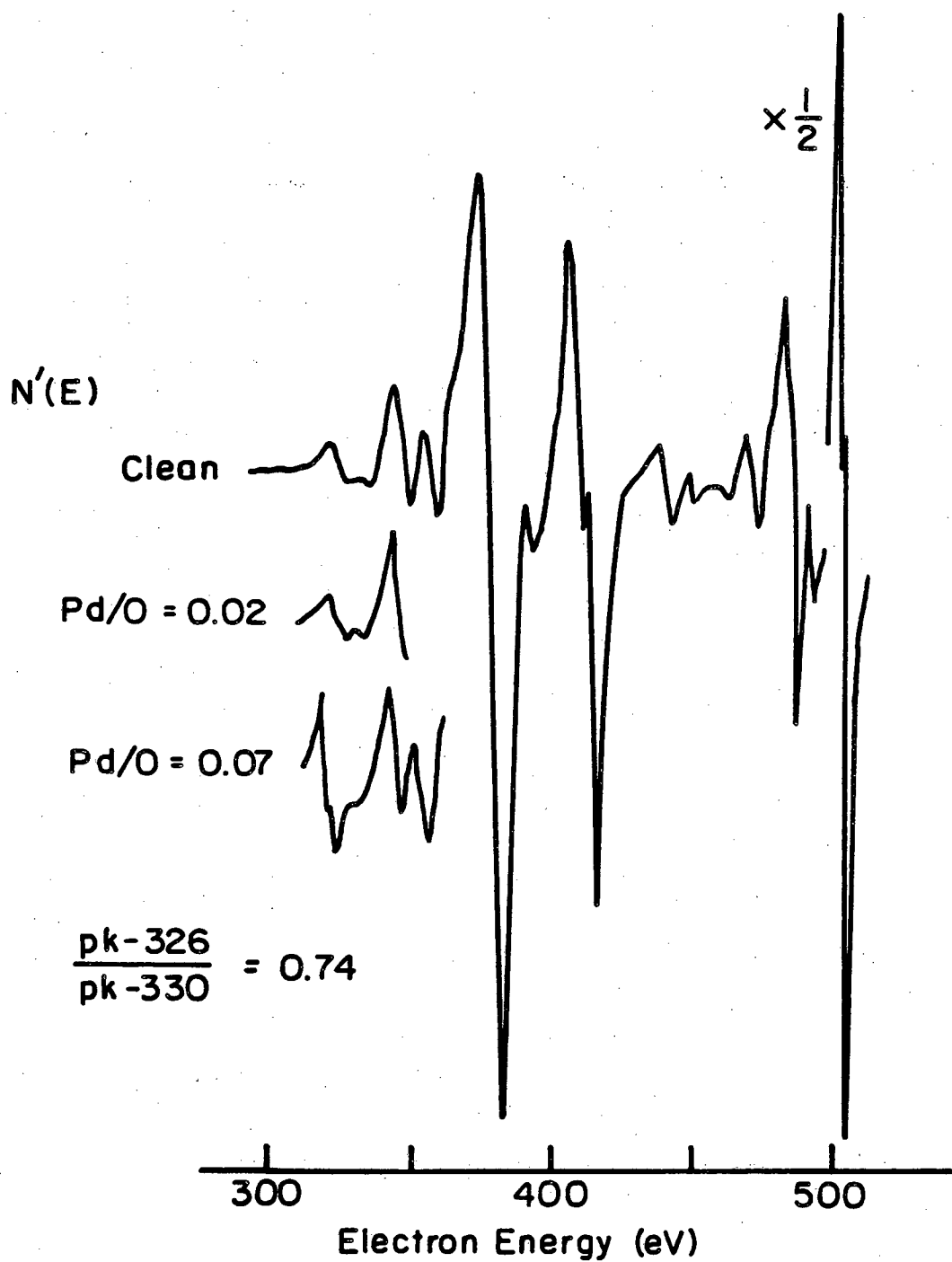
VI-4-3 Auger Spectroscopy and LEED of Pd and Au on TiO_2

In contrast to the situation on graphite and alumina, very small amounts of Pd deposited onto TiO_2 at room temperature give Auger spectra very similar to those of bulk Pd (Figure VI-19). A small TiO_2 peak interferes with the Pd signal, complicating analysis at very low coverages. The smallest detectable amount of Pd ($Pd(330eV)/O(506eV) = 0.02$, ~ 0.03 monolayer on surface) gives a clearly split spectrum with a low peak-to-peak ratio. By $Pd/O = 0.07$ (~ 0.11 monolayers Pd) the Auger peak



XBL818-6337

Fig. VI-18. $N'(E)$ and $N(E)$ Auger spectra of annealed and sputtered TiO_2 surfaces.



XBL818-6338

Fig. VI-19. Auger spectra of Pd on TiO₂ at low coverages.

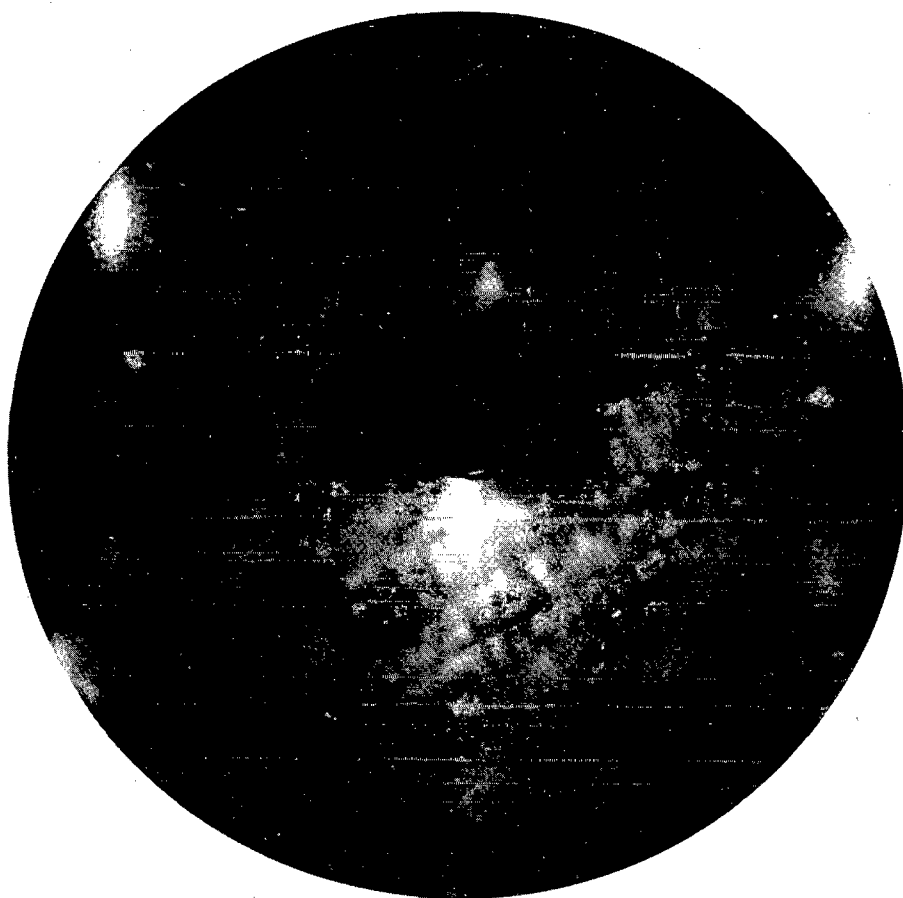
is well defined with a tweak-to-peak ratio of 0.74. The tweak does become more pronounced after heating to 500 C°, the change being slightly less pronounced than that shown in Figure VI-11 for Pd on Al₂O₃.

No ordered LEED patterns due to overlayers form when thin layers of Pd or Au are deposited onto clean, ordered TiO₂ (110) or (750) held at room temperature. There is a general increase in the diffuse background intensity as more metal is deposited, and the substrate spots are strongly attenuated at deposit thicknesses above one average monolayer.

1. LEED patterns indicative of weak substrate-overlayer interactions

Deposition of thick layers of either Au or Pd onto TiO₂ (110) or (750) at room temperature gave partially ordered LEED patterns the sharpness of which increased upon annealing the surface. Before the film was annealed no LEED spots due to the substrate were visible. Figure VI-20 shows the LEED pattern resulting from annealing a thick (~6 monolayer) film at 900°C. Substrate spots are seen, though dimly, even at this low beam voltage (51 eV), showing that some free substrate surface was exposed. The four most visible spots due to Pd lie outside the lines of spots for the 750 surface. Two more Pd spots appear near the top and at the bottom of the screen, in line with the substrate spots. The Pd spots are broadened along the substrate [001] direction by about the width of the step spot splitting, indicating some correlation of the Pd structure over the steps. On (110) surfaces the Pd spots were round.

Figure VI-21 gives a schematic of the thick Pd film LEED pattern (Structure A) and a real-space interpretation thereof. The Pd spots



51 eV

XBB 818-7907

Fig. VI-20. LEED pattern for thick Pd film annealed at 900°C on TiO₂ (Structure A).

Structure A (IIO and stepped)

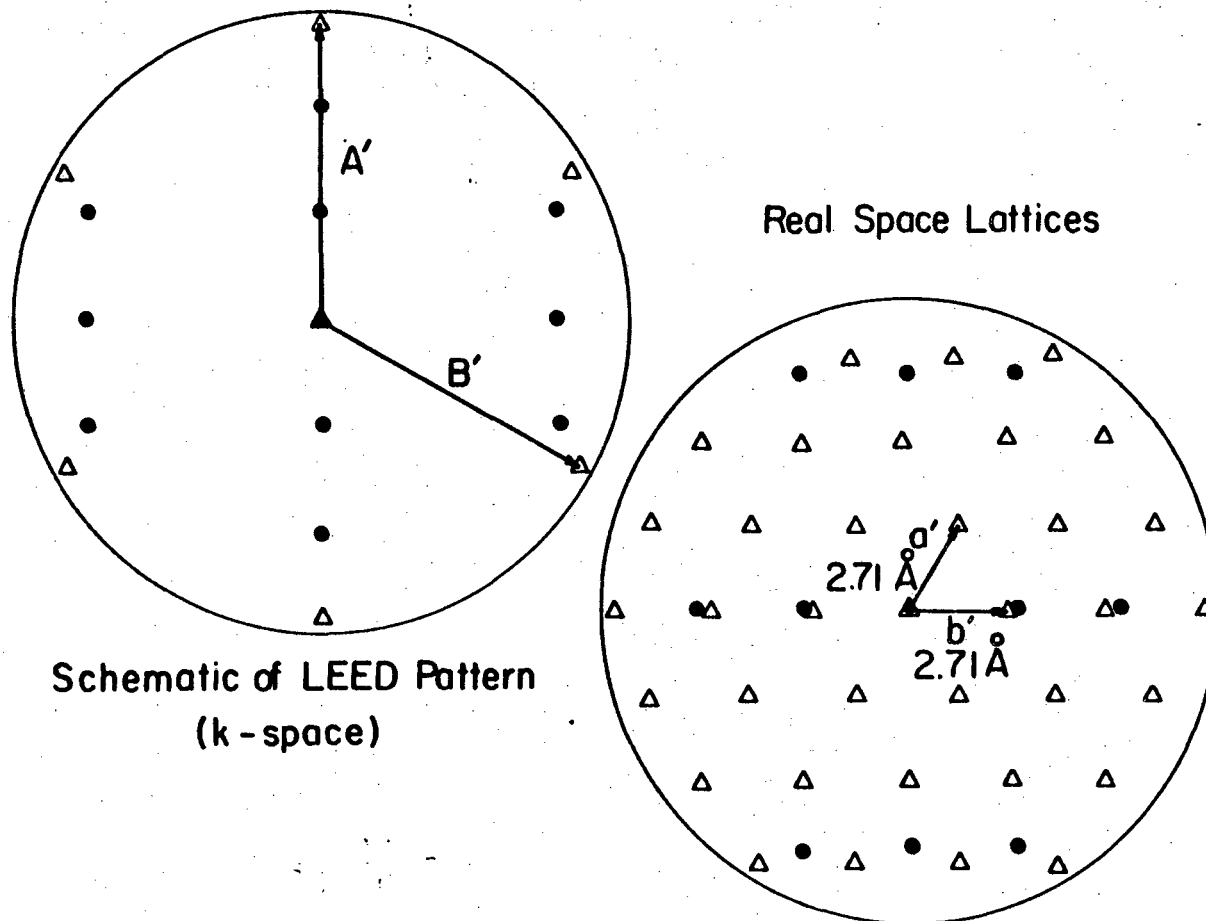


Fig. VI-21. Diagram of Structure A LEED pattern and real space interpretation. Dots= substrate; Triangles=deposit. XBL 781-4460

correspond closely to a hexagonal mesh. The real-space lattice parameter as calculated by comparison with the substrate is 2.7 \AA within experimental error of the 2.75 \AA unit mesh vector in Pd (111). One of the lines of closest packing in the Pd overlayer lines up with the [001] direction of the substrate. In this direction the lattice mismatch is 8%.

Thick layers of gold gave a similar pattern, with a unit mesh closer to that of Au (111), (2.88 \AA). Gold films did not order quite as well as Pd films, especially on the (750) surface. Order was never obtained in gold films less than 5 monolayers thick. Relatively thin layers of Pd partially ordered to give Structure A, provided that the substrate was held at high ($> 700 \text{ }^\circ\text{C}$) temperatures during evaporation. The Auger spectrum from such a partially ordered film is shown in Figure VI-22. If a smooth monolayer structure is assumed, the Pd peak height and O-Ti attenuation in Figure VI-22 lead to a Pd coverage of $1/2$ monolayer. However, the same Pd signal and substrate attenuation would obtain if an average of 2 monolayers-worth of Pd were distributed over the substrate as isolated hemispherical islands 50 \AA in diameter. The intensity of the substrate spots and the behavior of thick films upon annealing lend credence to the island supposition. After a thick (> 15 monolayer by initial substrate attenuation) Pd film was annealed at 950°C for a number of hours the substrate peaks grew considerably, indicating 1-2 monolayers Pd on the surface. The deposit, however, remained clearly visible to the eye, whereas freshly deposited films which gave 1-2 monolayers-worth of substrate attenuation were invisible. Annealing the film led to the growth of large Pd particles and the exposure of considerable naked substrate.

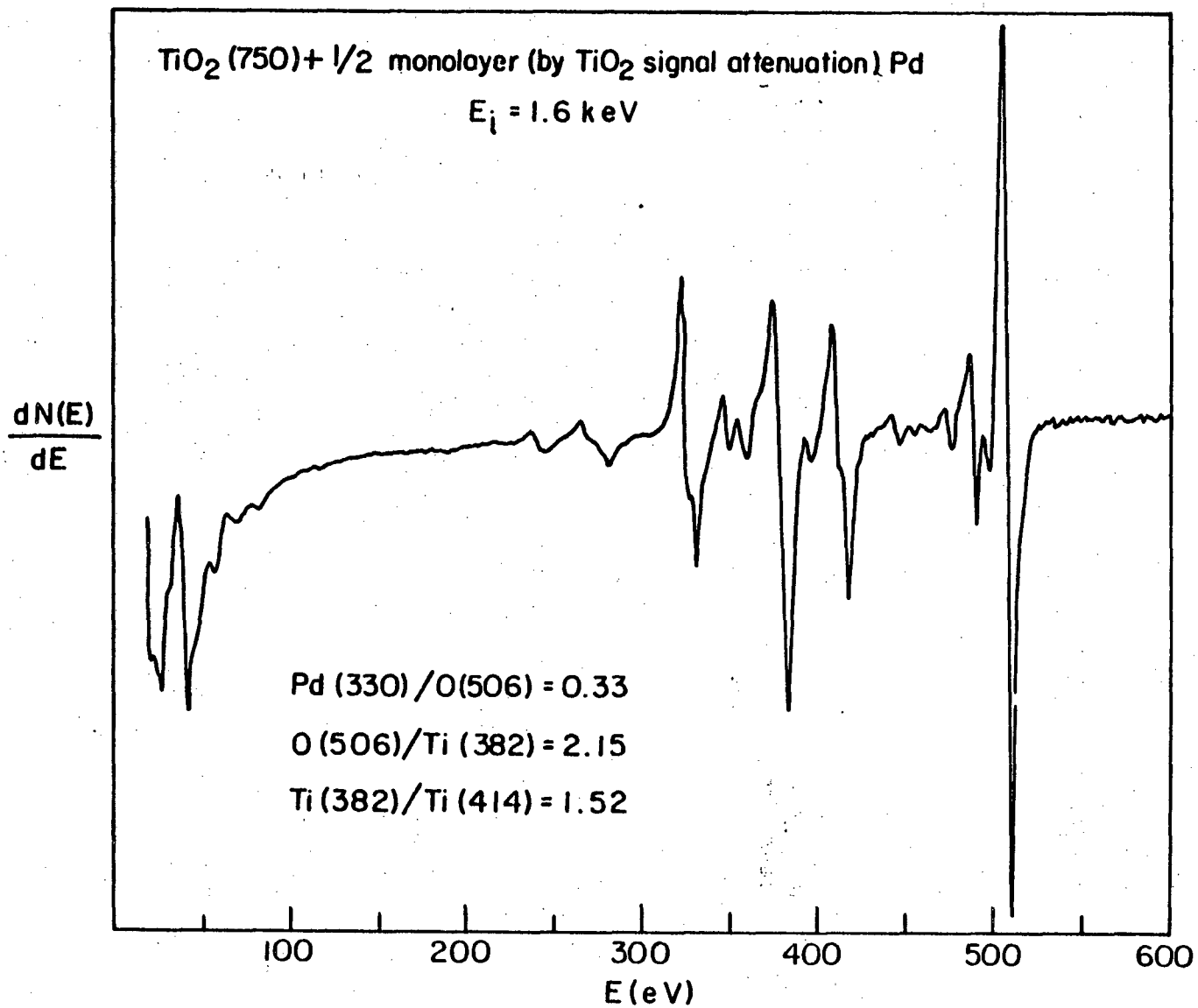


Fig. VI-22. Auger spectrum of Pd evaporated onto TiO₂ (750) held at ~700°C. XBL 781-4462

The Structure A LEED patterns for Pd and Au are indicative of a rather weak interaction with the substrate. The unit mesh is consistent with the lowest free energy plane of the bulk metal despite a fair degree of lattice mismatch with the substrate. Analogous patterns are obtained for Pd and Au despite the quite different chemistries of the two metals. The substrate-deposit interaction is strong enough to cause a preferred orientation of the Pd or Au particles with one of their lattice vectors along the [001] direction, but is not strong enough to distort the structure of the metal particles themselves. The greater difficulty in ordering deposits of gold may be due to a slightly weaker Au-TiO₂ interaction. It may, however, be due to differences in the preferred morphology of the small metal particles. Baetzold's calculations²² indicate that plane-faced small particles show greater d-band splitting than do hemispherical particles. For a metal with a partially-filled d-band, such as Pd, the flat-faced particles would be energetically favored. Hemispherical particles are more favored for a metal like gold with a filled d-band. Pd particles therefore would be more likely to have a flat (111) top, yielding a better LEED pattern.

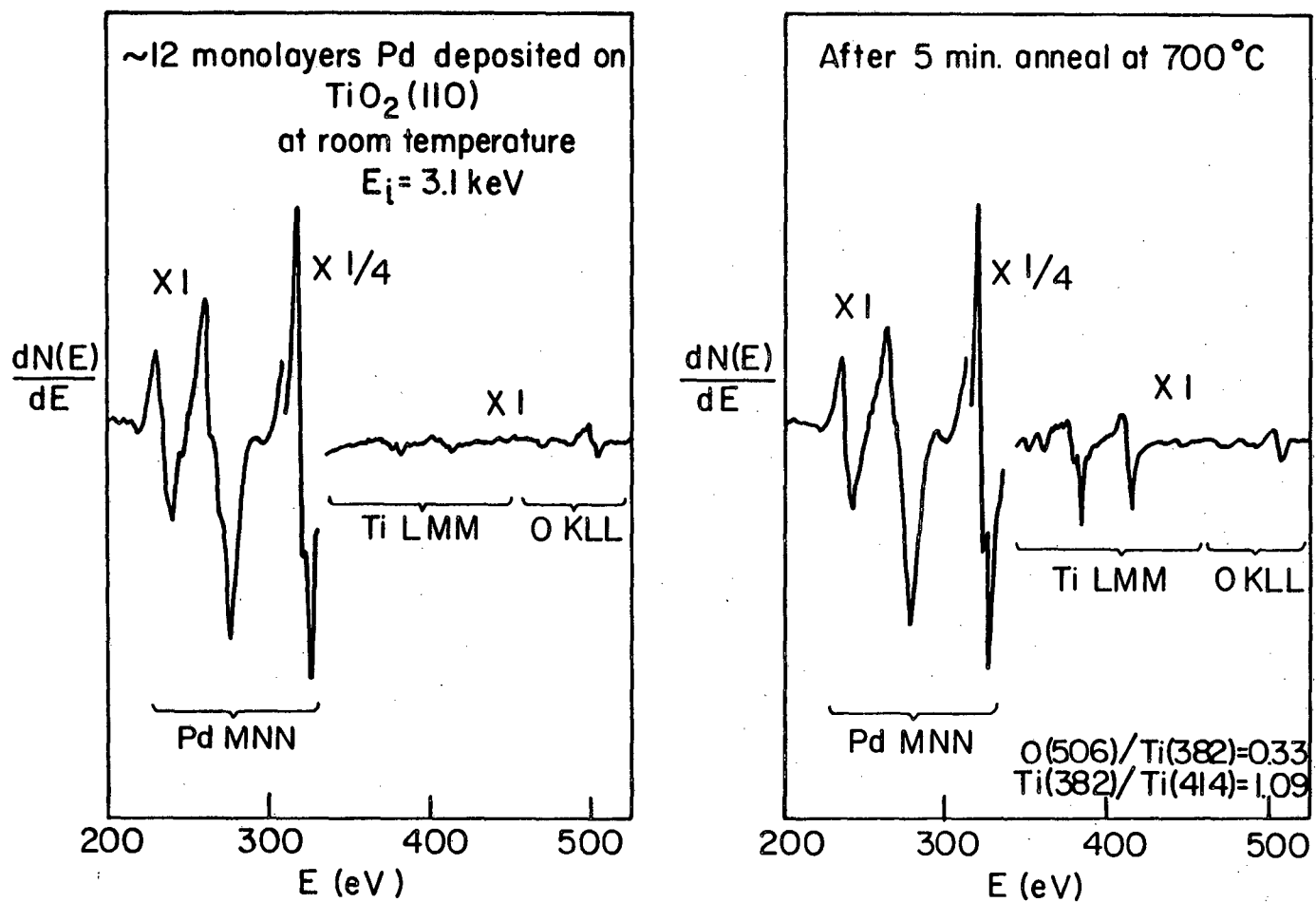
Although gold gave no other LEED patterns on TiO₂ indicative of a stronger metal-support interaction, two other LEED patterns were seen for Pd along with Auger evidence of intermetallic compound formation, as well be seen in the next section. At higher annealing temperatures the different chemistries of Au and Pd do come into play.

2. Auger evidence for intermetallic compound formation

Figure VI-23A shows the Auger spectrum of a thick (~12 monolayers) Pd deposit evaporated onto well-annealed TiO₂(110) at room temperature. The substrate Auger signals are almost completely extinguished. This deposit gave the partially ordered Structure A LEED pattern characteristic of Pd(111) microsurfaces. No substrate LEED spots were visible through this deposit. After annealing 5 minutes at 700°C the Auger spectrum of Figure VI-23-B was obtained. While the oxygen peaks have hardly grown at all, the Ti peaks have grown at least seven-fold, with a significant change in peak shape. The Ti(382 eV)/Ti(414 eV) peak height ratio, which is 1.4 on clean, annealed surface, is 1.1 here. The splitting in the 414 eV peak has disappeared, but splitting has appeared in the 382 eV peak, which has also had its maximum clipped. The peak shape is intermediate between that for clean TiO₂ and that for pure metallic titanium. Identical peak shapes have been observed from bulk Pt-Ti intermetallic compounds.³⁰ The spectrum in Figure VI-23B indicates that Ti, but not O, migrates through the thick Pd film and forms an intermetallic compound, part of which is near the surface. Alternately, during the high temperature anneal the Pd may partially agglomerate, leaving behind a film of the intermetallic, which must still be quite thick to account for the lack of growth in the oxygen signal.

3. LEED patterns indicative of stronger Pd-TiO₂ interactions

The LEED pattern taken at the edge of the Pd deposit corresponding to Figure VI-23B showed Structure A with a weak hemi-halo around each Pd spot on the inside. The halos were probably indicative of double dif-

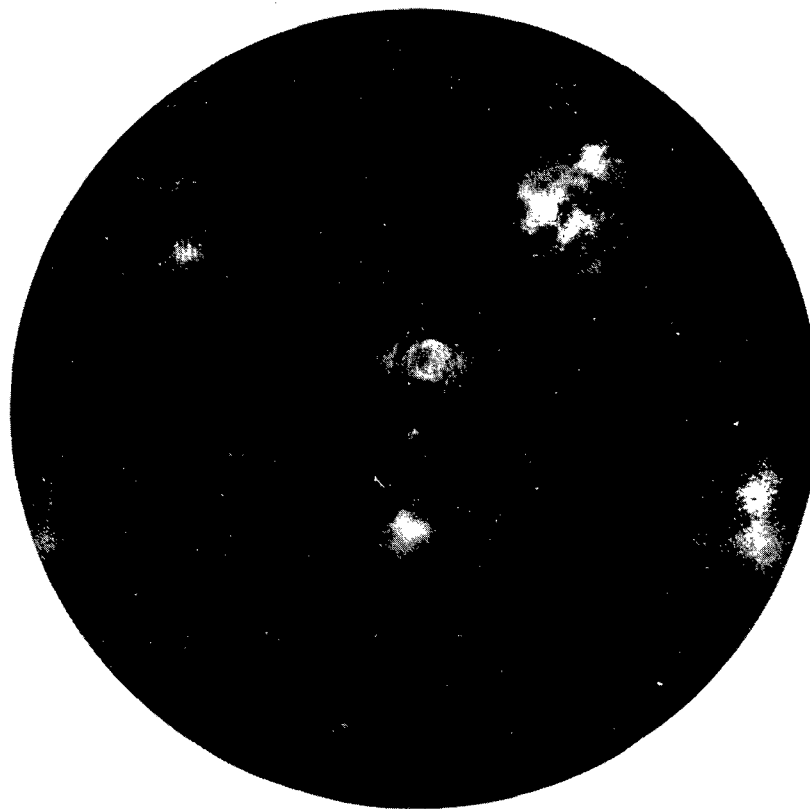


XBL 781-4464

Fig. VI-23. Auger spectra of thick Pd film on TiO₂ before and after annealing.

fraction features between the Pd(111) particles and a second ordered phase of somewhat larger lattice parameter, with ill-defined epitaxial orientation. Upon further annealing at 700°C this phase further crystallized to give the LEED pattern in Figure VI-24. A pair of extra spots lie just inside the original Structure A spots. No extra spots are found around the (0,0) direct beam spot, indicating that the extra spots are now not due to double diffraction effects. There is a smaller diffraction intensity around parts of the circle around the (0,0) spot defined by the radius of the new spots, probably due to a residual slight rotational disorder in the new phase. A schematic representation and "real-space" interpretation of this LEED pattern are given in Figure VI-25. The new spots are viewed as resulting from a separate phase from that producing Structure A. In the initial stage of the crystallization of this phase the crystallites were smaller than the coherence width of the LEED beam and could only add their amplitudes, not intensities, to the diffraction pattern of Structure A. Thus the new phase showed up only in double diffraction features -- hemi-halos around the Structure A spots. Upon further annealing, particles of the new phase grew larger, leading to single diffraction effects -- independent spots. The rotational registry of the new hexagonal phase with the substrate also became more definite, finally locking into two real-space orientations: with one of the two equal $3.2\overset{\circ}{\text{A}}$ unit vectors $+4^\circ$ or -4° from $\text{TiO}_2[001]$.

There is no clear physical interpretation of the unit mesh proposed in Figure VI-25. The $3.2\overset{\circ}{\text{A}}$ unit cell is 15% larger than that for Pd(111) but too small for any simple vacancy patterns (on) intermetallic lattices. One of the overlayer unit cell vectors is parallel to the

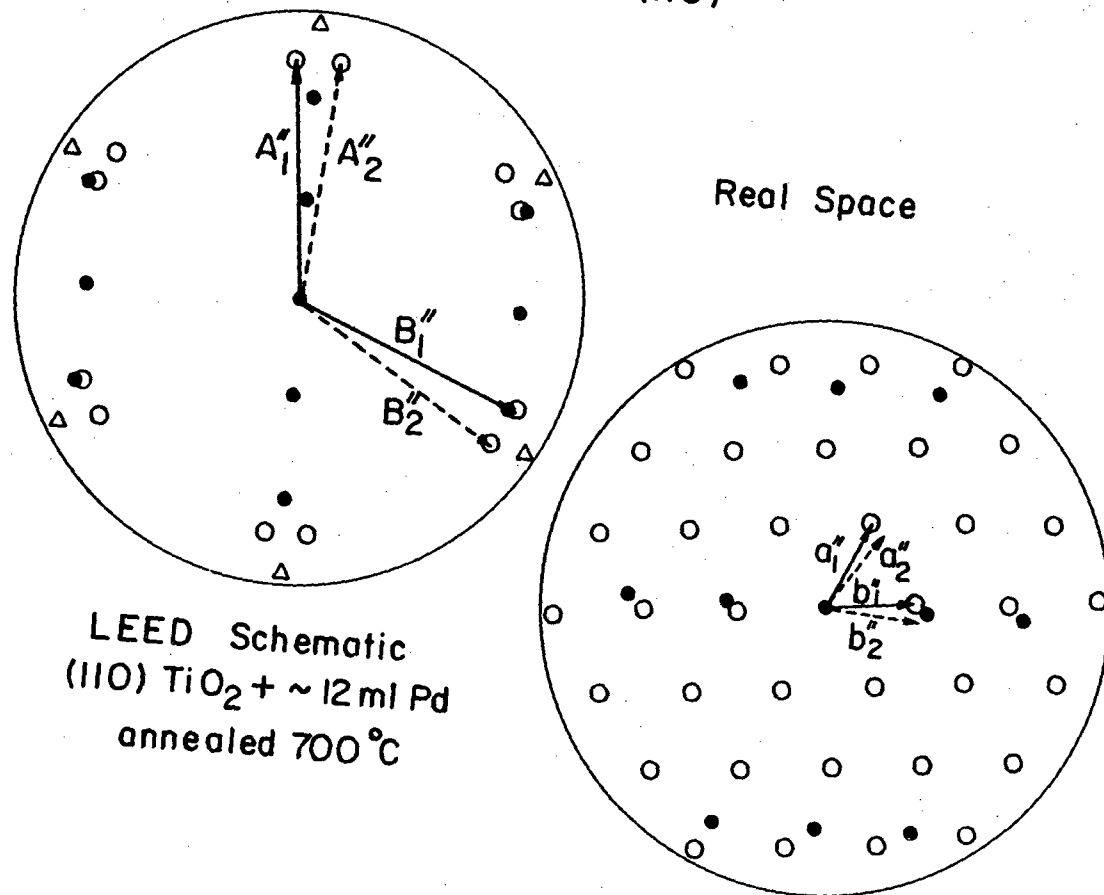


Pd on TiO₂ (110)
54 eV

XBB 818-7908

Fig. VI-24

Structure B (110)



LEED Schematic
 (110) $\text{TiO}_2 + \sim 12 \text{ ml Pd}$
 annealed 700°C

$$|a_1''| = |a_2''| = |b_1''| = |b_2''| = 3.17 \text{ \AA}$$

$$b'' \pm 4^\circ \text{ from TiO}_2[001]$$

Fig. VI-25.

XBL781-4459

diagonal of the TiO_2 unit cell in one of the two proposed orientations, but not in the other. This diagonal orientation could put adjacent overlayer atoms into adjacent hollows in the TiO_2 oxide ion lattice or into near coincidence with adjacent Ti ions. The structure could represent a compromise between strong interaction with the substrate and the tendency to form a closest-packed Pd layer. There is no clear explanation for this structure as an intermetallic, as there is for the second Pd structure found on the stepped surface.

Structure A and Structure B spots are ascribed to separate phases in the foregoing interpretation, based on the sequential development of the structure. If the triplets of spots are taken as defining a new hexagonal net, the unit cell vector would be 15.8 Å long, oriented $+30^\circ$ from the $TiO_2[110]$. Unless one postulates that this net forms on top of the Pd(111) deposit rather than on the TiO_2 , one is hard-pressed to explain why only those diffraction rays from the net situated near to the Pd(111) rays receive any intensity.

Extended exposure of the TiO_2 substrate to the Auger beam prior to evaporation of Pd enhanced, but was not essential to, the Auger behavior shown in Figure VI-23. Sputtered surfaces also reacted readily with the Pd overlayer to form an intermetallic. Either of these pretreatments increases the surface concentration of the reduced species ascribed to Ti^{3+} 27. The Ti^{3+} may disproportionate to metallic titanium and TiO_2 , with the metallic titanium diffusing through the Pd layer. Since no mass spectrometer was present in the vacuum system, it could not be determined whether evolution of gaseous oxygen, or reaction of lattice oxygen with CO or H from background gases, accompanied the intermetallic

formation.

A different LEED pattern was seen for thick Pd films annealed at 850°C on the TiO₂(750) surface (Figure VI-26). A schematic of this pattern and a real-space interpretation are shown in Figure VI-27. Spots due to Structure A are also present, though with decreasing intensity as the surface is annealed longer. The new spots form a hexagonal mesh with corresponding real-space unit mesh vector of 5.7 Å. In this pattern the overlayer unit cell vector is parallel to the [110] direction of the substrate. This is 90° from the direction of parallelism for Structure A and for the high temperature structure on the (110) surface. The [110] direction is perpendicular to the step edge; the somewhat corrugated proposed structure of the step face may prevent close packing in a direction parallel to the step edge. The observed periodicity is within 5% of 1/3 the terrace width for a (320) surface. The spots, however, are not appreciably split or streaked in the [110] direction, indicating poor coherence of the pattern over the steps. The 5.7 Å unit mesh parameter is close to the sum of two Pd atomic diameters (5.5 Å). A closest-packed Pd layer with one-fourth of the atoms missing from ordered sites (Figure VI-28A) could yield a LEED pattern close to the observed one. Even better agreement is seen between the sum of the nearest neighbor spacings of Pd and Ti (5.7 Å) and the experimental unit mesh length. A stoichiometry of PdTi could give the observed pattern without compression of atoms (Figure VI-28B); however, in intermetallic compounds interatomic distances are likely to be shorter than nearest neighbor spacings in pure metals. A PdTi phase with the CsCl structure and primitive unit cell vector of 3.18 Å has been reported.³¹ Such a structure would have a plane of hexagonal symmetry with unit mesh vector



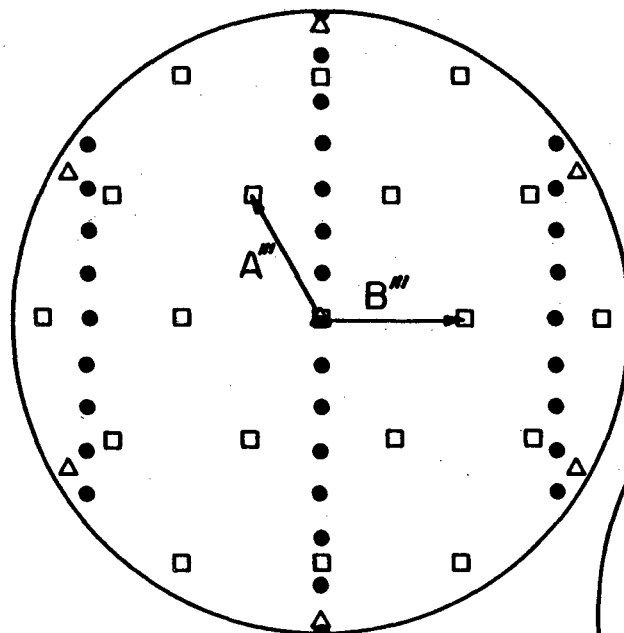
**Pd on TiO₂ (750)
76 eV**

XBB 818-7909

Fig. VI-26

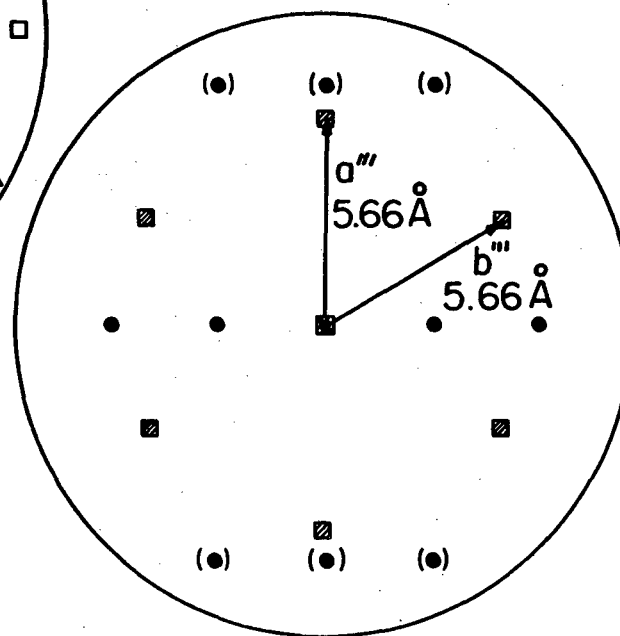
Fig. VI-27.

Structure B (stepped surface)



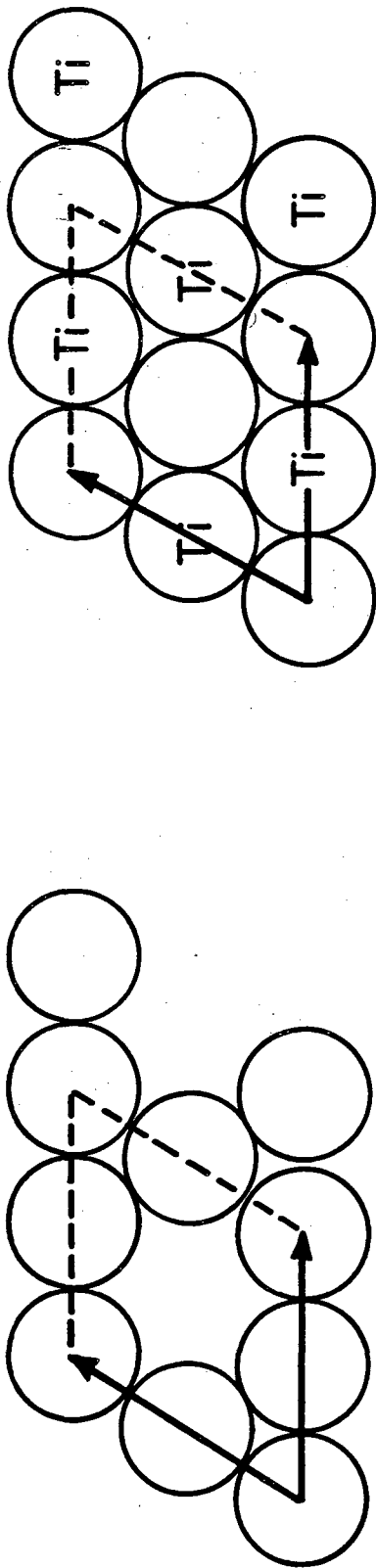
LEED Schematic
(750) TiO₂ + ~12 ml Pd
annealed at 850°C

Real Space



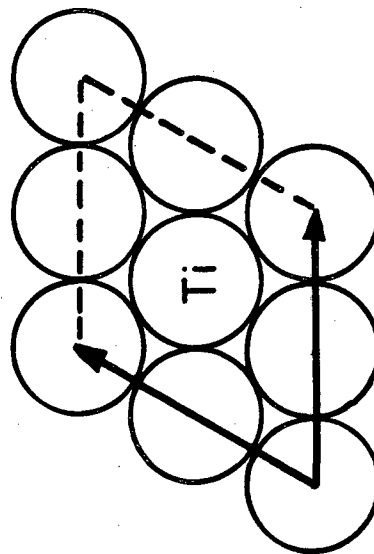
$a''' \parallel \text{TiO}_2 [1\bar{1}0]$

XBL 781-4461



A. $A = 2.75 + 2.75 = 5.50 \text{ \AA}$

B. PdTi $A = 2.75 + 2.92 = 5.67 \text{ \AA}$



C. Pd₃Ti $5.5 \text{ \AA} < A < 5.7 \text{ \AA}$

XBL818-6339

Fig. VI-28. Possible structures based on individual metallic diameters.

of 4.48 Å. Nishimura and Hiramatsu³² have reported a bulk Pd₃Ti phase with a hexagonal basal plane unit cell length 5.5 Å. Our pattern agrees with this unit vector length to within experimental error. The presence of naked TiO₂ surface and Pd (111) crystallites simultaneously with intermetallic crystallites precludes the use of Auger to determine the intermetallic stoichiometry.

4. Film morphology by Auger

Partially ordered LEED patterns have been observed for Pd and Au on TiO₂, but the actual morphology of the deposits is uncertain. Au formed partially ordered layers only in thick deposits, and only the LEED pattern corresponding to Au (111), indicative of very weak substrate effects, was seen. This, combined with Auger behavior upon heating, indicate that gold forms rather thick crystallites with a fair proportion of (111) plane exposed parallel to the substrate surface. Pd, on the other hand, forms several LEED patterns indicative of stronger interaction with the substrate. The Pd (111) structure could be formed with comparatively little metal (1/2 - 2 monolayers) on the surface. The other patterns required thicker Pd films for their formation, but remained visible after the Pd Auger emission decreased greatly following annealing. In sorting out this picture it is useful to consider Auger attenuation data obtained during film growth. Table VI-4 shows results from Auger data for Pd deposited onto TiO₂ at room temperature. Listed are the monolayer coverages calculated by the layer-by-layer model from the Pd peak height, Ti(383 eV) attenuation, and O attenuation respectively. Also calculated are the percentages of the substrate which must be covered by 50 Å Pd hemispheres to give the Pd peak height or O or Ti

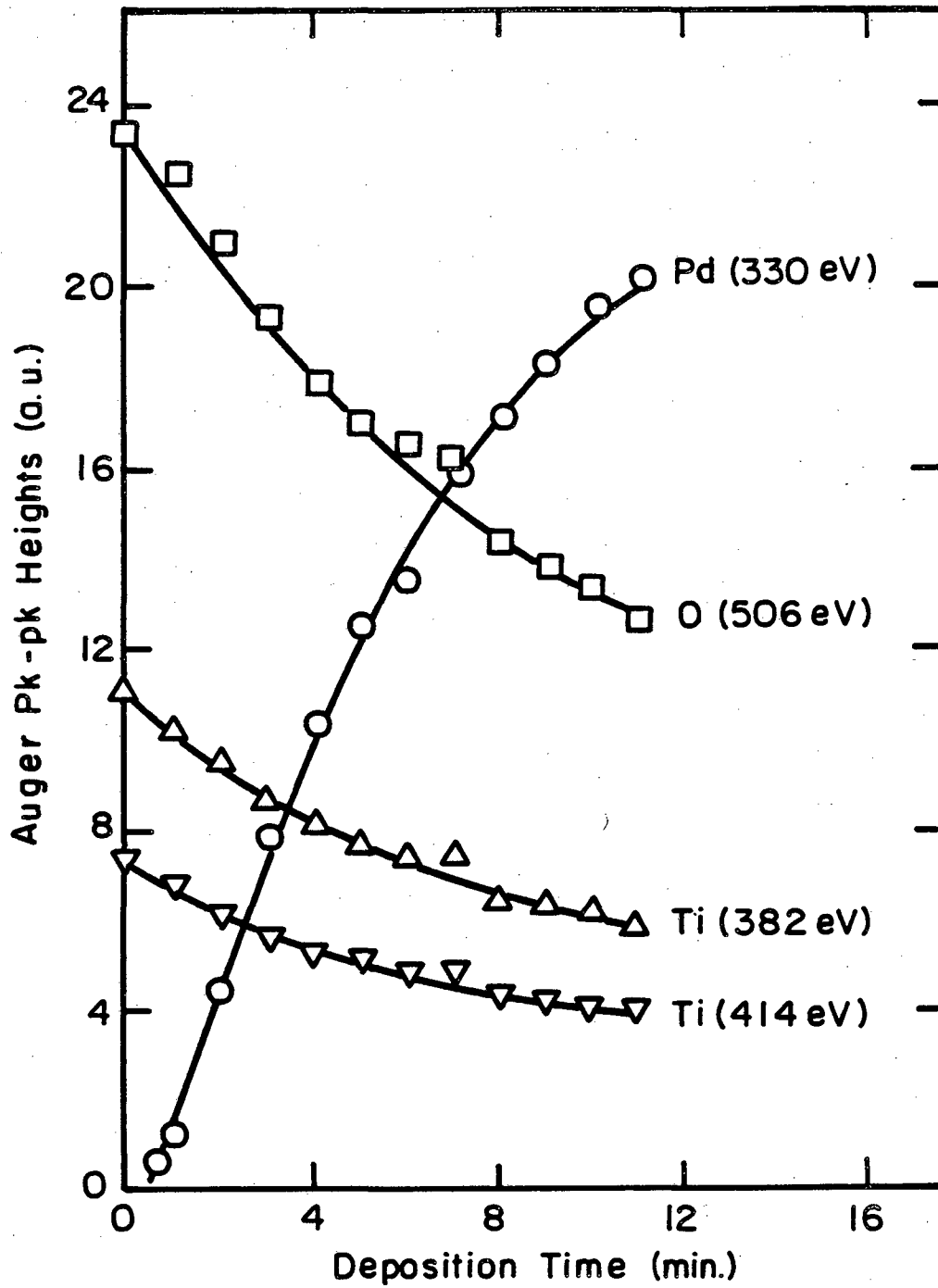
TABLE VI-4: Pd Deposited onto TiO₂ at Room Temperature

Time dep (min)	% ml coverage				% cov 50A islands			
	Pd	Ti	O	sd m	Pd	Ti	O	sd m
1	9.5	21	24	.42	2.6	6.4	6.4	.43
2	16.4	28	39	.41	4.5	8.5	10.6	.39
3	25.5	51	59	.39	6.9	15.5	16.0	.40
4	52.7	62	74	.17	14.3	18.8	20	.17
5	62.7	88	95	.21	17.0	27	26	.24
6	75	95	119	.23	20.4	29	31	.21
7	87	115	141	.24	23.6	34	36	.21
10	110	141	174	.23	30.0	40	43	.18
12	116	158	188	.24	31.5	43	46	.19
				2.54				2.42

attenuations. The internal consistency for the Pd, O, and Ti result within each model are compared. At low coverages (<1 monolayer equivalent) both models give the same degree of fit to the data, with the same trends: i.e. O attenuation always indicates a higher coverage. At higher coverages the island model gives a slightly better fit. The results are inconclusive, due to the similarity in attenuation lengths of the Pd, Ti, and O Auger electrons. No ordered overlayer LEED pattern was observed during Pd deposition onto the substrate at room temperature.

Table VI-5 shows the results of the same calculations on Auger data taken during deposition of Pd onto TiO₂ held at 800°C. The raw Auger peak-to-peak data is plotted against deposition time in Figure VI-29. The Pd flux to the surface during this period is believed to be constant, though in the absence of a film thickness monitor this could not be proven. At coverages less than ~1 monolayer the layer-by-layer model gives slightly better internal agreement. At higher coverages 50 A island populations calculated from the Pd, Ti, and O signals show excellent internal consistency, considerably better than the coverages calculated assuming layer-by-layer growth. At least at coverages over ~1 average monolayer, Pd appears to form islands on TiO₂ at 800°C. Below monolayer coverage no definite distinction between growth modes can be made. Better agreement of the submonolayer data with layer-by-layer growth than with 50 A islands is to be expected at very low coverages, as the islands would initially nucleate at much smaller sizes.

The ability of Auger data to discriminate between different growth modes for the Pd-TiO₂ systems is called into question by Figures VI-



XBL818-6340

Fig. VI-29. Auger signals vs. deposition time, Pd onto TiO_2 at 800°C .

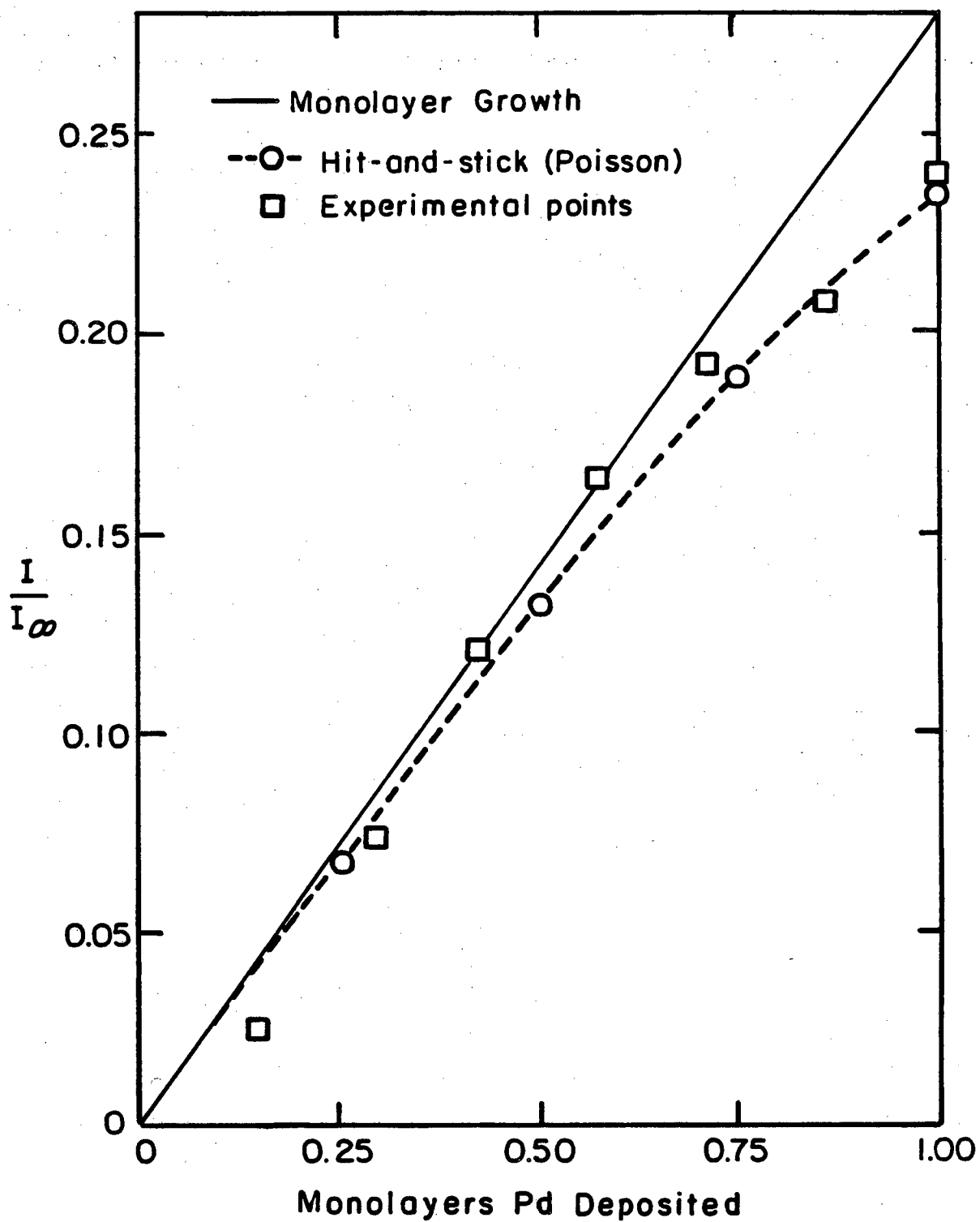
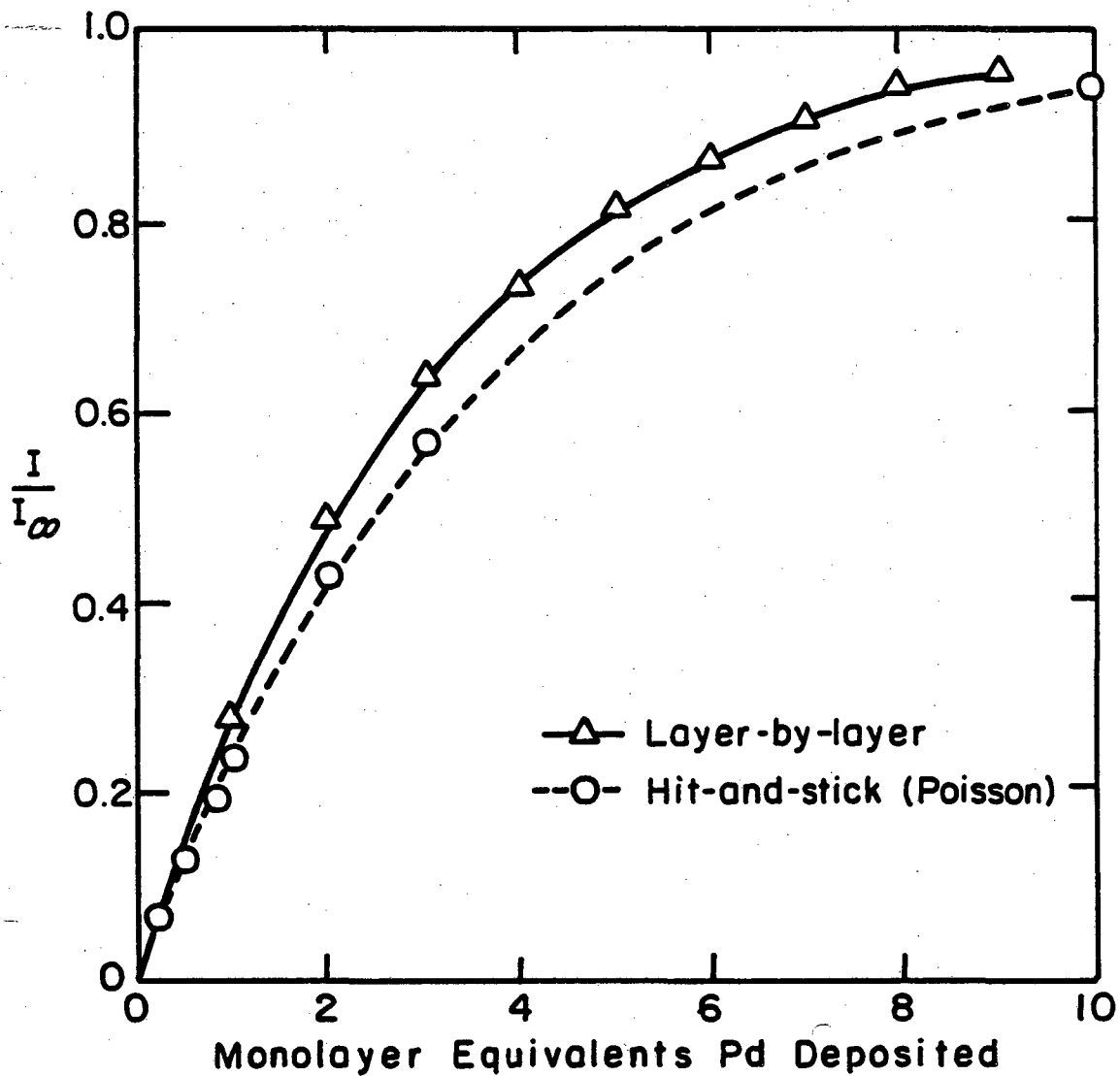


Fig. VI-30. Comparison of layer-by-layer and hit-and-stick models with experimental data, Pd on TiO_2 . Details in text. XBL 818-6341

30,31. In Figure VI-30 the Pd signal expected from layer-by-layer or hit-and-stick (Poisson) growth are plotted as a function of the absolute amount of Pd on the surface (average monolayer coverage). Poisson growth yields 16% lower Pd signal for 1 monolayer total Pd on the surface. The ~10% scatter in Auger measurements makes it doubtful that the perfect linearity of layer-by-layer growth could be distinguished from the slight downward concavity characteristic of Poisson growth, especially if the evaporator flux has any instability. Experimental points for Pd growth on TiO_2 at 800°C are superimposed on Figure VI-30. The x-scale for these points was originally chosen by finding the time required to give 1 monolayer's Pd signal assuming layer-by-layer growth. Since the points showed obvious downward concavity, the x-axis was expanded slightly to bring the final point in concordance with the Poisson-growth curve. The important point is that the experimental points show downward concavity even in the submonolayer region. Thus, even at low coverages, the growth proceeds by a Poisson distribution or an even more agglomerative island mechanism, rather than as a smooth monolayer.

Figure VI-31 compares the Pd signals calculated for layer-by-layer and hit-and-stick models at coverages up to 10 average monolayers. The monolayer growth curve is a series of line segments, the Poisson a smooth curve. The Figure indicates the subtle changes in slope which must be detected to distinguish the two growth modes and indicate the quality of Auger data and the evaporator stability required. The small magnitude of the changes in slope accompanying monolayer growth is due to the relatively high energy, and therefore long attenuation length, of the Pd Auger electrons.



XBL818-6342

Fig. VI-31. Comparison of layer-by-layer and hit-and-stick models. Straight line segments connect triangle points. Monolayer equivalents = mean thickness in monolayers.

TABLE VI-5: Pd on TiO₂ at 800°C

Dep min	ml coverage				fractional coverage 50A hemispheres			
	Pd	Ti	O	sd -- m	Pd	Ti	O	sd -- m
1	.095	.31	.15	.59	.026	.094	.042	.67
2	.364	.49	.47	.15	.099	.148	.127	.19
3	.636	.80	.80	.13	.173	.242	.217	.17
4	.841	1.04	1.09	.13	.229	.311	.291	.16
5	1.02	1.20	1.27	.11	.277	.348	.330	.12
6	1.13	1.36	1.39	.11	.307	.385	.355	.11
7	1.36	1.30	1.47	.06	.370	.369	.371	.003
8	1.49	1.77	1.91	.12	.405	.474	.467	.085
9	1.61	1.86	2.10	.14	.438	.495	.501	.073
10	1.76	1.93	2.26	.13	.478	.512	.528	.051
11	1.86	2.07	2.44	.14	.505	.538	.557	.05
12	1.88	2.13	2.52	.15	.511	.549	.571	.055
13	2.18	2.22	2.70	.12	.592	.564	.600	.032
14	2.21	2.38	2.78	.29	.601	.591	.614	.020
15	2.21	2.41	2.85	.13	.601	.596	.626	.026

Auger data suggests that Pd forms islands on TiO_2 at 800°C , at least at average thicknesses greater than one monolayer. The two LEED structures formed from thick Pd layers at high temperatures give evidence for a rather strong Pd- TiO_2 interaction. This seeming contradiction can be understood when it is realized that several phases are present on the surface at once. For all but the thickest layers deposited at room temperature before annealing, some TiO_2 surface is uncovered, allowing substrate LEED spots to be seen. Structure A (Pd or Au(111)) is seen from crystallites which can be either quite thick or thin (Figure VI-21). Formation of Structures B requires that Pd be in contact with TiO_2 at high temperatures. Unless the film is thick the Pd will agglomerate at high temperatures, leaving only a small fraction of the surface covered by Pd long enough to allow the Pd- TiO_2 reaction to occur. In thick layers where most of the surface is covered by large crystallites Pd is held in contact with TiO_2 long enough to form one of Structures B over much of the surface. Further annealing causes additional agglomeration of overlying Pd, leaving thin layers of the phases yielding Structures B exposed to the LEED beam.

VI-5 Comparison of Results for Pd and Au on Graphite, $\alpha\text{-Al}_2\text{O}_3$, and TiO_2

Parallel experiments on three different substrates with two metals have yielded several points of contrast:

- 1) Pd and Au formed partially ordered structures on TiO_2 but gave no indications of ordering on $\alpha\text{-Al}_2\text{O}_3$ or graphite. On TiO_2 , Pd ordered more readily than did Au.

- 2) The only system giving Auger evidence for a chemical reaction between substrate and deposit was Pd on TiO₂. This was also the only system giving LEED structures not explicable as due to unreconstructed crystallites of the pure deposit metal.
- 3) At very low coverages Pd gave evidence of electronic structure typical of very small particles on graphite and to a lesser extent on α -Al₂O₃, but not on TiO₂.
- 4) On all three substrates Auger attenuation data was most consistent with an island formation mode of film growth for average film thickness greater than 1 monolayer. Island growth also seemed most probable at submonolayer coverages on graphite and α -Al₂O₃; on TiO₂ no determination could be made.
- 5) The presence of steps on a TiO₂ surface altered the high-temperature Pd LEED structure, rotating the direction of epitaxial parallelism 90°. The presence of steps had no effect on the structure or epitaxial relations of the lower-temperature Pd and Au(111) crystallites.

Point (1) is indicative of the stronger interactions of metals with TiO₂ than with α -Al₂O₃, even at temperatures where no intermetallic compound is formed. In terms of lattice mismatch, epitaxy for Pd is more favored on α -Al₂O₃ than on TiO₂, yet the reverse behavior was observed. The results show an interesting parallel to chemisorption studies by Tauster¹, Horsely², and others which show a strong metal-support interaction for noble metals on TiO₂, with sintering temperatures below those required to produce a bulk intermetallic phase.

The special structures seen for Pd on TiO₂ are probably related to the exceptional stability of Pd-Ti intermetallic compounds predicted by the Engel-Brewer correlation.³³ The formation of these compounds can be viewed as a Lewis acid-Lewis base reaction wherein electrons from the nearly-filled Pd d-band flow into the Ti d-band to give a particularly stable configuration. Free energies of formation for Pt₃Ti³⁴ and Ni₃Ti³⁵ are -71.3 and 32 kcal/g atom Ti, respectively. Since the 2nd and 3rd rows transition elements are closer in d-electron character than the 2nd and 1st rows, the Pd₃Ti free energy of formation is expected to be closer to that of the Pt compound. This is still not enough to make intermetallic formation from Pd and stoichiometric TiO₂ exergonic at room temperature in the absence of a reducing agent, since ΔG_f^0 for TiO₂ is -203.8 kcal/g-atom Ti and a change to 10⁻¹⁰ torr oxygen pressure shifts this by only 18 kcal. Argon sputtering and electron beam damage enhanced intermetallic formation, which seems to involve the Ti³⁺ found in the vacuum-reduced crystal.

Point (3) seems at first inconsistent with points (1) and (2), since better ordering, if achieved through smooth monolayer formation, implies higher dispersion and thus less bulk-like electronic structure for the deposit. The results may provide some insight into the mechanism behind the splitting of the Auger peak. If the splitting is due primarily to crystal-field effects, the presence of an ordered environment, whether composed of Pd atoms or the TiO₂ substrate, in a specific orientation may be sufficient to split the Pd 3d levels. Alternately, the better ordering in TiO₂ may be due to higher rates of surface diffusion rather than to thermodynamic considerations. Detailed studies combining photoemission, electron microscopy, and absolute measures of metal

coverages are needed to sort this out.

The indications of overall island growth are in accordance with surface free energy considerations. The appearance of LEED patterns from thick island films lends credence to earlier calculations showing³⁶ that flat-faced polyhedral, rather than hemispherical, islands are often formed by fcc metals. The apparent presence of several ordered Pd-containing phases simultaneously on TiO_2 surfaces complicates studies of these systems. The development of advanced LEED systems with electron beam sizes small enough to sample single domains would advance the understanding of these multiphase surface systems.

Point (5) shows that epitaxial relations on stepped surfaces can be quite different from those on the vicinal low index surfaces. Such effects could modify the properties of thin-film electronic devices to disadvantage or advantage. While no superbly ordered structures such as those envisaged in Figure VI-1 were observed, the results reported here show that continued studies of the effects of substrate-deposit chemistry and of ordered defects, such as steps, on the morphology and crystal structure of metal films on semiconductor substrates can yield results of both catalytic and electronic interest.

REFERENCES:

1. S.J. Tauster, S.C. Fung and R.L. Garten, J. Am. Chem. Soc., 100, 170 (1978).
2. J.A. Horsley, J. Am. Chem. Soc., 101, 2870 (1979).
3. F.C. Frank and J.H. van der Merwe, Proc. Roy. Soc., A 198, 205 (1949).
4. M. Volmer and A. Weber, Z. Physik. Chem., 119, 277 (1925).
5. I.N. Stranski and L. Krastanow, Zeitschr. f. Krist., 83, 155, 1932.
6. J.P. Biberian and G.A. Somorjai, J. Vac. Sci. Technol., 16, 2073 (1979).
7. A. Sepulveda and G.E. Rhead., Surf. Sci., 66, 436 (1977).
8. D. Paraschkevov, W. Schlenk, R.P. Bajpai, and E. Bauer, Proceedings 7th Int. Vac. Congress, Vienna, 1977, p. 1737.
9. D. Schmeisser and K. Jacobi, Surf. Sci., 88, 138 (1979).
10. J. Mathews and R.L. Walker, Mathematical Methods of Physics, W.A. Benjamin, New York, 1965, p. 356.
11. T. Pynchon, Gravity's Rainbow, Viking/Compass, New York, 1973, p. 85.
12. J.W. Mitchell, in Structure and Properties of Thin Films, C.A. Neugebauer, J.B. Newkirk, and D.A. Vermilyea, ed., Wiley, New

York, 1959, p. 4.

13. R.B. Greeger and F.W. Lytle, Jour. Catal., 63, 476 (1980).
14. N.F. Graves, A.W. Moore, and S.L. Long, "Structure, Properties, and Applications of Highly Oriented Graphite", Union Carbide, presented at 9th Biennial Conf. on Carbon, Boston, 1969.
15. J.A. Bearden and A.F. Burr, Rev. Mod. Phys., 39, 125 (1967).
16. C. Norris and H.P. Meyers, J. Phys. F: Metal Phys. 1, 62 (1971).
17. L. Ley, S.P. Kowalczyk, F.R. McFeely, and D.A. Shirley, Phys. Rev., 10, 4881 (1974).
18. Y. Onder and Y. Togozaawa, J. Phys. Soc. Jpn., 22, 833 (1977).
19. R.P. Messmer, S.K. Knudsen, K.H. Johnson, J.B. Diamond, and C.Y. Wang, Phys. Rev. B, 13, 1396 (1976).
20. R.C. Baetzold, M.G. Mason, and J.F. Hamilton, J. Chem. Phys., 72, 366 (1980).
21. D.E. Eastman and W.D. Grobman, Phys. Rev. Lett., 30, 177 (1973).
22. T.M. French, Ph.D. Thesis, U. Calif., Berkeley, 1971.
23. C.C. Chang, in The Structure and Chemistry of Solid Surfaces, G.A. Somorjai, ed., Wiley, New York, 1969, p. 77-1.
24. F.J. Szalkowski, Ph.D. Thesis, U. Calif., Berkeley, 1973, p. 66.
25. F.T. Kuyers, B.M. Tieman and V. Ponec, Surf. Sci. 75, 657 (1978).

26. H. Bruining, Physics and Applications of Secondary Electron Emission, Pergamon Press, London, 1954.
27. Y.W. Chung, Ph.D. Thesis, U. Calif., Berkeley, 1977.
28. C.S. Hurlbut, Jr., C. Klein, Manual of Mineralogy, 19th ed., Wiley, New York, 1977, p. 272.
29. G. Ertl and J. Küppers, Low Energy Electrons and Surface Chemistry, Verlag Chemie, Weinheim, 1974, p. 169.
30. P.N. Ross, Jr., unpublished data.
31. H.C. Donkersloot and J.H.N. Van Vucht, J. Less-Common Metals, 20, 83 (1970).
32. H. Nishimura and T. Hiramatsu, J. Japan Inst. Metals, 22, 38 (1958).
33. L. Brewer, Science, 161, 115 (1968).
34. P.J. Meschter and W.L. Worrell, Metallurgical Transactions A, 299 (1976).
35. O. Kubaschewski, Trans. Faraday Soc., 54, 814 (1958).
36. W. Romanowski, Surf. Sci., 18, 373 (1969).

Chapter VII General Discussion

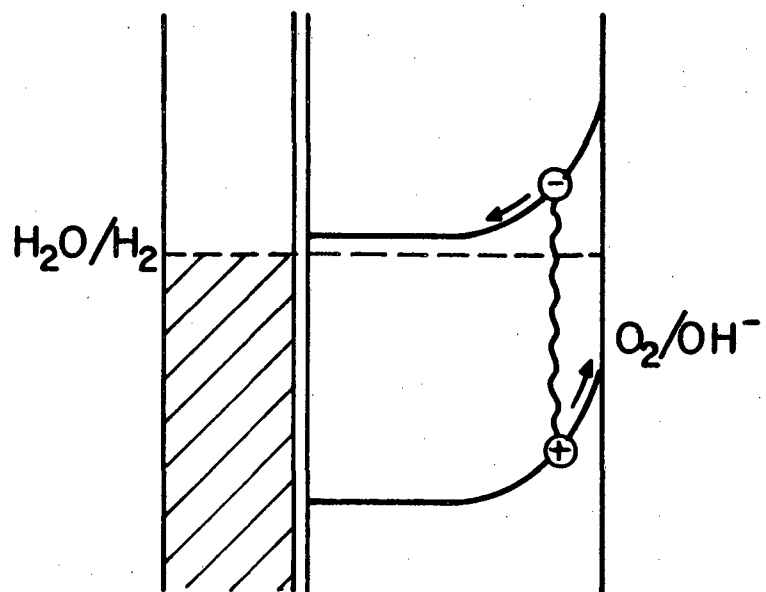
VII-1 Hydrogen Production on Metal-Free Oxides

The photogeneration of hydrogen on metal-free SrTiO_3 raises several questions. Does it occur through a mechanism totally analogous to the operation of a photoelectrochemical cells, or is some other mechanism, possibly more amenable to single-surface gas-phase photocatalytic reactions involved? Does correlation of a low flatband potential for the semiconductor with successful operation of a water-photolysis cell also hold for this process? And what role, if any, do "surface states", or surface impurities, play?

According to the standard photoelectrochemical paradigm no hydrogen should be evolved from Pt-free SrTiO_3 , as shown in Figure VII-1. Upon immersion of SrTiO_3 in an aqueous electrolyte, a majority carrier depletion layer forms at all exposed semiconductor surfaces. When a photon is absorbed within the depletion layer the photogenerated hole is driven by the electric field towards the semiconductor surface, while the photogenerated electron is driven into the semiconductor bulk. If part of the SrTiO_3 is platinized the electron can pass relatively freely to the platinum, from which point it is in equilibrium with the $\text{H}_2\text{O}/\text{H}_2$ couple, providing the Pt surface has already been charged with hydrogen. On a metal-free crystal significant depletion layers and therefore surface barriers form at all crystal surfaces; by the simple photoelectrochemical model the electrons would not be expected to reach the semiconductor surface, and thus no reductive photochemistry is expected.

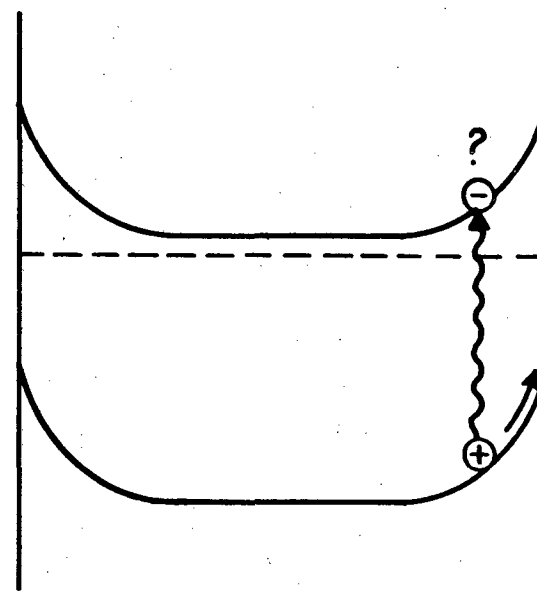
Photogenerated electrons can under some circumstances tunnel through the depletion layer barrier to a surface state (Figure VII-2).

Photochemical Diode



Pt n-SrTiO₃

Metal-free Crystal



n-SrTiO₃

XBL802-4704

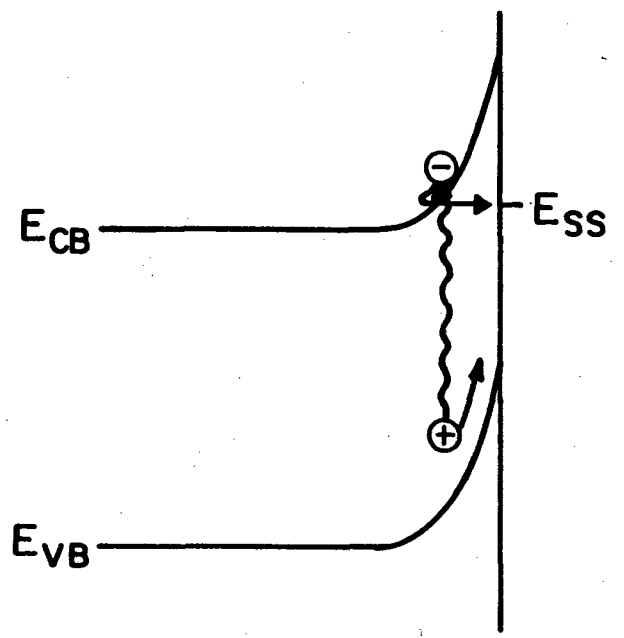
Fig. VII-1. Comparison of charge carrier access to the surfaces of platinized and metal-free SrTiO₃ crystals.

Parkinson et. al. ¹ have invoked such a "shunting" mechanism to explain current losses in GaAs-based liquid junction solar cells and their mitigation through the adsorption of ruthenium ions. For such tunneling to occur with adequate probability several requirements must be met: (1) A surface state must lie between the surface conduction band edge (\sim at U_{fb} for a highly doped semiconductor) and the bulk position of the conduction band, and (2) the width of the depletion layer barrier at the energy of the surface state must be quite narrow to allow a sufficiently high probability of elastic tunneling. Condition (1) may be met on $SrTiO_3$. Although the major surface state identified on $SrTiO_3$ by photoelectron spectroscopy, a Ti^{3+} state 0.6 eV below the Fermi level, lies below (anodic of) the hydrogen couple and thus is an unlikely intermediate in hydrogen production, there is some evidence for states due to the ubiquitous carbonaceous impurities which lie in the proper energy range. However, condition (2) runs awry of experimental results, as equivalent rates of hydrogen photogeneration were seen on highly reduced and on stoichiometric crystals. The depletion layer barrier at a given energy is much narrower in the former, and any mechanism relying on tunneling through the surface barrier would be expected to proceed much more rapidly on the strongly doped crystal.

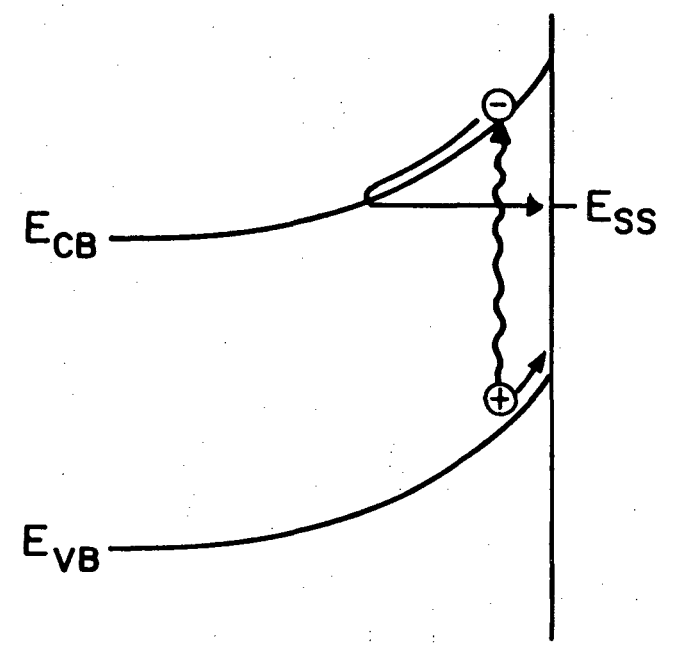
Another mechanism whereby photogenerated electrons could reach the semiconductor surface despite the depletion layer barrier is through hot carrier injection, a concept proposed in a photoelectrochemical context by Boudreaux et. al. ² The principles of hot carrier injection from an n-type semiconductor are sketched out in Figure VII-3. When a photon with energy greater than the bandgap is absorbed, electrons and holes will be formed in states removed energetically from the conduction and

Figure VII-2. ELECTRON TUNNELING TO SURFACE STATE

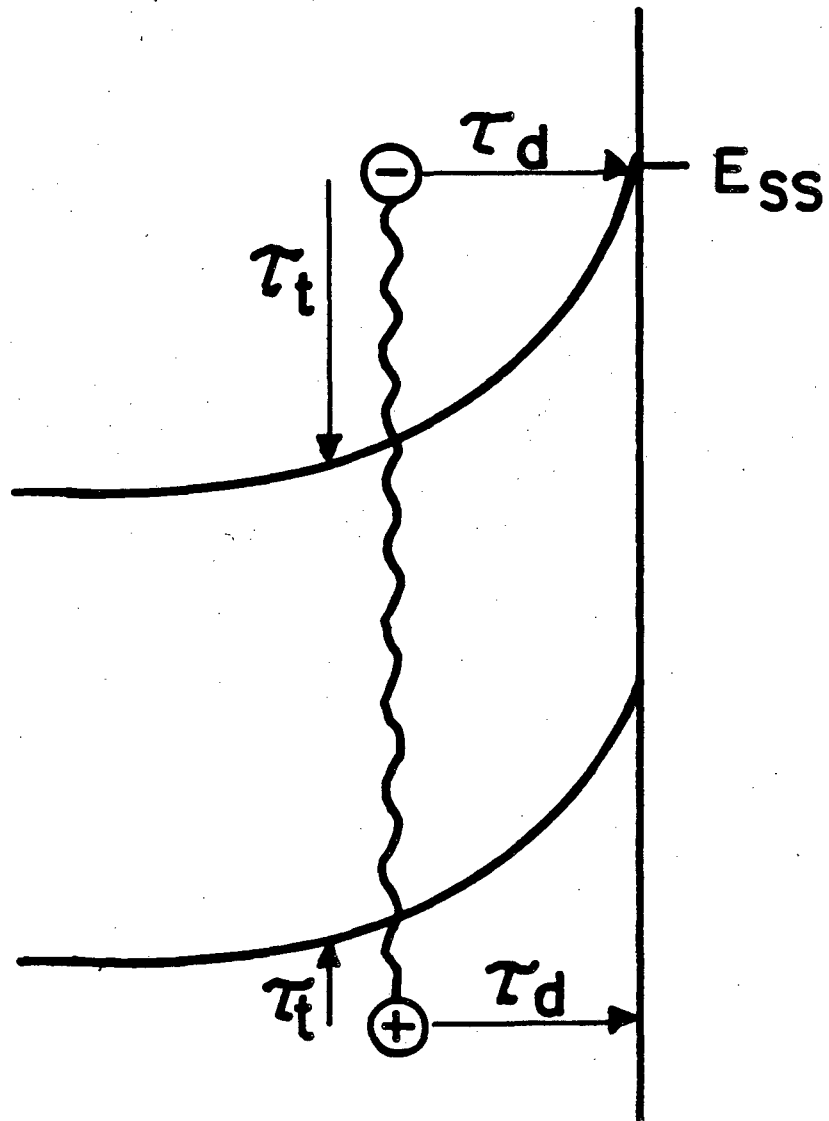
Heavily Doped Crystal



Lightly Doped Crystal



XBL 802-4705

Fig. VII-3. **HOT CARRIER INJECTION**

XBL802-4706

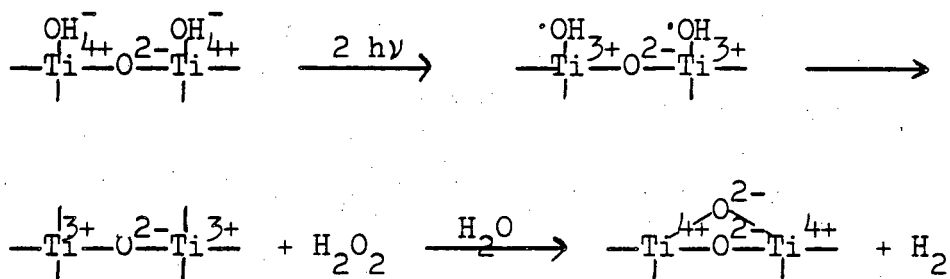
valence band edges. Under normal conditions, the hot carriers will be thermalized (with a characteristic time τ_t) through interactions with phonons and will rattle down in energy through the near-continuum of available states until they reach the band edges. However, if the characteristic time for diffusion to the surface τ_d is short with respect to τ_t , hot carriers may reach the surface with supra band-edge energies. If the rate of reaction of surface carriers with the fluid phase is again more rapid than thermalization, or if hot carriers can be trapped by a surface state, chemistry outside the thermodynamic limits imposed by the band edges can occur, and the depletion layer barrier can be effectively surmounted by majority carriers.

Dickson and Nozik³ have reported evidence for the injection of hot minority carriers from p-GaP, and Boudreaux et. al.² have argued that hot hole injection from n-TiO₂ is probable. Nozik⁴ has expressed some belief that hot injection of majority carriers may be possible. However, the probability of hot carrier injection decreases with an increase in the effective mass of the carriers; if the effective mass of holes in TiO₂ is taken as >0.1, hot hole injection becomes much less probable. Though no effective masses for electrons in SrTiO₃ have been reported, similarities to TiO₂ indicate that it is probably a light hole-heavy electron material.⁵ Unless actual measurements indicate a lighter electron in SrTiO₃, injection of hot electrons from SrTiO₃ should be considered unlikely. It should be noted that the details of Boudreaux et. al.'s calculations require quantization of the levels available to hot minority carriers in the potential well defined by the depletion layer barrier and the Helmholtz layer. For majority carriers this is not a well but a hill, and the quantum approach breaks down.

One must then rely on classical estimates of diffusion rates, which are also treated by Boudreaux and still indicate the likelihood of hot carrier injection, at least of minority carriers. The classical arguments, however, are weaker.

Neither a tunneling shunt nor hot carrier injection provide an acceptable explanation of how electrons photogenerated within SrTiO_3 can surmount the depletion layer to reach the surface of a metal-free crystal and drive the observed evolution of hydrogen. Since the method by which bulk electrons could reach the surface is not clear, it is of interest to consider whether all of the driving force for the observed hydrogen production could be due to photons absorbed in the first Ti-O layer of the surface. The total flux of photons with energies greater than 3.2 eV under experimental conditions was about $2 \times 10^{16} \text{ cm}^{-2} \text{ s}^{-1}$. About half of these photons were in a spectral peak about 3.4 eV; the other half were centered about 3.9 eV. Around room temperature the absorption coefficient α for SrTiO_3 is $6 \times 10^3 \text{ cm}^{-1}$ at a photon energy of 3.4 eV⁶ and $3 \times 10^5 \text{ cm}^{-1}$ at 3.9 eV.⁷ By use of these absorption coefficients one can calculate that 0.3% of the incident bandgap light would be absorbed within 2.26 \AA (the interlayer spacing of closest-packed Sr-O (111) planes) of the surface. This 0.3% of the incident light would lead to hydrogen production of 100 monolayers per hour assuming a 100% quantum yield. The observed hydrogen production rates were up to 100 monolayers per hour and were thus in a range consistent with effective photoexcitation in the surface layer only. Figure VII-4 shows one possible mechanism involving direct absorption of light by surface species (after Van Damme and Hall).⁸ In this mechanism absorption of a photon causes conversion of a surface bound hydroxyl group to a hydroxyl radical, with

Fig.VII-4 DIRECT ABSORPTION OF LIGHT AT THE SEMICONDUCTOR SURFACE

Van Damme and Hall, JACS 101 4373

$$\alpha_{3.4\text{eV}} = 6 \times 10^3 \text{ cm}^{-1} \implies 0.01\% \text{ of light absorbed in surface layer (2.3 \AA)}$$

$$\alpha_{3.9\text{eV}} = 3 \times 10^5 \text{ cm}^{-1} \implies 0.7\% \text{ of light absorbed in surface layer (2.3 \AA)}$$

the accompanying reduction of a surface Ti^{4+} to Ti^{3+} . Such localized absorption of light could lead to quite different spectral absorptivities from those reported for bulk $SrTiO_3$. If purely local excitation of the $Ti-OH^-$ bond were involved, one might expect TiO_2 to be as active as $SrTiO_3$. In actuality no photoactivity was observed on metal-free TiO_2 . Very rough spectral characteristics of hydrogen photogeneration were studied by interchanging 7-51 and 7-54 filters. The 7-54 filter passes a higher proportion on 3.9 eV vs. 3.4 eV light.⁹ The results did not show much greater efficacy for 3.9 eV light as predicted by the surface absorption model assuming bulk absorption coefficients. Though the magnitude of hydrogen production from metal-free crystals is such that effective photoexcitation of only the surface is a plausible model, the wavelength dependence appears wrong.

The results of Ferrer¹⁰ on hydrogen photogeneration and crystal oxidation in low pressure water vapor (Section V-2) also argue against direct photogeneration of surface Ti^{3+} as the source of reducing power for hydrogen generation. Illumination of $SrTiO_3$ in water vapor caused a decrease in Ti^{3+} as measured by UPS, apparently due to oxidation of Ti^{3+} directly by photogenerated holes or by an adsorbed oxygen species of valence greater than -2 which had been produced through illumination. In the absence of any evidence for a reduced surface species whose photogeneration correlates with the generation of hydrogen from water, it appears that reductive chemistry proceeds through electrons photoinjected into delocalized states in the conduction band. One is then still left with the problem of getting these electrons up over the depletion layer-barrier of metal-free crystals.

To this point it has been assumed that a full depletion layer barrier will form on SrTiO_3 , even when no metal is present to serve as a counterelectrode. This cannot be taken for granted. As discussed in Chapter II, no single Fermi level can be defined for an electrolyte containing both dissolved oxygen and dissolved hydrogen. SrTiO_3 is a reversible electrode for the evolution of neither of these gases. Although the Fermi level of n- SrTiO_3 in contact with H_2 -charged Pt will be fixed at the energy of the hydrogen couple, the electron Fermi level of Pt-free SrTiO_3 in contact with electrolyte will not be well-defined. On the metallized surface, the tying of the electron Fermi level to the $\text{H}_2\text{O}/\text{H}_2$ couple prevents complete flattening out of the band structure during illumination. In the absence of metal the bands will be almost completely flattened out during illumination, and photogenerated electrons could face but a small barrier in diffusing to the surface. The hydrogen production seen on metal-free crystals corresponds to a quantum efficiency of $\sim 0.3\%$. The Fermi-Dirac distribution indicates that 0.3% of electrons at 41°C have an energy 0.16 eV above the Fermi level. Under dark conditions a SrTiO_3/Pt PEC cell has 0.18 V band bending. 11

Even without much flattening of bands upon illumination, the level of hydrogen photoproduction observed on metal-free crystals is thus in accord with simple thermal excitation of electrons over the small depletion layer barriers expected at zero applied potential.

The above discussion has assumed that no islands of cathodically active material are present on the metal-free surface. The possibility of metallic impurities or locally reduced areas of the SrTiO_3 serving as microcathodes in strict analogy to PEC cell operation has been dealt with in Chapter V. The nearly ubiquitous presence of a hydrocarbon or

graphitic residue on the surface of SrTiO_3 exposed to liquid water raises similar questions. Besides providing surface states which can make possible elastic tunneling of electrons to states in the electrolyte, the carbon deposit could serve as a simple cathode. Although the carbon coverage seemed uniform, Auger analysis may have missed or integrated over local concentrations of carbon. Carbon, while not an excellent electrocatalyst for hydrogen evolution, does give measureable activity, especially in concentrated alkali solutions. Exchange currents of up to $30\mu\text{A}/\text{cm}^2$ with a Tafel slope of 148 mV have been measured¹² for graphite in 40% NaOH at 40°C . This is sufficient to explain the μA equivalent photocurrent levels observed on metal-free crystals, even if only a small portion of the surface is covered by carbon sufficiently thick to be cathodically active.

No hydrogen photogeneration was observed on metal-free TiO_2 or $\alpha\text{-Fe}_2\text{O}_3$. If a purely local process were responsible for hydrogen generation, TiO_2 as well as SrTiO_3 would be expected to be active since they both contain similar Ti-O quasi-octahedra as the optically active centers. The electron affinities of both TiO_2 and Fe_2O_3 are sufficiently high that their conduction band edges lie below the electron acceptor state in water. The correlation of low semiconductor electron affinity with photoactivity at zero applied potential thus appears valid for this single-surface photocatalytic reaction as well as for PEC cells.

In conclusion, although the equivalent hydrogen photoproduction observed on stoichiometric and n-type SrTiO_3 and the evolution of H_2 on only the illuminated surface seem to hint at a more localized process

than that responsible for the majority of photocurrent in SrTiO₃-Pt PEC cells, no direct evidence for such a localized process has been obtained. The photoactivity of metal-free crystals can be understood in terms of photogeneration of electrons and holes in the delocalized bands of SrTiO₃ and the diffusion of both carriers to the surface. Although the primary excitation appears to be into delocalized bands, it remains possible that, in contrast to PEC cells, the photogenerated electrons and holes reach the surface at sites interspersed on the atomic scale. Such interspersions could explain some of the disproportionation chemistry discussed in Section V-2-2, and may be a clue to the choice of reactions for which heterogeneous photocatalysis may be particularly suitable.

The correlation of a negative flatband potential (vs. RHE) with activity for water photolysis at zero applied potential appears valid for photocatalytic systems as well as for PEC cells. The Ti³⁺ surface state probably plays a role in binding water to the semiconductor surface. It does not appear to be the primary reductant for water. Carbon-containing impurities with energy levels suitable for mediating charge transfer between semiconductor and electrolyte, are present on all SrTiO₃ surfaces exposed to liquid water.

VII-2 Hydroxide Concentration Effects on SrTiO₃ Photoactivity

The effects of changing the concentration of a sodium hydroxide electrolyte on hydrogen photoproduction from platinized and metal-free crystals were shown in Figures V-14 and V-19, respectively. On platinized crystals the concentration dependence of hydrogen photoproduction

is weak in the concentration range 10^{-3} -5N but becomes stronger above 5N. Roughly parallel behavior was observed on metal-free crystals although no hydrogen photogeneration could be detected below 5N. No hydrogen evolution was seen in either case from neutral or acidic solutions (Tables V-3 and V-4) or from pure water vapor at room temperature when no crust of a basic ionic compound was present. No definite cation effects were observed. The different rate observed with vapor saturated films of CsOH is believed to arise from the different water-absorbing properties of this compound relative to other alkali hydroxides. We will therefore describe the observed phenomenon simply as "hydroxide dependence", although the possible role of other bases has not yet been thoroughly explored.

The observed hydroxide dependence could arise from (1) indirect kinetic control through an increase in band-bending associated with hydroxide adsorption, (2) direct participation of hydroxide in a rate-limiting step, or (3) stabilization of new activated complexes or products or destabilization of reactants in highly alkaline solutions. Our data and those of others provide some means of distinguishing between these possibilities.

In section II-2-3 it was argued that the thermodynamic parameters controlling water photodissociation on platinized SrTiO_3 would be unaltered by changes in the electrolyte pH since the SrTiO_3 band edges and the hydrogen and oxygen redox couples would all undergo the same potential shift. As these arguments were based on the assumption of unit activity coefficients, they should be reexamined for applicability at very high electrolyte concentrations.

The activity of water, the mean molal activity coefficient for NaOH, and dissociation constant of water undergo significant changes at high NaOH concentrations. Macdonald and McKubre¹³ have assembled extensive data on these effects. Table VII-1 gives results derived from their tables, with concentrations in molarity at 20°C (as has been used throughout this work) despite the fact that the data is for 40°C, the operating temperature of the borosilicate reaction vessel. As expected, the activity of water decreases monotonically with NaOH concentration, dropping to half the activity of pure water at 14M. The dissociation constant of water decreases at higher NaOH concentrations, as indicated by the increase in the pKs. The pH, as calculated from the a_w , pKw, and γ_+ values and assuming a NaOH dissociation constant of 0.2 kg mol^{-1} , shows a shallow maximum at 6M, which is also the concentration at which KOH solutions show the highest conductivity. Ferse,¹⁴ using a method involving ternary electrolytes, has derived individual activity coefficients for Na^+ and OH^- ions in concentrated aqueous NaOH. By his determination γ_{OH^-} reaches a shallow minimum of 0.3 at 3M, then climbs monotonically through 0.7 at 14M. γ_{Na^+} , on the other hand, shows a steep monotonic rise with increasing concentration, exceeding 4.0 at 6M.

A drop in water activity from 1.0 in dilute solutions to 0.53 in 14M NaOH causes a theoretical increase in the overall ΔE^0 for water electrolysis of 8 mV, not a significant change. Table VII-2 shows the shifts in the H_2 and O_2 evolution redox couples associated with the a_w 's listed in Table VII-1 and either the γ_+ from VII-1 or the γ_{OH^-} from Ferse. At 1M the redox couples are slightly anodic (further from vacuum level) than would be predicted using activity coefficients of unit. Ignoring activity coefficients, one would expect a cathodic shift of

TABLE VII-1

Activity coefficients for water, negative logs of autoionization molality products, mean molal activity coefficients, and pH's for concentrated aqueous NaOH solutions at 40°C. Data from reference 13.

NaOH conc.	a_w	pQ_w^*	γ_{\pm}	pH
1M	0.97	13.28	0.60	13.4
5M	0.84	13.64	0.74	14.3
10M	0.66	13.84	1.29	14.2
14M	0.53	13.88	2.01	14.0

* $pQ_w = -\log (m_{H^+} m_{OH^-})$.

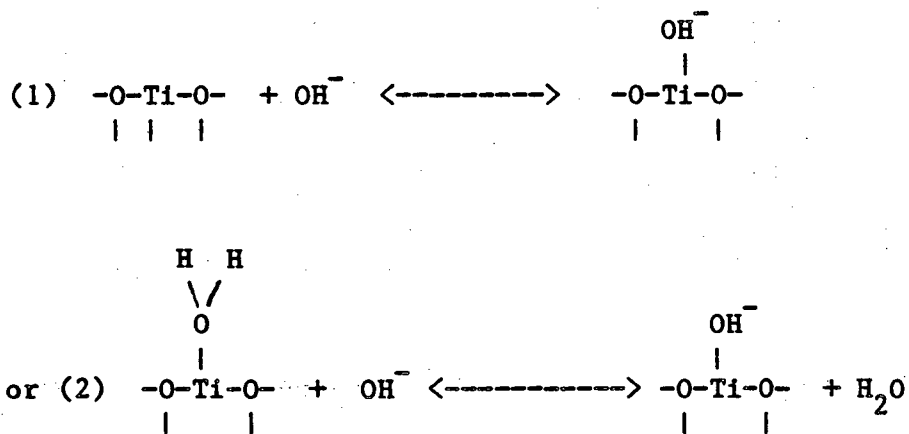
TABLE VII-2

Deviations of redox couple energies from values calculated assuming unit activity coefficients. Negative values denote a cathodic shift (towards vacuum level).

	NaOH conc.	
	1M	14M
Using γ_{OH^-} :		
$\Delta E \text{ H}_2\text{O}/\text{H}_2$	31 mV	-7 mV
$\Delta E \text{ O}_2/\text{OH}^-$	31 mV	1 mV
$\Delta U_{\text{fb}}(1)$	31 mV	9 mV
$\Delta U_{\text{fb}}(2)$	31mV	-7mV
Using γ_+ :		
$\Delta E \text{ H}_2\text{O}/\text{H}_2$	13 mV	-34 mV
$\Delta E \text{ O}_2/\text{OH}^-$	13 mV	-26 mV
$\Delta U_{\text{fb}}(1)$	13 mV	-18 mV
$\Delta U_{\text{fb}}(2)$	31mV	-34 mV

both redox couples by 59 mV for each decade increase in hydroxide concentration. Taking into account the activity coefficients, this cathodic shift is augmented by ~30 mV/decade at high concentrations. Consideration of the activity coefficients thus leads to predicted shifts in the redox levels which would lead to a net decrease in band-bending at higher concentrations if the band edges were not similarly altered by the activity coefficients.

The effects of deviations from ideality on the energies of the band edges are harder to predict than the effects on the redox couple energies. The pH-dependent part of the flat-band potential can be described as due to one of two reactions, depending on whether or not one views molecular water as being strongly bound to SrTiO₃:



If reaction (2) determines the flatband potential both the hydroxide activity coefficient and the activity of water will have effects; if (1) holds only γ_{OH^-} is important. The changes in flat-band potentials associated with each of these reactions is also given in Table VII-2.

The thermodynamic value most likely to affect the quantum efficiency of water photolysis on $\text{SrTiO}_3\text{-Pt}$ is $U_{\text{fb}} - E_{\text{H}_2\text{O}/\text{H}_2}$, as this quantity determines the maximum possible band-bending at zero applied potential. This value should be large (and negative on the electrochemical energy scale) to ensure strong band bending and thus efficient separation of photogenerated charge carriers. If molecular water is not strongly adsorbed on SrTiO_3 (in agreement with chemisorption studies in vacuo) and reaction (1) determines the flatband potential, the change in the activity of water should lead to a 16 mV decrease in band bending as the NaOH concentration is raised from 1 to 14M. If reaction (2) determines U_{fb} , the band-bending should be totally independent of electrolyte concentration. Thus the addition of experimentally-derived activity coefficients to the theory which otherwise predicts no hydroxide concentration effects is not sufficient to bring the theory in line with experimental results. If anything, the activity coefficient effects, which are very small, push the results in the wrong direction.

The foregoing theoretical model assumes that the flatband potential can be shifted through the adsorption of H^+ and OH^- only. In view of the high Na^+ concentrations used here and the very high γ_{Na^+} reported by Ferse in concentrated solutions, this assumption is probably false. Adsorption of Na^+ would shift U_{fb} to more cathodic potentials, thereby increasing the band bending. Though such an effect almost surely occurs to some extent, it alone is not responsible for the higher photoactivity of SrTiO_3 in concentrated NaOH, since no photoactivity was observed in highly concentrated NaClO_4 or concentrated NaF.

In using bulk activity coefficients to predict changes in adsorption onto the semiconductor, one is on shaky footing. The three-dimensional solute-solute interactions which lead to non-unity activity coefficients may be quite different near the surface. The flatband potential can also be shifted by other changes in surface composition. Butler and Ginley¹¹ have demonstrated a correlation of the electron affinity, and thus the flatband potential of a semiconductor, with the geometric mean of the Mulliken electronegativities of the constituent atoms. Under this scheme the vacuum-prepared SrTiO₃ surfaces, which are enriched with Sr compared to surfaces which have had contact with liquid water, would have a lower electron affinity and thus might be expected to be superior for hydrogen generation under conditions of zero applied potential. This encouraging result could not be tested due to the lack of significant photoactivity of SrTiO₃ with water vapor at room temperature. The Auger studies of SrTiO₃ before and after illumination in various electrolytes showed no such changes in surface composition which correlated with photoactivity variations. Compositional changes may have been masked by the rinse in pure water required before surface analysis; otherwise it appears that this second possible cause of a change in band-bending is also not operative.

Experimental data on flatband potentials in highly concentrated media are scarce. Bolts and Wrighton¹⁵ report that U_{fb} for SrTiO₃ follows the ideal 59 mV per decade change in [OH⁻] up to at least pH 13. Mavroides¹⁶ mentions some unexpected decrease in U_{fb} above pH 13, but gives no details. Such a decrease in U_{fb} , leading to higher band-bending and thus more efficient separation of electrons and holes, could explain the higher photoactivity of platinized SrTiO₃ in concentrated

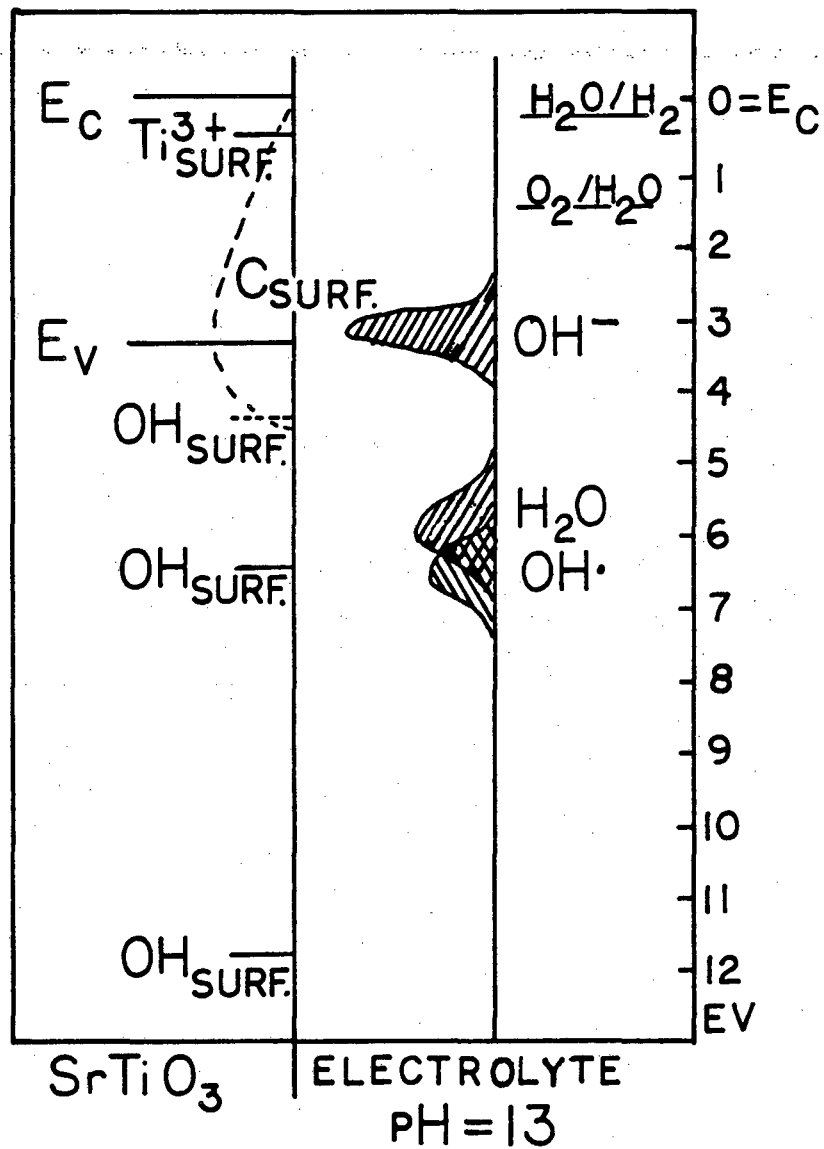
NaOH. It is not clear how increased band-bending would explain the observed increase in activity of metal-free SrTiO_3 , where the simple analogy to the PEC cell may not hold, as discussed in section VII-1.

From a purely thermodynamic point of view hydrogen evolution would seem the marginal part of water dissociation on SrTiO_3 -Pt, since the conduction band edge lies only slightly above the hydrogen redox potential, while the valence band edge lies far below the oxygen couple. Experimental results from cells operated with external potentials lend credence to this focus on hydrogen evolution. Provided an anodic potential sufficient to maintain sufficient band-bending is applied to the SrTiO_3 electrode, Pt/ SrTiO_3 PEC cells can operate at quantum efficiencies very close to unity.¹⁷ Under these conditions, then, rates of the electrocatalytic reactions are not limiting. The losses in quantum efficiency seen at lower applied potentials have been ascribed to recombination of photogenerated charge carriers due to inadequate band-bending.

A decrease in band-bending decreases the effective lifetime of photogenerated charge carriers within the depletion zone and at the semiconductor surface. With these decreased carrier lifetimes, the rate of charge transfer to the electrolyte becomes more important. High quantum yields at zero applied potential require rapid and irreversible (for at least one half-cell) charge transfer out of the semiconductor. Since equivalent hydroxide concentration dependencies were seen for platinized and for metal-free crystals where hydrogen is evolved from different surfaces, it seems most probable that the enhancement of photoactivity in highly concentrated hydroxide solution is due to improved kinetics of

oxygen evolution. Oxygen evolution is a very complex electrocatalytic reaction involving transfer of four holes per oxygen molecule evolved. The mechanistic details are as of yet poorly understood. The following discussion will focus initially on the transfer of the first hole from the semiconductor, but this is not unambiguously the rate limiting step.

A particular form of hydroxide, either adsorbed on the SrTiO_3 or in solution phase, may serve as a very facile hole acceptor. If this hydroxide were an adsorbed species it would also have to be a poor recombination center. Vohl¹⁸ has proposed the existence of similar surface carrier traps to explain details of a photographic process based on TiO_2 . By trapping holes as they reach the surface such a center would inhibit recombination and increase the lifetime of surface holes to equal or exceed the characteristic time for the oxygen evolution reaction. Alternately, a particular form of hydroxide may be the primary hole acceptor of a faster reaction path which comes into play at high electrolyte OH^- concentrations. The rate of the reaction may be set by formation of this active surface hydroxide. Ferrer¹⁹ has shown that some hydroxyl groups are formed very readily on SrTiO_3 even under ultra-high vacuum conditions. However, UPS spectra show that the filled states due to this hydroxyl formation lie far below the valence band edge (Figure VII-5) and thus are unlikely to be involved in the photochemistry. Munuera et.al.²⁰ have identified several distinct forms of hydroxide on TiO_2 powders. Activity for photodesorption of oxygen correlated with the presence of one type of hydroxyl group on the surface. These active surface hydroxyls were destroyed by light and could not be regenerated by contact with water vapor or liquid water at room temperature - harsher treatments were required. It thus seems possible



XBL 808-11543

Fig. VII-5. Surface states, filled states in the electrolyte, and redox couples on one energy scale.

that high electrolyte hydroxide concentrations are necessary to rapidly rehydroxylate at temperatures around 330°K the surface sites most active for hole transfer from the SrTiO_3 . Such a direct kinetic role for the hydroxide ion would account for the parallel hydroxide dependence observed on platinized and metal-free crystals with changing hydroxide concentration even though photogenerated charge carriers may be delivered to the active surfaces of these two types of crystals by quite disparate mechanisms with different sensitivities to changes in band-bending.

The increase in the strength of the hydroxide dependence above 5N is dramatic. A change in solvation state of the hydroxide ion, both in solution and, to a lesser extent, adsorbed on SrTiO_3 , could occur at these high concentrations. Kislina et. al.²¹ have employed infrared spectroscopy to study the solvation of hydroxide ions in 2.89-14.19N aqueous KOH. They have found that the mean hydration number for OH^- decreases from 3 to 2 over this concentration range. Evidence for significant amounts of the proposed dihydrated hydroxide species first appears near 5N. Such a change in the actual chemical nature of the hydroxide ion could account for the discontinuous behavior of photoactivity with increasing hydroxide concentration by changing the distribution of hole-acceptor states in the electrolyte.

Although hydrogen photoproduction from platinized and metal-free SrTiO_3 crystals shows a strong dependence on the electrolyte hydroxide concentration,, SrTiO_3/Pt photoelectrochemical cells have been shown to operate efficiently in basic, neutral, or acidic media provided a sufficiently anodic potential is applied to the photoelectrode. Wrighton et.

al.¹⁷ found no significant change in photocurrent for such a cell operated at 2.8 V applied potential over a hydroxide concentration range of 0.025-9.1N. Nasby and Quinn²² have found that the photocurrent in a BaTiO₃/Pt cell operating at zero applied potential decreased with decreasing electrolyte pH, in agreement with our results on SrTiO₃. Essentially all of an anodic potential applied to an n-type semiconductor appears across the depletion layer - almost none of the drop falls across the inner Helmholtz layer, where it would affect the level of hydroxylation of the surface. This distribution of the applied potential is due to the low maximum density of positive charge carriers which can be maintained in the depletion layer. If the applied potential is sufficiently strong that the Fermi level comes within thermal range of the valence band edge a drastic modification of this potential distribution can occur. The thermal creation of holes in the near surface region as the inversion layer forms increases the maximum positive charge density sustainable in the semiconductor near-surface region to the point that the charge density on the two sides of the semiconductor-electrolyte interface are roughly equal. Under these conditions part of the applied potential appears across the inner Helmholtz layer, increasing the surface hydroxide coverage and possibly the rate of rehydroxylation. The applied potential then, also shifts the position of the band edges with respect to the redox couples in solution. Turner et. al.²³ have identified several cases where such "band-edge unpinning" appears to expand the range of potentials accessible to PEC cells. Although the 2.8 V potential applied by Wrighton et. al. during their studies of pH dependence was not enough to cause formation of a full inversion layer, it was probably large enough that some of the

applied potential fell across the Helmholtz layer, augmenting surface hydroxylation. The pH independence of SrTiO₃-Pt PEC cells at high applied potential may be due to this potential-induced hydroxylation, though the long hole lifetimes produced by the large band bending may also allow oxygen evolution to proceed with high quantum efficiencies through a slower path not involving adsorption of active hydroxyls.

In summary, electrolyte hydroxide concentration has been found to be important to the rate of hydrogen photogeneration on platinized and metal-free SrTiO₃ crystals. Although explanations for this effect based on changes in band-bending are possible, they seem less likely in light of the similar concentration dependence seen on platinized and metal-free crystals. The presence of a surface hydroxyl species highly active for hole acceptance appears necessary for photoactivity under conditions of zero applied potential, where carrier recombination lifetimes are short. Either the rate of formation of this species or its electronic properties (through solvation, etc.) are improved in more concentrated hydroxide solutions. These results bear upon the future of heterogeneous photocatalysis at the gas-solid interface, as will be seen in the next section.

VII-3 Gas-Phase Considerations

We could measure no hydrogen production from platinized or metal-free SrTiO₃ crystals illuminated in water vapor at room temperature at a pressure of about 20 torr. Hydrogen production rates as low as twelve monolayers per hour could have been unequivocally detected. Some hydrogen was generated in mixtures of ammonia and water vapor, but this was

probably due to exergonic ammonia decomposition rather than endergonic water dissociation. The lack of hydrogen evolution from water vapor is not due solely to the lower number density of water molecules in the vapor than in the liquid (a factor of $\sim 5 \times 10^4$) since no hydrogen evolution was observed in neutral or acidic aqueous electrolytes. The same crystals when coated with basic deliquescent compounds, saturated with water vapor, and illuminated yielded hydrogen at readily measurable rates.

The high quantum yields (up to 100% of photons absorbed)¹⁷ attainable in photoelectrochemical reactions are in part due to two factors involving the spatial separation of oxidized and reduced species. The first is the efficient separation of photogenerated electrons and holes by the electric field within the semiconductor depletion layer. This separation inhibits electron-hole recombination and allows the mobile charge carriers produced by photons absorbed hundreds of Angstroms beneath the crystal surface to reach the interfaces with the electrolyte and carry out redox chemistry. This harvesting of light absorbed deep beneath the surface is of great importance to overall quantum efficiency since a monolayer of a material, even of one with a high absorption coefficient (10^5 cm^{-1}) can absorb only about 1% of the incident light of bandgap energy.

The second factor leading to high quantum yields in photoelectrochemical cells is the inhibition of back-reactions by the spatial separation of reductive and oxidative surface sites. The possible importance of back reactions in the presence of platinum is shown in the "dark" and "visible" portions of Figure V-10 and is further suggested by

the observation that the presence of platinum foil in pressure contact with a SrTiO_3 crystal seemed to decrease the observed rate of hydrogen production.

While these two factors involving separation of reduced and oxidized species lead to high quantum yields, they also require a net flow of charge in the form of ions between the cathodic and anodic surfaces to complete the circuit started by the solid-state flow of electrons from anodic to cathodic surfaces. Although the photoelectrochemical process is highly efficient for reactions at the solid-aqueous electrolyte interface, it is unlikely to be efficient for reactions at the gas-solid interface since the gas phase cannot readily support such an ion current. Diffusion of ionic species across the surface can occur, but the activation energies for the diffusion of charged species across an ionic surface are likely to be considerably higher than those for ions through aqueous solutions. Exergonic photoreactions at the gas-solid interface are most likely to occur when the anodic and cathodic active sites are interspersed on a near-atomic scale so that diffusion distances for charged intermediates are minimal. The hydrogen photogeneration activity we have observed on metal-free stoichiometric crystals, though small, indicates that water dissociation by such a more local process is possible. The hydroxide concentration dependence of photoactivity in aqueous electrolytes may explain why no sustained gas-phase photochemistry was observed.

Van Damme and Hall⁸ have proposed that gas-solid "photocatalytic" reactions reported to date^{24,25} have actually been stoichiometric reactions of surface hydroxyl groups; the reactions stop after all active

surface hydroxyls have been consumed. The inability of water vapor to rehydroxylate the surface at reasonable rates may have prevented sustained photoreactions at the gas-solid interface. Boonstra and Mutsaers²⁴ reported photohydrogenation of acetylene on TiO_2 powders which stopped after the formation of a monolayer of products. Thermally dehydroxylated surfaces showed no photoactivity. The results of Munuera et. al.²⁰ correlating the photoactivity of TiO_2 with hydroxyl groups which can only be regenerated through harsh treatment in liquid water have already been discussed.

Schrauzer and Guth²⁵ have reported the photodissociation of water vapor on TiO_2 powders. However, the process stopped within several hours and could not be sustained to produce catalytic amounts of hydrogen. As discussed in the photocatalytic theory section, product yields, to serve as a criterion for catalytic activity, should be normalized to the total surface area of the catalyst. Using the high end of their reported 0.5- μ m particle size range and assuming spherical particles, the maximum hydrogen accumulation they observed corresponded to ~2 monolayers. Their results, which several groups^{8, 26} have not succeeded in duplicating, are thus probably due to a stoichiometric consumption of surface hydroxyl groups or to the consumption of a (probably carbonaceous) surface impurity.

The ion-transport problems associated with photoelectrochemical reactions in the gas phase have already been discussed. We have, however, demonstrated that UV-illuminated metal-free SrTiO_3 crystals in aqueous alkaline solution can evolve thousands of monolayers of hydrogen by a photocatalytic mechanism in which all chemistry occurs on the

illuminated semiconductor surface. This finding lends support to the argument advanced by Van Damme and Hall⁸ that some surface chemical problem, rather than problems with the delivery of photogenerated electrons and holes to the semiconductor surface, has restricted the yield of photoreactions at the gas-solid interface to one monolayer or less. The hydroxide dependence of the liquid phase photocatalytic reaction lends some support to their contention that the yield of the gas-phase reaction is limited by an inability to rehydroxylate the surface with water vapor. Development of techniques for the facile rehydroxylation of oxide semiconductor surfaces may prove a key to sustainable photocatalytic water dissociation at the gas-solid interface.

VII-4 Photochemical and Catalytic Significance of Intermetallic Compound Formation

The studies of Pd and Au film growth were performed on TiO_2 rather than $SrTiO_3$ because of the superior ordering and simpler Auger stoichiometry shown by the former material. Unfortunately, since the electrochemical correlation of a small flatband potential with photactivity at zero applied potential held true for all photocatalysts examined, no photochemistry could be studied on the TiO_2 surfaces. Nevertheless, several surface analytical results of photocatalytic and catalytic interest were observed.

Platinum intermetallics have proven superior to pure platinum as electrocatalysts for fuel cell oxygen reduction electrodes to be operated at high temperatures. ²⁷ The intermetallics show higher intrinsic activity and prove more resistant to the loss of catalyst sur-

face area. Wrighton et. al. ²⁸ have observed losses in photochemical activity of platinized SrTiO_3 due to degradation of the Pt film which might be retarded through intentional growth of the intermetallic. Surface Ti^{3+} was shown to enhance intermetallic growth. Illumination of TiO_2 , at least in UHV, increases the concentration of surface Ti^{3+} . Intermetallic compounds may therefore form photochemically on TiO_2 coated with Pt-group metal films, leading to somewhat different chemistry on directly metallized TiO_2 than is found with the analogous metal- TiO_2 PEC cell. Since TiO_2 cannot dissociate water at zero applied potential, a reaction requiring a less cathodic couple would be needed to probe the differences.

Most interest in the (Pt-metal on TiO_2) system for heterogeneous catalysis has settled not on the intermetallic phases but rather on the intermediate case where the pure metal phase shows a moderately strong interaction with the substrate. ²⁹ The LEED Structure B observed for Pd on $\text{TiO}_2(110)$ with its enigmatic unit cell mesh and epitaxial relationships may indicate such a species. UPS, XPS, and catalytic studies of this phase could well prove interesting. The problems associated with studying a surface on which particles of several phases coexist point out the advisability of developing a LEED system with a high resolution electron gun to be used in association with a scanning Auger microprobe. The problems in growing truly well-ordered metal films on oxides indicate that, until such advanced instruments are developed, model ordered supported catalysts might best be made by depositing metals of lower surface free energy onto metals of higher surface free energy. Molybdenum would appear to be a particularly suitable substrate for Pt. Molybdenum has a higher surface free energy, the solid solubility on

both ends of the phase diagrams is limited, and both metals have both high and low energy Auger peaks free from interference from the other metal. Intermetallic formation for Mo-Pt should be less favorable than for Ta-Pt, with which it could be compared.

VII-5 Suggestions for Future Research

VII-5-1 Choice of Future Photocatalysts for Water Photolysis

The Holy Grail of photocatalytic research is a material showing the stability and activity for water photolysis at zero applied potential of SrTiO_3 , yet absorbing a much larger portion of the solar spectrum. The maximum solar excitation efficiency ($X(E_g)$) for a single junction quantum absorber is 44% for $E_g = 1.2\text{eV}$. This threshold energy is very close to the 1.23 eV/electron required for water electrolysis by a two electron per water molecule path. If no further energy losses occurred, water dissociation would be the ideal reaction for storing solar energy. However, a more realistic assessment of losses due to activation energies (mostly for oxygen evolution) fixes the minimum bandgap for water dissociation at 1.7 eV ($X(E_g) = 36\%$) or more likely 2.0 eV ($X(E_g) = 28\%$). There are many semiconductors with bandgaps in this range - the problems are in finding one which (1) has a sufficiently low electron affinity (or flatband potential) that hydrogen can be evolved without an external potential, (2) is sufficiently stable in water at both the hydrogen and oxygen evolution potentials that photocorrosion occurs at negligible rates, (3) contains no localized states which can serve as efficient recombination centers, and (4) has a sufficiently large light absorption coefficient α that most light will be absorbed close to the surface.

Semiconductor Electron Affinity

To date it appears that photocatalytic systems are under the same constraints as to semiconductor electron affinity as are photoelectrochemical cells. The conduction band edge of the semiconductor must lie closer to the vacuum level than the electron acceptor state in water, and it appears that this acceptor state is about the same distance from the vacuum level at the gas-solid interface as at the liquid-solid interface. In the photocatalytic (metal-free) solid-liquid reaction reported here SrTiO_3 ($U_{fb} = -0.18 \text{ V}$)¹¹ was effective while TiO_2 , whose electron affinity puts its conduction just slightly above the hydrogen couple,³⁰ and Fe_2O_3 ($U_{fb} = +0.42$)¹¹, whose conduction band edge is well below the electron acceptor level in water, were ineffective. Platinized SrTiO_3 gave rapid evolution of hydrogen, platinized TiO_2 very slight hydrogen production (which has also recently been reported in TiO_2 -Pt PEC cells at zero applied potential), and platinized Fe_2O_3 gave no measurable hydrogen production. Roger Carr³¹ has found similar results working at the steam-semiconductor interface; Pt- SrTiO_3 gives rapid hydrogen evolution while Pt- TiO_2 gives very low activity levels.

A method of predicting the electron affinity and flatband potential has been outlined by Butler and Ginley¹¹. If the bandgap of a heavily-doped semiconductor is known, the electron affinity of the n-type semiconductor can be estimated by taking the geometric mean of the Mullikan electronegativities of the constituent atoms and subtracting half of the bandgap. Table VII-3, after Butler and Ginley, lists the calculated electron affinities and measured flatband potentials corrected to pH 13 for a number of oxide semiconductors. The flatband potential versus the

TABLE VII-3: Flatband potentials and electron affinities of various oxide semiconductors. Data from ref. 11.

	U_{fb} vs. RHE at pH 13	EA
ZrO ₂	-1.03	3.42
Ta ₂ O ₅	-.43	4.08
BaTiO ₃	-.21	3.60
SrTiO ₃	-.18	3.71
ZnO	-.08	4.15
TiO ₂	+.11	4.33
SnO ₂	+.19	4.49
FeTiO ₃	+.42	4.30
Fe ₂ O ₃	+.69	4.71
CdO	+.79	4.55
WO ₃	+.81	5.18

hydrogen electrode at pH 13 can be predicted from this calculated electron affinity by the following empirical relation: $U_{fb} = 1.1 EA - 4.5$, where a negative value is favorable to water dissociation. However, actual U_{fb} measurements show up to 0.5 V scatter about this line due to specific adsorption effects, so in the absence of quantitative information on adsorption (point of zero zeta potential measurements or relevant gas phase data) the above equation has limited quantitative applicability. However, the relationship between flatband potentials and atomic electronegativities can predict the relative magnitudes for the applied potentials of related compounds. Taking, for example, compounds where most light is absorbed in $O\ 2p \rightarrow Ti\ 3d$ transitions, TiO_2 has a U_{fb} of +0.11 V (though more recent measurements³⁰ place it at -0.15 V, where slow hydrogen evolution at zero applied potential should be possible). Addition of low-electron affinity Sr to form $SrTiO_3$ gives a flatband potential of -0.18 V, while addition of high-EA Fe to form $FeTiO_3$ gives a flatband potential of 0.42 V, meaning that at least 1/3 of the energy used to dissociate water on this material must come from an external source of electric power. Addition of Si to Fe_2O_3 has been shown to increase photocurrent in certain electrochemical cells operating with applied potentials.³² However, it would not be expected from this effect that addition of Si to iron oxide could lead to water photolysis at zero applied potential, since silicon has an even higher electronegativity than iron. The low PZZP (indicative of strong hydroxide bonding) of SiO_2 could shift V_H and thus V_{fb} to a more negative potential, partially compensating for the unfavorable shift in EA due to Si. The enhanced photocurrent in Si-doped Fe_2O_3 PEC cells is probably due to the catalytic consequences of specific adsorption on SiO_2 or to promo-

tion of n-type behavior in Fe_2O_3 rather than to shifts in band structure which could enable photoactivity for water dissociation at zero applied potential.

The necessity of a small electron affinity also means that new materials for water photolysis should be sought in which the metal is in a relatively low oxidation state. WO_3 , for example, requires an applied potential of more than 0.8 V due to the high oxygen-to-metal stoichiometric ratio and consequent high electron affinity. Thus despite the lower atomic electronegativities of 2nd and 3rd row transition metals, it is unlikely that the binary oxides of these metals would make good photodissociation semiconductors since the stable oxides involve higher oxidation states. It is possible that some of these metals could be useful in mixed oxides patterned on SrTiO_3 , say the known compounds such as BaRuO_3 or CaIrO_3 ,³³ but one similar compound, LuRhO_3 , has been shown to require a considerable applied potential for water dissociation.³⁴ Use of lanthanides or actinides rather than alkaline earths as the low electron affinity metals may be attractive, as the aquated ions of some of these metals are photoactive for hydrogen or oxygen evolution with short wavelength visible light³⁵ and thus could add to total photoactivity while Sr or Ba could not. The lanthanides might also be used to modify the oxidation state of the other metal in a perovskite. For example, $\text{Sr}_{1-x}\text{Eu}_x\text{TiO}_3$ would be expected to have $\frac{x}{1-x}$ of the Ti in the +III state since the most stable form of Eu is +III and the sum of metal oxidation states in a perovskite is VI. Whether Eu^{3+} , with an ionic radius of $\sim 0.97 \text{ \AA}$,^o could substitute freely for Sr^{2+} (1.44 \AA)^o is questionable.

While the oxides of the lanthanides share no stability regions with water ³⁶ (tending to form gelatinous hydroxides unsuitable for electrode fabrication, though possibly useful as photocatalysts), some of the actinide oxides are stable in contact with water over certain pH and potential ranges. Above pH 9 PuO_2 is thermodynamically stable at both the hydrogen and oxygen evolution potentials ³⁶, but the intentional coverage of many square miles of solar collector area with this material would seem unwise. Uranium oxides are considerably more tractable materials. Natural uraninite lies between UO_2 and UO_3 in composition. ³⁷ Stoichiometric UO_2 has a band-gap of 2.14 eV. ³⁸ UO_2 is stable at the hydrogen evolution potential above pH ~4. At oxygen evolution potential insoluble UO_3 formation is expected above pH 11, with possible formation of some soluble uranates ³⁶. Attempts to induce n-type conductivity by Nb-doping have born negative results. When excess oxygen is present UO_2 becomes a p-type semiconductor. Conductivity is not through a delocalized band, but rather via a hopping mechanism between local centers ³⁸. This does not bode well for photochemistry, as such local centers often facilitate electron-hole recombination. At the UO_2 end of composition the electron affinity would appear to be favorable for hydrogen photogeneration from water at zero applied potential, but the U_3O_8 end is suspect. PZZP measurements are needed to estimate the potential drop across the specifically adsorbed layer and thus determine the position of the conduction band more accurately.

p- UO_2 , in conjunction with Pt or RuO_2 as an oxygen evolution catalyst or counterelectrode, may be active for hydrogen photogeneration from water. As with all p-type semiconductors used to date the kinetics of hydrogen evolution may be very slow, and addition of a very thin film of

Pt to the photocathode may also be necessary.

The probable flatband potential and known bandgap of urania are encouraging. Problems with conductivity, some corrosion during anodic potential excursions, and with toxicity are to be anticipated. In light of some of the favorable properties of urania and the ready availability of tons of depleted uranium presently suitable only for use as radioactive paperweights, some exploratory research into the photoelectrochemical and photocatalytic properties of urania is desirable.

Kung et. al. ³⁹ have noted that the valence bands of the n-type oxide semiconductors examined to date all lie about 3.3 ± 0.5 eV below the hydrogen evolution potential. Since in all cases the valence band is formed primarily of O 2p orbitals with little admixture of metal orbitals, the position of this band is relatively invariant going from one n-type oxide to another. This means that the small bandgap n-type oxide semiconductors which can absorb a larger proportion of the solar spectrum than SrTiO_3 are likely to require high applied potentials for water photolysis. There are several possibilities for getting around this seemingly fundamental limitation on the use of oxide semiconductors. The first is the use of a p-type oxide, such as UO_2 , where admixture of some metal character into the valence band could raise it towards the vacuum level. The second is to try to introduce optical centers responsive to visible light into a material with a favorable flatband potential, either by homogeneous solution ^{40,41} or by simple physical admixture. ^{42,43} While very slight activity at longer wavelengths has been noted in such systems, the overall solar conversion efficiencies are poorer than for the pure large-bandgap materials due to increased recombination at

local centers and phase boundaries. When enough of the lower bandgap material is added to significantly change the light absorption properties, the flatband potential resembles that of the lower bandgap material. If this approach is to yield a useful photoanode two criteria must be met: (1) large quantities (>10%) of the lower bandgap material must be incorporated into a single phase with the low electron affinity host to give adequate visible light absorption within the depletion layer and to minimize phase-boundary recombination, and (2) the low bandgap material must form a delocalized band within the bandgap of the host material to avoid recombination at local centers. The criteria for successful photocatalysts are likely to be about the same. No system studied to date has satisfied these criteria.

The large energy difference between the vacuum level and the $O\ 2p$ -derived valence band of n-type semiconductors makes unlikely the discovery of an n-type oxide which can dissociate water at zero applied potential utilizing most of the visible solar light. The goal of operation at zero applied potential can be achieved if one switches to a chalcogenide with a lower electron affinity, such as S, Se, or Te. Unfortunately, these materials are beset by photocorrosion problems, as will be discussed in the next section.

Photocorrosion

n-CdSe, with a bandgap of 1.7 eV and a V_{fb} which places the conduction band above the hydrogen redox potential, would appear to be an ideal material for the photodissociation of water. However, illumination of CdSe in most aqueous solutions leads to oxidation of Se^{2-}

(crystal) to Se_2^{2-} (aqueous) rather than to oxidation of water to O_2 . Similar self-oxidation is a general property of non-oxide semiconductors and can be suppressed only through addition of other electroactive species (usually S^{2-} , Se^{2-} , Te^{2-} , or I^-) to the electrolyte.⁴⁴ Oxidation of these ions proceeds more rapidly than electrode self-oxidation, but unfortunately none of the oxidized products are capable of oxidizing H_2O or OH^- to O_2 . Thus these systems, while showing promise for liquid junction solar cells, cannot be used for water-dissociating PEC cells. Since the self-oxidation products are aqueous ions stabilized by solvent molecules, it is possible that use of water vapor as the reactant might suppress the corrosion. This hypothesis should be tested to determine: (1) whether CdSe is active for photodissociation of water vapor, and (2) what changes in surface composition occur. Even if no photoactivity were observed, basic surface studies of CdSe oxidation and corrosion would be of interest.

Photocorrosion in materials such as CdSe occurs as holes are created in a band composed of Se orbitals - the selenide is in a sense oxidized directly by photon absorption. Tributsch⁴⁵ initiated the study of a class of materials, typified by MoSe_2 , which circumvent these problems. In these materials the top of the valence band is formed primarily from non-bonding Mo d-orbitals, and photoexcitation does not directly oxidize selenide. At pH 1 the flatband potentials of MoSe_2 and MoS_2 lie just below the hydrogen redox potential. Since the flatband potentials of sulfides and selenides do not shift with electrolyte pH, it is possible that in concentrated acids, particularly in exceedingly strong acids such as trifluoromethanesulfonic acid, hydrogen photogeneration at zero applied potential may be possible with these materials. Some oxygen

evolution has been measured on MoS_2 , but the primary oxidized product is selenious acid or selenate SeO_3^{2-} . The lack of formation of diselenide or elemental selenium is taken as an indication that an adsorbed oxygen species is formed. By addition of a suitable catalyst for the reaction $\text{O}(\text{a}) + \text{O}(\text{a}) \rightarrow \text{O}_2(\text{g})$, and by working in a concentrated acid electrolyte, it may be possible to achieve photodecomposition of water at zero applied potential on these materials using visible light. Development of the proper oxygen catalyst and the proper strong acid electrolyte to effect the required flatband potential change could constitute a very interesting line of research. UHV studies of I_2 adsorption on MoSe_2 would be of great interest in light of the successes achieved with MoSe_2 liquid junction solar cells employing the I_2/I^- redox couple. ⁴⁶

One possible drawback to the use of materials such as MoSe_2 which rely on d-d transitions for optical absorption is a relatively low absorption coefficient. In materials such as SrTiO_3 , TiO_2 , and CdS , where optical excitation is essentially a charge transfer process, absorption coefficients (α) as high as $5 \times 10^6 \text{ cm}^{-1}$ are common (though right at the absorption edge, where indirect transitions occur, α is closer to 10^3 cm^{-1}). For a d-d transition in octahedral symmetry, which is forbidden by the LaPorte selection rule ($\Delta l = \pm 1$), absorption coefficients greater than 10^3 cm^{-1} are unlikely. Photons are absorbed, on the average, farther from the surface, and a greater degree of band-bending will be required to prevent electron-hole recombination. Thus even if the hydrogen redox energy can be pushed slightly below the flatband potential of MoSe_2 by use of a strong acid electrolyte, the quantum efficiency of hydrogen evolution at zero applied potential is likely to be very low due to electron-hole recombination. A significant applied

potential is likely to be required for acceptable quantum yields. A similar problem is found for Fe_2O_3 . Although the bandgap of Fe_2O_3 is 2.0 eV, corresponding to a wavelength of 6200 \AA , the lowest energy absorption band due to a charge-transfer transition occurs at about 4000 \AA (3.1 eV).⁴⁷ Photons with wavelengths between 4000 \AA and 6000 \AA travel far into the semiconductor before being absorbed. While they may contribute to the photoactivity under conditions of high band-bending induced by an external potential, they are unlikely to contribute much at minimal applied potentials. Kung *et. al.*³⁹ have found that the spectral dependence of water electrolysis on Fe_2O_3 does not parallel the optical absorption spectrum - only higher energy photons lead to chemistry. One mechanism whereby Si doping increases the photactivity of Fe_2O_3 may be through mixing of Si orbitals in with the d-bands due to iron. Such mixing could remove the LaPorte interdict on the d-d transition, increasing α and thereby decreasing carrier recombination for a given degree of band-bending. Photoemission studies of Si evaporated onto $\alpha\text{-Fe}_2\text{O}_3$, preferably in conjunction with diffuse reflectance optical spectroscopy, might be able to define such an effect.

Although the layered chalcogenides show promise as photocatalysts, other structural forms of chalcogenides may well prove superior. Lewerenz *et. al.*⁴⁸ have found evidence that the gross anisotropy of layered compounds can lead to high carrier recombination rates. It may be possible to "scale up" the perovskite structure which proves so stable for ternary oxides. BaCeS_3 , BaTbS_3 , BaThS_3 , and BaUS_3 have ionic radius ratios which should permit perovskite formation. If stable, these materials should have the low electron affinity required for hydrogen evolution at zero applied potentials. Sulfur analogs of

spinel also might prove interesting. At least one cobalt sulfospinel has shown moderate activity as an electrocatalyst for oxygen reduction.

⁴⁹ If stable mixed oxysulfides can be formed they should combine the low electron affinities of sulfides with the catalytic activity for oxygen evolution of oxides.

VII-5-2 Other Photocatalytic Reactions

Although water photolysis has received the most research attention, other photocatalytic reactions are of interest both in defining the scope of surface photochemistry and in possible technical processes for synthesis and energy conversion. Photocatalytic, as opposed to photoelectrochemical, processes would have unique applicability in reactions requiring simultaneous oxidation and reduction of discrete sections of a molecule, where the interspersed oxidative and reductive active sites of a photocatalyst could come into play. In energy conversion the best application might be in the disproportionation of carbohydrate plant materials to higher energy density fuels and CO₂. Photocatalytic disproportionation of carboxylates has been demonstrated;⁵⁰ this work should be extended to sugars, starches, and possibly even to cellulose and lignin. The different reductive potentials for these materials could allow use of stable oxides with bandgaps in the visible range, such as Fe₂O₃. Although such processes would be of technological importance, they are not likely to occur as gas-solid reactions. Study of related, but simpler, reactions which could occur at the gas-solid interface would prove more advantageous to the surface scientist. Evidence for a disproportionation of ethanol to formaldehyde and methane was discussed briefly in Chapter V. In a future where alcohols derived

from biomass or coal may be important chemical feedstocks such reactions could prove important. Although most surface photoreactions of small, partially oxidized organic molecules are likely to be at least slightly exergonic and thus lack the immediate attractiveness of "thermodynamically uphill" reactions, they should be studied because of: (1) their greater likelihood to proceed at the gas-surface interface where the tools of modern surface science can be used to study the reaction in depth, and (2) their possible future utility in the synthesis and utilization of coal and biomass.

Considerable interest has developed in recent years in the use of TiO_2 as a support for noble metals to alter the product distribution in hydrocarbon catalysis. ⁵¹ Illumination of the TiO_2 catalyst may still further alter the product distribution. Illumination might also be useful in regenerating such catalysts - witness the amazingly carbon-free Auger spectrum of Pt on $SrTiO_3$ shown in Figure V-21D. Several possible experiments related to metal particle size on oxides have been mentioned in Chapter VI. Photodeposition of metals from aqueous solutions onto oxides, an area partially explored by Bard *et. al.*, ⁵² may yield films of unique morphology and catalytic properties. An electron micrographic study of the dependence of metal film morphology on the orientation of the substrate oxide crystal could yield information on the atomic-scale structural identity of reducing centers on photocatalysts.

VII-6 Summary of Proposed Future Photochemical Work

1) At the liquid-solid interface:

- a. Try oxygen evolution catalyst on n-MoSe₂ under applied anodic potential and/or in strongly acidic electrolytes.
 - b. p-UO₂ as a photocathode for water electrolysis.
 - c. Photodisproportionation of aqueous sugars, alcohols, and polysaccharides on oxide semiconductors.
 - d. Testing of new materials for stability and photoactivity: oxy-sulfides, sulfoperovskites, sulfospinel.
 - e. Effects of single-crystal substrate structure on photodeposition of metals on oxides.
- 2) At the gas-solid interface:
- a. Try water vapor dissociation on n-CdSe/Pt.
 - b. Photodisproportionations of alcohol, aldehyde, and carboxylic acid vapors
 - c. Effects of light on I₂ adsorption on MoSe₂. Attempt photosorption of water, other molecules on MoSe₂.
 - d. Effects of light on hydrocarbon catalysis on Pt/TiO₂.

REFERENCES:

1. B.A. Parkinson, A. Heller, and B. Miller, *J. Electrochem. Soc.*, 121, 1160 (1974).
2. D.S. Boudreaux, F. Williams, and A.J. Nozik, *J. Appl. Phys.*, 51, 2158 (1980).
3. C.R. Dickson and A.J. Nozik, *J. Am. Chem. Soc.*, 100, 8007 (1978).
4. A.J. Nozik, personal communication.
5. H. Gerischer, in Topics in Applied Physics, Solar Energy Conversion, B.O. Serophin, ed., Springer, Berlin, 1979, V. 31, pp. 115-172.
6. D. Redfield and W.J. Burke, *Phys. Rev. B*, 6, 3104 (1972).
7. M. Cardona, *Phys. Rev.*, 140, A651 (1965).
8. H. Van Damme and W.K. Hall, *J. Am. Chem. Soc.*, 99, 7189 (1977).
9. R.C. Weast, ed., Handbook of Chemistry and Physics, Chemical Rubber Co., Cleveland, 1969, p. E-238.
10. S. Ferrer and G.A. Somorjai, submitted to *Phys. Rev. Lett.*
11. M.A. Butler and D.S. Ginley, *J. Electrochem. Soc.*, 125, 228 (1978).
12. M.M. Jaskic, D.R. Jovanovic, and I.M. Csonka, *Electrochim. Acta*, 13, 2077 (1968).
13. D.D. Macdonald and M.C.H. McKubre, Temperature Limitations of Al-

kaline Battery Electrodes. SRI Report No. 7775, Stanford Research Institute, 1979, Vol. 2.

14. A. Ferse, *Z. Chem.*, 18, 8, (1978).
15. J.M. Bolts and M.S. Wrighton, *J. Phys. Chem.*, 80, 2641 (1976).
16. J.G. Mavroides, J.A. Kafalas, and D.F. Kolesar, *Appl. Phys. Lett.*, 28, 241 (1976).
17. M.S. Wrighton, A.B. Ellis, P.T. Wolczanski, D.L. Morse, H.B. Abrahamson, and D.S. Ginley, *J. Am. Chem. Soc.*, 98, 2774 (1976).
18. P. Vohl, *Phot. Sci. Eng.*, 13, 120 (1969).
19. S. Ferrer and G.A. Somorjai, *Surf. Sci.*, 94, 41 (1980).
20. G. Munuera, V. Rives-Arnau and A. Saucedo, *J. Chem. Soc. Faraday Trans. I*, 75, 736 (1979).
21. I.S. Kislina, V.D. Maiorov, H.D. Librovich and M.I. Vinnik, *Zh. Fiz. Khim.*, 50, 2812 (1976).
22. R.D. Nasby and R.K. Quinn, *Mat. Res. Bull.*, 11, 985 (1976).
23. J.A. Turner, J. Manassen, and A.J. Nozik, in Photoeffects at Semiconductor-electrolyte Interfaces, A.J. Nozik, ed., ACS Symposium Series no. 146, 1980, p. 253.
24. A.H. Boonstra and C.A.H.A. Mutsaers, *J. Phys. Chem.*, 79, 2025 (1975).
25. G.N. Schrauzer and T.D. Guth, *J. Am. Chem. Soc.*, 99, 7189 (1977).

26. S. Sato and H.S. Jarrett, personal communications.
27. P.N. Ross, Jr., Proceedings, Electrochem. Soc. Meeting, Minneapolis, May 1981.
28. M.S. Wrighton, P.T. Wolczanski, and A.B. Ellis, J. Solid State Chem., 22, 17 (1977).
29. S.J. Tauster, S.C. Fung and R.L. Garten, J. Am. Chem. Soc., 100, 170 (1978).
30. M. Tomkiewicz, J. Electrochem. Soc., 126, 1505 (1979).
31. R. Carr, unpublished results.
32. J.H. Kennedy, R. Shinar and J.P. Ziegler, J. Electrochem. Soc., 127, 2307 (1980).
33. R.D. Shannon, D.B. Rogers and C.T. Prewitt, Inorg. Chem., 10, 713 (1971).
34. H.S. Jarrett, Surf. Sci. and Catalysis Seminar, U.C. Berkeley, 1980.
35. K.I. Zamaraev and V.N. Parmon, submitted to Catal. Rev.
36. M. Pourbaix, Atlas of Electrochemical Equilibria in Aqueous Solutions, Pergamon Press, 1966.
37. C.S. Hurlbut, Jr. and C. Klein, Manual of Mineralogy, 3rd ed., Wiley, New York, 1977, p. 275.
38. J.L. Bates, C.A. Hinman and T. Kawada, J. Amer. Ceram. Soc., 50,

652 (1967).

39. H.H. Kung, H.S. Jarrett, A.W. Sleight, and A. Ferretti, *J. Appl. Phys.*, 48, 2463 (1977).
40. H.P. Maruska and A.K. Ghosh, *Solar Energy Materials*, 1, 237 (1979).
41. K.Dwight and A. Wold, in reference 23, p. 207.
42. J.G. Mavroides, J.C. Fan, and H.J. Zeiger in ref. 23, p. 217.
43. R.D. Rauh, J.M. Buzby, T.F. Reise, and S.A. Alkaitis, *J. Phys. Chem.*, 83, 2221 (1979).
44. H. Gerischer, *J. Vac. Sci. Technol.*, 15, 1422 (1978).
45. H. Tributsch, *J. Electrochem. Soc.*, 125, 1086 (1978).
46. H. Tributsch, *Solar Energy Mat.*, 1, 257 (1979).
47. S. Tandon and J. Gupta, *Spectrosc. Lett.*, 3, 297 (1970).
48. H.J. Lewerenz, A. Heller, H.J. Leamy and S.D. Ferris, in ref. 23, p. 17.
49. D. Baresel, W. Sarholz, P. Scharner and J. Schmitz, *Ber. Bunsengesell.* 78, 608 (1974).
50. B. Krautler and A.J. Bard, *J. Am. Chem. Soc.*, 100, 5985 (1978).
51. J.A. Horsley, *J. Am. Chem. Soc.*, 101, 2870 (1979).
52. B. Krautler and A.J. Bard, *J. Am. Chem. Soc.*, 100, 4317 (1978).

APPENDIX I: Film Morphology By Auger Electron Spectroscopy

Auger electron spectroscopy can provide information about the morphology of thin metal films on single-crystal substrates. In Chapter VI a number of film morphology models were compared with experimental results for Pd and Au on α -Al₂O₃, graphite, and TiO₂. This appendix provides details of the models used and outlines the conditions under which Auger data could be expected to give more definitive results.

N'(E) vs. N(E) spectra

Auger data are collected as derivative spectra to accentuate the Auger features above the large, steeply-sloping background of secondary electrons. If the N(E) peak is a simple Gaussian on top of a background of constant slope, the peak-to-peak height of the N'(E) spectrum will be proportional to the area under the N(E) peak. Although Auger N'(E) features are not in general Gaussian in shape, the proportionality between the N'(E) peak-to-peak height and the area under the N(E) curve still holds to a good approximation as long as the N'(E) peak shape does not change with coverage. Although for Pd at low coverages the peak shape does change slightly, in all the quantitative work done here the pk-pk height is assumed proportional to the area under the N(E) curve, since the backscattering factor introduces a greater degree of uncertainty than this approximation.

Auger Electron Intensity: Geometric and Backscattering Factors

The high energy (2-5 keV) primary electrons used to excite Auger transitions have longer mean free paths in solid materials than do the

Auger electrons (30 - 550 eV) which they create. Thus, to a fair approximation, all of the near-surface region which can emit Auger electrons feels the same flux of exciting primary electrons. The contribution of each near-surface layer to the total Auger intensity from a homogeneous solid is then treated by a simple continuum model for the attenuation of the Auger electrons of a given energy E , using Lambert's law of constant proportional attenuation:

$$\ln(I_x/I_x^0) = -x/\lambda \quad (1)$$

where I_x^0 is the flux of Auger electrons passing through the plane a distance x below the (flat) surface, I_x is the part of that flux which emerges from the surface, and λ is the characteristic attenuation length for electrons of energy E through the solid. λ changes relatively little in different solids and will be considered here to have a unique value for a given electron energy; rough values can be obtained from "the universal curve". Although the attenuation model is that for a continuum, in ultra-thin film morphology determination one deals with attenuation through only a few atomic layers. For metallic substrates, where much of the Auger electron attenuation arises through interactions with the free electron gas, the continuum approximation may not be bad. For an insulator, such as Al_2O_3 , the continuum approximation is more suspect, but more accurate treatments would require large amounts of computer time. We thus proceed to "quantize" our continuum model by atomic layers, with the realization that layers can be partially filled.

Consider the clean surface of a homogeneous solid. The Auger inten-

sity due to the i^{th} layer below the surface of substance A is given by

$$I(E_A)_i = k(E_A, E_p) r(E_A, E_p) C_{A_i} \exp\left(\frac{-(i-1)d}{\lambda(E_A) \cos \phi}\right) \quad (2)$$

$i=1$ for the surface layer

Here E_A is the Auger electron energy and E_p the primary beam energy. $k(E_A, E_p)$ is the "intrinsic" Auger intensity, a product of the core hole generation cross-section and the Auger transition probability. $r(E_A, E_p)$ is the "backscattering factor". Since core holes can be created by secondary, as well as by primary, electrons, the energy distribution of the secondary electron cascade will influence the Auger yield. A metal atom in a non-metallic matrix will thus give a different Auger yield than one in the bulk metal. Backscattering factors for different matrices are very difficult to determine accurately, they range plausibly over a factor of about 2 even in purely metallic systems. In the absence of an independent means of determining film coverages, backscattering factors for a given atom had to be considered independent of environment. This is the most serious source of error in the model. The backscattering factor has historically lent the phrase "quantitative Auger analysis" its similarity to the term "army intelligence".

C_{A_i} is the concentration of A in the i th layer beneath the surface. d is the interlayer spacing, $\lambda(E_A)$ the Auger electron attenuation length, and ϕ the effective acceptance angle of the electron analyzer (42° for the CMA used here). Let us lump the non-geometric factors into a "constant", I_1 . Then the Auger intensity from a bulk material, I_∞ is

given by

$$I_{\infty} = I_1 \sum_{i=1}^{\infty} \exp\left(-\frac{i-1}{\lambda \cos \theta}\right) \quad (3)$$

The summation, being of the form $\sum_{n=0}^{\infty} \alpha^n$, where $|\alpha| < 1$ converges, yielding

$$I_{\infty} = I_1 [1 - \exp(-d/\lambda \cos \theta)]^{-1} \quad (4)$$

$$= I_1 [1 - \alpha]^{-1}$$

where $\alpha = \exp(-d/\lambda \cos \theta)$. Thus, by using a bulk foil or a very thick evaporated film as a standard for the determination of I_{∞} , one can calculate the expected Auger intensity for a smooth monolayer film (with the uniform backscattering assumption).

Layer-by-layer Growth: Deposit Signal

During the growth of the first layer the Auger signal grows linearly with coverage: $I_{\theta} = \theta I_1$. After completion of the first layer additional film atoms add Auger intensity but attenuate the intensity of atoms below them - post monolayer growth is equivalent to, and more easily visualized as, adding new atoms under the first monolayer. For $0 < \theta < 1$

$$I_{1+\theta} = I_1 + \alpha \theta I_1$$

$$I_{2+\theta} = I_1(1+\theta\alpha^2)$$

$$I_{n+\theta} = I_1 \left[\left(\sum_{j=0}^{n-1} \alpha^j \right) + \theta \alpha^n \right] \quad (5)$$

$$\frac{d(I_{n+\theta})}{d\theta} = \alpha^n$$

As film growth progresses, the plot of I vs. total coverage will yield a sequence of line segments of decreasing positive slope. If the evaporation rate and sticking coefficient are constant a plot of I vs. time will give line segments with breaks in slope at coverages corresponding to the completion of each monolayer. Data must be collected frequently and the α value must be sufficiently small (λ small, $E_A \approx 50\text{eV}$) so that changes in slope can be unambiguously determined despite the (c.10%) scatter in the Auger data.

Layer-by-layer Growth-Substrate Signal

Suppose a clean substrate gives signal I'_0 . Adsorption of a smooth monolayer attenuates the signal $I'_1 = \alpha' I'_0$ where α' is calculated with λ appropriate for the substrate Auger electron energy and d from the interlayer spacing of the deposit. Then

$$I'_{n+\theta} = [\theta \alpha'^{n+1} + (1-\theta) \alpha'^n] I'_0$$

$$= \alpha'^n (1 - \theta + \alpha')$$

(6)

$$\frac{dI'}{d\theta} = -\alpha'^n$$

The I' vs. coverage plot is a sequence of line segments of steadily diminishing negative slope. The substrate plot should give more ideal behavior than the deposit plot, as backscattering changes are less severe for the substrate.

If the I vs. t plots for both deposit and substrate show several clean, evenly spaced, breaks in slope while evaporator flux is strictly constant, a clear indication of Frank-van der Merwe (layer-by-layer) growth is obtained. One then has an absolute calibration of Auger signal vs. coverage and one can calculate more accurate values for the λ 's. Some simple deviations from ideal behavior (largely in the deposit signal) can be understood by invoking a coverage-dependent backscattering factor. If, however, no clean breaks in the $I(t)$ curves are obtained, determination of film coverage and morphology are much less simple, especially if no independent measure of the quantity of material deposited, such as that obtainable through use of a quartz oscillator thickness monitor, is available.

Auger Signals for the Poisson (Hit-and-Stick) Growth Mode

The thickness distribution curves for films with mean thicknesses of $1/4$ to 10 monolayers were shown in Figure VI-3. The deposit Auger sig-

nal from such a film with a mean thickness of a monolayers is related to that from the bulk:

$$I_a = \sum_{m=0}^{\infty} P_a^{(m)} I_m \quad (7)$$

$$= (1-\alpha) I_{\infty} \sum_{m=0}^{\infty} \left[\frac{a^m e^{-a}}{m!} \sum_{j=0}^{m-1} \alpha^j \right]$$

Plots of I_a/I_{∞} (hit-and-stick) and I_m/I_{∞} (layer-by-layer) are shown for Pd in the mean thickness ranges of 0-1 and 0-10 monolayers in Figures VI-30 and VI-31, respectively. The Poisson model gives significant (>10%) deviation from the layer-by-layer model in the mean coverage range from .6 to 5 monolayers Pd, but, even with an independent coverage measurements, the growth modes cannot be distinguished by simple comparison of magnitudes due to the uncertainty in λ . The modes can be best distinguished by looking for downward concavity in the coverage range of 0-1 mean monolayers, but, unless one has an independent measure of mean coverage, it is easy to mistakenly divide the Poisson I_a/I_{∞} vs. t curve into two line segments with a break at $a=0.5$. If good Auger peaks with shorter λ 's were available the breaks in slope in the layer-by-layer model would be more obvious and the distinction between growth modes would be more definite.

The substrate Auger signal for the hit-and-stick mode can be treated similarly:

$$I'_a = \sum_{m=0}^{\infty} P_a(m) I'(m) \quad (8)$$

$$= (1-\alpha') I'_o \sum_{m=0}^{\infty} \frac{a^m e^{-a}}{m!} \alpha'^m$$

The ability to distinguish this from the corresponding expression for layer-by-layer growth also improves with a decrease in λ' , the attenuation length for substrate Auger electrons. I vs. t curves are meaningful only if the evaporator flux is constant throughout the deposition. For much of the data reported in Chapter VI this is not the case, and the alternative comparison technique which follows must be used.

Auger Signals for Hemispherical Islands

Hemispherical islands are treated by viewing them as "wedding cake" stacks of layers with areas decreasing away from the substrate surface. The fraction of the projected area of each island covered by 1, 2, ..., n layers is then calculated and substituted into Equations 7 and 8 in place of the $P_a(m)$'s.

Using Kuyser's value for $\lambda_{Pd330} = 12A$, one finds that a surface 27% covered by hemispherical Pd islands 50A in diameter would yield the same Pd 330 eV Auger signal as would a smooth monolayer of Pd. A substrate Auger peak with the same λ value would be equally attenuated by these two film forms. However, if $\lambda' < \lambda$ (primes refer to the substrate), the monolayer will provide greater attenuation of the substrate signal. If $\lambda' > \lambda$ the island form will yield greater attenuation, as can be seen in

Table VI-3. This different attenuation of substrate peaks by different film morphologies which should yield the same overlayer Auger intensity could provide a means to distinguish between film morphologies even when the evaporator flux to the surface is not constant as is the case for most of the data in Chapter VI.

The best method of judging the fit between the various film morphology models and the experimental data changes with different substrate-overlayer combinations. For Pd on graphite, interferences between the C and subsidiary Pd peaks impair the quality of the C attenuation data, but the Pd 46 eV peak is free from interference. One then compares monolayer or island coverages calculated from the Pd 46 eV, and Pd 330 eV signals and the attenuation of the C peak and checks for consistency amongst these three values. The internal consistency is poor, though slightly better for the island models at all coverages.

For Pd on TiO₂, overlap of peaks knocks out the low energy Auger data, and one is left with peaks having λ values too close for comfort. The method of comparison is to calculate the monolayer or island coverages consistent with the Pd 330 eV signal and the attenuations of the Ti 383 eV and O 597 eV signals, then to check for consistency amongst the three values. For deposition at room temperature (Table VI-4) the internal consistency is equally poor for the monolayer and 50A island models, and no conclusions can be drawn. For deposition with the surface at 800°C the internal consistency is better overall, and is quite good for the 50A island model at all except very low coverages. In the submonolayer region layer-by-layer growth gives slightly better fit than 50A islands, and Fig. VI-30 shows that the Poisson model gives an even

better fit. A model involving nucleation sites upon which islands grow would probably fit the data better at all coverages.

Pd on Al_2O_3 provides three substrate peaks at widely varying energies, but the Pd 46 eV peak is buried in stronger Al_2O_3 emissions. The coverage of Pd in monolayers or 50Å islands consistent with the Pd 330 eV signal were calculated, and the expected attenuation factors for the substrate peaks due to these coverages were calculated and compared with the measured attenuation factors. The results are not very conclusive, but again island growth gives a slightly better fit. This earlier method of data analysis is probably not as good as that used for graphite and TiO_2 in that the Pd data receive undue weighting.

The methods of Auger morphology determination used here did not give very definitive results. All that can be said for certain is that Pd evaporated onto TiO_2 at 800°C tends in large part to agglomerate. More conclusive results could be obtained with a quartz oscillator present to provide an absolute calibration of coverage and to determine any variation in evaporator flux.

Necessary Conditions for Determination of Film Morphology by Auger

Auger electron spectroscopy, with no auxiliary techniques, can provide absolute coverage calibration if (1) strict layer-by-layer growth occurs, (2) the sticking coefficient and evaporator flux are constant, and (3) substrate and overlayer Auger peaks of low-energy are available. In this case λ 's can be determined. If an independent measure of total coverage is available, backscattering factors can be calculated.

Even if layer-by-layer growth does not occur, some information on film morphology can be obtained, providing high and low-energy Auger peaks are available for both substrate and deposit. Fairly accurate coverages can be calculated provided that evaporator flux and sticking coefficients are constant.

If high or low-energy peaks are missing for substrate or deposit, morphology determination requires an independent measure of coverage. Complete determination of film morphology by Auger when the film consists of more than one phase is well-nigh hopeless.

For the study of metal overlayers on metals, where layer-by-layer or Stranski-Krastanov growth often occurs, LEED and Auger are appropriate techniques. For metals on nonmetals, where island growth and complex multiphase systems tend to occur, RHEED and electron microscopy appear to be more useful techniques, though advanced, high-resolution LEED systems might do well.

This report was done with support from the Department of Energy. Any conclusions or opinions expressed in this report represent solely those of the author(s) and not necessarily those of The Regents of the University of California, the Lawrence Berkeley Laboratory or the Department of Energy.

Reference to a company or product name does not imply approval or recommendation of the product by the University of California or the U.S. Department of Energy to the exclusion of others that may be suitable.

TECHNICAL INFORMATION DEPARTMENT
LAWRENCE BERKELEY LABORATORY
UNIVERSITY OF CALIFORNIA
BERKELEY, CALIFORNIA 94720